Robocasting of Complex Structural Ceramics

Qiaosong Cai

Supervisors:

Eduardo Saiz

Luc Vandeperre

Finn Guiliani

Centre for Advanced Structural Ceramics

Department of Materials

Imperial College London

Submitted for the degree of

Doctor of *Philosophy* (PhD)

‘Blank’ Page

Statement and Declaration

The work is all my own, except for all parts which have been appropriately referenced and acknowledged are someone else's.

Qiaosong Cai

The copyright of this thesis rests with the author. Unless otherwise indicated, its contents are licensed under a Creative Commons Attribution-Non Commercial 4.0 International Licence (CC BY-NC).

Under this licence, you may copy and redistribute the material in any medium or format. You may also create and distribute modified versions of the work. This is on the condition that: you credit the author and do not use it, or any derivative works, for a commercial purpose.

When reusing or sharing this work, ensure you make the licence terms clear to others by naming the licence and linking to the licence text. Where a work has been adapted, you should indicate that the work has been changed and describe those changes.

Please seek permission from the copyright holder for uses of this work that are not included in this licence or permitted under UK Copyright Law.



Abstract

Additive manufacturing (AM) has been recognized as a significant manufacturing method since it was developed in early 1980s. It is a technology usually based on 3D model files (CAD model) and layer by layer fabrication. Many AM technologies have been developed for manufacturing different range of materials such as metals and polymers while only a few of them are suitable for producing ceramic objects.

Robocasting (also called direct ink writing) is a ceramic AM technology which was developed to produce complex ceramic parts. The technology is based on extrusion of a paste that has to exhibit a shear thinning behaviour. However, one of the remaining challenges is the fabrication of parts with complex hierarchical structures or combining different materials.

In this thesis, porous ceramics with porosity from 10 % to 60 % and average pore size from 3 μm to 8 μm were produced by robocasting emulsion-based inks. Ceramic matrix composites with continuous steel fibres were fabricated successfully by extruding filaments with a novel core/shell structure. The composites reinforced with the steel fibres have an increasing of toughness without sacrificing the strength of the products. Density, strength and toughness of the products were measured to analyse their reliability.

Acknowledgements

I would like to give my appreciation to people who helped me go through my PhD project.

First, I want to thank the CASC industrial consortium to give me the opportunity to do the research project in CASC.

My fantastic supervisors: Eduardo, Luc and Finn. Thank you for your supporting during this period.

All the technical staff who gave me a lot help with my experiments: Mahmoud, Cati, Garry, Richard.

Sylvain and Jerome from INSA Lyon, thanks for your kindness and patience to let me do the mechanical test in France.

Surely, my parents, thank you for supporting me doing my PhD, I love you forever.

Finally, my dear friends and colleagues in CASC: Alba, Annalisa, Claudio, Dan, Eleonora, Esther, Ezra, Francesca, Giorgio, Gloria, Harry, Iuliia, Jack, Jiahui, Justine, Kathryn, Maktari, Ming, Na, Nasrin, Ollie, Oriol, Pin, Rowan, Sam, Shitong, Tianhui, Tomomaso, Yinglun. You made my PhD a real fun and wonderful period.

Conference and Papers

Out of IC

Rheology of emulsion-based inks for robocasting (poster, flash presentation, MAPP 1st International conference, 30th-31st January 2018, Sheffield, UK)

Robocasting of ceramics with core/shell structures (poster, flash presentation, 9th International Workshop on Interfaces New Frontiers in Biomaterials, 16th-18th April 2018, Santiago De Compostela, Spain)

Robocasting of structural ceramics with core/shell structures (Presentation, 2019 young Ceramists Additive Manufacturing Forum, 3rd-5th April 2019, Mons, Belgium)

Non-Newtonian Club: Rheology for Processing, 19th September 2019, Nottingham, UK

Robocasting of long fibre composites using core/shell filaments (poster, MAPP Mid-term Review, 12nd March 2020, Sheffield, UK)

In IC

1 Day Research meeting on Advanced Ceramics(1-DRAC), 7th April 2017, Imperial College, UK

1st Meeting of the UK Chapter of the American Ceramic Society

CASC 10-year Anniversary, 14th of September 2018, Imperial College, UK

CASC Industry Day of CASC (2017-2020)

CASC Summer School (2017-2019)

European Ceramics Society Student Speech Contest, 26th March 2019, Imperial College, UK

Two papers in preparation:

1) Printing of porous ceramics with emulsion-based inks

2) Robotic assisted deposition of metal-ceramic composites

Table of Contents

Introduction....27

Chapter 1: Literature Review....29

1.1Additive Manufacturing of Ceramics....30

1.2 Introduction to Robocasting....32

1.2.1 Factors for Robocasting....32

1.2.2 Process of Robocasting....35

1.2.3 Advantages and Limitations of Robocasting....36

1.2.4 The Wide Range Applications of Robocasting....36

1.2.5 Inks for Robocasting....36

1.2.5.1 Hydrogel Inks....37

1.2.5.2 Colloidal Inks....38

1.2.5.3 Emulsified Inks and foam gels....40

1.2.5.3.1 Introduction to emulsions....40

1.2.5.3.2 Emulsions and foam gels for gel-casting ceramics....41

1.2.5.3.3 Emulsions for robocasting....44

1.2.6 Rheology of the Inks....45

1.3 Porous Ceramics....52

1.3.1 Introduction to porous ceramics....52

1.3.2 Manufacturing Routes of Porous Ceramics....52

1.4 Core/shell structures....55

1.4.1 Composites produced by robocasting....55

1.4.2 Co-extrusion technology 57
1.4.2.1 Blocked Nozzle Method (for hollow filaments only) 57
1.4.2.2 Co-extrusion Method 58
1.4.2.3 Multicore/shell structure 59
1.4.2.4 Core/shell structure with short carbon fibre reinforcement 59
1.4.2.5 Limitations of the co-extrusion technologies 60
1.5 Summary 61
Chapter 2: Aims and Objects 62
Chapter 3: Methods 63
3.1. Sample preparation 64
3.1.1 Emulsion based inks 64
3.1.1.1 synthesis of Branched Copolymer Surfactant (BCS) 64
3.1.1.1.1 Materials 64
3.1.1.1.2 Process 64
3.1.1.2 Ink preparation 65
3.1.2 Pluronic based inks 66
3.1.2.1 Materials 66
3.1.2.2 Ink preparation 67
3.1.3 Core/shell structure 69
3.2. Manufacturing Processes 71
3.2.1 Printing 71
3.2.2 Post-processing 73
3.3. Characterization 75
3.3.1 Rheology 75

3.3.1.1 Introduction to rheology and use of the rheometer 75
3.3.1.2 Rheology measurement 76
3.3.2 Droplet size of emulsions 77
3.3.3 Measurement of porosity and density 78
3.3.4 Mechanical testing of emulsion-based samples 80
3.3.5 Mechanical characterization of core/shell samples 80
3.3.5.1 Mechanical measurements 80
3.3.5.2 Microstructural and Compositional Analysis 85
3.3.5.2.1 X-ray Diffraction (XRD) 85
3.3.5.2.2 Scanning Electron Microscopy (SEM) and SEM- Energy Dispersive Spectrometer (EDS) 86
Chapter 4: Rheology of emulsion-based inks for robocasting 89
4.1. Robocasting of Porous Ceramics 90
4.2 Sample components 91
4.3. Results and discussion 92
4.3.1 Rheology of emulsified slurries 92
4.3.1.1 Time sweep measurement 92
4.3.1.2 Temperature ramp measurement 93
4.3.1.3 Flow ramp and oscillation amplitude measurement 93
4.3.1.4 Rheology of samples with different oil content or stirring speed 116
4.3.1.4.1 Evolution of viscoelastic fingerprints 116
4.3.1.4.2 Hysteresis 119
4.3.2 Size of oil phase in emulsions and microstructure of printed emulsion samples 126
4.3.3 Printability of the emulsion-based inks 129

4.3.3.1 Largest span that can be printed using the emulsion inks.....130

4.3.3.2 Criterion for a minimum yield stress, a maximum height of the emulsion inks.....131

4.3.3.3 Criterion about the relationship between storage modulus and flow point 133

4.3.3.4 Shear stress profile of the inks in the nozzle during printing 134

4.3.4 Printed Samples with Different emulsion-based inks.....136

4.3.5 Microstructure and Strength of the printed samples.....137

4.4. Conclusion 142

Chapter 5: Core/shell structural ceramic composites.....143

5.1 Introduction.....144

5.2 Results.....145

5.2.1 Rheology Property of the hydrogel inks 145

5.2.1.1 Effect of Pluronic concentration on liquid-gel temperature transition 145

5.2.1.2 Effect of alumina concentration on liquid-gel temperature transition 145

5.2.1.3 Properties of different inks.....146

5.2.1.3.1 Properties of alumina inks 146

5.2.1.3.2 Properties of C-alumina inks 150

5.2.1.3.3 Properties of iron oxide inks.....152

5.2.1.3.4 Properties of iron and steel inks.....155

5.2.1.3.5 Property of three inks for co-extrusion 157

5.2.1.3.5.1 Flow ramp 157

5.2.1.3.5.2 Oscillation amplitude sweep.....157

5.2.2 Structural characterization 158
5.2.2.1 Shrinkage of the printed samples 158
5.2.2.2 SEM analysis 158
5.2.2.3 Volume fraction of steel in the core/shell structure 162
5.2.2.4 Density and porosity 163
5.2.2.5 Analysis of interface between the fibre and the alumina about the possible reactions 164
5.2.2.5.1 X-ray diffraction (XRD) 164
5.2.2.5.2 SEM-EDS map results 166
5.2.3 Mechanical testing 171
5.2.3.1 Single fibre mechanical testing 171
5.2.3.2 Strength and fracture of grids 173
5.2.3.3 Strength of polished and un-polished bars 174
5.2.3.3.1 Four-point bending test of bar shaped samples 174
5.2.3.3.2 Three-point bending test of SENB samples 176
5.2.3.4 In-situ Tensile test of dog-bone samples 179
5.2.3.5 Fracture toughness (K_{IC}) 180
5.2.3.6 Work of fracture 181
5.2.3.7 Cyclic three-point bending tests 184
5.3 Discussion 187
5.3.1 Factors that affect the liquid-gel transition 187
5.3.2 Rheological property of different inks. 188
5.3.3 Printability of the hydrogel inks 189
5.3.4 The shear stress profile of the inks across the nozzle during printing 190
5.3.5 Rheology of inks not suitable for co-extruding 191

5.3.6 Structure characterization of the core/shell samples....193
5.3.6.1 Microstructure....193
5.3.6.2 Steel volume fraction, density and porosity....194
5.3.6.3 Analysis of interface reactions....195
5.3.7 Mechanical tests....196
5.3.7.1 Thermal residual stress in the samples....196
5.3.7.2 Three-point bending test of single filaments....201
5.3.7.3 Compressive measurement of grids....201
5.3.7.4 Mechanical property of bar shaped samples....201
5.3.7.4.1 Strength of different bar shaped samples....201
5.3.7.4.2 Fracture behaviour of the bar shaped samples....204
5.3.7.4.3 Predicted work of fracture calculated using work of deformation....206
5.3.7.5 Variation of strength with fibre content....208
5.3.7.5.1 Flexural strength....208
5.3.7.5.2 Tensile strength....208
5.3.8 Cyclic three-point bending tests....209
5.3.9 Hardness test of the core/shell composites....210
5.3.10 The influence of the fibre shape on the mechanical properties of the products....211
5.4 Conclusion....212
6. Conclusion and Future work....213
6.1 Conclusion....214
6.2 Future Work....215
6.2.1 Light materials....215

6.2.2 Core/shell ceramic/ceramic.....216

6.2.3 Interfacial engineering.....217

References.....218

List of Tables

Table 1. Categories of fluids that can be described by Herschel-Bulkley model. Reproduced with permission from[20]……...…..33

Table 2. Rheology of different ink from literature……..…50

Table 3. Comparison of short carbon fibre reinforced composites. Reproduced with permission from[20]……..……...57

Table 4. Compositions of the emulsified samples…….91

Table 5. Rheological properties of emulsion samples…….……105

Table 6. Rheological properties of emulsions/foams from different reports……...115

Table 7. Degree of recovery of different emulsified slurries……...118

Table 8. σ_y^{Stat} , σ_y^{Dyn} and flow points of the selected emulsion samples……..126

Table 9. The density and largest span of different emulsion samples……..130

Table 10. Minimum τ_{fp}, h_{max}, Ξ and Ξ_γ of different emulsified slurries…….…..132

Table 11. Density and Porosity of emulsion samples. Although standard sample 2 bars cannot be printed, a small bar was cut from the extruded paste for the measurement……..138

Table 12. Strength of porous ceramics (mostly robocasting and gel-casting with emulsions/foams) from different reports…….140

Table 13. Al_2O_3 and steel volume fraction, density, ratio and porosity of different samples……...164

Table 14. Average strength of different single filaments……173

Table 15. Tensile strength of dog-bone samples…….180

Table 16. Rheology of hydrogels used in this work (25 wt% Pluronic at 25 ℃)……...189

Table 17. Elastic modulus, Poisson ratio and coefficient of thermal expansion of Al_2O_3 and steel……..199

Table 18. Thermal residual stresses in the core/shell samples…….200

Table 19. Fracture toughness, works of fracture and strengths of different composites.205

Table 20. Predicted work of fracture of different samples……...207

List of Figures

Figure 1. Categorization of ceramic additive manufacturing technologies (based on Feilden's PhD thesis). Adapted with the permission from[20]……..31

Figure 2. Yield stress *vs.* storage modulus for different pastes. Reproduced with permission from[20]…….34

Figure 3. A warped SiC bar due to drying too fast. Reproduced with permission from[20]……...35

Figure 4. A) Extruding inks from a syringe, B) Sintered ceramics manufactured by Robocasting. Adapted with permission from[11]…….35

Figure 5. A) The chemical formulation of a Pluronic F-127® molecule; B) Viscosity of a 25 wt% Pluronic solution at a shear rate of 1 s^{-1} as a function of temperature, there is a sharp increasing of viscosity between 20 ℃ to 25 ℃. Adapted with permission from[11]…….38

Figure 6. a) Fluid-to-gel transition; b) Plot of zeta potential as a function of pH for PEI-coated and un-coated silica microspheres suspended in water; c) The different shear elastic modulus of a weak gel (pH 9.5) and a strong gel (pH 9.75) as a function of shear stress. Adapted with permission from[16]…….39

Figure 7. A, B) An emulsion system; C, D) The interface between continuous phase and dispersed phase in a Pickering emulsion; E) Interfacial tension balance between different interfaces (γ_{wp} is the water/particle interfacial tension, γ_{op} is the oil/particle interfacial tension and γ_{wo} is the water/oil interfacial tension). The ideal contact angle (θ) is 53° for emulsification with Pickering approach.[31]…….41

Figure 8. A) Structure of a BCS molecule and the attachment of BCS molecules on a ceramic particle; B) The aggreation of BCS attached particles in the emulsion water/oil interface. Adapted with permission from[34]……...42

Figure 9. Dissolution and hydrolyzation of GδL molecules in water……43

Figure 10. Relationship of solid loading, emulsification speed, porosity, pore size and cell type. Adapted with permission from[34]……..44

Figure 11. A)top: scheme of a shear experiment; bottom: individual layers of a material during a shear experiment; B) scheme of a extension experiment. Adapted with permission from[41]……..……47

Figure 12. A) Stress-strain curve of a shear experiment; B) Loading-unloading curves of a shear experiment. Adapt with permission from[41]……...48

Figure 13. The relationship among G*, G' and G'' using the phase-shift angle δ…….48

Figure 14. The oscillation behaviour as a function of frequency for A) Liquid; B) Gel; C) Solid response. Adapted with permission from[30]……..49

Figure 15. Conventional routes for manufacturing porous ceramic: a) Replica technique; b) Sacrificial template technique; c) Direct foaming technique. Reproduced with permission from[32]……...53

Figure 16. A) SEM image of a crack in Al_2O_3 platelet-polymer composite; B) Fracture surface of the PMC composite; C) Fracture surface of a green SiC – Cf part. Adapted with permission from[20]…….56

Figure 17. A) Hollow filaments printed in an oil bath, B) Process of co-axis printing of bioceramics. Adapted with permission from[70,71]……58

Figure 18. Example of the use of co-extrusion method to print filaments with hollow cores. Adapted with permission from[72]……...59

Figure 19. Method for multicore/shell structure. Adapted with permission from[74]…..59

Figure 20. Schematic of preparing core/shell parts. Adapted with permission from[75]...60

Figure 21. Synthesis of BCS via thiol-regulated free radical polymerization……..64

Figure 22. A BCS molecule, an oil droplet, a ceramic particle (top); Change of aggregation with pH. In this schematic, all BCS molecules are absorbed on the ceramic particles and there is no free BCS in the oil-water emulsion system (bottom)……65

Figure 23. SEM images of A) Al_2O_3; B) Steel; C) Graphite; D) Iron particles…….67

Figure 24. A) A Thinky ARE-250 mixer, courtesy of Intertronics Ltd; B) Hydrogel paste before, during and after mixing; C) syringes and supplements for robocasting……68

Figure 25. Process of preparing printing cartridges with core/shell structure……70

Figure 26. The schematics and images of plastic conical nozzle and the steel straight nozzle……...……72

Figure 27. A picture of a robocaster in an enclosed cabinet…….72

Figure 28. Printing orientation of A) Emulsion and hydrogel bars; B) hydrogel dog-bones; C) Hydrogel grids (3D models at right bottom corner)……..73

Figure 29. The schematics of A) parallel geometry; B) cone-plate geometry; C) concentric cylinder; D) capillary rheometer……...75

Figure 30. A) A Discovery HR-1 hybrid rheometer, courtesy of TA Instrument®; B) a picture of 40 mm parallel steel geometry, courtesy of TA Instrument®……76

Figure 31. The image of an emulsified suspension. The spheres are oil droplets dispersed in water. The BCS-functionalized particles segregate to the water-oil interface and are made visible due to the rhodamine……77

Figure 32. Image J analyse of the pore size and distribution of an emulsion-based sample. A) Original SEM image; B) The image after finding edges and smoothing; C) The image after threshold; D) The image after size analysing……79

Figure 33. Image J analyse of the volume fraction of the steel in the core/shell structure. A) Original SEM image; B) The image after threshold; C) The image after size analysing…...80

Figure 34. A) Four-point bending; B) Three-point bending on a SENB sample (LVDT); C) microtest stage and tools for in-situ tests…….83

Figure 35. A) A single filament on the microtest stage; B) A SENB sample; C) A dog-bone shaped sample on the microtest stage……..83

Figure 36. A) Grids; B) Bar shaped samples; C) Designed dog-bone; D) Printed dog-bone……..84

Figure 37. Compression test on a grid……..84

Figure 38. Bragg diffraction of two incident x-ray beams with identical wave length and phase onto a crystalline solid. Adapted with permission from[39]……..85

Figure 39. Signals generated from the interaction between the focused electron beam and the specimen. Adapted with permission from[39]…….87

Figure 40. SEM-EDS Map images of a two cores core/shell composite (steel core, alumina shell)…….88

Figure 41. Time sweep of emulsions at 1Hz and 5×10^{-5} rad after addition of GδL. G' is storage modulus and G'' is loss modulus. When G' is larger than G'', the emulsion acts like a gel while if G'' is larger than G', the suspension has a liquid-like behaviour. All these samples were emulsified under a stirring speed of 8000 rpm…….…..……92

Figure 42. Temperature ramp of 40-2-2, 40-2-1, 40-1-2, 30-2-2 emulsified slurries (stirred under 8000 rpm)……93

Figure 43. Variation of viscosity with shear rate for a 40-2-2 emulsified slurry. The approximate shear rates during printing are indicated in the graph…….94

Figure 44. Oscillation amplitude sweep of a 40-2-2 emulsion to obtain flow point, yield point and equilibrium storage modulus……94

Figure 45. Shear rate and applied stress of emulsion samples…….101

Figure 46. A) Viscosity at printing speed, B) equilibrium storage modulus, C) flow point and yield stress [The solid symbols are flow points gained from modulus cross point (Figure 44) and the open symbols are yield stress gained from shear stress *vs.* shear rate graphs (Figure 45)] and D) yield point of emulsions with different compositions……...103

Figure 47. FTI of emulsions with different compositions……..104

Figure 48. Viscosity, yield stress, yield point, flow point and equilibrium storage modulus of samples with different GδL concentration……..106

Figure 49. Viscosity, yield stress, yield point, flow point and equilibrium storage modulus of samples with different BCS concentration…….108

Figure 50. Viscosity, yield stress, yield point, flow point and equilibrium storage modulus of samples with different solid loading……...110

Figure 51. Plot of relative viscosity as a function of solid volume fraction……111

Figure 52. Viscosity, yield stress, yield point, flow point and equilibrium storage modulus of samples with different oil content……..112

Figure 53. Plot of relative viscosity as a function of decane volume fraction…….113

Figure 54. Viscosity, yield stress, yield point, flow point and equilibrium storage modulus of samples with different emulsification speed……..114

Figure 55. Oscillation sweeps for emulsified slurries…….117

Figure 56. Hysteresis viscosity measurement of emulsions……121

Figure 57. Hysteresis stress measurement of samples (the measurement of static yield stress is agreed with the results also shown in Figure 45)……123

Figure 58. Viscosity *vs.* Shear rate of hysteresis measurement……..125

Figure 59. Microstructure and average size of bubbles in emulsions and pores of printed emulsion samples (sample 7 and 9 were not printable; sample 1, 2 and 3 start from the same suspension before adding GδL)……..129

Figure 60. Storage modulus *vs.* Flow point of different inks…….…….134

Figure 61. Shear stress profile of emulsion samples extruded through a 410 μm nozzle…….135

Figure 62. The loss of organisation of emulsions during printing. (a) Initial emulsion structure in the nozzle when the emulsion starts to flow. (b) Oil droplet disruption due to the high shear stress near the nozzle wall. (c) Oil droplet structure breakdown causes oil droplet coalescence. (d) The formation of large oil droplets on the surface of extruded filaments. Reproduced with permission from[39]……...136

Figure 63. Sintered printed emulsion samples…….…137

Figure 64. Stress applied on the representative specimen during three-point bending test……..138

Figure 65. Porosity *vs.* bending strength of the sintered emulsion samples……139

Figure 66. Relative density vs. bending strength of the sintered emulsion samples…...139

Figure 67. Comparison of strength of porous alumina ceramics……..……..141

Figure 68. Temperature ramp of solutions with different Pluronic concentration……...145

Figure 69. Temperature ramp of pastes prepared with a 25 wt% Pluronic solution but different solid loadings……...146

Figure 70. Flow ramp of inks with Al_2O_3 concentration from 30 vol% to 45 vol%. (Colour band is the viscosity and shear rate during printing and Pluronic concentration is 25 wt% here)……...147

Figure 71. Oscillation amplitude sweep of inks with Al_2O_3 concentration from 30 vol% to 45 vol% (The lines indicate the flow point of the 30 vol%, 35 vol%, 40 vol%, 45 vol% from left to right respectively)……...147

Figure 72. Relationship between viscosity and solid concentration at a shear rate of 6 s^{-1}……148

Figure 73. Example of calculation of *n* and *K* using 35 vol% Al_2O_3 ink……149

Figure 74. *n* of inks with different solid loading……..149

Figure 75. *K* of inks with different solid loading……150

Figure 76. Flow ramp of 35 vol% C-Al_2O_3 ink……151

Figure 77. Oscillation amplitude sweep of 35 vol% C-Al_2O_3 ink……151

Figure 78. $ln(\tau - \tau_{fp})$ *vs.* $ln(\dot{\gamma})$ of 35 vol% C-Al_2O_3 ink……152

Figure 79. Flow ramp of 25 vol% and 35 vol% Fe_2O_3 ink……153

Figure 80. Oscillation amplitude sweep of 25 vol% and 35 vol% Fe_2O_3 ink (The lines indicate the flow point of the 25 vol% and 35 vol% Fe_2O_3 from left to right respectively)……153

Figure 81. $ln(\tau - \tau_{fp})$ *vs.* $ln(\dot{\gamma})$ of 35 vol% Fe_2O_3 ink……154

Figure 82. Optical microscopy of cross section of composite samples printed core/shell Fe_2O_3/Al_2O_3 filaments (Sintered in vacuum at 1550 ℃ and the dark holes indicate the Fe_2O_3 cores)……154

Figure 83. Flow ramp of different steel and iron ink……..155

Figure 84. Oscillation amplitude sweep of different steel and iron ink (The lines indicate the flow point of the 35 vol% Iron, 30 vol% Steel, 35 vol% Steel from left to right respectively)……..156

Figure 85. $ln(\tau - \tau_{fp})$ *vs.* $ln(\dot{\gamma})$ of different steel and iron ink……156

Figure 86. Flow ramp of three different inks……..157

Figure 87. Oscillation amplitude sweep of different inks……158

Figure 88. Unpolished and polished cross section of pure Al_2O_3 bars and core/shell bars…….160

Figure 89. Polished cross section of grid samples: A) Al_2O_3; B) 1-core; C) 2-core; D) 3-core; E) C-interface……161

Figure 90. Image J analyse of the volume fraction of the steel in the core/shell structure……..162

Figure 91. Photographs of A) ground 1 core sample; B) the steel fibres which can be separated using a magnet……164

Figure 92. XRD pattern of A) Al_2O_3 matrix; B) Steel fibres; C) samples with different components…….165

Figure 93. SEM-EDS map results of an Al_2O_3 grid sample (bottom part is epoxy resin)……...166

Figure 94. SEM-EDS map results of a 1-core grid sample…….167

Figure 95. SEM-EDS map results of a 2-core grid sample…….168

Figure 96. SEM-EDS map results of a 3-core grid sample……..169

Figure 97. SEM-EDS map results of a C-interface grid sample……..170

Figure 98. A-B) a 1-core single filament before and after bending test; C) Displacement-Stress curve of the 1-core single filament during bending; D-E) a 2-core single filament before and after bending test; F) Displacement-Stress curve of the 2-core single filament during bending; G-H) a 3-core single filament before and after bending test; I) Displacement-Stress curve of the 3-core single filament during bending; J-K) a C-interface single filament before and after bending test; L) Displacement-Stress curve of the C-interface single filament during bending; M-N) an Al_2O_3 single filament before and after bending test; O) Displacement-Stress curve of the Al_2O_3 single filament during bending…….172

Figure 99. A) Compression test of an Al_2O_3 grid (breaking with steps); B) Compression test of a 1-core steel/Al_2O_3 grid (steel filaments hold the grid together by bending)……173

Figure 100. Deformation-stress curves of grids with different components……..174

Figure 101. Strain-stress of A) polished and B) unpolished samples……...175

Figure 102. Strengths of different samples……..176

Figure 103. A) continuous Displacement-force curves of SENB samples; B) continuous Strain-stress curves of SENB samples……177

Figure 104. A) SEM graphs of a 1 core SENB bar under in-situ bending test; B) Displacement-stress curve of the 1 core sample during the bending……..178

Figure 105. A) Before cracking; B) after cracking; C) Displacement-Stress curve of a 1 core dog-bone sample; D) Displacement-Stress curve of an Al_2O_3 dog-bone sample; E) Displacement-Stress curve of a C-Interface dog-bone sample……179

Figure 106. K_{IC} of different SENB samples……181

Figure 107. The displacement-load curve which gives the energy input during fracture process of a 1-core bar sample……182

Figure 108. Works of fracture of different SENB samples……183

Figure 109. Works of fracture of different samples……184

Figure 110. A) Cyclic Displacement-force curves of SENB samples; B) Cyclic Strain-stress curves of SENB samples……...185

Figure 111. A) Slopes of Displacement-force curves of SENB samples; B) Slopes of Strain-stress curves of SENB samples……186

Figure 112. Liquid-gel transition temperature of solutions with different Pluronic concentration (the empirical liner fitting is valid from 20 to 40 wt%)……187

Figure 113. Storage modulus *vs.* Flow point of different hydrogel inks……..190

Figure 114. Shear stress profile of hydrogel inks extruded through a 410 μm nozzle…..191

Figure 115. (A) Flow ramp and (B) Oscillation amplitude ramp of 40 vol% Al_2O_3 and 25 vol% Fe_2O_3 inks (two lines indicate the flow points of 25 vol% Fe_2O_3 and 40 vol% Al_2O_3, respectively)……..192

Figure 116. A) A syringe with a perfect Al_2O_3/Fe_2O_3 core/shell loading; B) The cross section of the printed Al_2O_3/Fe_2O_3 core/shell sample……193

Figure 117. Photograph of a 1-core sample sintered at 1550 ℃ with steel drops on the sample surface……194

Figure 118. Ellingham Diagram. Reproduced with permission from[96]……...195

Figure 119. A concentric cylinder with core/shell structure and stress on a piece of the structure. Reproduced with permission from[97]……196

Figure 120. Polished surface of an alumina dog-bone sample……203

Figure 121. The stress-strain curve of a cement reinforced with long steel fibres. Reproduced with permission from[105]…….204

Figure 122. Work of fracture of the samples with different experimental fibre concentration……..206

Figure 123. Strain-stress curves of 430 stainless steel at different temperature. Adapted with permission from[109]…….207

Figure 124. Flexural strength *vs.* experimental fibre content of the core/shell samples (An average value of polished and unpolished samples is used here as they are similar)…..……..208

Figure 125. A) Indentation on the Al_2O_3 part; B) Indentation on the steel part; C) Indentations on the cross section……211

Figure 126. SEM graphs of A) polished cross section of a porous/dense core/shell bar; B) polished cross section of a porous/dense core/shell grid; C) the interface between the porous core and dense shell of a polished grid……215

Figure 127. Optical microscopy graph of the cross section of a porous/dense core/shell bar with some water permeating through the porous channels (the arrows indicate the position of water droplets)……216

Figure 128. Cross section of a core/shell sample with graphene interface…….217

Abbreviations

Acronym	*Meaning*
AIBN	2, 2-Azobisisobutyronitrile
AM	Additive Manufacturing
BCS	Branched Copolymer Surfactant
BSE	Backscattered Electrons
BJ	Binder Jetting
CIP	Cold Isostatic Press
CMC	Ceramic Matrix Composite
DDT	1-Dodacanethiol
DED	Direct Energy Deposition
DUDMA	Diurethane Dimethacrylate
EGDMA	Ethylene glycol Dimethacrylate
EO	Ethylene Oxide
FDC	Fused Deposition of Ceramic
FDM	Fused Deposition Modelling
FTI	Flow Transition Index
GO	Graphene Oxide
GδL	Gluconic-δ-lactone
HA	Hydroxyapatite
IJP	Ink Jet Printing
LENS	Laser Engineered Net Shaping

LOM	Laminated Object Modelling
LSD	Layerwise Slurry Deposition
LVDT	Linear Variable Differential Transformer
MAA/MA	Methacrylic Acid
PAN	Poly(acrylonitrile)
PEG	Poly(ethylene glycol) Methyl Ether Methacrylate
PEGMA	Poly(ethylene glycol) Methacrylate
PEI	Poly(ethylenimine)
PEO	Poly(ethylene) Oxide
PMC	Polymer Matrix Composite
PO	Propylene Oxide
PPGDMA	Poly(propylene glycol) Dimethacrylate
PPO	Poly(propylene) Oxide
PTFE	Poly Tetra Fluoroethylene
PVA	Poly(vinyl alcohol)
RC	Robocasting
SEM	Scanning Electron Microscope
SENB	Single-Edge Notched Bend
SLA	Stereolithography
SLM	Selective Laser Melting
SLS	Selective Laser Sintering
β-TCP	β-tricalcium phosphate
XRD	X-ray Diffraction

Introduction

Additive manufacturing (AM) is a technology which builds a three-dimensional structure layer by layer. Due to the differences with other conventional manufacturing technologies that often use moulds or machining to build parts, AM has received interest from industry and academia and has been used in a wide range of fields. The possible advantages of AM over conventional processing technologies include complex shapes, less energy waste, possibility of mould free fabrication and rapid prototyping.[1, 2]

Most AM technologies focus on manufacturing metallic[3] or polymeric[2] materials while only a few of them focus on producing ceramic products. Some of these technologies fabricate ceramic parts directly such as Selective Laser Sintering/Selective Laser Melting (SLS/SLM)[4-6] and Laser Engineered Net Shaping (LENS)[7]. Some technologies create a green body first which is followed by drying (sometimes) and sintering to form a dense part. Robocasting is such a kind of technology which creates the green body layer by layer by extruding a ceramic paste.[8, 9]

Researchers have done a lot work on producing objects, including dense parts and woodpile structures by robocasting different ceramic materials.[10-16] Some microporous ceramics were also produced successfully by using emulsion-based[17, 18] or foam-based inks[17, 19]. However, to produce porous structures with specific predesigned pore parameters is still difficult. Besides, almost all researchers use homogeneous inks to produce ceramic parts. In some case platelets or short fibres are added to the ink to introduce some reinforcements.[20] To produce more complex structures like ceramic matrices with long continuous fibres by robocasting remains an open challenge.

In this thesis, chapter one is a literature review which gives an overall review of the AM technologies for ceramics, especially robocasting. This chapter also reviews the work done on printing porous ceramics and composites. Chapter two gives the aims and objects of this thesis. Chapter three is the methods section describing the experimental details. Chapter four concentrates on the rheology of emulsions for robocasting, the emulsions are used to fabricate porous ceramics with designed microstructures. Chapter five describes the robocasting of ceramic parts reinforced with continuous metallic fibres using robocasting. The mechanical

properties of the materials are related to their structure. Finally, chapter six provides a summary of the main conclusions and some ideas for future research.

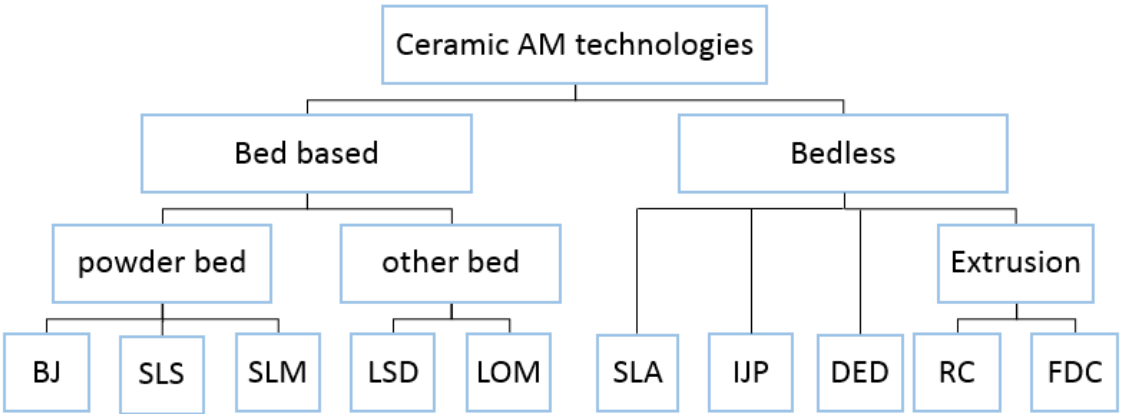
The porous ceramics fabricated by robocasting can be used as filters or thermal insulators. The composites with core/shell structures have an increasing of toughness which can be used for aerospace or healthcare applications.

Chapter 1: Literature Review

1.1Additive Manufacturing of Ceramics

ISO/ASTM 52903 defines additive manufacturing (AM) as 'process of joining materials to make parts from three-dimensional model data, usually layer upon layer, as opposed to subtractive manufacturing and formative manufacturing methodologies'.[21] Additive manufacturing was developed in the early 1980s and has received increasing attention from industry, academia and the public since then.[1, 2] AM can be used in a wide range of fields due to its advantages over traditional manufacturing methods such as the capability of building complex shaped objects and the shortening production cycles. AM technologies for printing polymeric[2] and metallic[3] materials have developed faster than those designed for ceramics. This is partly due to the high melting points of ceramic powders and their lower thermal conductivity which are problems when using direct sintering and melting technologies.[22]

There are several technologies that can be used for the additive manufacturing of ceramics. Normally, there are two principles to classify these technologies into different categories. One is dividing them into single-step processes and multi-step processes. The only two single-step processes are direct energy deposition (DED) and single-step powder bed fusion while other technologies are all multi-step processes.[23] Another way is separating them into powder-bed based processes and bed-less processes. Figure 1 shows the categorization of ceramic AM technologies using this criterion.



BJ – Binder jetting

SLS – Selective Laser Sintering

SLM – Selective Laser Melting

LSD – Layerwise Slurry Deposition

LOM –Laminated Object Modelling

SLA – Stereolithography

IJP – Ink jet printing

DED – Direct Energy Deposition

RC – Robocasting

FDC – Fused Deposition of Ceramics

Figure 1. Categorization of ceramic additive manufacturing technologies (based on Feilden's PhD thesis). Adapted with the permission from[20]

Each technology has its own advantages and disadvantages. Similar as FDC, robocasting fabricates a green body in a manner of layer-upon-layer stacking. However, robocasting relies on the shear thinning behaviour of the pastes, rather than the solidification, to maintain the shape of the products after being printed on the substrate. Robocasting can build up products with relatively dense parts while this is hard for some other technologies such as SLS/SLM, LOM and IJP. Robocasting can produce parts faster than other technologies in some cases as large nozzle (>1 mm) can be used in this technology. Another advantage of robocasting is that it can be used to print products with different materials while other technologies are mainly based on a single material. The main limitation of robocasting is printing spanning and overhanging features while some other technologies can overcome this such as SLS/SLM, LOM and BJ.[20]

1.2 Introduction to Robocasting

Robocasting (also called Direct Ink Writing) is a promising technology developed by Cesarano in 1997 to print complex ceramic shapes.[8, 9] It is a freeform fabrication technique based on the layer-wise deposition of ceramic pastes(also called inks). Similar to fused deposition modelling (FDM)[3], an ink loaded in a syringe is continuously extruded through a fine nozzle on a substrate layer by layer in a controlled environment (controlled temperature and humidity) to produce a periodic lattice or a monolithic body which is subsequently dried and sintered.[10] The FDM technology for producing 3D plastic structures uses a heater at the nozzle to keep a thermoplastic material at a temperature just above its melting point so that it can go through the nozzle smoothly. FDM have also been used to fabricate ceramics by introducing the ceramics powders into the thermoplastic polymer. After printing the polymer is burned out to leave the sintered ceramic part. Robocasting uses shear thinning pastes as the printing inks so that it in most cases does not need a heater at the nozzle.

1.2.1 Factors for Robocasting

Successful robocasting of ceramics requires the control of some factors.

Firstly, the solid loading of the ink is typically from 20 vol% to 60 vol% with the ceramic particle size ranging between 0.1 and 100 μm. The ink acts like a Newtonian fluid if the solid loading is too low, while for an ink with high solid loading, it is difficult to get the right rheology to make the ink flow through a nozzle at a reasonable pressure.[11] Generally, a high solid loading is desired as the higher the solid content, the higher the density of the final part and the smaller the dimensional changes (shrinkage) during sintering.

The rheology of the ink is another significant factor. Rheology is the study of the flow properties of liquids or soft solids which exhibit a viscoelastic response to an applied force.

The basic rheological property of a fluid should be the viscosity μ which defines as:

$$\mu = \frac{\tau}{\dot{\gamma}} \tag{1}$$

where τ is the applied shear stress and $\dot{\gamma}$ is the shear rate. Thus, the viscosity describes the resistance of a fluid to flow: a higher viscosity means the fluid needs more force to flow at a given shear rate.

The rheology of the robocasting inks is usually described using the Herschel-Bulkley model:

$$\tau = \tau_y + K\dot{\gamma}^n \quad (2)$$

where τ is the shear stress, τ_y is the yield stress, K is the viscosity parameter, $\dot{\gamma}$ is the shear rate and n is the shear thinning coefficient.[11, 24] The fluids that can be described by the model is shown in Table 1.

Table 1. Categories of fluids that can be described by Herschel-Bulkley model. Reproduced with permission from[20]

	$\tau_y = 0$	$\tau_y > 0$
$0<n<1$	Power Law Fluid (Shear thinning)	Herschel-Bulkley Fluid (Shear thinning)
$n=1$	Newtonian Fluid	Bingham Plastic
$n>1$	Power Law Fluid (Shear thickening)	Herschel-Bulkley Fluid (Shear thickening)

An ideal printable ink should have a high solid loading to decrease shape deformation during drying and sintering. It should be shear thinning (0<n<1) so that it can be extruded smoothly through the nozzle and maintain its shape under its own weight after being printed. In addition, the ink should have a moderate yield stress (100-2000 Pa) which is described as τ_y in equation 1, and high elastic modulus (G'>10 kPa). These are suggested value of τ_y and G' but the actual printability of the inks is also determined by the nozzle sizes and the robocaster parameters. Figure 2 gives a plot of G' and yield stress of a range of printable inks used in Feilden's thesis.[20]

If the yield stress is too low, the ink will flow like a liquid under small forces which means the part cannot maintain its shape, it will deform under its own weight or the capillary forces in which case the surface tension will deform the part.[25] If the yield stress is too high, the ink will not be extruded through a nozzle under a reasonable pressure. A high elastic modulus ensures that in wood pile structures or overhangs, the beams do not sag and maintain the shape after being printed.[12]

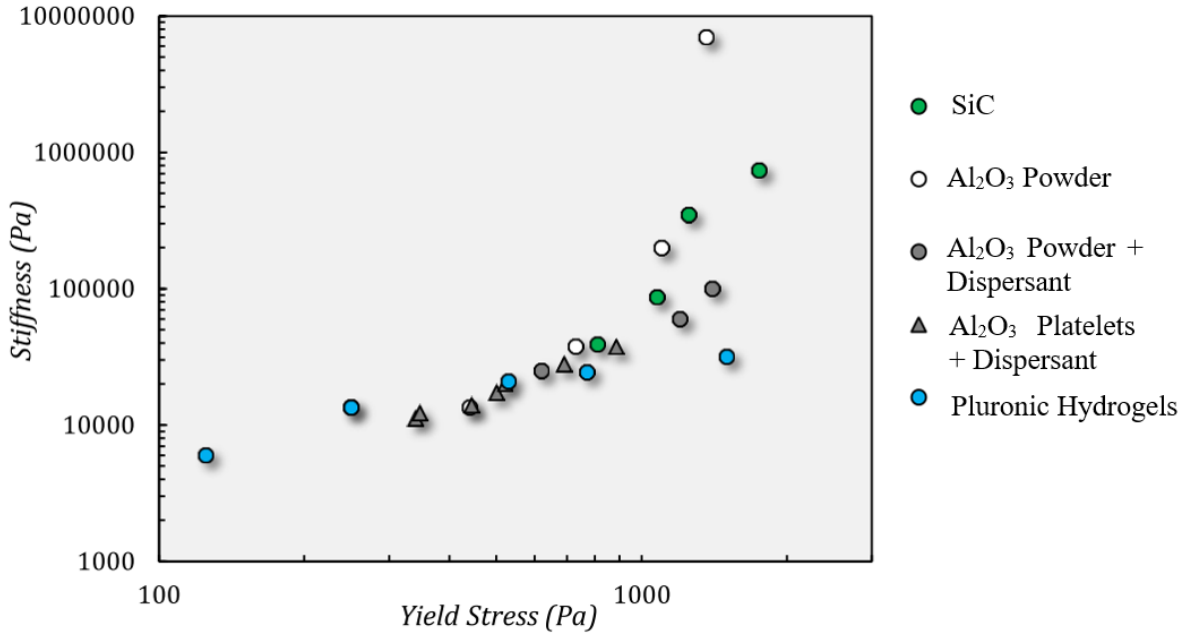


Figure 2. Yield stress *vs.* Storage modulus for different pastes. Reproduced with permission from[20]

The nozzle size determines the diameter of the printed filament which is typically between 100 to 1000 μm. Deposition with a finer nozzle can be used to build structures with a higher precision, while the use of large nozzles can increase the processing rate.

The printing speed of the filament is also important. Generally, a faster printing speed decreases the production time. However, it also reduces the accuracy of the path especially at corners when changing the printing direction. Normally, the suitable printing speed which gives a stable flow varies from 2 mm/s to 20 mm/s for most of the inks.[11]

The drying kinetics of the inks after being printed is of great importance. If the inks dry too fast during printing just after they leave the nozzle, the new printed layers will not be located above the drier layers below at the designed position which causes misalignment. In general, if the inks dry too fast after being printed, the printed objects may warp (due to inhomogeneous drying shown in Figure 3) or crack.[20] While if drying is too slow, the lower layers may sag under the weight of the upper ones and drying prior to sintering will take quite a long time which is undesirable for mass production. In addition, the drying shrinkage of the inks should be taken into consideration so that the final products have the desired sizes and structures. The drying kinetics is normally controlled by controlling the ink composition as well as the printing and drying environment including temperature and humidity.[20]



Figure 3. A warped SiC bar due to drying too fast. Reproduced with permission from[20]

1.2.2 Process of Robocasting

Before printing, fine powders such as alumina powders are mixed with solutions to form the shear thinning inks which are loaded into syringes ready for printing. Then, a digital 3D model is designed with the assistance of a software and the model is sliced into layers with a similar thickness to the nozzle diameter. A robocaster is used to extrude a continuous filament or ink on a flat and smooth substrate at a controlled speed in a controlled environment (temperature and humidity) from the syringe and form the 3D object layer by layer (Figure 4 A). Servo motors are used to control the path of nozzles with a high accuracy. The green body is typically very fragile and soft after being printed so drying, de-binding and sintering usually follow the printing step to give the object desired mechanical properties (Figure 4 B).

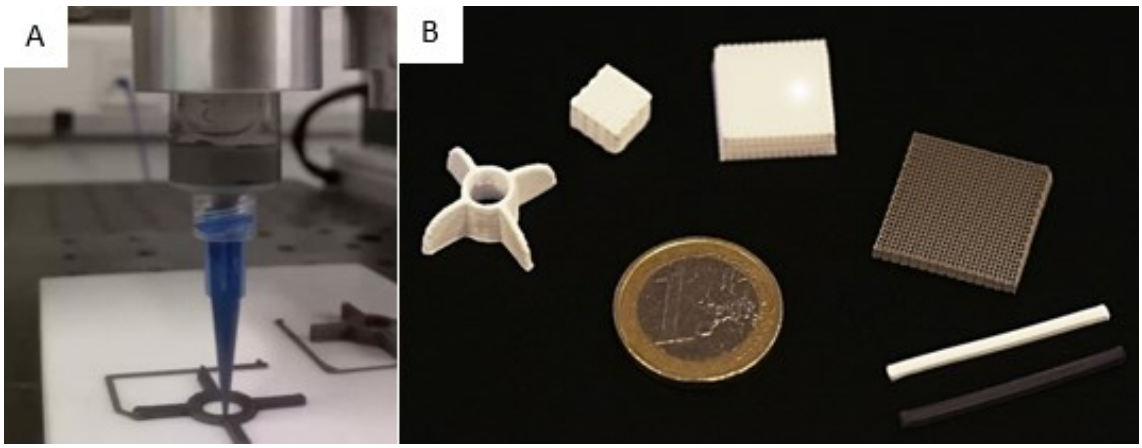


Figure 4. A) Extruding inks from a syringe, B) Sintered ceramics manufactured by Robocasting. Adapted with permission from[11]

1.2.3 Advantages and Limitations of Robocasting

Robocasting is a technology that can fabricate complex structures with a wide range of materials once these materials can be made into shear thinning inks. In addition, the inks can be extruded at room temperature which means saving a great deal of energy during manufacturing. Hence, robocasting is a promising technology for manufacturing ceramics with a significant flexibility to design the structures. Dense ceramics can be printed directly by stacking the printed filaments. Ceramics with macroporous structures can be printed by designing the tool paths of the nozzles[11] and microporous ceramics can be manufactured by using emulsified inks[17] or foam gels[19].

One of the main limitations of robocasting is the surface finish, in particular the step edges of the printed parts. The size of a step edge is determined by the diameter of the printed filament which is typically 100-1000 μm, while in other AM methods such as stereolithography (SLA) it can be as fine as 20 μm.[11] Another disadvantage of robocasting is that it is not suitable to deal with overhangs unless using some sacrificial structures.[13] In addition, very large parts are unable to be printed due to the limitation of the nozzle size which needs plenty of time to build large parts and the drying kinetics which may cause deformation and collapse during printing.

1.2.4 The Wide Range Applications of Robocasting

The ceramic structures produced by robocasting have been used in a wide range of applications, from photonic crystals[26] to bone engineering scaffolds[18]. The applications of robocasting are not limited to ceramic products. Structural metals can be manufactured by extruding metallic oxide inks into the scaffolds and sintering them in vacuum to reduce them into metals.[27] Metallic powders can also be made into pastes to be printed directly.[28] Polymers and sol-gel inks can also be printed into complex structures by using much finer nozzles with a diameter less than 2 μm.[14] Graphene has been successfully printed by robocasting as well.[15] This makes it possible to manufacture composite products with ceramics and other materials.

1.2.5 Inks for Robocasting

Robocasting was initially developed to fabricate structural ceramics with colloidal slurries.[8] Since then, different kinds of inks have been used for robocasting such as dense hydrogel inks and colloidal inks, emulsified or foamed inks with high porosity.

1.2.5.1 Hydrogel Inks

Hydrogel-based inks are prepared by dispersing fine particles in a hydrogel that provides the viscoelastic response required for robocasting. Several kinds of solutions have been used to prepare hydrogel inks for their shear thinning behaviour after being mixed with ceramic powders.

In Feilden's work, alumina powders and silicon carbide powders were mixed with Pluronic F-127 ® solutions to form the printing gels. The solid loading of the ink can reach up to 43 vol%.[11]

With polyethylene oxide and polypropylene oxide in a ratio of 2:1(PEO-PPO-PEO), a Pluronic F-127 ® solution has a temperature responsive behaviour. The structure of a Pluronic F-127 ® molecule is shown in Figure 5 A. When dissolved in aqueous solutions, these copolymers have a thermal reversible behaviour. They exist as molecules when the temperature or the Pluronic concentration is low. However, by increasing the temperature or Pluronic concentration, thermodynamically stable micelles are formed which results in an increasing of viscosity. The PPO content affects the critical micellization temperature: a higher PPO content makes the micellization temperature lower. As the temperature increases, the polarity of ethylene oxide (EO) and propylene oxide (PO) segments are decreased which leads to the micellization process.[29] As a result, the concentrated Pluronic F-127 ® aqueous solution has a liquid-like behaviour at low temperature (near 0 ℃) while a gel-like behaviour at high (normally around 20 ℃). This characteristic makes it an ideal solution to prepare hydrogels for robocasting. The most suitable concentration for a Pluronic solution here was ranging from 20 to 25 wt% with a micellization temperature around 20 ℃. A high concentration decreases the solid loading capacity of the solution and a low concentration gives insufficient stiffness and strength to the gels so that the inks cannot maintain their shape after being printed. The rheology of the inks can be varied by playing the Pluronic and particle concentrations in the ink and further manipulated by controlling the environment temperature and humidity during printing. In Feilden's work, the temperature and humidity were controlled within an enclosure. The heater was set to 23 ℃ and a humidifier was used to give the environment a humidity which was measured from 65 to 85 %.[11]

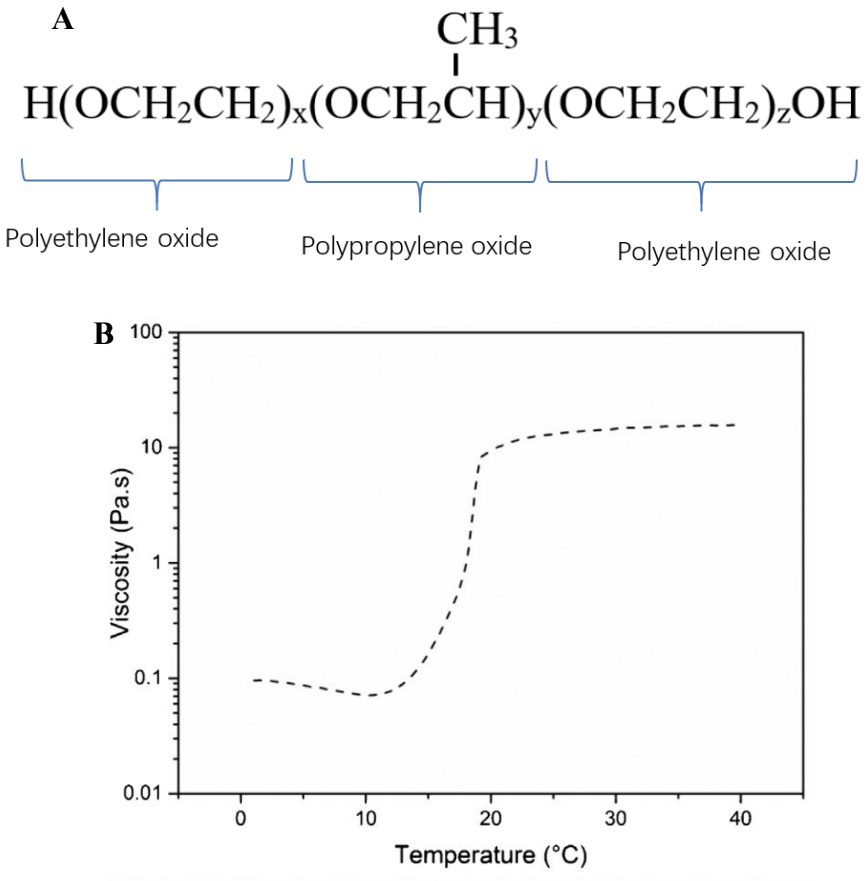


Figure 5. A) The chemical formulation of a Pluronic F-127® molecule; B) Viscosity of a 25 wt% Pluronic solution at a shear rate of 1 s^{-1} as a function of temperature, there is a sharp increasing of viscosity between 20 ℃ to 25 ℃. Adapted with permission from[11]

T. Schlordt's research group mixed alumina powders with CH_3COONH_4 (NH_4Ac) solutions and used NII_4 polymethacrylate as the dispersant to form hydrogel inks for robocasting. This system can achieve a solid loading as high as 52 vol%. During the printing, the temperature and humidity of the fabrication chamber were kept at 20 ℃ and 22 %, respectively. The rheology of the inks was mainly controlled by changing the content of the NH_4Ac coagulant.[12]

These hydrogel inks can be used to printing structural dense scaffolds or macroporous cellular structures such as woodpile frameworks.

1.2.5.2 Colloidal Inks

Colloidal inks are prepared by manipulating the influence of the interparticle (or surface) force on the suspension behaviour to create a gel. In order to get a gel, attractive interactions achieved by controlling the interparticle forces in the suspension and a concentration of particles above the gel point are required.[30]

Lewis's group used silica spheres coated with poly(ethylenimine) (PEI) as the matrix powders. The colloidal inks were prepared by directly suspending the powders in deionized water and the rheology was controlled simply by changing the pH of the suspension. The pH of the suspension was adjusted near the point-of-zero charge to make the suspension strong enough for printing. A strong flocculated particle network which has strong attractive interaction is achieved at this pH (Figure 6).[16]

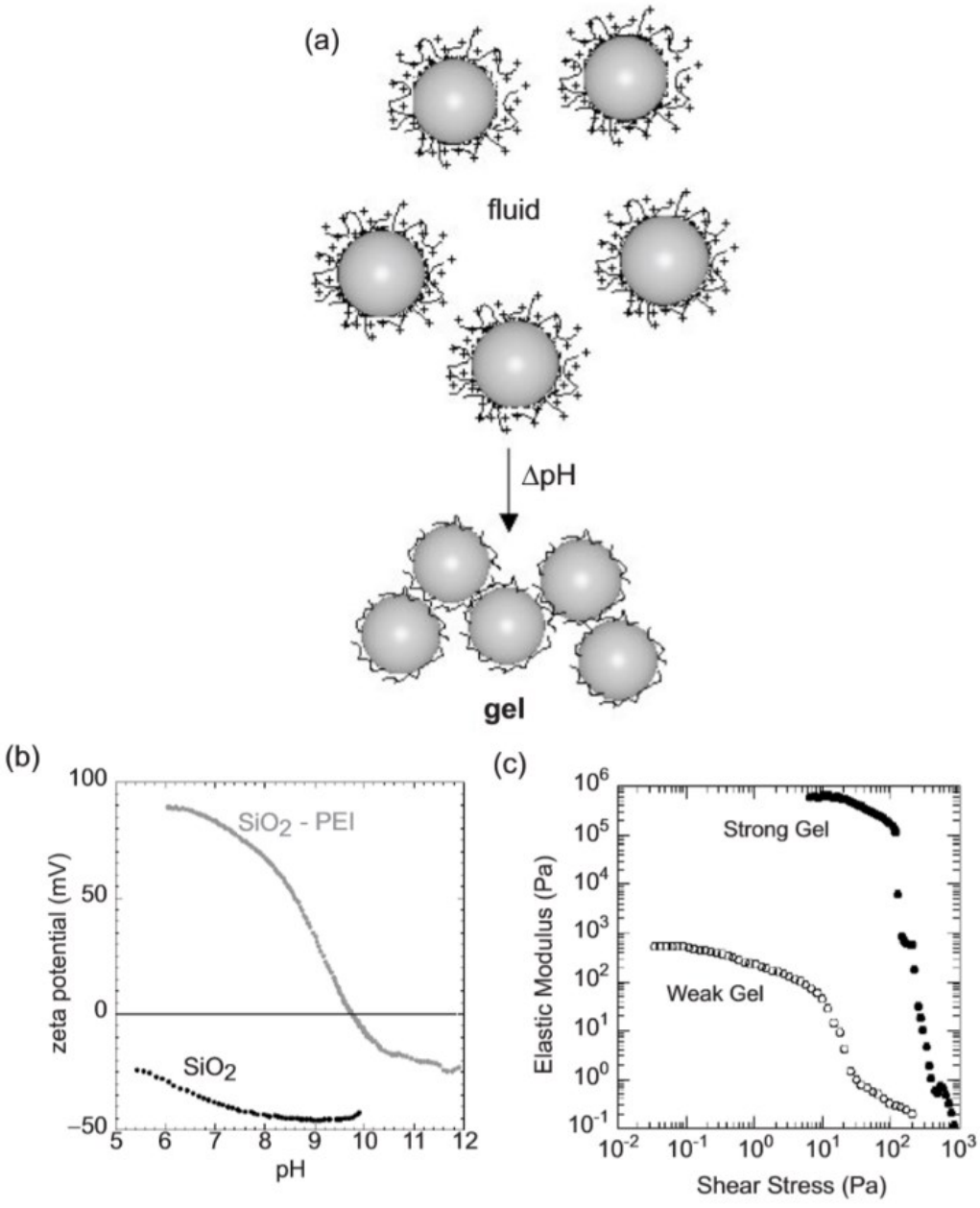


Figure 6. a) Fluid-to-gel transition; b) Plot of zeta potential as a function of pH for PEI-coated and un-coated silica microspheres suspended in water; c) The different shear elastic modulus of a weak gel (pH 9.5) and a strong gel (pH 9.75) as a function of shear stress. Adapted with permission from[16]

Graphene which is normally used in 2D printable electronics[31] has been successfully 3D printed by robocasting. This colloidal ink was prepared by adding a branched copolymer surfactant (BCS) which acts as the dispersant and the surfactant into a graphene oxide (GO) solution containing 0.2 wt% GO sheets. At basic conditions (pH>6.46), BCS provides electrostatic and steric stabilization to the GO suspensions which gives the suspensions a high fluidity, while at acid conditions, multiple hydrogen bonds and con-covalent bonds are formed to increase the storage modulus and loss modulus of the suspensions. A gluconic-δ-lactone (GδL) which hydrolyses to gluconic acid in water was added into the suspensions to drop the pH gradually. The rheology of the inks was controlled by changing the concentration of the BCS solutions and the amount of GδL.[15]

1.2.5.3 Emulsified Inks and foam gels

1.2.5.3.1 Introduction to emulsions

An emulsion is a mixture of two or more liquids that are normally immiscible. Generally, the droplets in an emulsion system are recognized as the dispersed phase and the other part is the continuous phase. In oil in water emulsions, surfactants which contain hydrophobic groups (tails) and hydrophilic groups (heads) are always added into the liquids to lower the interfacial tension between different phases, hence the dispersed phase is stabilized in the continuous phase (Figure 7 A, B). However, due to droplet coalescence, the emulsions get de-stabilized, so the system is not suitable for long time storage.

A Pickering emulsion is an emulsion system stabilized with fine particles. By adding particles which are absorbed on the continuous-dispersed phases interfaces, the system can be further stabilized because they prevent droplet coalescence (Figure 7 C, D). The attachment of the particles at the oil/water interfaces is determined by the balance among the oil/particle (γ_{op}), water/particle (γ_{wp}), oil/water (γ_{ow}) interface tensions, as shown in Figure 7 E. In the case that water is the continuous phase, the contact angle of the particles in the water phase (θ) should below 90°.[32]An ideal contact angle which is also called Brewster angle is 53° for this emulsion system.[31]

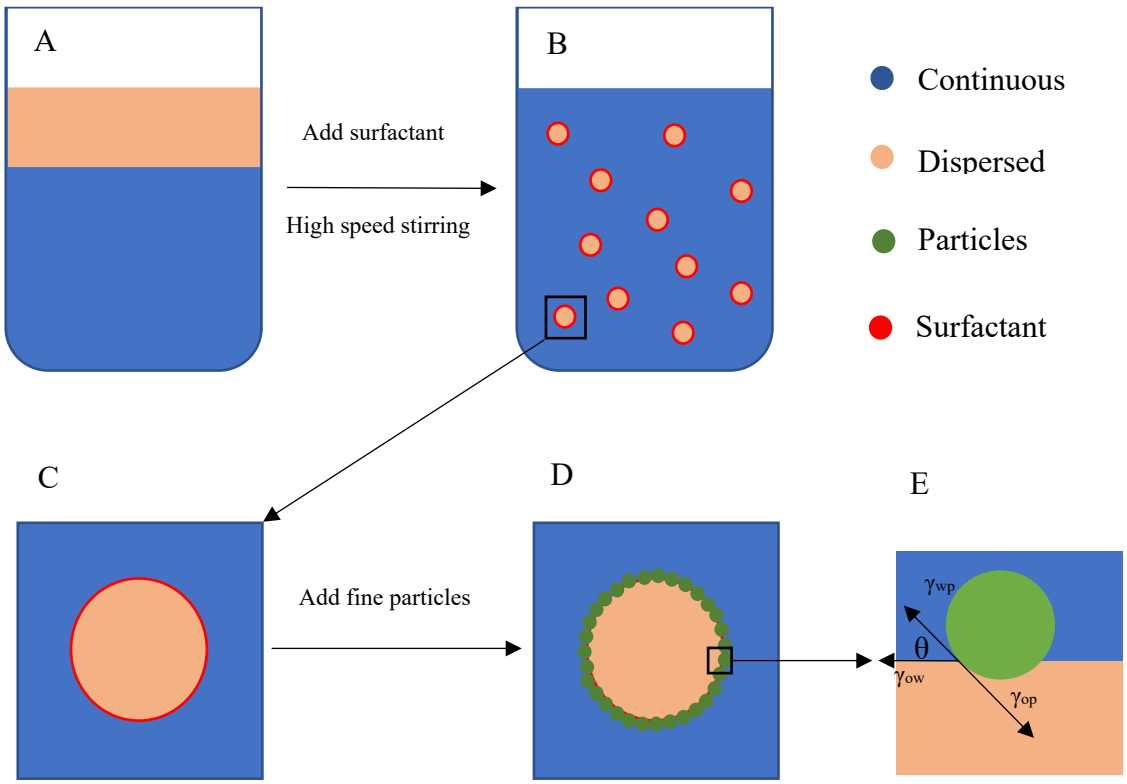


Figure 7. A, B) An emulsion system; C, D) The interface between continuous phase and dispersed phase in a Pickering emulsion; E) Interfacial tension balance between different interfaces (γ_{wp} is the water/particle interfacial tension, γ_{op} is the oil/particle interfacial tension and γ_{wo} is the water/oil interfacial tension). The ideal contact angle (θ) is 53° for emulsification with Pickering approach.[31]

Emulsification is achieved by high speed stirring which breaks the dispersed phase into small droplets. Emulsified inks are studied for manufacturing porous ceramics recently as the porosity, pore size can be controlled during emulsification. Different research groups have different routes to produce emulsions which are discussed in following sections.

1.2.5.3.2 Emulsions and foam gels for gel-casting ceramics

Emulsions and foam gels have been studied to fabricate ceramic products by gel-casting.

In Bakumov's research, poly(allylhydridocarbosilane) and poly(methylsilsesquioxane) were used as the dispersed phases. Sodium dodecylsulfate, dodecyl trimethy-lammoniumbromide and poly(ethylene-glycol)–block–poly(propylene-glycol)–block–poly(ethylene-glycol) (PEO–PPO–PEO) were used as the surfactants to form the emulsified Si/C/O ceramic products. However, this approach can only be used to manufacture bulk ceramic products in moulds. The emulsification needs to be conducted between 60 and 80 ℃ and the emulsions were poured into an autoclave, then sealed, heated, kept at 150 ℃ overnight for crosslinking and finally

sintered. These emulsions cannot be made into shear thinning pastes at room temperature, hence this route is only suitable for gel-casting but not suitable for robocasting.[33]

There is another approach to prepare porous emulsified gels which is described in Garcia-Tuñon's recent research.[34] A branched copolymer surfactant (BCS) which acts as the surfactant and the dispersant was used here. The BCS was original developed by Weaver et al. [35-37] .

BCS is an amphiphilic pH-responsive polymer which can be used as the dispersant and the surfactant at the same time. It is normally used to produce stable and functional suspensions and emulsions.

The structure of BCS and how the BCS works in an emulsion are shown in Figure 8. The components of a BCS molecule are methacrylic acid (MAA), poly(ethyleneglycol) methacrylate (PEGMA), ethyleneglycol dimethacrylate (EGDMA) and 1-dodacanethiol (DDT). In addition, a small amount of 2, 2-azobisisobutyronitrile (AIBN) is used to initiate the polymerization during the synthesis of BCS. MAA, PEGMA and EGDMA form multiple hydrogen and non-covalent bonds in acidic solutions (pH<pKa, where pKa=6.46[15]), while they can be electrostatic stable under basic conditions (pH>pKa). This is the cause of pH-responsive behaviour of the BCS solutions. The addition of DDT gives the structure hydrophobic chain ends that connected to the dispersed phase in the emulsion. The highly-branched structure ensures that each BCS molecule has sufficient points to attach to the droplet surface of the emulsion as well as the ceramic particle surface thus gives the emulsion a high stability. The pH-responsive behaviour of the BCS solutions and the high stability of the emulsion give a possibility for the emulsion to be robocasted.

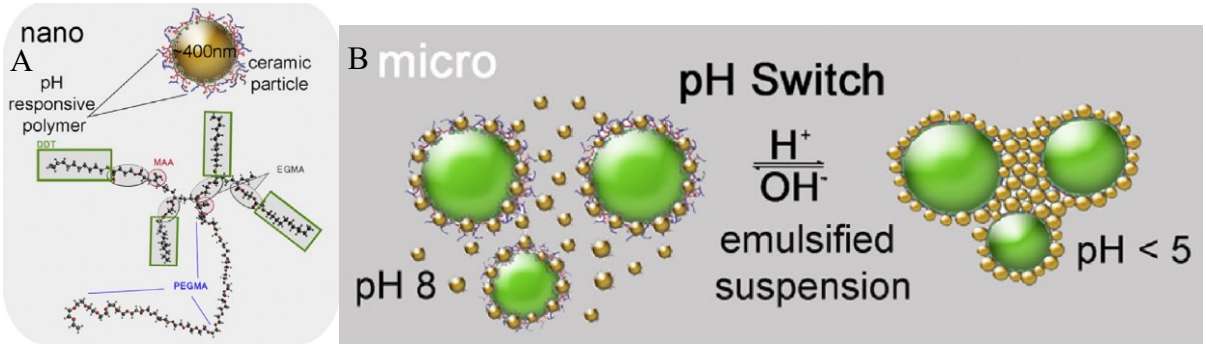


Figure 8. A) Structure of a BCS molecule and the attachment of BCS molecules on a ceramic particle; B) The aggreation of BCS attached particles in the emulsion water/oil interface. Adapted with permission from[34]

Alumina powders were mixed with BCS solutions at pH=8 with the volume percentage of solid ranging from 20 vol% to 40 vol% to form suspensions. Subsequently, the suspensions were ball milled for at least 24 hours. After being ball milled, the suspensions were conditioned by adding 2.5 wt% 1-octanol and stirring for 2 hours in an ice bath. The suspensions were then mixed with 50-60 vol% decane which acts as the dispersed phase and emulsified at stirring speeds ranging from 3000 rpm to 24000 rpm by using a homogenizer.

Initially, these emulsified slurries exhibit low viscosity (below 0.2 Pa.s)and can be aggregated by adding a pH trigger called gluconic-δ-lactone (GδL) combining with gently shaking. GδL dissolves in water and then hydrolyses into gluconic acid to reduces the pH in a gradual manner so that there is time to disperse it before it starts acting (Reaction shown in Figure 9).

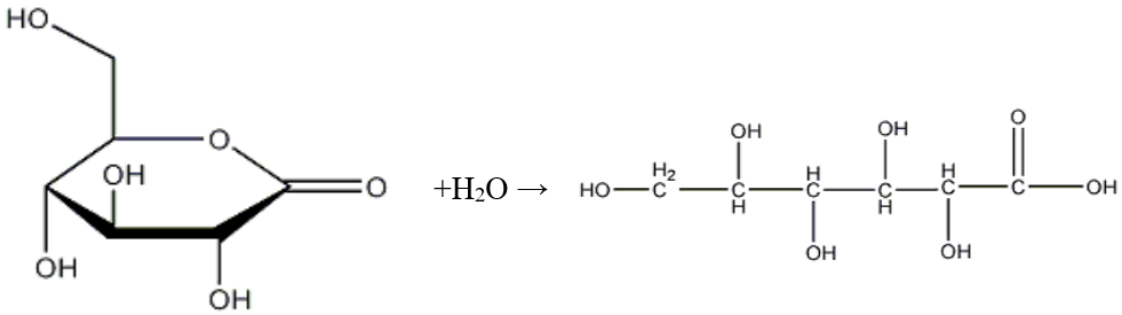


Figure 9. Dissolution and hydrolyzation of GδL molecules in water.

The amount of added GδL ranged from 2 to 10 wt/vol% (weight/volume percentage) depending on the suspension solid loadings. For suspensions with the same solid loading, the more GδL was added the faster the aggregation. The pore size and total porosity were controlled successfully in this research. The suspensions with high solid loadings emulsified at low speeds (3000-6000 rpm) formed materials with closed cells, large pore sizes (D_{50}=30 μm) and relatively low porosities (50-60 %), while the suspensions with low solid loadings emulsified at high speeds (6000-24000 rpm) formed structures with open cells, small pore sizes (D_{50}=9-15 μm) and relatively high porosities (70-90 %)(Figure 10).

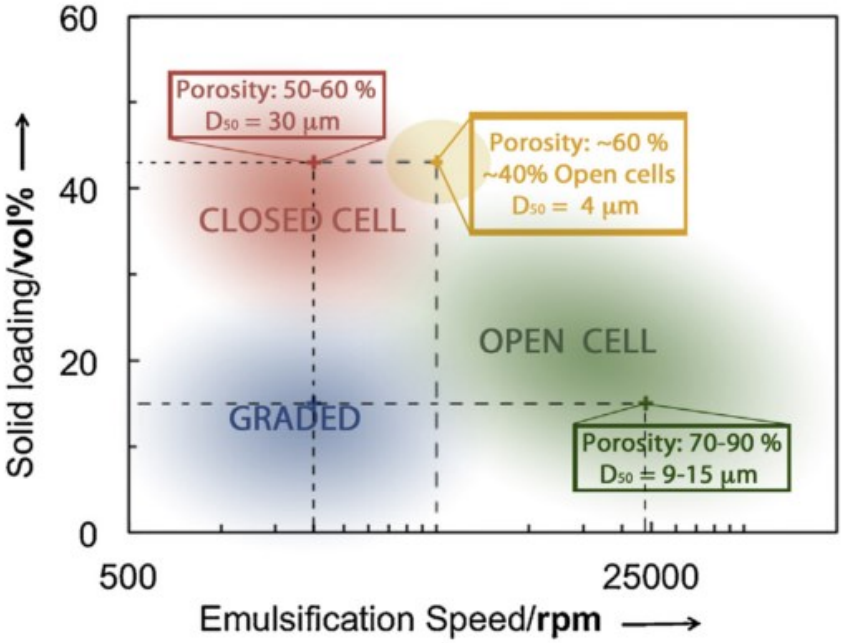


Figure 10. Relationship of solid loading, emulsification speed, porosity, pore size and cell type. Adapted with permission from[34]

Foam gels are also used by researchers to produce ceramics. In Muth's research, alumina powders were mixed with deionized water at pH<3 (adjusted with HCl) to form the suspension. Sodium X-sulfonate (X varies from 5 to 7) was added into the suspensions to hydrophobize the alumina particles. A four-bladed impeller and an overhead mixer were used to entrain the air into the suspensions at stirring speeds ranging from 400 to 1500 rpm. The sizes of the bubbles in the foam were controlled by using Sodium X-sulfonate with different X values and the stirring speeds of the mixer. The rheology of the foam gels was controlled by adjusting the pH of the suspensions.[19]

Generally, emulsified suspensions and foam gels have similar forming mechanisms and structures, emulsified suspensions have oil-water interfaces (two liquid phases), whereas foams have liquid-gas interfaces. Ideally, foam gels can achieve a porosity of 99.99 % if all the particles absorb onto the surface but emulsions cannot reach such high porosities. The disadvantage of the foam gels is that they are unstable because coarsening or drainage usually happens within 24 h.[19]

1.2.5.3.3 Emulsions for robocasting

Most emulsions and foam gels do not have the proper rheology for robocasting, they cannot maintain their shape after being extruded out on a substrate because of their low viscosity (<1

Pa.s) and low storage modulus (~1 Pa).[34] Hence researchers have tried to modify the rheology of the emulsions to make them suitable for robocasting.

Sears' group prepared emulsions which can be used for 3D printing. In their research, the emulsions were prepared with a hydrophobic photopolymer, surfactants and water. The viscosity of the printed parts increased immediately after the emulsified inks were extruded with an ultraviolet cure-on-dispense technique. A low viscosity component, poly(propylene glycol) dimethacrylate (PPGDMA) and a high viscosity component diurethane dimethacrylate (DUDMA) were used to control the rheology of the inks.[38]

Sears' work is relatively complex because the need to cure the polymer during printing. To simplify the process of robocasting, alumina suspensions modified with poly(vinyl alcohol) (PVA) were mixed with decane to form the emulsions by Minas et al. The solid loading of the initial suspension can reach up to 58 vol% and the porosity of the final emulsions is as high as 77 %. The emulsified inks are shear thinning and the printed ceramics have high strength.[17]

According to Garcia-Tuñon's research[34], it is easy to control the pore size and porosity of emulsions prepared with BCS solutions. However, these emulsions were cast in a mould in their work. If these emulsions have suitable rheology for printing, porous ceramics with desired microstructures can be easily manufactured by robocasting. There is some preliminary work done by Gil Machado which shows that this is possible. He used BCS to functionalise calcium phosphate with specific Ca/P ratio (Pure HA，pure β-TCP and HA/β-TCP 50/50 in weight) with the BCS concentration of 2 wt%, amount of GδL between 0.5 and 2 wt/vol%, solid content of 43 vol%. In Machado's work, he used bioceramic materials (β-TCP and HA), while a systematic study of the parameters to control the printability of BCS emulsions is still needed as well as proving that the system can be used with technical structural ceramics such as Al_2O_3.[39]

1.2.6 Rheology of the Inks

In contrast to other AM technologies in which the building of structures relies on solidification of the materials, robocasting manufactures layer-wise objects based on rheology of the inks. As mentioned in 1.2.1, the rheology is the most important factor of the inks used for robocasting. Based on the Herschel-Bulkley model ($\tau = \tau_y + K\dot{\gamma}^n$[11, 24]), a printable ink should exhibit a significant yield stress (τ_y>100Pa) and be shear thinning (0<n<1) at stresses above the yield stress, i.e. the apparent viscosity of a shear thinning ink decreases as the shear rate increases.

According to Herschel-Bulkley model, the viscosity parameter (K) and the shear thinning coefficient (n) can be calculated once the yield stress (τ_y) and the shear stress (τ) at a shear rate ($\dot{\gamma}$)are known. This can be achieved by using the flow ramp data alongside the modified Herschel-Bulkley model;

$$ln(\tau - \tau_y) = lnK + nln(\dot{\gamma}) \quad (3)$$

thus, the shear thinning coefficient can be described as the slope of the $ln(\tau - \tau_y)$ vs. $ln(\dot{\gamma})$ plot. The K can be calculated by using the modified equation:

$$\tau - \tau_y = K\dot{\gamma}^n \quad (4)$$

when shear rate ($\dot{\gamma}$) is 1 s^{-1}, the value of K is equal to the value of shear stress at 1 s^{-1} minus yield stress.

In most case, an accurate fitting can be achieved by using the power law model ($\tau = K\dot{\gamma}^n$). A viscosity plot is made [log μ (Pa.s) *vs.* log $\dot{\gamma}$ (s^{-1})] to determine the flow index after the point of yield. The data used in this model are at the mid-shear rate in the shear thinning region.[40]

The rheology of an ink is measured using a rheometer. Normally, a flow ramp test measures the viscosity of the ink and the shear stress used to make the ink flow as a function of the shear rate. The flow ramp measurement can be used to calculate the yield stress (τ_y), the viscosity parameter (K) and the shear thinning coefficient (n). Another significant measurement is oscillation amplitude sweep test which is used to determine the equilibrium storage modulus (G_{eq}') and the flow point (τ_{fp}, the crossover point of storage modulus and loss modulus, or sometimes some people also call it yield stress) of the ink. It measures the storage modulus (G') and loss modulus (G'') as a function of oscillation stress.

The characterization of the modulus of robocasting inks is usually done in shear (Figure 11 A). The modulus for an extension experiment (Figure 11 B) is similar but the modulus is about three times as that for a shear experiment because during extension the material deforms in three directions. When the material is undergoing shear, the stress-strain curve normally has a linear elastic region followed by a non-linear strain-stress zone (Figure 12 A). If the material is not broken, when the strain is released, the stress in the material goes back to zero. However, it does not simply follow the loading curve back, typically the unloading curve is lower (Figure 12 B).

The slope of the shear stress- shear strain loading curve is called the storage modulus, G'. And at the linear elastic region, the storage modulus can also be recognised as the equilibrium storage modulus or elastic modulus of the material. The G' is related to the energy needed to distort the material.[41] Thus, in a viscoelastic behaviour, the G' describes the elastic behaviour of the material (or the solid-state like behaviour).[42]

Loss modulus, G'', is related to the energy loss (difference between the loading and unloading curves) during the loading-unloading cycles (through internal friction when flowing). But why there is a loss of energy? The physical crosslinks (such as chemical bonds) as well as the encountered chains which forms occlusions during the shear experiment give the material the resistance to further deformation. When the strain is released, the material goes back to its original shape but the chains do not have to go back to their original conformations as they may move back to their start position following a lower-energy pathway which caused a loss of energy.[41] Thus, in a viscoelastic behaviour, the G'' describes the viscous behaviour of the material (or the liquid-state like behaviour). [42]

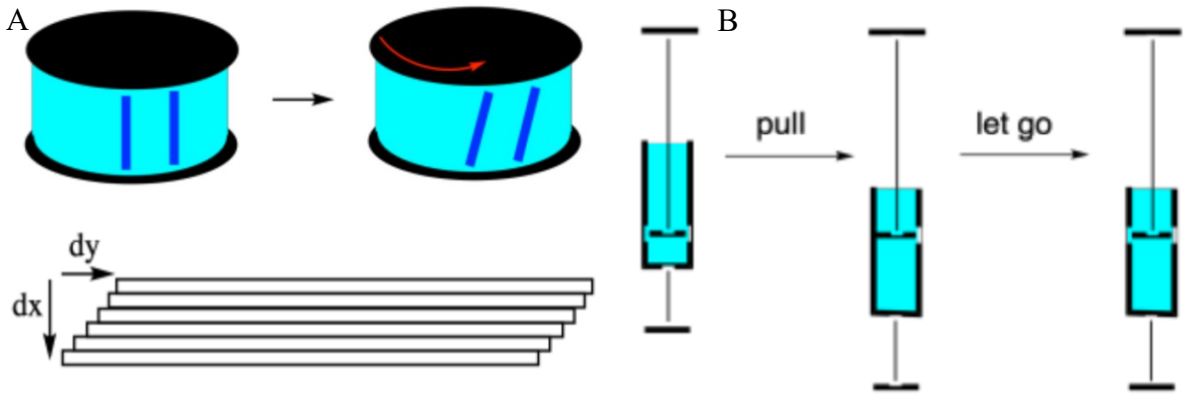


Figure 11. A)top: scheme of a shear experiment; bottom: individual layers of a material during a shear experiment; B) scheme of a extension experiment. Adapted with permission from[41]

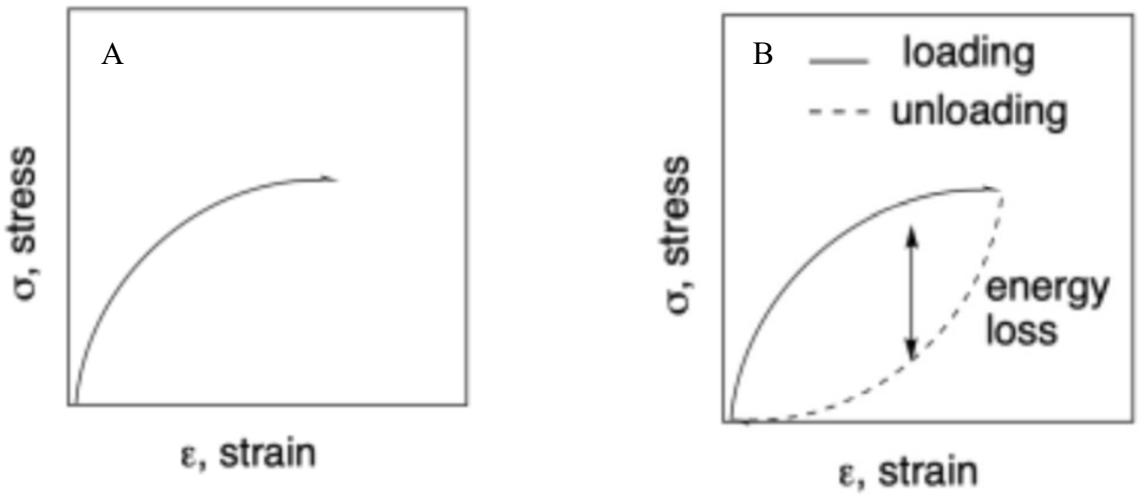


Figure 12. A) Stress-strain curve of a shear experiment; B) Loading-unloading curves of a shear experiment. Adapt with permission from[41]

A complex shear modulus *G** is always used to describe the entire viscoelastic behaviour of a material.[42] The relationship among *G**, *G'* and *G''* using the phase-shift angle δ are given with the equation

$$G^*=G'+iG'' \tag{5}$$

Where $G'=G^*\cos\delta$, $G''=G^*\sin\delta$, and δ is the phase angle (Figure 13). When δ=0°, i.e., the strain and stress are in phase, the material is elastic (solid-like), while if $\delta\approx$90°, the strain and stress are fully out of phase, the material is viscous (liquid-like). When 0°<δ<90°, the material exhibits a viscoelastic behaviour.[30]

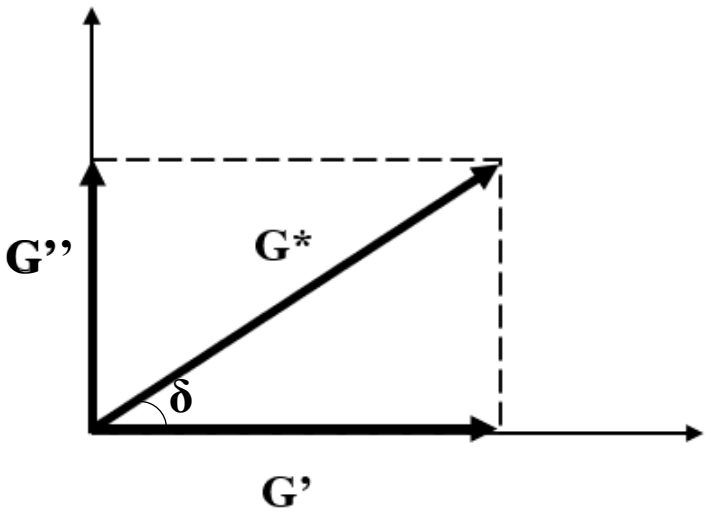


Figure 13. The relationship among G*, G' and G'' using the phase-shift angle δ.

A frequency (ω) sweep in the linear viscoelastic regime (low shear rate and shear stress) can gives the structural information of the material (Figure 14). If the G''>G' over the entire frequency sweep, G'~ω^2, G''~ω as ω→0, the material has a liquid-like response. If the G'>G''; G' and G'' varies as ω^j where 0.3<j<0.7 (two parallel lines), the material has a gel-like response. If the G'>G'' but G' is independent of ω as ω→0, the material has a solid-like behaviour (Figure14).[30]

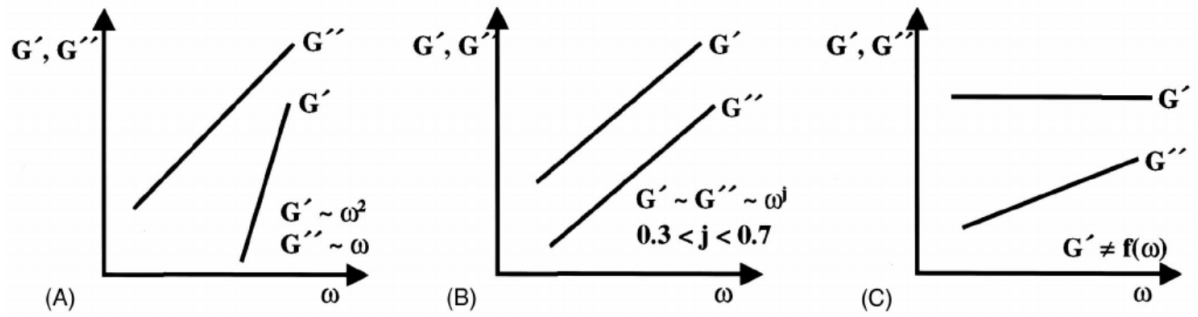


Figure 14. The oscillation behaviour as a function of frequency for A) Liquid; B) Gel; C) Solid response. Adapted with permission from[30]

In an oscillation amplitude sweep test, at a low oscillation stress, the ink exhibits a linear viscoelastic response (G'>G'') and the elastic modulus of the ink equals to the storage modulus. As the oscillation stress increasing, G' falls faster than G'' until G'= G'', indicating the ink starts to have a liquid like behaviour. The oscillation stress at the modulus crossover point (flow point) is a bit smaller than the yield stress. The yield stress is the stress when the ink starts to deform plastically, while the flow point is the stress when the ink starts to behave as a liquid.[43]

The rheological parameters of different kind ink systems for robocasting are summarized in Table 2.

Table 2. Rheology of different ink from literature.

	Researcher [Reference]	Solid loading (in continuous phase for emulsions)	Shear thinning coefficient (n)	Viscosity parameter (K)	Yield stress (τ_y)	Equilibrium storage modulus (G_{eq}')
Hydrogel inks	Feilden[11, 20]	30-43 vol%	0.2-0.3	100-1100 Pa.s^n	500-800 Pa	40-100 kPa
	Schlordt[12]	52 vol%			225-600 Pa	191-300 kPa
	Yetna[28]	45 vol%			600 Pa	50-200 kPa
	Glymond[44]	45~50 vol%			200-300 Pa	40-100 kPa
Colloidal inks	Lewis[16]	46 vol%			100 Pa	100-1000 kPa
	Smay[13]	47 vol%	0.72	101 Pa.s^n	25 Pa	150 kPa
Emulsion or foam inks	Sommer[45]	50 vol%			700 Pa	10 kPa
	Minas[17]	30-50 vol%			58-660 Pa	1.6-17 kPa
	Muth[19]	20-60 vol%			30-100 Pa	4-80 kPa

Although solid contents as high as possible are desired, in hydrogel and colloidal inks the solid loading is usually limited at around 50 vol%. Emulsion or foam inks do not have the requirement as the hydrogel or colloidal inks do but the solid loading in the continuous phase still has a limitation of 50 to 60 vol%. Not a lot information about the shear thinning coefficients and viscosity parameters has been reported. According to the data reported by Feilden and Smay, the shear thinning coefficient of hydrogel inks is lower than that of colloidal inks, while the viscosity parameter of hydrogel inks is relatively higher than that of colloidal inks. The yield stress depends on the solid loading of the inks, but other parameters such as the copolymer solution concentration[12, 20] may also influence it. Hydrogel inks and emulsion/foam inks have similar yield stress by a given solid loading (~600 Pa at ~50 vol%), while colloidal inks have a much lower yield stress at the same solid loading (~100 at 50 vol%). The hydrogel inks and colloidal inks have similar equilibrium storage modulus (100-1000 kPa) but emulsion/foam inks have a lower equilibrium storage modulus (10-100 kPa).

A printable ink should have suitable rheological properties with a high storage modulus (G'>10 kPa), a moderate yield stress (τ_y>100 Pa) and a proper shear thinning coefficient (0<n<1).[12] The key factors that influence the rheology of inks depend on their forming mechanisms. For hydrogel inks, the solid volume percentage, the concentration of the solution and the amount

of the dispersant used are important.[11] For colloidal inks, the solid loading, the amount of binder and the pH of the gels can influence the rheology.[16] For emulsified inks and foam gels, the solid loading of suspensions, the volume percentage of the dispersed phase, the amount of the surfactant used and the stirring speed during foaming or emulsification (that determines droplet or bubble size) are the main factors.[17, 19]

1.3 Porous Ceramics

1.3.1 Introduction to porous ceramics

Traditionally, pores were undesirable in ceramic materials because they adversely affect the mechanical properties of the products. Pores in ceramics act as stress concentrators which decrease tensile strength and cause catastrophic failure.[46] However, the amount of applications that require porous ceramics has increased since the end of the 20th century because of their unique properties. Examples of sectors where they are used are refractories and thermal insulation[47], filters for metal manufacturing[48] and diesel engines[49], catalyst supports[50], seals in aero-engines[51], sound proofing[52], electrodes in fuel cells[53] and implants for bone regrowth[54]. The increasing number of the applications is due to their properties which mainly depend on their structure, including volume fraction, size, distribution and tortuosity of the pores. In order to achieve desired structures, different manufacturing routes have been developed.[32, 55, 56] However, none of these techniques today is capable of delivering fully designed porous structures in which the engineer has a wide freedom in specifying the pore parameters.

Much effort has gone into controlling the fabrication of porous ceramic with mostly homogeneous porous structures and developing new manufacturing routes. For example, freeze casting which is based on the crystal growth of ice during freezing is used to fabricate laminar porous ceramics. The thin gaps inside the ice crystals are filled with ceramic powders and lamellar ceramics with very thin layers and pores are formed by removing the ice.[57-59] Porous ceramics have been fabricated using different materials. Alumina is the most common material due to its high strength and thermal resistance. Other ceramics include silicon carbide which exhibits high thermal stability and mechanical strength is an excellent material for the fabrication of light and strong porous structures.[60] The properties of porous ceramics are mainly based on their microstructures. Porosity, pore size, pore distribution and the type of the pores are significant factors that determine the applications of porous ceramics. A higher porosity means a lower density with a lower strength. Porous ceramics with different pore distribution can be used for different applications. Closed-cell ceramics tend to have high thermal capacities for thermal insulators, while open-cell ceramics are suitable for catalyst supports and filters.[56]

1.3.2 Manufacturing Routes of Porous Ceramics

Several routes have been developed for manufacturing porous ceramics with different structures. The most straightforward process is to sinter the a mixture of powders which can

undergo reactions during sintering to create porous structures[61] or partially sinter initial porous green bodies[62]. Other conventional routes can be classified into three main categories which are shown in Figure 15. Replica techniques are used to manufacture open-cell ceramics with low stiffness by using synthetic or natural templates. Direct foaming by agitation or evolution of gas is used to prepare ceramics with less open structures than those fabricated by replication techniques. Another approach which relies on sacrificial templates can give either open or close structures depending on the quantity and structure of the template used. A porous ceramic manufactured by a sacrificial template method displays a negative of the initial template, while a porous ceramic fabricated by a replica technique obtains the positive.[32, 55] However, none of these routes is flexible to manufacture porous ceramics with fully designed structures under a high degree of freedom to control the pore parameters. Hence, researchers are trying to develop new processes to manufacture porous ceramics, such as additive manufacturing.

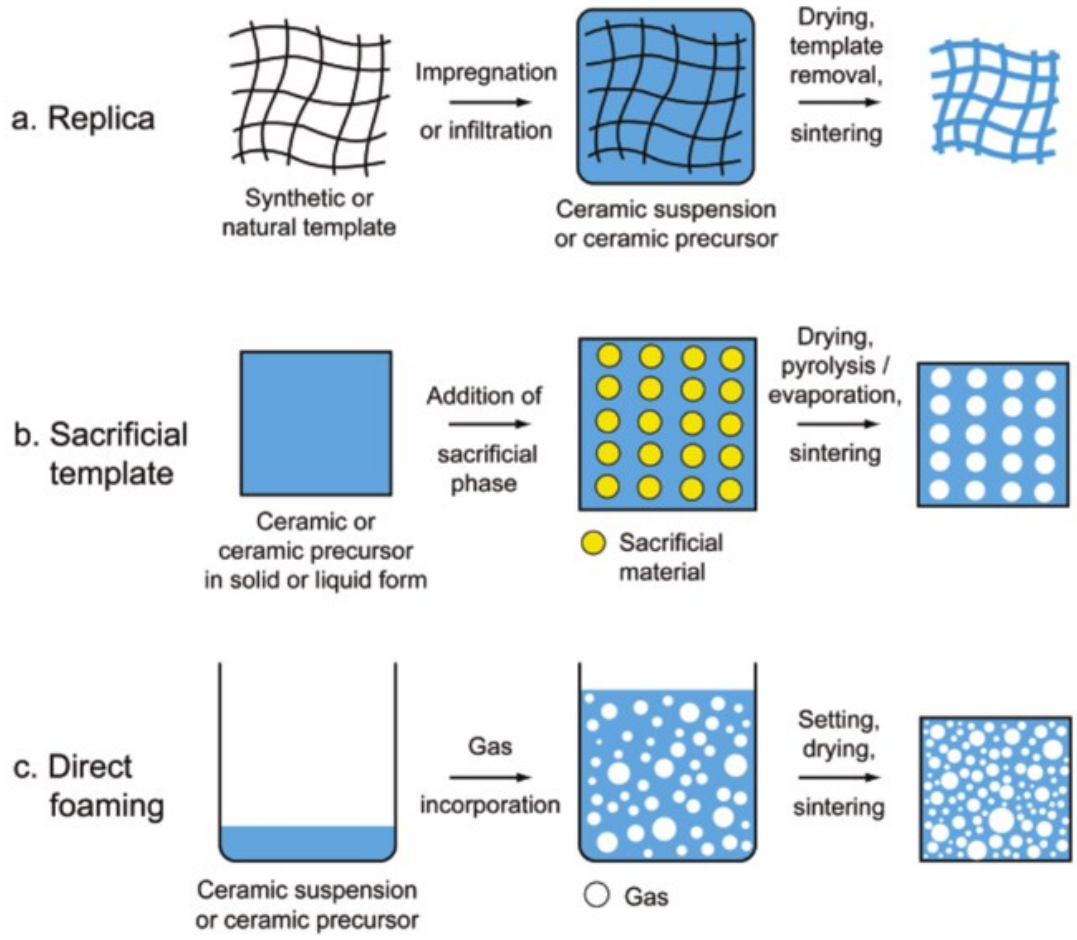


Figure 15. Conventional routes for manufacturing porous ceramic: a) Replica technique; b) Sacrificial template technique; c) Direct foaming technique. Reproduced with permission from[32]

There are few papers that report printing microporous ceramics by using emulsions/foams. In most of the papers, researchers used robocasting (direct ink writing) to do the printing process. The emulsions/foams are soft materials and robocasting is the most suitable technology for 3D printing objects using soft materials as other additive manufacturing technologies may destroy the microstructure of the emulsions/foams. To print emulsions, an oil/water emulsion system has always been used to prepare the inks.[17, 45] For foam, air/water foams are the most commonly used.[17, 63]

Products with designed porosity can be achieved by robocasting. By using emulsions or foams as the inks for robocasting, the porosity of printed filaments can reach up to 70 vol%. A structure with macropores such as a grid can further increase the porosity to above 90 vol%.[17]

1.4 Core/shell structures

Most researchers use robocasting to print monolithic green bodies and periodic patterns (e.g. woodpile structures). The inks used exhibit a smooth flow during printing. However, monolithic inks have limitations regarding the fabrication and application of the technology and the final products. Therefore, it is a good idea to find a way to print more complex structures (e.g. composites) to broaden the use of the technology.

1.4.1 Composites produced by robocasting

Several researchers have worked on printing ceramic-polymer and fibre reinforced composites by robocasting. Some of the processes take advantage of the alignment of microscopic platelets and short fibres during extrusion to manipulate the final structure of the material. During Feilden's PhD research[20], ceramic-polymer composites were fabricated by using robocasting to build green bodies with Al_2O_3 powders and aligned alumina platelets. These green bodies are subsequently infiltrated with epoxy (Figure 16 A). The toughness of these products increases significantly. Feilden tried to fabricate carbon fibre reinforced polymer matrix composites (PMCs) and carbon fibre reinforced ceramic matrix composites (CMCs) as well (Figure 16 B, C). The PMCs were produced by printing green bodies consisting of aligned carbon fibres which were infiltrated with polymer after drying and burning out the organic binders used to formulate the inks. The CMCs were produced by printing pastes consisting of carbon fibres and ceramic powders directly.

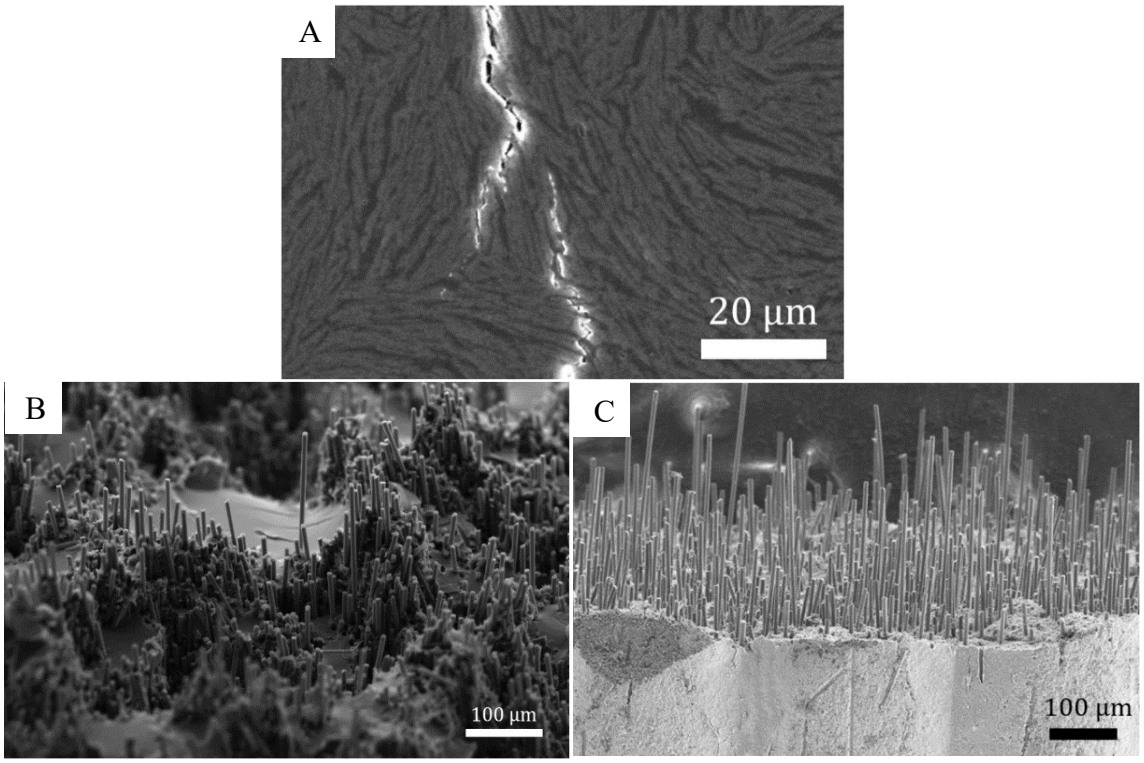


Figure 16. A) SEM image of a crack in Al_2O_3 platelet-polymer composite; B) Fracture surface of the PMC composite; C) Fracture surface of a green SiC – Cf part. Adapted with permission from[20]

The carbon fibres used in Feilden's work were Polyacrylonitrile (PAN)-derived short carbon fibres with a diameter of 7 µm. These fibres were chopped and milled to make sure they can go through the nozzle successfully. Highly aligned carbon fibre PMCs with attractive mechanical properties were printed. However, there were some issues with the fibre distribution: there were some fibre free regions. The trials of CMCs with carbon fibres were not so successful because of the delicacy of the carbon fibres. The high sintering temperature caused chemical reactions and physical damage to the fibres and the difference of the thermal expansion between the fibre and the matrix destroyed the composites during cooling.[20]

Other researchers also used short carbon fibres to reinforce ceramic and polymeric matrices. Table 3 compares the mechanical properties of different materials reported in the literature. In most of these works, the addition of short carbon fibres decreases the strength of the matrix but also gives an increasing of fracture toughness (K_{IC}). All these researchers used short carbon fibres except Hitchen who used longer carbon fibres. They all used epoxy as the polymer matrix except Tekinalp[64] used acrylonitrile–butadiene–styrene as the polymer matrix.

Table 3. Comparison of short carbon fibre reinforced composites. Reproduced with permission from[20]

Researcher	Strength (MPa)	K_{IC} (MPa.m$^{0.5}$)	Fibre Content (vol%)
Hitchen 1994[65]	127	5.2	14.4
Zhang 2004[66]	112		15
Zhang 2007[67]	108		15
Compton 2014[68]	75		17.4
Dong 2014[69]	130	0.9	3
Tekinalp 2014[64]	70		40
Feilden 2017[20]	211	3.5	20

1.4.2 Co-extrusion technology

Most of the fibre reinforced ceramic matrix composites fabricated by robocasting used short fibres to enable them to go through the nozzle. Producing CMCs with long continuous fibres is still a challenge. In this work, printing filaments with a novel core/shell structure are used to fabricate ceramic matrix composites reinforced with long fibres. The filaments use one kind of ink in the centre and another kind as the shell. The idea of using the core/shell structure comes from research related to the 3D printing of hollow ceramics.

Robocasting of hollow filaments has been developed to give the products unique structures which expand the usage of these ceramics. This hollow structure can be achieved by extruding the ink through a tip with a block at the centre which gives the printed filament a hollow channel.[70, 71] Another method uses a sacrificial core in the centre of the printed filament and produces the channel by removing the core after the green body is printed.[72]

1.4.2.1 Blocked Nozzle Method (for hollow filaments only)

A nozzle with a block at the centre is used so that the filament extruded out from the syringe has a hollow channel. Schlordt successfully printed alumina hollow scaffolds in an oil bath in 2013 (Figure 17 A).[70] Bioceramics with hollow structures, which can be used for regeneration of bone defects, were printed in air by Luo's group in 2015 by using a block at the nozzle centre (Figure 17 B).[71]

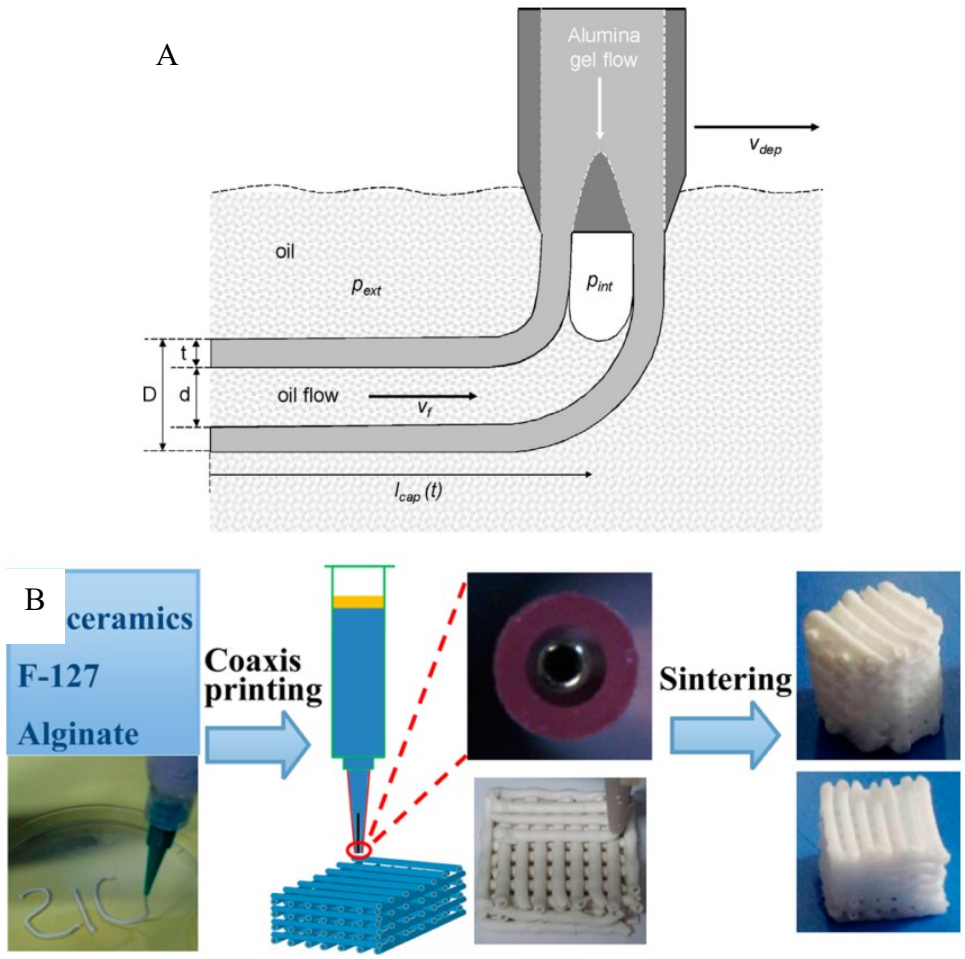


Figure 17. A) Hollow filaments printed in an oil bath, B) Process of co-axis printing of bioceramics. Adapted with permission from[70, 71]

1.4.2.2 Co-extrusion Method

Co-extrusion was initially a manufacturing method for plastics.[73] The co-extrusion of ceramics was used to manufacture alumina hollow filaments with microporous shells by Moon's group in 2015. They used sacrificial camphene cores to fabricate the hollow channels and mixed alumina and camphene to form the shells with micropores. After the green bodies were printed, the camphene was removed by freeze drying and the final alumina scaffolds were sintered at 1600 °C.[72] This method uses a sacrificial material instead of blocking the tips to produce the channels (Figure 18).

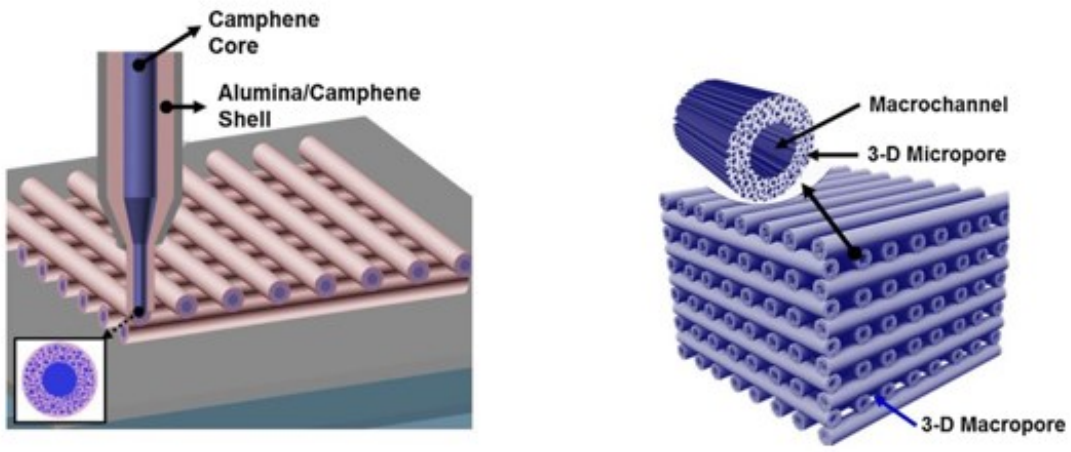


Figure 18. Example of the use of co-extrusion method to print filaments with hollow cores. Adapted with permission from[72]

1.4.2.3 Multicore/shell structure

Jennifer Lewis's group found a way to print multicore/shell structures. They used special designed nozzles for multilayers and achieved structures with both high stiffness and toughness (Figure 19).[74] This method can also be used for printing ceramic products although it is a bit complex because it uses three concentric tips and requires three different syringes to store the inks.

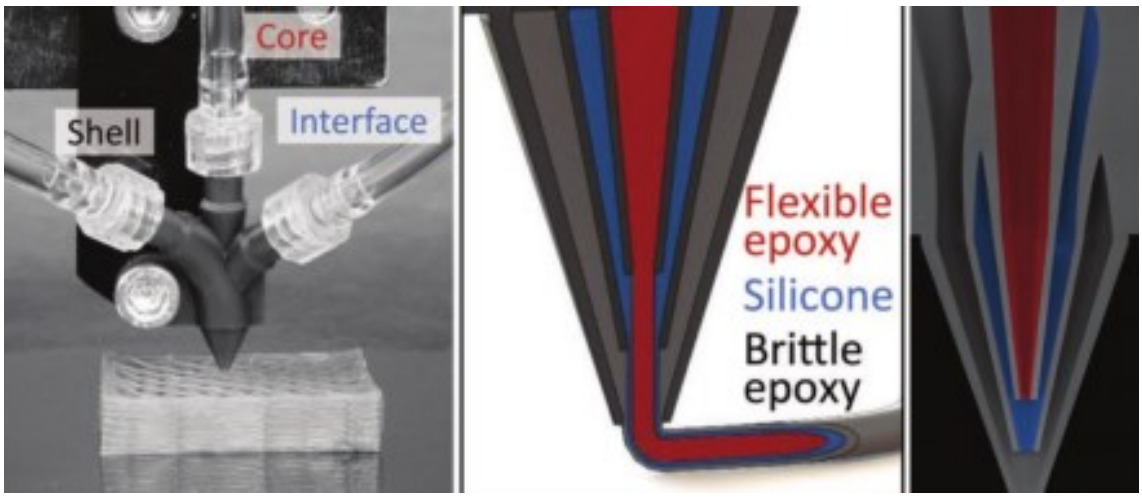


Figure 19. Method for multicore/shell structure. Adapted with permission from[74]

1.4.2.4 Core/shell structure with short carbon fibre reinforcement

Xia has also managed to fabricate Cf(short carbon fibres)/SiC core/shell composite by DIW.[75] In this research, a frozen cylinder shaped carbon fibre ink was used as the core and SiC ink was used as the shell, the frozen Cf ink was directly push inside the SiC ink to form the core/shell structure and these two inks were co-extruded by DIW (Figure 20).

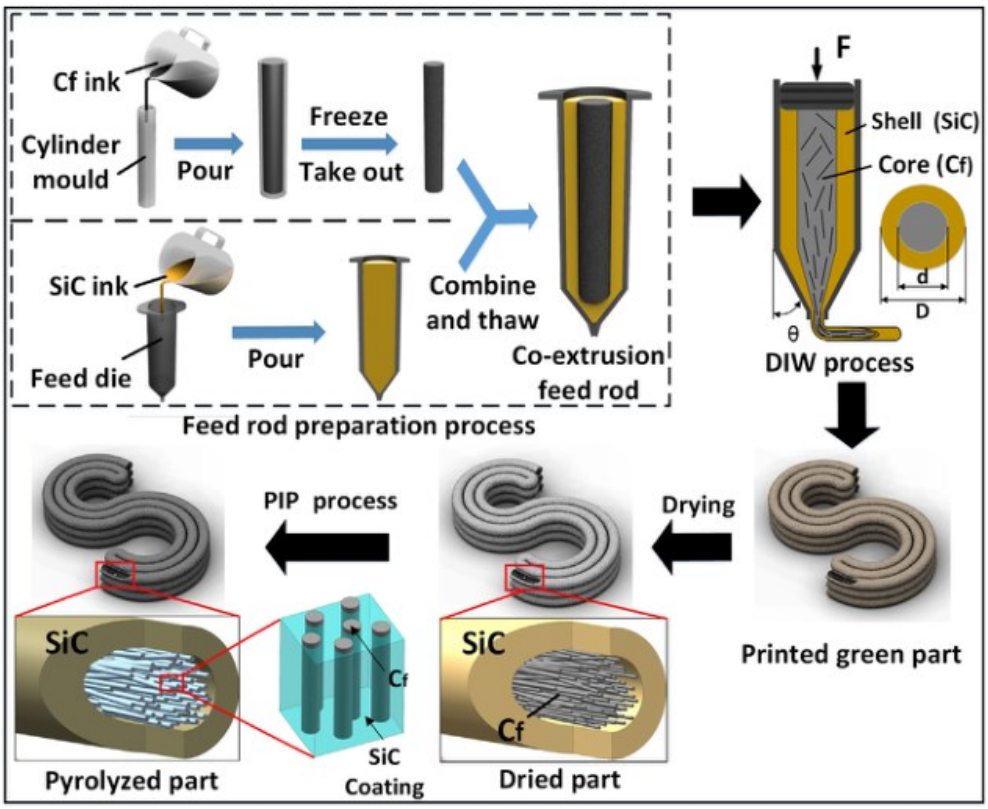


Figure 20. Schematic of preparing core/shell parts. Adapted with permission from[75]

1.4.2.5 Limitations of the co-extrusion technologies

In conclusion, the technologies reviewed above used two co-extrusion methods. One is using a frozen core and another is using a nozzle that has concentric cylinders. However, there are some limitations of these methods. The first one is the diameter of the core. It is difficult to freeze very thin sticks suitable for co-extrusion or fabricate nozzles with very thin concentric rings. For the frozen core method, another limitation is the difficulties in engineering the interface between the core and the shell. For the nozzle with concentric cylinders, it is difficult to increase the numbers of cores in one single filament. Usually, it can only print a filament with one core.

Another limitation for the co-extrusion methods is in the materials used for robocasting. Most of the work focuses on the hollow core[70, 71] or polymer core[73, 74] systems but not much on ceramic-ceramic or metal-ceramic systems. The only ceramic-ceramic system reported used short carbon fibres and the improvement of the mechanical properties was not so significant.[75]

1.5 Summary

There are several AM technologies that can be used to fabricate ceramic products among which robocasting is one of the distinct technologies that fabricate ceramic products by extruding shear thinning pastes layer by layer to build the 3D objects. The significant factors that affect the printability of the pastes include the solid loading, rheology of the pastes, the nozzle type, the printing speed and the drying kinetics.

Different kinds of pastes have been used for robocasting. Hydrogel inks[11] and colloidal inks[13] have been used to print monolithic ceramic parts, while emulsion-based[45] inks and foam gels[63] have been developed to print porous ceramic parts.

Porous ceramics can be fabricated by several approaches. Robocasting may be the more suitable than other AM technologies to print porous ceramic with emulsion-based inks and foam gels. As the emulsions/foams are soft materials while other additive manufacturing technologies may destroy the microstructure of the emulsions/foams during printing.

In order to broaden the application of robocasting, core/shell structural products have been fabricated successfully by co-extrusion approaches. The co-extruded core/shell structure is a specific structure that can only be fabricated by robocasting. Other AM technologies normally build monolithic ceramic parts while the printing of core/shell structure needs at least two different kinds of inks.

Chapter 2: Aims and Objects

Robocasting has been used to fabricate more complex structures with more architectural control than simple grids or bars with homogeneous microstructures [8-11, 14-16]. However, the degree of structural control is still limited, in particular when it comes to print composites combining different materials. The main aim of this work is to develop approaches to increase the complexity of robocasted structures and to enable further microstructural control. The main specific objectives to achieve this goal are:

- To print ceramics with designed porous structures by using emulsified inks. Printable emulsions using BCS are developed. The rheology of the emulsions (that defines their printability) as well as the porosity and pore size of the final ceramic are related to the emulsion composition (including the BCS concentration, GδL content, oil content and solid loading of the continuous phase) and the stirring speed during emulsification.
- To develop a new approach to create printing filaments with a core/shell structure. This structure is obtained by co-extruding filaments based on thermally reversible hydrogels (using Pluronic F-127 ®). This approach is demonstrated by printing composites: ceramic matrix reinforced with long/continuous metallic fibres. The core/shell method is also used to engineer an interphase between fibre and matrix in composites using an ink cartridge with a cross section of three concentric rings.

In all cases the structural and mechanical characterization is used to understand the relationship between processing conditions (ink formulation and printing conditions), structure and mechanical response of the materials.

Chapter 3: Methods

3.1. Sample preparation

3.1.1 Emulsion based inks

3.1.1.1 synthesis of Branched Copolymer Surfactant (BCS)

3.1.1.1.1 Materials

Poly(ethylene glycol) methyl ether methacrylate (PEG, average Mn=950 g mol^{-1}), methacrylic acid (MA, 99 %) and Azobis(isobutyronitrile) (AIBN, 98 %) were purchased from Sigma Aldrich. Ethylene glycol dimethacrylate (EGDMA, 98 %), 1-dodecanethiol (DDT, 98 %) and Rhodamine B were purchased from Alfa Aesar. Ethanol and diethyl ether were of standard laboratory grade. All the materials were used as received.

3.1.1.1.2 Process

The synthesis of BCS with a composition of PEG_5/MA_{95}-$EGDMA_{10}$-DDT_{10} followed the processes described by Weaver and Woodward[35-37] via thiol-regulated free radical polymerization (Figure 21). A mixture of PEG (5.7 g, 6 mM), MA (10.000 g, 116 mM), EGDMA (2.428 g, 12 mM) and DDT (2.478 g, 12 mM) was charged in a 250 mL round bottom flask and degassed with N_2 for 20 min. Ethanol (200 ml) was degassed separately for 20 min and subsequently added into the flask. AIBN (0.200 g) was added into the solution to initiate the polymerization. The flask was then placed into an oil bath at 70 °C and left stirring for 48 h. The remaining ethanol was removed by distilling and the polymer was washed with cold diethyl ether. Finally, the polymer was dried in vacuum overnight. Rhodamine B (<1 mg) was added into the flask before the reaction to synthesis the rhodamine doped BCS powders.[15]

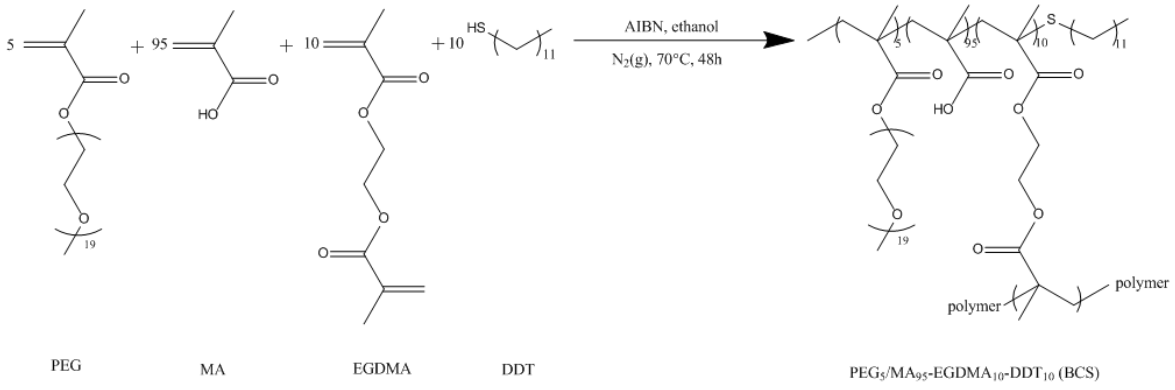


Figure 21. Synthesis of BCS via thiol-regulated free radical polymerization.

3.1.1.2 Ink preparation

BCS solutions with compositions from 1 wt% to 4 wt% were prepared by mixing BCS powders with distilled water. The BCS molecules aggregate in the solution when the pH of the solution is lower than pKa (6.46[15]) while a clear solution is achieved by increasing the pH to 8 (adjusted using a NaOH solution) (Figure 22). Alumina powders (SMA6, Baikalox, D_{50}=0.20 µm, meshed with a 100 µm sieve) were directly mixed with BCS solutions to form the suspensions with solid loadings ranging from 30 vol% to 50 vol%. The suspensions were then added into plastic bottles and ball milled with alumina milling balls for over 24 h. The suspensions were conditioned by adding 2.5 wt% of 1-octanol (99.5 %, Fluka Analytical) and stirred under a light vacuum to eliminate bubbles.

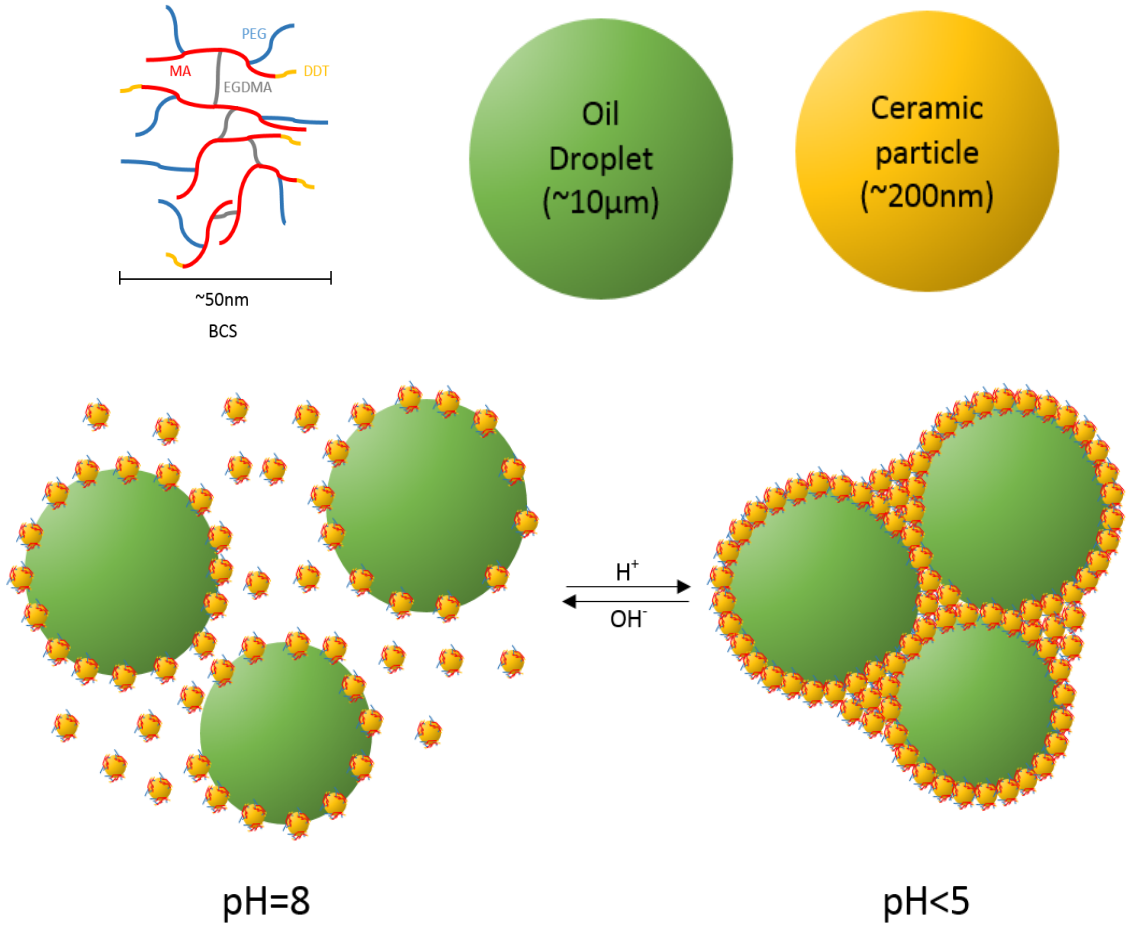


Figure 22. A BCS molecule, an oil droplet, a ceramic particle (top); Change of aggregation with pH. In this schematic, all BCS molecules are absorbed on the ceramic particles and there is no free BCS in the oil-water emulsion system (bottom).

Afterwards, the suspensions were mixed with n-decane (99 %, Sigma Aldrich) at different volume ratios. Emulsification was carried out by using a homogenizer (IKA T25 Digital Ultra Turrax, UK) at stirring speeds from 3000 rpm to 13000 rpm for 3 min. For a high solid loading suspension (40 vol%-50 vol%), a low stirring speed (3000 rpm-8000 rpm) was enough to produce a stable emulsion, while for a suspension with a low solid loading (30 vol%-40 vol%), a high stirring speed (8000 rpm-13000 rpm) was required to break the droplets into smaller ones to make the system stable. The emulsified suspensions were of low viscosity which make them flow well. In order to make the emulsions printable, a pH trigger acid, gluconic-δ-lactone (GδL, 99 %, Alfa Aesar), was added just before transferring the emulsions into 3 ml syringes (Nordson EFD) to decrease the pH to form a shear thinning emulsified gel.[15]

3.1.2 Pluronic based inks

3.1.2.1 Materials

Pluronic F-127 ® powders were purchased from Sigma Aldrich. Alumina powders bought from Baikowski (Baikalox B-Series, SMA6, D_{50}=0.2 µm) were sieved with a 100µm mesh using a vibratory sieve to break large aggregates (d>0.5 mm) which result in poorly printed paste and blocked tips. 430L stainless steel powders (Cr: 16-18) with average particle size of ~5 µm were purchased from US Research Nanomaterials. Iron oxide powders (30 µm, 98 %), iron powders (5 µm, 99 %) and fine synthetic graphite powders (APS 7-11 µm, 99 %) were purchased from Alfa Aesar. 430L stainless steel, iron oxide and iron were chosen because they have a melting point between 1450 and 1550 ℃ which is similar as the sintering temperature of Al_2O_3 ceramics. Dolapix CA was purchased from Zschimmer & Schwarz in Germany. All these materials were used as received. The particle size and shape of these powders was assessed using scanning electron microscopy SEM (JSM 6010 LA, JEOL, USA) (Figure 23).

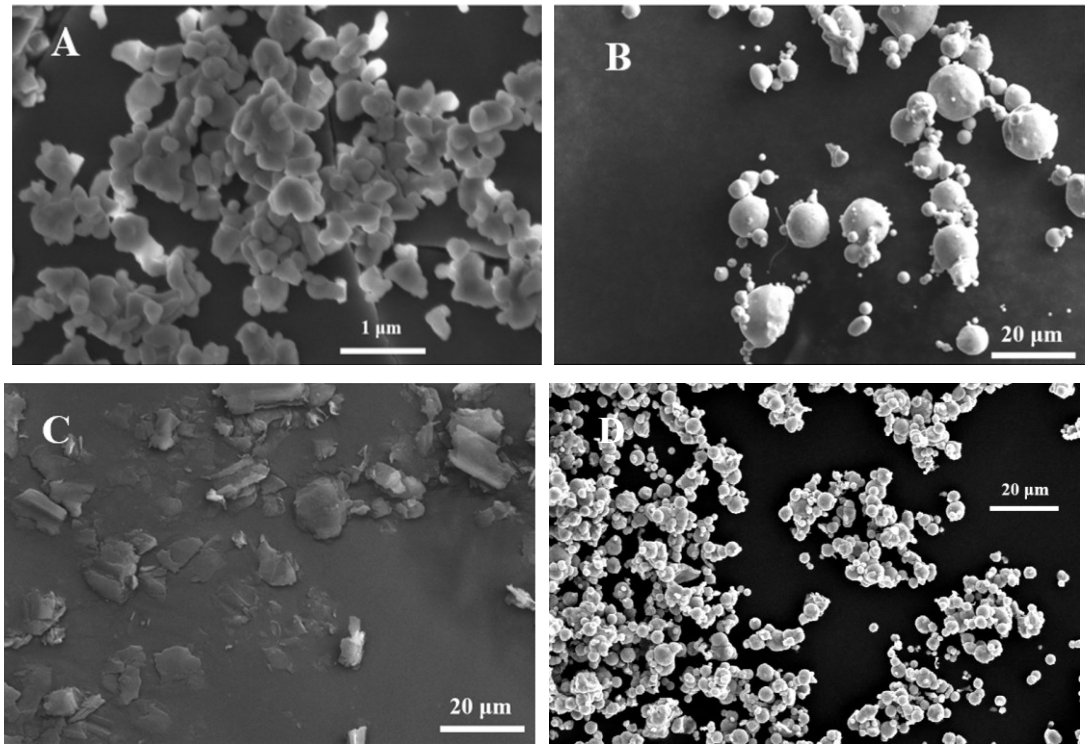


Figure 23. SEM images of A) Al_2O_3; B) Steel; C) Graphite; D) Iron particles.

3.1.2.2 Ink preparation

Pluronic F-127 ® contains polyethylene oxide (PEO) and polypropylene oxide (PPO) roughly in a 2:1 ratio. When mixed with water, the polypropylene oxide groups in Pluronic F-127® have hydrophobic or hydrophilic behaviour depending on temperature and water content (hydrophobic at higher temperature and lower water content while hydrophilic at lower temperature and higher water content). This thermally reversible behaviour of water based Pluronic® solution makes it possible for the inks to flow at a low temperature (around 0 °C) and to form printable shear thinning pastes at a high temperature (around 25 °C) (As shown in Figure 5 B).

Pluronic F-127® solutions with concentrations ranging from 15 wt% to 40 wt% were made by stirring flasks of deionised water mixed with the proper amount of Pluronic at 4 °C. The solutions were left in a fridge at 4 °C for 24 hours to dissolve the powders and release the bubbles until they become clear and homogeneous. These Pluronic® stocks were prepared to measure their rheological response as a function of temperature. The goal is to find out a suitable concentration for robocasting. According to the temperature-viscosity curves of these Pluronic® stocks, the 25 wt% solution, with a liquid-gel transition temperature between 20 to 25 °C, was chosen.

Fine pre-weighted powders were mixed with 25 wt% Pluronic® solution and dispersed by adding 0.5 wt% of Dolapix CA in a 150 ml Poly tetra fluoroethylene (PTFE) container (Thinky, USA). Subsequently, the ink was mixed using a planetary centrifugal mixer (Thinky ARE-250, USA, Figure 24 A) at 2000 rpm for 2 min. Prior to mixing the suspensions were cooled to ~0 °C in an ice bath. After cooling down to 0 °C, the ink became a flowing liquid and a stirring spatula was used to break the powder agglomerates stuck on the inner walls of the container. It is necessary to remove these stuck agglomerates because they decrease the solid loading of the paste and could block the printing nozzle if they are incorporated into the final ink. This process was repeated several times (normally 4 to 6 times depending on the solid loading and the total volume of paste) until the powders and the solution were fully mixed. The ink was then defoamed at room temperature at 2200 rpm for 5 min to remove bubbles (particles and solution may segregate if defoamed in liquid state). The defoamed inks were then stored in the container and sealed with films. The inks can be stored at room temperature for a period up to 2 months without water segreation, paste condensation, drying or cracking. The solid contents of inks used to print the final core/shell structures are 35 vol% Al_2O_3, 35 vol% $(Al_2O_3)_{0.9}$-$C_{0.1}$ (in volume) and 30 vol% steel.

Figure 24 B shows how a bottle of paste for robocasting looks like before, during (1-2 times of mixing) and after (4-6 times of mixing) using the mixer.

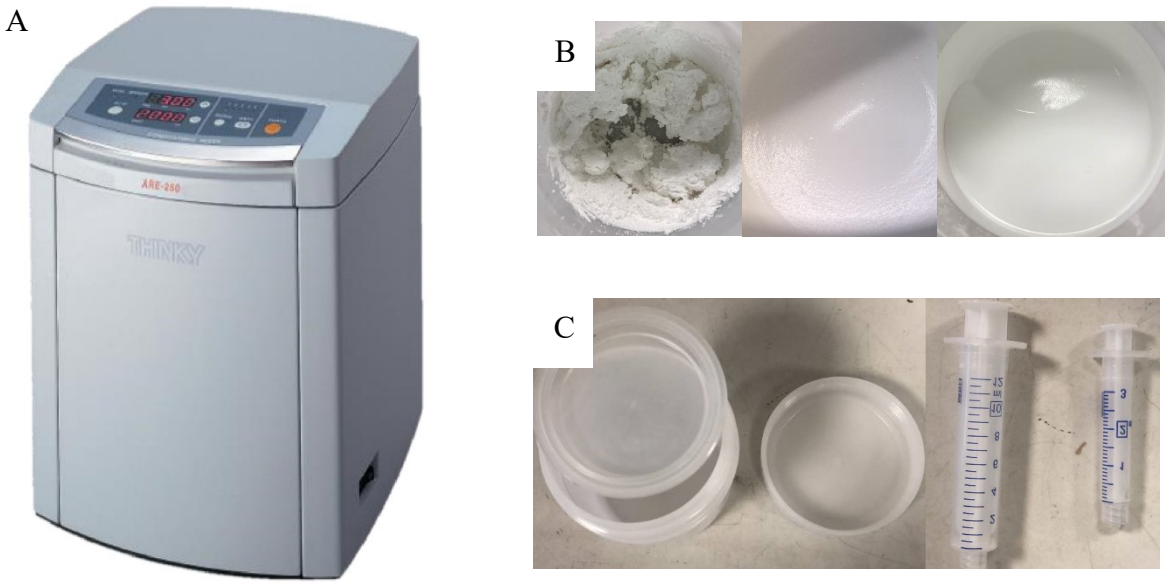


Figure 24. A) A Thinky ARE-250 mixer, courtesy of Intertronics Ltd; B) Hydrogel paste before, during and after mixing; C) syringes and supplements for robocasting.

Pastes stored in PTFE containers were transferred to 10 ml syringes (Nordson EFD, Figure 24 C) for robocasting. A paste with high flowability at low temperature can be dropped into the syringe with a pipette through the top mouth of the syringe or be sucked up into the syringe directly. Care should be taken to avoid trapping air bubbles during transfer. However, for a paste of a high viscosity, it is impossible to drop or suck it into the syringe. The container was firstly placed in an ice bath to decrease the viscosity of the paste. Afterwards, the paste was scooped out of the container using a flat spatula and spread into a 10 ml syringe through the top mouth carefully to ensure that there are no trapped air bubbles. Air bubbles were trapped around the top mouth when placing the piston into the syringe. Hence, a female-female luer-lock connector was used to extrude the paste from the pre-loaded syringe to another empty syringe.

3.1.3 Core/shell structure

Different kinds of core/shell structures were fabricated by loading inks in syringes as shown in Figure 25. First the 10 ml syringe (diameter of 15.6 mm) is immersed in an ice bath and filled with alumina ink at 0 ℃. At this temperature the ink behaves as a liquid. Then, one large cylinder spacer or multiple small cylinder spacers (depending on the number of cores per cartridge) are placed inside the syringe. The diameters of the spacers are 4.5 or 8 mm. Subsequently, the syringe is placed in a hot bath (70 ℃) to gel the Al_2O_3 ink and the spacers are removed leaving one or several cylindrical holes that are filled with a flowing steel ink kept at 0 ℃. Afterwards, the syringe is placed again in the hot bath to gel the core. In order to create an interphase between the steel core and the ceramic shell the process is done in three steps: i) an alumina ink is introduced in the syringe, a large cylindrical spacer is placed and the ink is gelled, ii) an Al_2O_3/C ink is introduced in the cylindrical hole and a smaller cylindrical spacer is paced in the middle, this ink is subsequently gelled and the spacer is removed leaving a hole; iii) the steel ink is introduced in the cylindrical hole and subsequently gelled.

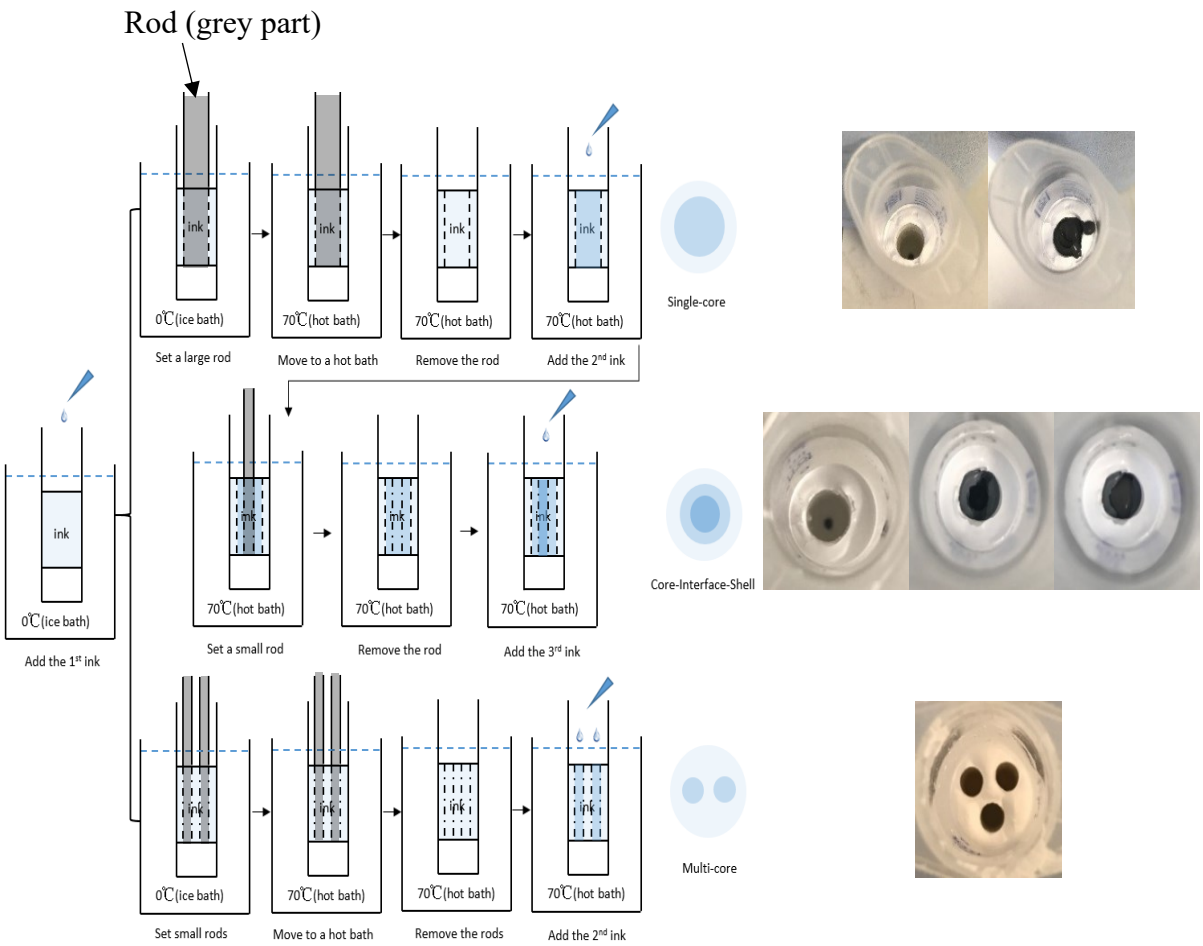


Figure 25. Process of preparing printing cartridges with core/shell structure.

3.2. Manufacturing Processes

3.2.1 Printing

The path of the raster pattern and the printing orientation were defined using G-code (coded by A3200 Motion Composer, Aerotech, UK) which is visible with the RoboCAD software. Simple structures such as bars and grids were designed and drawn by RoboCAD. A STL tool in this software was used to build up more complex geometries like dog-bones. This tool sliced STL models downloaded from Internet or created by Solidworks into layer wise continuous filaments with a thickness close to tip diameter. The printing speed, road width, structure dimensions were pre-set and can be adjusted in the software.

Nozzles with different kinds of shapes and diameters can be used for robocasting. For example, Nordson offers conical plastic and straight steel nozzles (Figure 26) with diameters ranging from 0.1 to 1.56 mm. Less pressure is needed when using a conical nozzle compared to a straight nozzle, but a straight nozzle gives higher accuracy. Also, the metal nozzle is more durable as it will wear less as the ceramic inks flow through it (ceramic particles can grind down plastic).

A robocaster (3D inks LLC, USA) was used to print the green bodies on flat and smooth substrates (polished poly tetra fluoroethylene or flat steel plate) (Figure 27). The robocaster is equipped with three independent plungers powdered by servo motors which give a nominal precision of 1 μm. Before starting printing, the syringe was equipped with a nozzle and placed in a holder which can be fixed on the robocaster. Next the syringe was moved down slowly until the tip of the nozzle just touched the substrate. Then the nozzle was moved up by a distance equivalent to the diameter of the printed line (the nozzle internal diameter) to allow for the paste to come out and touch the substrate surface. After the nozzle was set up properly, the plunger was lowered in a controlled manner (using RoboCAD or A3200 Motion Composer) until it contacted and pressed the piston to extrude the paste out of the syringe on the substrate layer by layer. Conical plastic nozzles (Nordson, USA) with a diameter of 410 μm were used here to give homogeneous extrusion during the printing. A 30 mm ‘lead-in’ path was used before printing each part to make sure that the ink was flowing steadily at constant plunger displacement speeds when the part was printed.

Printing parameters and environment are important. The robocaster uses three motors to control the nozzle movement and its speed in the X, Y and Z directions. Additional motors are used to control the plungers’ position and speed. The main printing parameters are printing speed,

raster pattern (road width and structure dimensions), nozzle type and size. The printing speed (nozzle speed in the x-y directions) varies from 2 mm/s to 20 mm/s depending on the nozzle type, the viscosity of the paste and the structure of the parts. The printing speed and the raster pattern were pre-set by RoboCAD. The robocaster was placed in an enclosed cabinet to control the environment. The printing temperature in the cabinet was regulated using a heater set and maintained at 23 ℃. The humidity was usually kept between 65 % and 85 % with a humidifier (measured using a humidity measuring instrument).



Figure 26. The schematics and images of plastic conical nozzle and the steel straight nozzle.

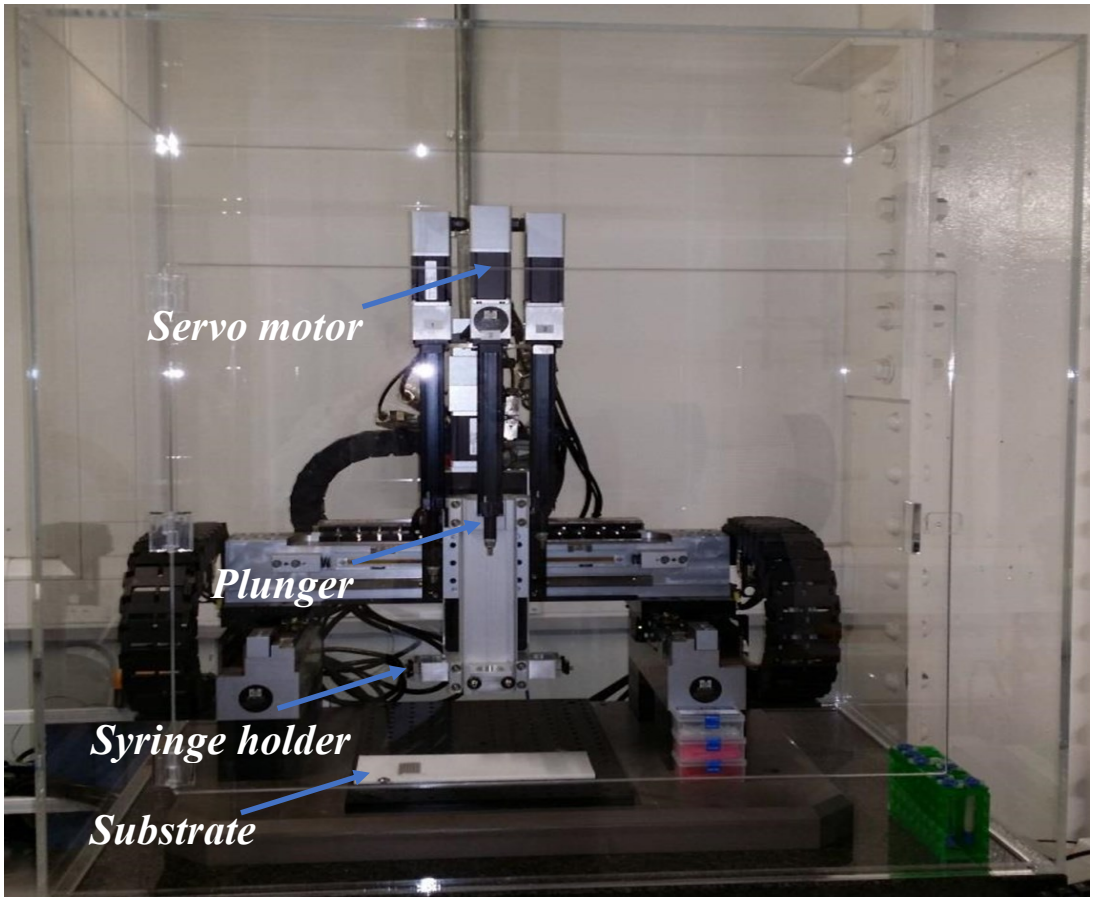


Figure 27. A picture of a robocaster in an enclosed cabinet.

As shown in Figure 28, different kinds of samples were printed by robocasting. For emulsions, long bars were printed for mechanical tests. The printed lines were aligned along the length of the bars. The dimensions of the printed green bodies were 35×3×3 mm. As for core/shell samples, bars, dog-bone samples, and grids with different dimensions were printed. The dimensions of the bars were 35×3×3 mm. The length of the dog-bone samples was 30 mm with a 6×2×2 mm neck. The grids were of 10×10×2 mm with a 0.6 mm road width (i.e. distance between two nearby filaments on the same plane) and 45° rotation. All the dimensions mentioned here correspond to the green bodies. The corresponding linear dimensions of the sintered samples were 70-80 % of the green bodies because of shrinkage during drying and sintering.

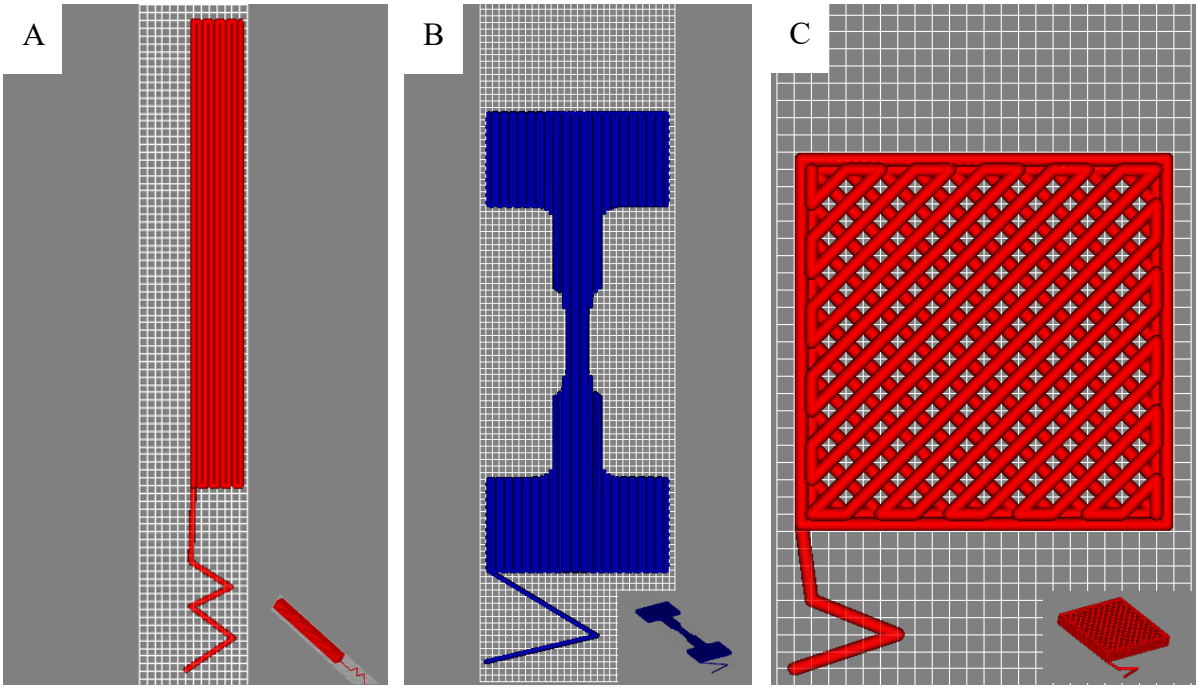


Figure 28. Printing orientation of A) Emulsion and hydrogel bars; B) hydrogel dog-bones; C) Hydrogel grids (3D models at right bottom corner).

3.2.2 Post-processing

The printed ceramic green bodies were dried in a controlled environment at room temperature (20 to 25 ℃) and 60 to 70 % humidity (in an enclosed box with several drops of water) overnight to avoid bending and cracking. After that, the dried green bodies were removed from the substrate carefully. A very thin layer of butter was placed on the substrate such that the printed parts will not stick to it and can be easily removed after drying. Because the parts do not stick to the substrate, butter also enables homogenous shrinkage preventing cracking and

warping. Dried bars and dog-bone green bodies were cold isostatic pressed (CIP, Stansted Fluid Power LTD, UK) at 300 MPa to enhance densification and close large defects.

A chamber lift furnace was used to sinter emulsion-based printed ceramics, the ceramic green bodies were de-bound at 500 ℃ for 2 hours to burn out the remaining BCS and then heated up to 1550 ℃ followed by a 2-hour dwell. A vacuum furnace (pressure 10^{-6} torr) with a W heating element was used to sinter the core/shell ceramics. First, the dried green bodies were de-bound in vacuum at 600 ℃ for 2 hours to burn out the Pluronic. Next, they were sintered at 1400 ℃ for 2 hours. The heating up rate was 5 ℃/min for all heating process and there was no temperature control during cooling (power off for cooling).

3.3. Characterization

3.3.1 Rheology

3.3.1.1 Introduction to rheology and use of the rheometer

The rheology is the study of the flow properties of liquids or soft solids which exhibit a viscoplastic response to an applied force. For a shear thinning paste made with ceramic particles and a polymer solution, when there is no applied force, the particles and polymers in the paste are randomly arranged and the connecting bonds (e.g. hydrogen bonds) give the paste a high viscosity. However, when the paste starts to move, the particles and the polymers start to flow in a fixed direction and the bonds start to break which decreases the viscosity of the paste. The storage modulus (G') relates to the energy stored in the material under an applied force and the loss modulus (G'') to the energy lost under an applied force. The G' is equal to Elastic modulus when there is no applied force. When G' is higher than G'', the material has solid like behaviour while when G' is lower than G'', the material has liquid like behaviour.

A rheometer is used to measure the rheology of pastes. It measures the viscosity, storage modulus or loss modulus under different shear rate, applied force or temperature.

There are several set-ups to measure the rheology of robocasting pastes. Most researchers use parallel or cone-plate geometries (Figure 29 A, B).[68, 76] Other techniques have also been used to study the viscosity of pastes such as concentric cylinder[13] and capillary rheometers (Figure 29 C, D)[77]. The parallel or cone-plate geometries were chosen mostly because these set-ups require a very small amount of paste, the test times are relatively short and they can be used for high viscosity pastes.

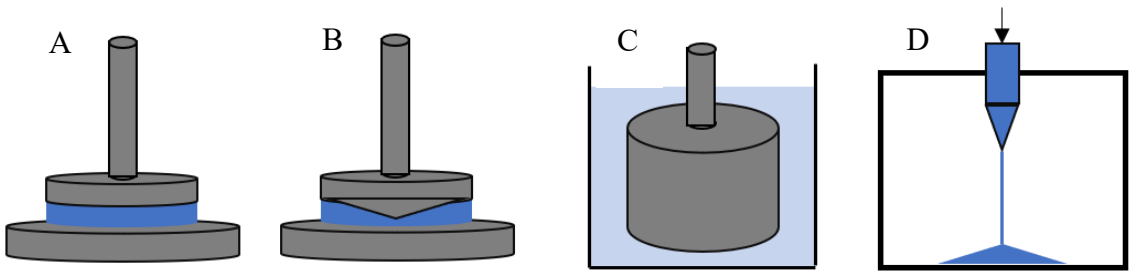


Figure 29. The schematics of A) parallel geometry; B) cone-plate geometry; C) concentric cylinder; D) capillary rheometer.

3.3.1.2 Rheology measurement

A Discovery HR-1 hybrid rheometer (TA instrument, UK) was used here to measure the rheology of the inks (Figure 30 A). A 40 mm parallel plate steel geometry was chosen to do the measurement (Figure 30 B). There are also some other geometries such as an 8 mm parallel plate steel geometry which is suitable for highly viscous materials (like rubbers) and a 60 mm cone geometry which is designed for fluids with low viscosity (like milk). The testing gap was set as 1000 μm and a solvent trap was used to prevent the inks from drying. Around 2 ml of pastes were placed at the center of the bottom part of the rheometer by a pipette (fluid) or a spatula (gel). Then, the plates were moved to compress the sample leaving a 1000 μm gap that is fully filled by the paste without any trapped bubbles. The excess paste was trimmed carefully by spatula as this excess may influence the accuracy of the results.



Figure 30. A) A Discovery HR-1 hybrid rheometer, courtesy of TA Instrument®; B) a picture of 40 mm parallel steel geometry, courtesy of TA Instrument®.

For Pluronic based inks, the temperature ramp tests were conducted from 0 ℃ to 40 ℃ (-5 ℃ to 20 ℃ for the 40 wt% Pluronic solution) at a shear rate of 1 s^{-1}. The flow ramp tests were set at 20 ℃ at shear rates ranging from 0.01 s^{-1} to 100 s^{-1}. Oscillation amplitude sweep tests were carried out at 1 Hz with oscillation stresses ranging from 1 Pa to 1000 Pa.

For emulsified inks, in addition to the measurements above, time sweep tests of emulsions were measured immediately after adding the GδL into the emulsions with a frequency of 1 Hz and a strain of 5×10^{-5} rad. Oscillation tests were carried out by five steps:

-fixed oscillation at 0.5 Hz and 0.5 % strain for 200 s,

-frequency sweep at 0.5 % strain from 0.5 Hz to 50 Hz,

-fixed oscillation at 0.5 Hz and 0.5 % strain for 200 s,

-amplitude sweep at 0.5 Hz from 0.5 % to 30 % strain,

-fixed oscillation at 0.5 Hz and 0.5 % strain for 200 s.

The fixed oscillation steps indicate the static conditions of the emulsions, the frequency sweep shows the G' and G'' changing with the increasing of frequency and the amplitude sweep shows the G' and G'' changing with the increasing of strain.

The hysteresis of the emulsified slurries is measured with shear rates increasing from 0.01 s^{-1} to 30 s^{-1}, 3 min setting and decreasing from 30 s^{-1} to 0.01 s^{-1}. Similar methodology has been used to characterize comparable systems by García-Tuñón et al.[78]

3.3.2 Droplet size of emulsions

The droplet size and distribution in the emulsified suspensions were assessed using optical microscopy. Rhodamine B (<1 mg), a fluorescent molecule was added into the reaction flask before the reaction to synthesize the rhodamine doped BCS powders with the aim to visualize the ceramic particles (with BCS attached) that stick to the oil/water interface in the suspensions.[15] A drop of rhodamine-doped suspension was dropped on the surface of a glass slide by pipette, and then compressed by another glass slide for optical microscopy. The final gap between the glass slides is ~ 150 μm. The images of the emulsified suspensions were taken using an optical microscopy (AxioScope. A1 ZEISS) with an immersion ocular (N-Achroplan 100×/1.25 Oil iris), fluorescence free immersion oil and rhodamine fluorescence filter (FL Filter Set 43 CY 3 Shift free) (Figure 31).

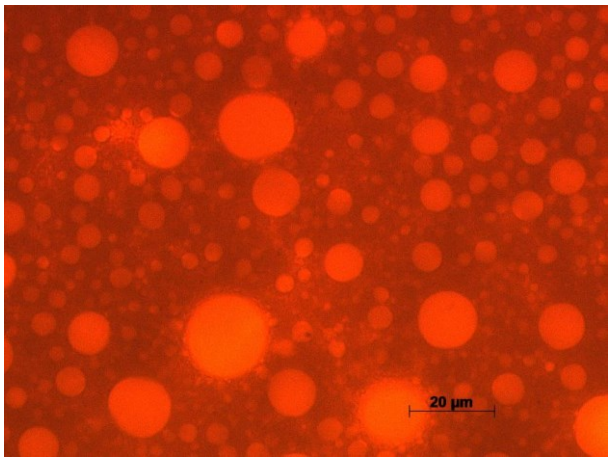


Figure 31. The image of an emulsified suspension. The spheres are oil droplets dispersed in water. The BCS-functionalized particles segregate to the water-oil interface and are made visible due to the rhodamine.

3.3.3 Measurement of porosity and density

The porosities and densities of the sintered samples were measured by the Archimedes method. First, a dry sample was weighed in air (weight is m_1). Then the sample was immersed in water and weighed (weight is m_2). The real density of the sample ρ_{real} was calculated using equation:

$$\rho_{real} = \frac{m_1}{m_1 - m_2}\rho_{water} \quad (6)$$

The porosity P of the samples was calculated using equation:

$$P = 1 - \frac{\rho_{real}}{\rho_{theoretical}} \quad (7)$$

where the ρ_{real} is the calculated density and the $\rho_{theoretical}$ is the theoretical density.

The average pore size and pore distribution of emulsion-based ceramics and the volume fraction of steel fibres in the core/shell samples were quantified using Image J to analyse SEM images of polished samples taken using a JSM 6010 LA (JEOL, USA) microscope at 20kV acceleration voltage. The samples were mounted in epoxy grinded and polished down to 1 μm diamond. A gold coating was applied on the sample surface before imaging by secondary electrons.

In order to get the average pore size and pore distribution of an emulsion-based sample as shown in Figure 32, some adjustments need to be done. First, set the correct scale. Then, 'Finding Edges' and 'Smoothing' for 5 times were done on the original image (from Figure 32 A to Figure 32 B). Next, the threshold was done on the image using 'Huang Default' from 0 to 60 (Figure 32 C). Finally, 'Analyse Size' was 5 to infinity mm^2, 'Circularity' was 0.15 to 1.00. The average pore size can be achieved by knowing the average area of the pores (Figure 32 D).

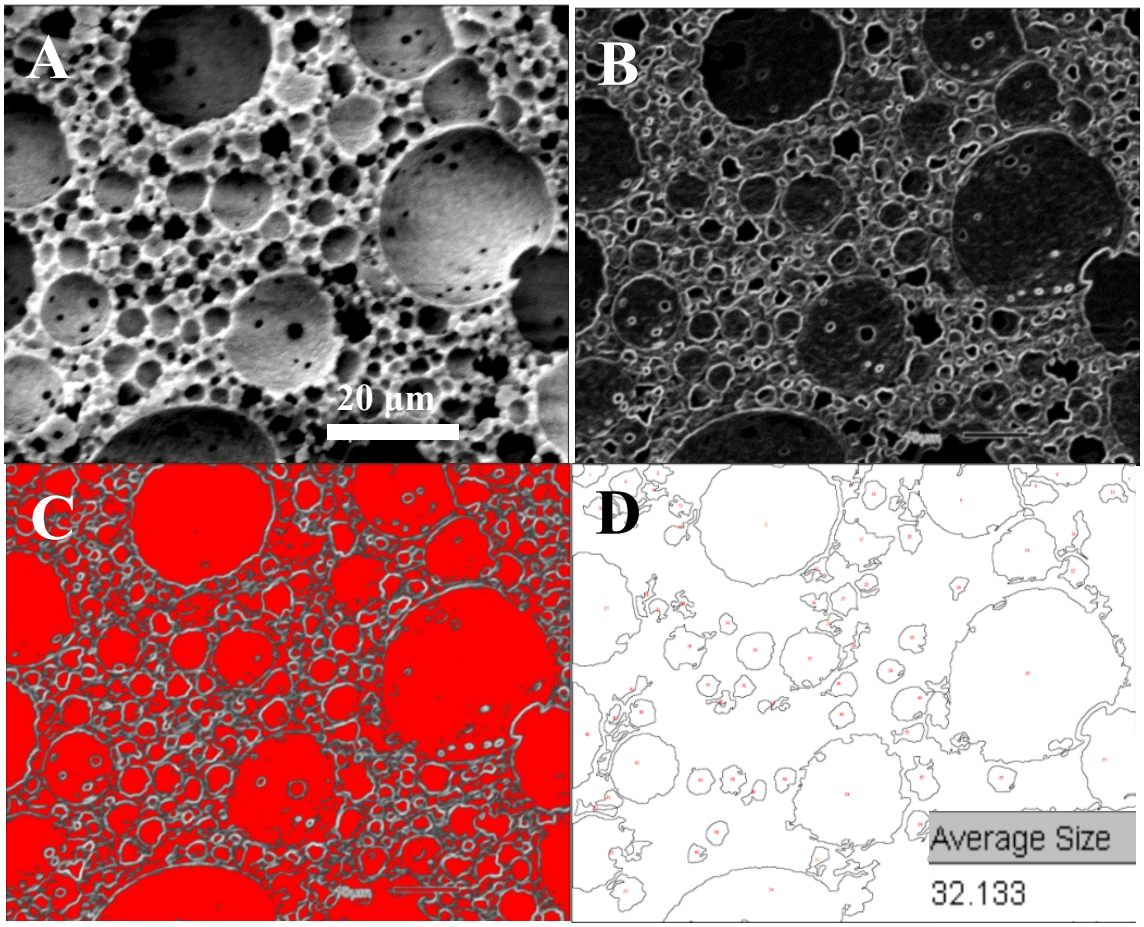


Figure 32. Image J analyse of the pore size and distribution of an emulsion-based sample. A) Original SEM image; B) The image after finding edges and smoothing; C) The image after threshold; D) The image after size analysing.

In order to obtain the pictures shown in Figure 33 to calculate the volume fraction of the steel fibres in the core/shell samples, a colour threshold was used with the 'Hue' from 0 to 255, the 'Saturation' from 0 to 255 and the 'Brightness' from 95 to 255. The thresholding method was default, threshold colour was red and the colour space was HSB. After the scale was set correctly, the 'Analyse Size'(mm^2) was 50 to infinity and the 'Circularity' was 0.10 to 1.00.

Assuming the steel/alumina ratio is constant in different cross-sections of the bar. The steel volume fraction should be equal to the area fraction gained by Image J.

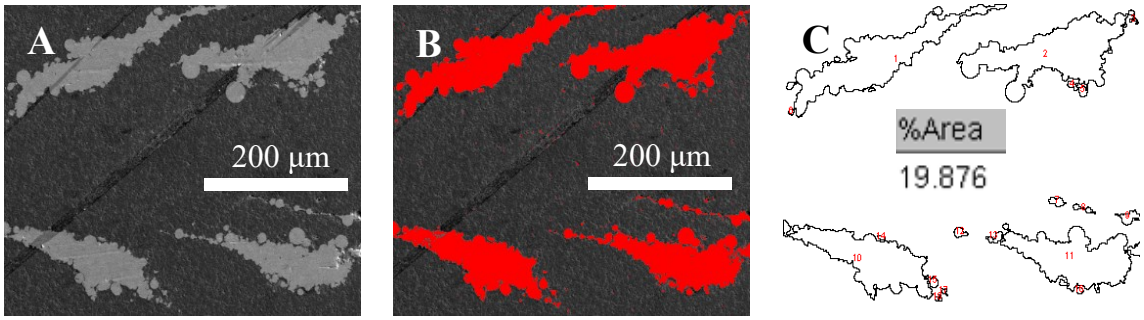


Figure 33. Image J analyse of the volume fraction of the steel in the core/shell structure. A) Original SEM image; B) The image after threshold; C) The image after size analysing.

Each sample has been analysed using ImageJ at three different positions to get the average size for the emulsions or average core area for the core/shell composites. For emulsion-based samples and core/shell samples, the threshold parameters need to be adjusted for each single SEM image for the Image J software to identify the ceramic/pore interface or core/shell interface.

3.3.4 Mechanical testing of emulsion-based samples

Three-point bending tests were done on the printed emulsion-based samples. A Zwick universal testing machine (Zwick/Roell Z2.5) was used to measure the strength of the samples according to the equation:

$$\sigma_f = \frac{3FL}{2bd^2} \tag{8}$$

where σ_f is flexural stress, F is the applied force, L is the support span, b is the width of test bar and d is the thickness of the test bar. The stress where the sample starts to fail is recognized as the strength. The dimension of the samples was 25×2.5×2.5 mm. The span was 20 mm and the displacement speed was 0.1 mm/s.

3.3.5 Mechanical characterization of core/shell samples

3.3.5.1 Mechanical measurements

The following tests were performed and the stress where the sample starts to fail is recognized as the strength for the bending, compressing and tensile tests.

- Four-point bending. The strength of the samples was measured using four-point bending tests on printed bars (Figure 34 A, Figure 36 B). The dimensions of the bar-shaped samples were 25×2.5×2.5 mm with four side surfaces polished down to 1 µm diamond. The support span of four-point bending tests was 20 mm and loading span was 10 mm. The displacement rate was

0.2 mm/min. The stress and strain of the four-point bending test were calculated using the equations:

$$\sigma_f = \frac{3F(L-L_l)}{2bd^2} \quad (9)$$

$$\varepsilon = \frac{48Dd}{11L^2} \quad (10)$$

where L is the support span, L_l is the loading span, F is the applied force, b is the width, d is the thickness and D is the displacement.

- Three-point bending tests on Single-Edge Notched Bend (SENB) samples. Tests on notched samples (Figure 34 B, Figure 35 B) were performed under different conditions (using the universal test machine [Instron 8562, US] and in-situ bending tests [MT300 Tensile Tester, DEBEN, UK]) to measure toughness and calculate strength. The notches were made in two steps. First, a 0.84 mm thickness diamond wafer blade was used to cut a large notch with a depth of about 1/3 of the sample thickness in a bar-shaped sample. Then, a razor blade and 1μm diamond suspension were used to sharpen the notch by reciprocating cutting. A force between 2 N to 10 N was applied during notching to ensure that the razor blade is in contact with the sample (The force needs to be added gradually to avoid breaking the sample at the notch). It took around one hour to make a notch on one sample. For the tests done using the universal test machine, the span of three-point bending tests was 15 mm and the displacement rate was 5 μm/min. A Linear Variable Differential Transformer (LVDT) was used here to monitor the minor deformation of the samples during bending. For the in-situ bending test, the span was 21 mm and the displacement rate was 0.1 mm/min.

The stress and strain of the three-point bending test were calculated using equations:

$$\sigma_f = \frac{3FL}{2bd^2} \quad (8)$$

$$\varepsilon = \frac{6Dd}{L^2} \quad (11)$$

where L is the span, F is the applied force, b is the width, d is the thickness and D is the displacement.

-Compression tests of grids (Figure 36 A). Compression test on printed grids were done in a universal test machine (Zwick/Roell Z2.5). Grids with a size of 8×6×1.5 mm were placed between two parallel plates to measure the applied force during compression at a loading rate

of 1mm/min. The top and bottom surface of the grids were polished to make sure they are parallel to each other (Figure 37).

The compressive stress of the samples was calculated using equation

$$\sigma_e = \frac{F}{A_0} \tag{12}$$

where F is the applied force and A_0 is the surface area of the top/bottom

-In situ bending and tensile tests in the scanning electron microscope. For the in-situ experiments, a microtest stage (Figure 34 C, MT300 Tensile Tester, DEBEN, UK) was used to do bending or tensile tests inside a Zeiss Sigma 300 (Germany) SEM. In-situ three-point bending tests in the scanning electron microscope were done on single extruded filaments (Figure 35 A) with a diameter ~ 300 μm and SENB samples using a span of 21 mm and a displacement rate of 1mm/min. The single filaments were too thin to do any polishing or notching without damaging them, so they were used as sintered. The stress σ_f was calculated by equation

$$\sigma_f = \frac{FL}{\pi R^3} \tag{13}$$

where F is the applied force, L is the support span, R is the radius of the filament.

In-situ tensile tests in the SEM were done on dog-bone shaped samples (Figure 36 C, D). Tensile tests were performed on dog-bone shaped samples with a length of 25 mm and a neck of 5×1.2×1.2 mm with both sides polished to 1 μm diamond. The displacement rate for all in-situ tests was 0.1 mm/min. The tensile stress of the samples was calculated using equation:

$$\sigma_b = \frac{F}{S_0} \tag{14}$$

where F is the applied force and S_0 is the area of the rectangular cross section.

- Indentation hardness. An Indentec 6040LKV was used to measure the Vickers hardness of the samples. The loading force was 5 kg.

After all the tests, the fracture and polished surfaces where characterized using optical microscopy (Olympus BX51, Japan) and SEM (JSM 6010LA, JEOL, Japan).

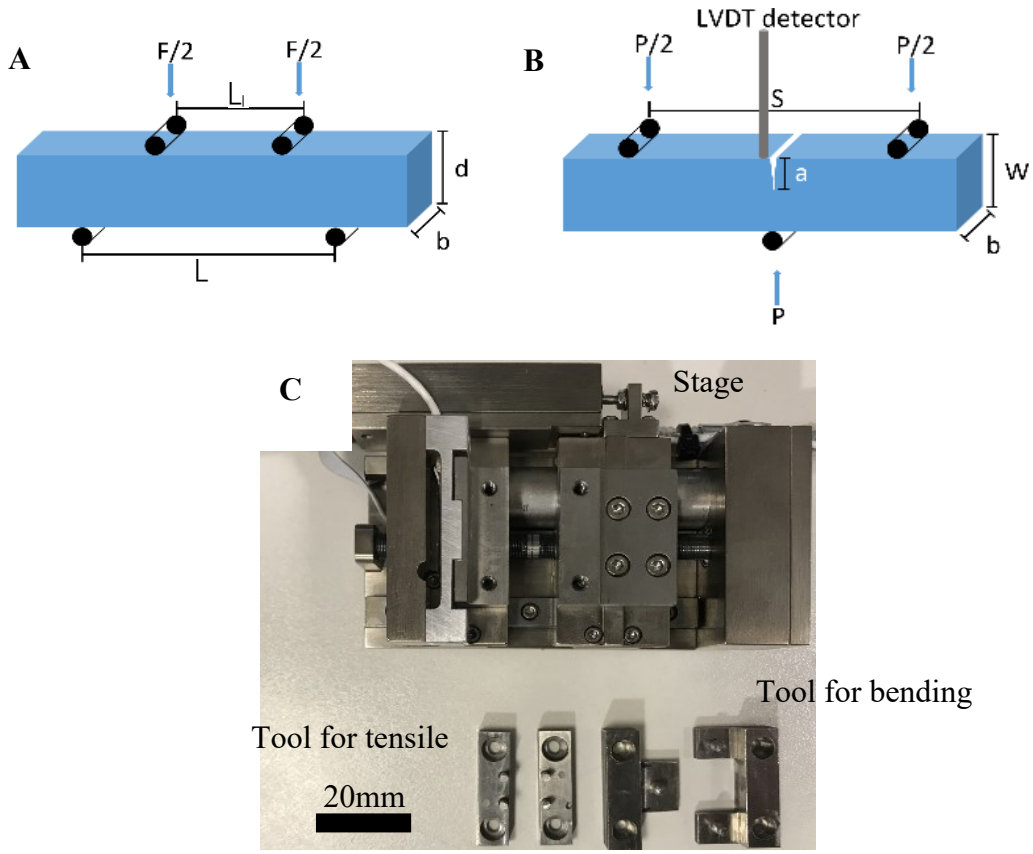


Figure 34. A) Four-point bending; B) Three-point bending on a SENB sample (LVDT); C) microtest stage and tools for in-situ tests.

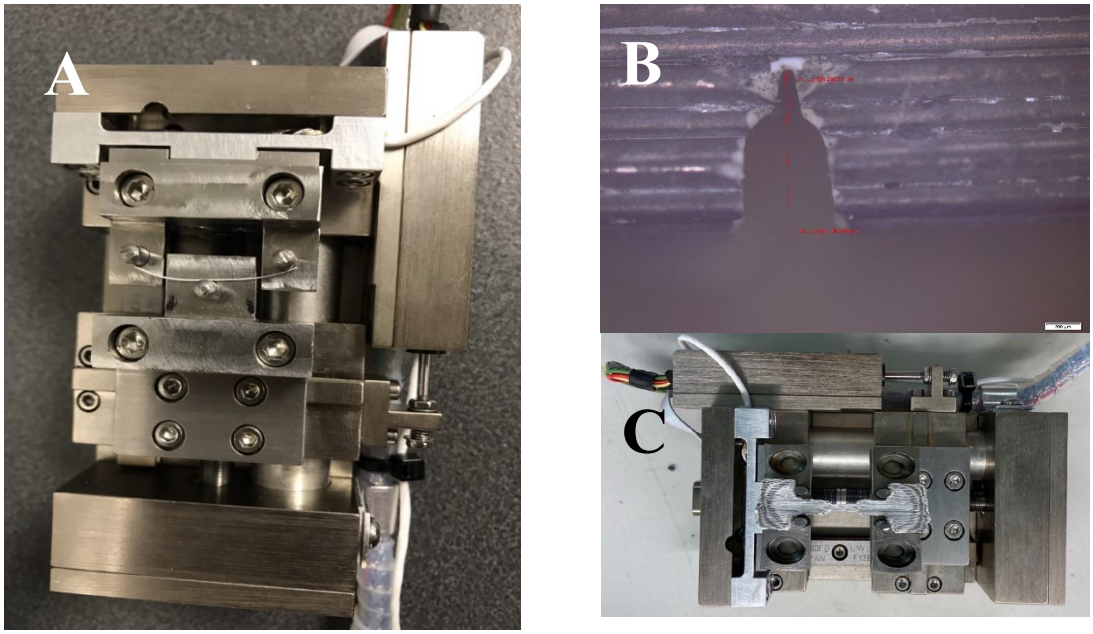


Figure 35. A) A single filament on the microtest stage; B) A SENB sample; C) A dog-bone shaped sample on the microtest stage.

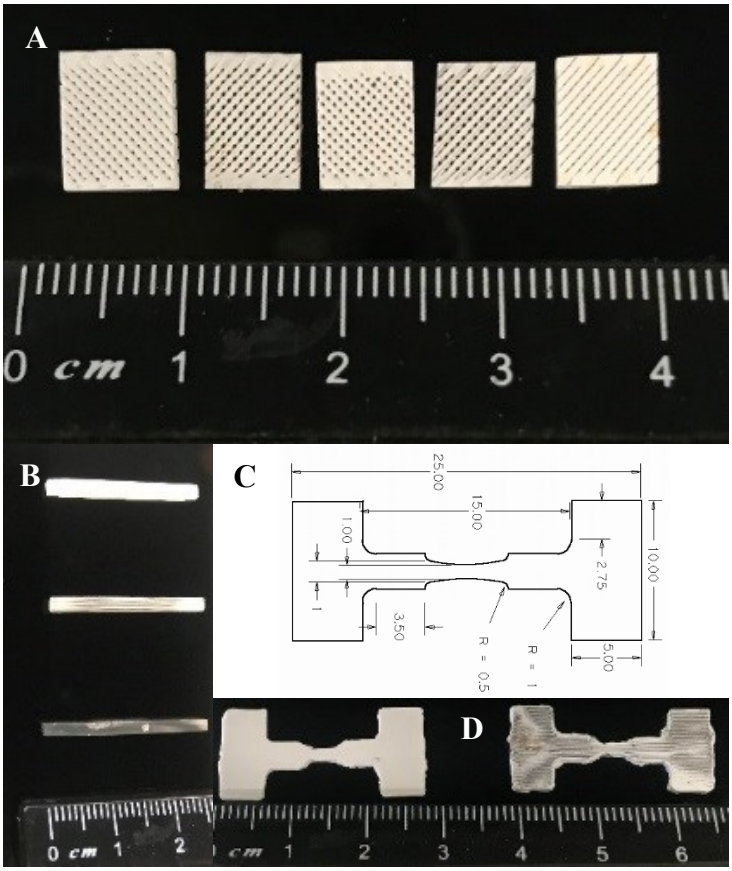


Figure 36. A) Grids; B) Bar shaped samples; C) Designed dog-bone; D) Printed dog-bone.

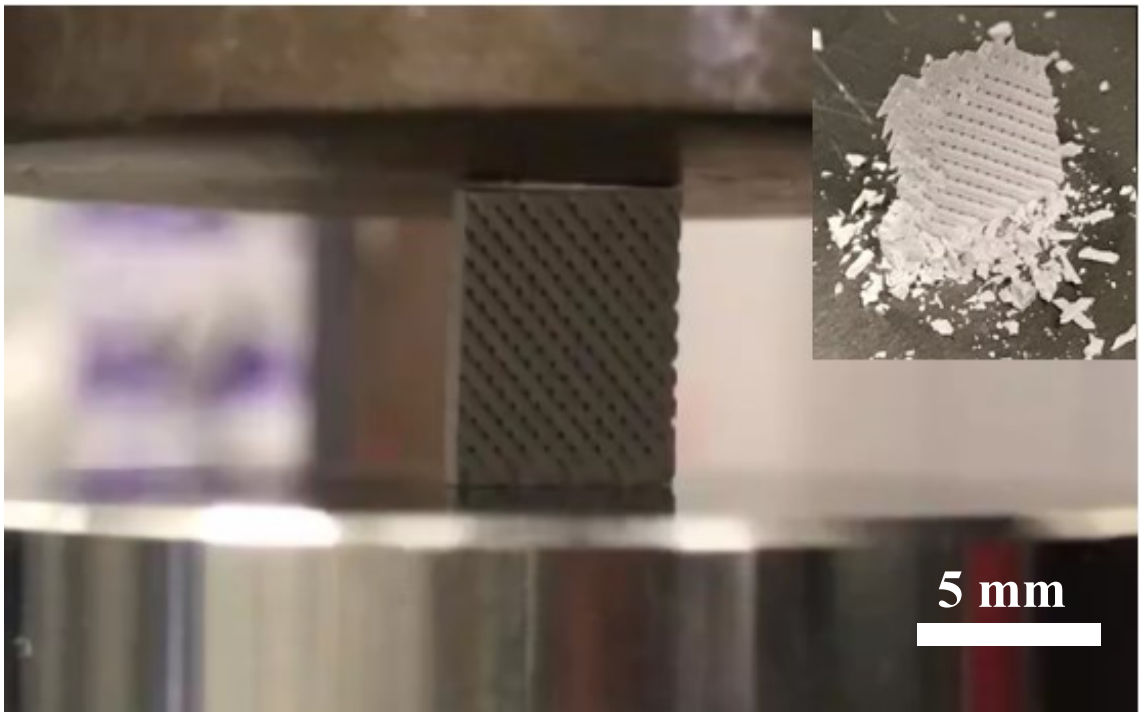


Figure 37. Compression test on a grid.

3.3.5.2 Microstructural and Compositional Analysis

3.3.5.2.1 X-ray Diffraction (XRD)

Several technologies such as infrared spectra and Raman spectra analysis[79] can be used to analyse the molecular or atomic structure of crystalline materials. X-ray diffraction is the first technology to study materials microstructure and it is one of the most effective, most widely used technologies. A beam of X-rays generated in a cathode ray tube are collimated and directed towards the sample. Materials with an organised microstructure (atomic arrangement) diffract the X-ray beams and the reflected X-rays are detected by a detector. When incident rays scattered by the arranged atoms, the scattered rays are in phase (mutually reinforcing each other) and a diffracted beam is formed.[80]

Figure 38 gives the details of a Bragg diffraction. A and C are two atoms that in the planes with a distance of *d*. Two incident rays (ray-1 and ray-2) with similar wavelength are scattered by A and C separately with scattering angle as θ. Thus, the travel distance of ray-2 is about BC+CD longer than that of ray-1. As

$$BC = CD = d\,sin\,\theta \tag{15}$$

the additional travel distance of ray-2 is $2dsin\theta$. The two rays are in phase when the scattering conditions satisfy Bragg's Law

$$n\lambda = 2dsin\theta \tag{16}$$

Where λ is the wavelength of the incident X-ray, n is a positive integer, d is the interplane distance in the crystalline structure and θ is the scattering angle[39].

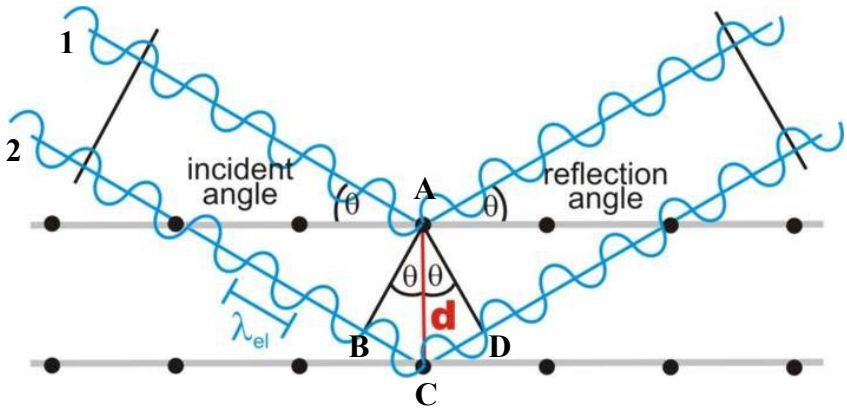


Figure 38. Bragg diffraction of two incident x-ray beams with identical wave length and phase onto a crystalline solid. Adapted with permission from[39]

During the X-ray Diffraction measurement, the sample is scanned through a specific scattered range of 2θ angles and all the possible diffraction directions of the crystalline structure should be detected. By comparing the measured X-ray diffraction pattern with the characteristic patterns stored in pattern database, the material's crystal structure and composition can be identified.

In this work, X-ray diffractometer (D2 Phaser X-ray diffractometer BRUKER AXS, Germany) was used to identify the different phases in the materials. Sintered samples were ground into powders with an agate mortar before the analysis. The scanning angle (2θ) ranged between 6° to 90°, the scanning speed was 4 °/min and the step size was 0.043°. The XRD patterns of the measured samples were compared with reference patterns to identify the phases present and the steel, Al_2O_3 and graphite reacted or not during the sintering process.

3.3.5.2.2 Scanning Electron Microscopy (SEM) and SEM- Energy Dispersive Spectrometer (EDS)

Scanning electron microscopy (SEM) is a non-destructive technique that gives details of the microstructure of a specimen. Optical microscopy uses visible light (wavelength ranging from 380 nm to750 nm) as the light source, while SEM uses electrons as the source and has a higher resolution than the optical microscopy. The resolution of the SEM can be influenced by several factors including the size of the beam (given by the apertures), the interaction volume which depends on the material and acceleration voltage, charging of the samples and the focusing ability.

By using condenser lenses to focus the electron beam on the sample surface and scanning the surface in a raster pattern, a high resolution, as low as 1 nm, can be achieved. The electron beam's position is combined with the detected signal to create the image of the surface.

During scanning using a high energetic electron beam on the sample's surface, the interaction between the electrons and the sample atoms generates signals containing varying information.

Figure 39 shows the signals generated from the interaction between the electrons and specimen. Signal from secondary electrons is the most widely used signal in SEM. The secondary electrons are emitted by atoms near the specimen surface once the atoms' electrons are excited by the scanning electron beam and thus have enough energy to escape from the surface of the material. The images gained from secondary electron are more surface sensitive and have higher resolution. Another common signal which is also been usually used is from backscattered electrons (BSE). The backscattered electrons escape from the region deeper than

the secondary electrons, thus gives a worse resolution of the surface topography than the secondary electrons. However, backscattered electrons are the electrons scattered back when they interact with the nuclei. Hence, they are sensitive to the atomic mass of the nuclei they scatter from. As a result, in a backscattered electron image, heavier elements are brighter than lighter elements as the heavier elements can backscatter more efficiently. Inelastic interactions may also create Auger electrons and X-rays. Vacancies of the surface atoms created by emitted secondary electrons must be re-filled with electrons. The energy is discharged from the atoms with the form of electromagnetic radiation (X-ray) or another electron with lower energy (Auger electron). This kind of signal can be used to determine the composition of the sample material.[39]

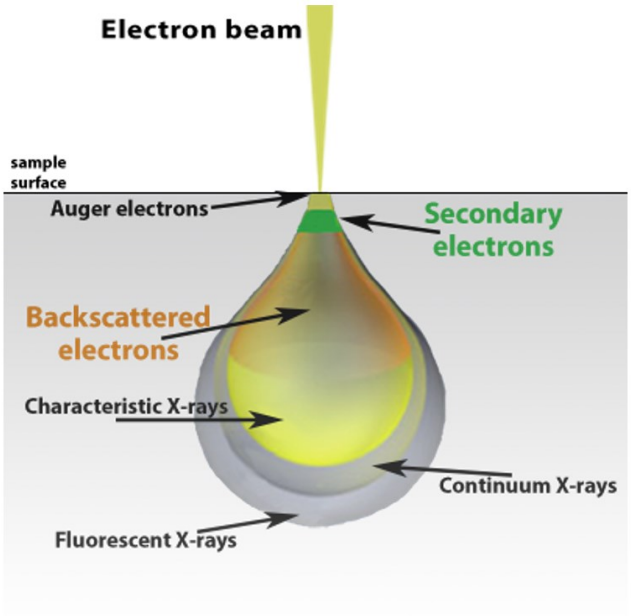


Figure 39. Signals generated from the interaction between the focused electron beam and the specimen. Adapted with permission from[39]

SEM-EDS is an additional function of the SEM which can be used to do analysis of the element type and content in a micro-area of the specimen. It detects the characteristic X-rays produced form the interaction between the electron beam and the specimen (Figure 39). As different elements have characteristic X-rays with different energy, the information of the element can be identified by measuring the energy of the characteristic X-ray.

SEM using secondary electrons is used to gain the images of the surface of the samples to study the microstructure of the samples. SEM-EDS map measurement was done on the samples' polished cross sections as well to view the elements distribution in the samples (Figure 40). The samples were mounted in epoxy grinded and polished down to 1 μm diamond. A JSM

6010 LA (JEOL, USA) microscope was used to do the measurement. The scanning was conducted using secondary electron at 20 kV. The SEM-EDS Map analysis is done using 512×384 Pixels and 5 sweep times with a dwell time of 1 ms.

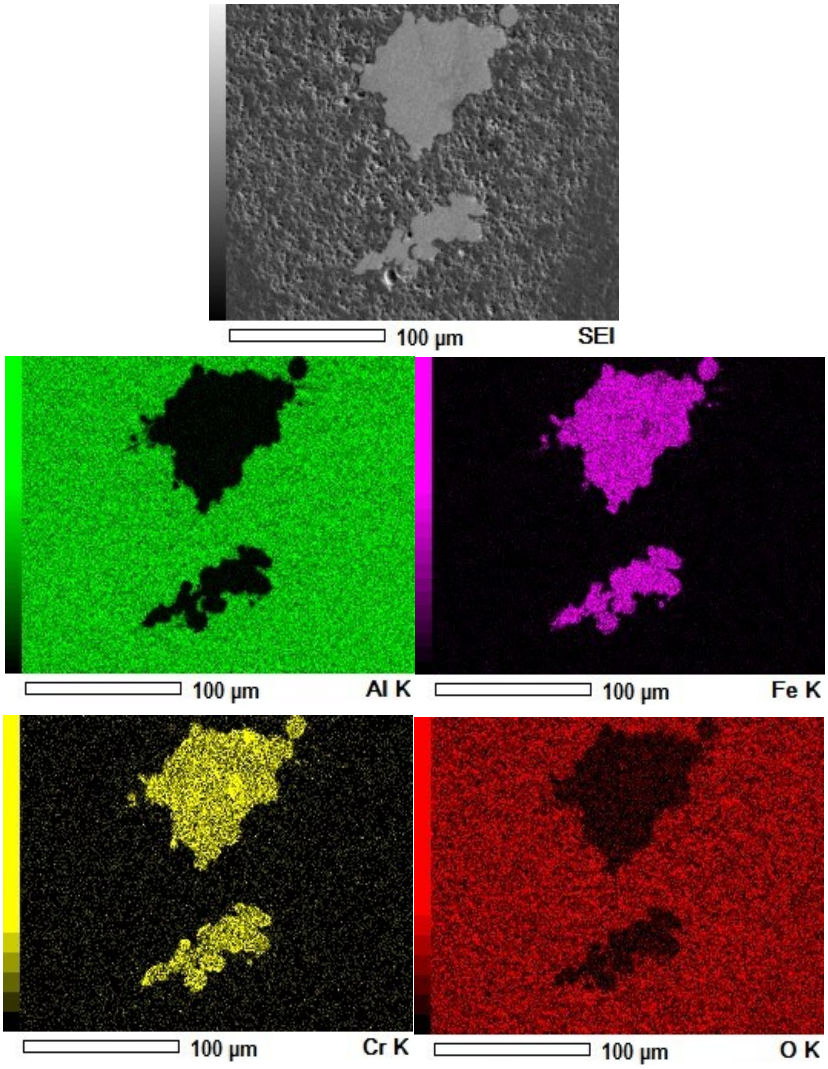


Figure 40. SEM-EDS Map images of a two cores core/shell composite (steel core, alumina shell).

Chapter 4: Rheology of emulsion-based inks for robocasting

4.1. Robocasting of Porous Ceramics

One of the areas where robocasting is finding application is in the fabrication of porous structures. Porous ceramics have a wide range of applications such as thermal insulation[47], catalyst supports[50], tissue engineering scaffolds[54],etc. These applications rely on their unique properties which mainly depend on their structures. Different manufacturing routes have been developed to achieve the desired structures.[32, 55, 56] However, it is still a challenge for engineers to fabricate materials with specific pore parameters with a large degree of freedom.

One way to overcome this limitation in the printing of microporous ceramics is the use of inks based on emulsions and foams.[17, 19, 38, 45] By using emulsion-based inks, it is possible to control simultaneously the macroscopic shape and the porosity of the object from the macro to the micro level. This opens new opportunities for microstructural control.

The most influential factor for successful robocasting is the rheology of the ink. A suitable ink should be shear thinning so that it can be extruded smoothly through the nozzle and maintain the shape of the printed part. In the case of emulsion-based inks, the emulsion should also remain stable during extrusion in order to avoid droplet coalescence. In this work, we study the factors that control the rheology of ceramic inks based on oil in water emulsions stabilized using particles functionalized with branch copolymer surfactants (BCS). In previous works our group has shown that BCS can be used to create responsive particle suspensions and emulsions that could be amenable for the wet processing of ceramics.[34, 81] The effect of solid and oil content and droplet size on the viscosity, shear rate, shear stress, storage modulus (G') and loss modulus (G'') of the emulsions are discussed in order to formulate guidelines for the design of printable inks. The structures and mechanical properties of the final products are characterized and related to the processing conditions.

4.2 Sample components

Samples with different decane content, solid loading, BCS concentration, GδL amount and stirring speed were prepared for testing. The compositions are listed in Table 4.

Table 4. Compositions of the emulsified samples.

Sample	Decane(vol%)	Solid loading in water phase (vol%)	BCS (wt%)	GδL(wt/vol%)	Stirring speed(rpm)
1	50	40	2	2	8000
2	50	40	2	1	8000
3	50	40	2	4	8000
4	50	40	1	2	8000
5	50	40	4	2	8000
6	50	30	2	2	8000
7	50	50	2	2	8000
8	30	40	2	2	8000
9	70	40	2	2	8000
10	50	40	2	2	3000
11	50	40	2	2	13000

Sample 1, 2 and 3 (Defined as group 1) give a comparison among samples added different amount of GδL. Sample 1, 4 and 5 (Defined as group 2) compares the emulsions prepared with different BCS concentration. Sample 1, 6 and 7 (Defined as group 3) are the emulsions with different solid loading while sample 1, 8 and 9 (Defined as group 4) are the emulsions with different decane content. Sample 1, 10 and 11 (Defined as group 5) are emulsions with same component but emulsified under different stirring speed.

4.3. Results and discussion

4.3.1 Rheology of emulsified slurries

4.3.1.1 Time sweep measurement

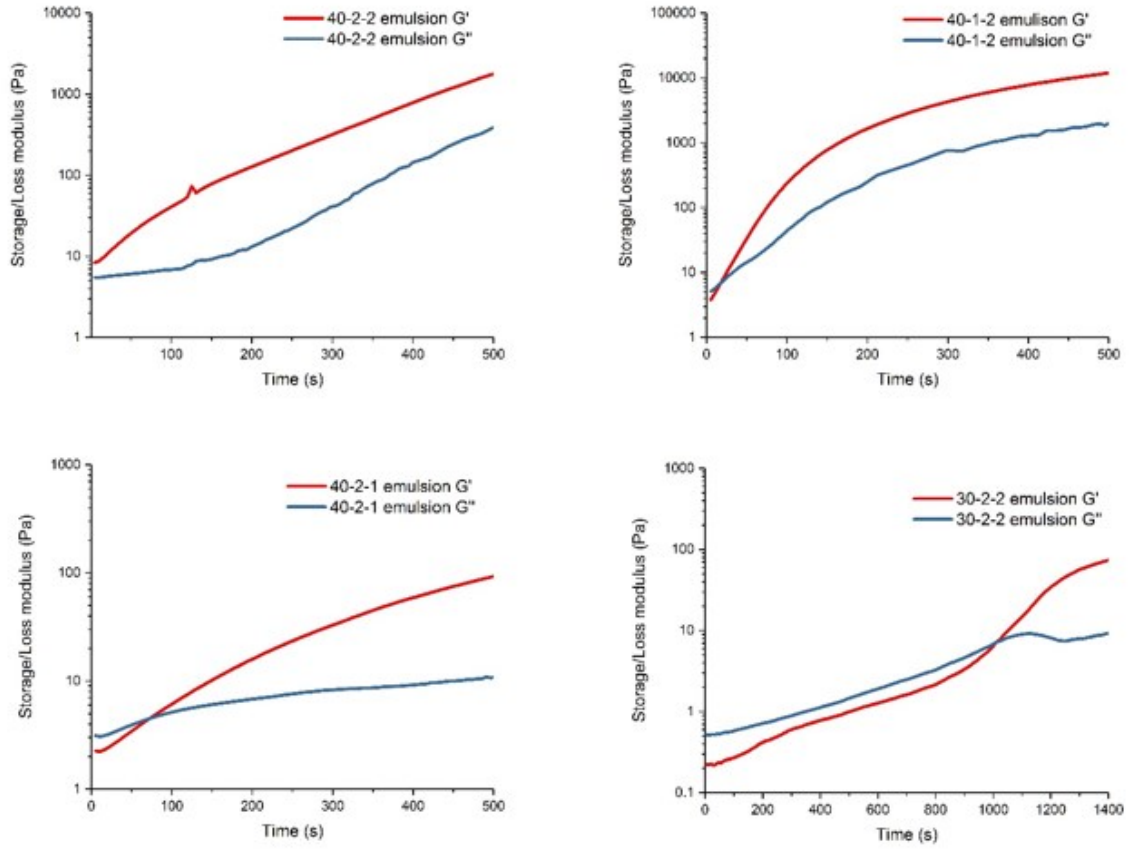


Figure 41. Time sweep of emulsions at 1Hz and 5x10^{-5} rad after addition of GδL. G' is storage modulus and G'' is loss modulus. When G' is larger than G'', the emulsion acts like a gel while if G'' is larger than G', the suspension has a liquid-like behaviour. All these samples were emulsified under a stirring speed of 8000 rpm.

We define the gelling time as the time required for the emulsion to transition between a liquid (storage modulus, G', lower than loss modulus, G'') to a solid (G'>G'') behaviour. In order to study the influence of solid loading, BCS concentration and amount of GδL on the gelling time, the gelling time of emulsions with different compositions are measured using a time sweep (Figure 41). The term 40-2-2 in the graphs means the solid loading of the emulsion(vol%), the concentration of the BCS solution(wt%) and the amount of GδL added in the emulsion(wt/vol%). The gelling time increases with decreasing of BCS concentration or decreasing of GδL content. The effect of GδL seems to be more pronounced but in both cases the differences are small in the range of concentrations used in this work. The solid content has

a more marked effect. Samples with higher solid loading gel faster than those with lower solid loading. For most of the slurries, gelling only takes few minutes.

4.3.1.2 Temperature ramp measurement

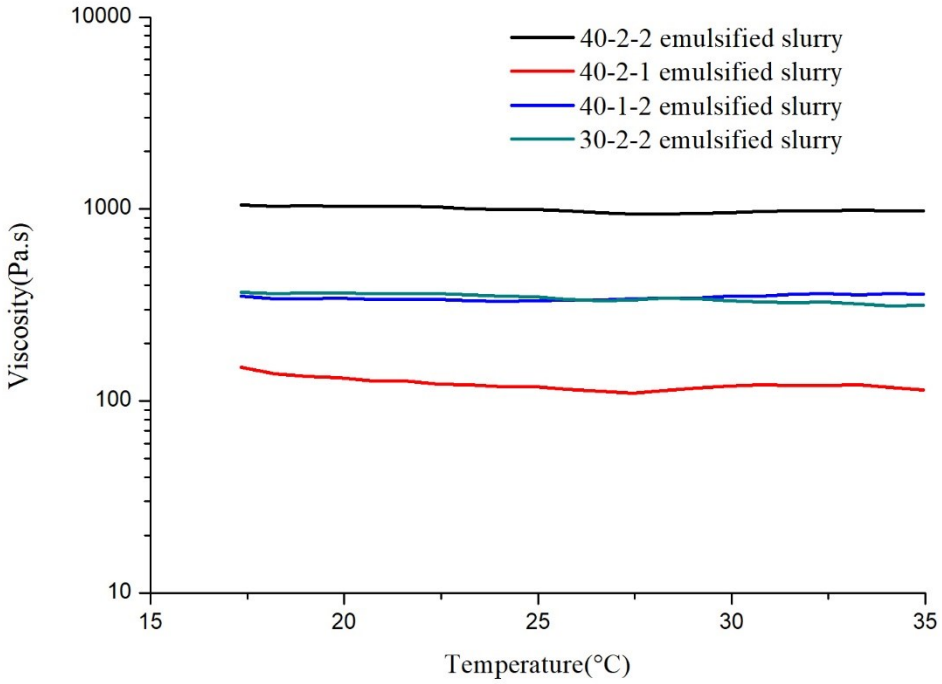


Figure 42. Temperature ramp of 40-2-2, 40-2-1, 40-1-2, 30-2-2 emulsified slurries (stirred under 8000 rpm).

Temperature ramp measurements were carried out at a shear rate of 1 s^{-1} and the temperature varied between 15 to 35 °C. It is obvious that, in this range, the temperature has no influence on the rheology of the slurry (Figure 42).

4.3.1.3 Flow ramp and oscillation amplitude measurement

The factors which may affect the rheology of the slurries are the amount of GδL, the solid loading of the suspension, the decane content, the concentration of the BCS solution and the emulsification speed. Samples with different components were prepared and measured to analyse systematically how these factors influence the viscosity, yield point (defined as the stress when the storage modulus is equal to 95 % of equilibrium storage modulus), yield stress, flow point (defined as the cross over stress between storage and loss modulus) and equilibrium storage modulus of the slurries.

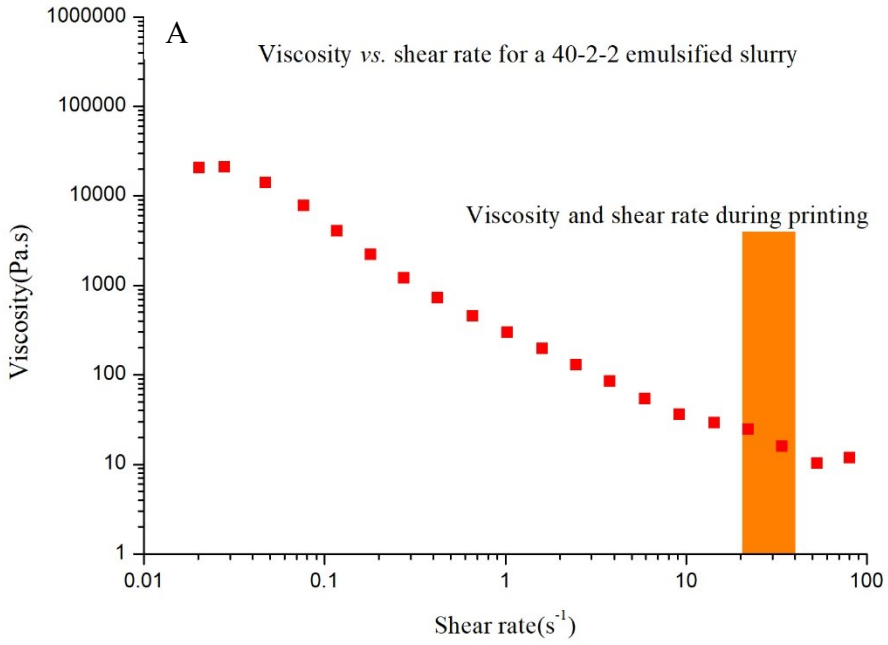


Figure 43. Variation of viscosity with shear rate for a 40-2-2 emulsified slurry. The approximate shear rates during printing are indicated in the graph.

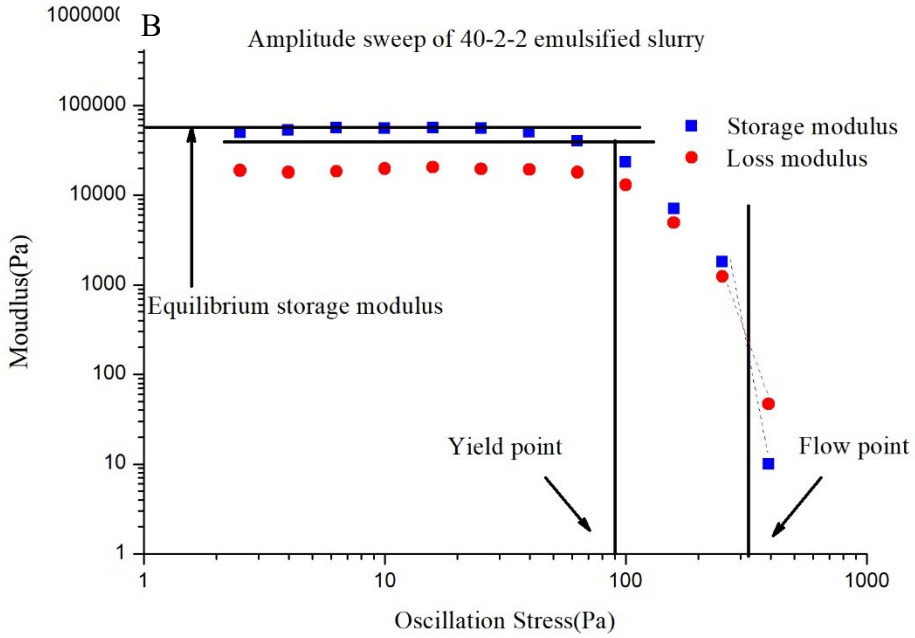


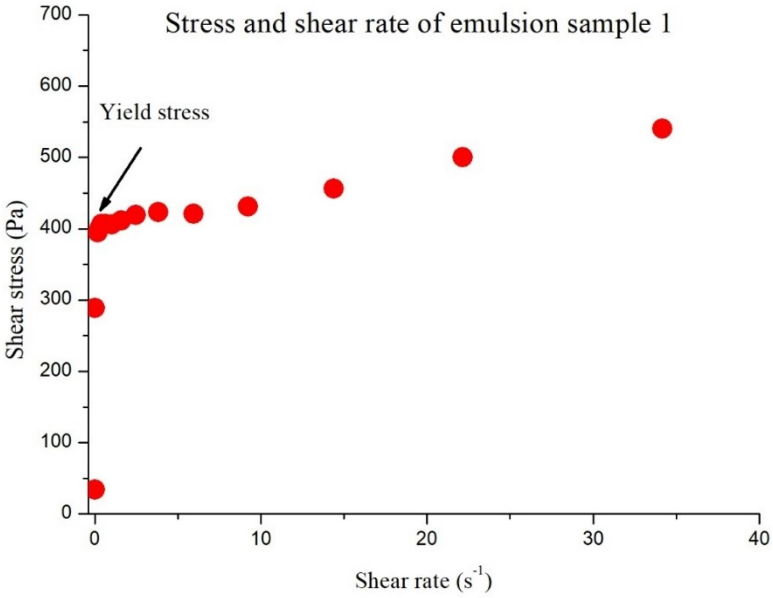
Figure 44. Oscillation amplitude sweep of a 40-2-2 emulsion to obtain flow point, yield point and equilibrium storage modulus.

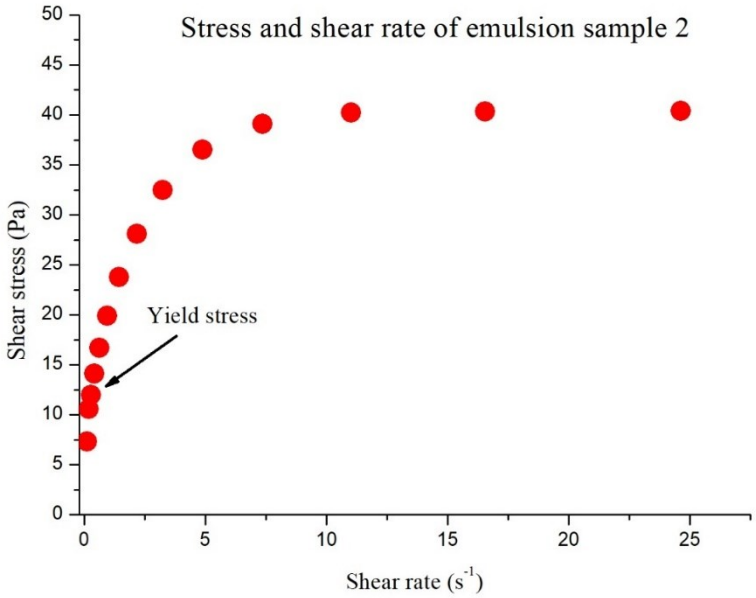
The maximum shear rate in the paste during printing, $\dot{\gamma}_{max}$, can approximated as:

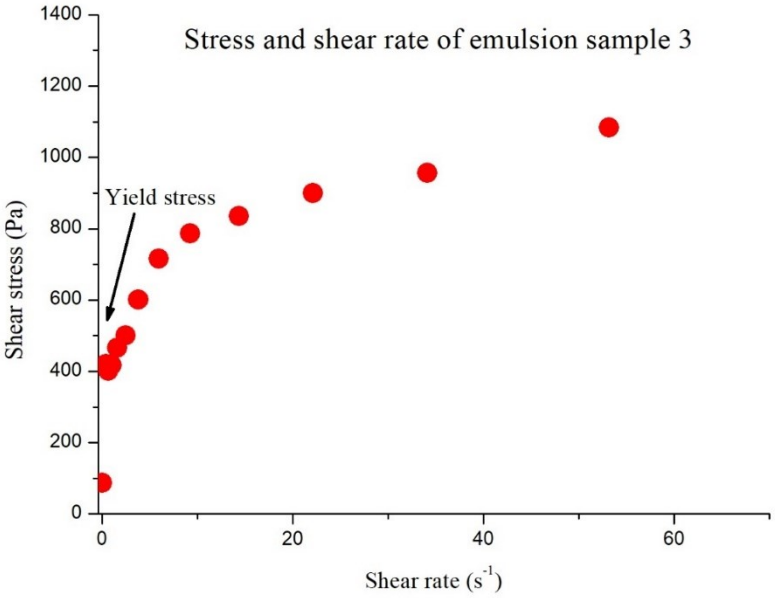
$$\dot{\gamma}_{max} = \frac{4\dot{Q}}{\pi r^3} \quad (17)$$

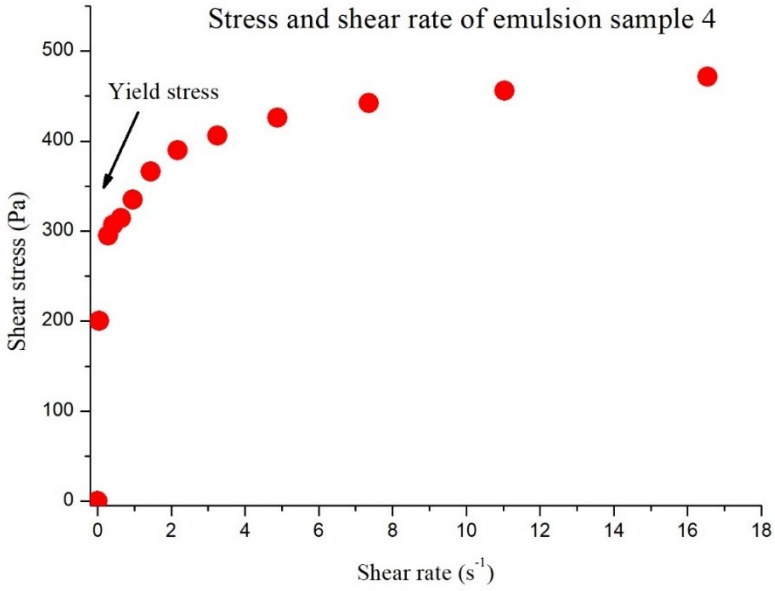
where $\dot{Q}$ is the volumic flow rate, calculated as $\dot{Q} = Sr^2$, S is the printing speed and *r* is the nozzle radius.[25, 82] The equation is for a cylindrical (straight) nozzle but the nozzle used in this work is conical nozzle which have more complex solutions. The simple equation is used here to have an estimation of the maximum shear rate. The printing speed is around 6 mm/s and the nozzle diameter used here is 410 μm, the calculated shear rate is ~35 s^{-1}. To compare the different emulsions, the apparent viscosities of the slurries were calculated at a shear rate of 35 s^{-1} from the flow ramp measurement (Figure 43). From the oscillation amplitude sweep graph (Figure 44), yield point, flow point and equilibrium storage modulus of an ink can be gathered.

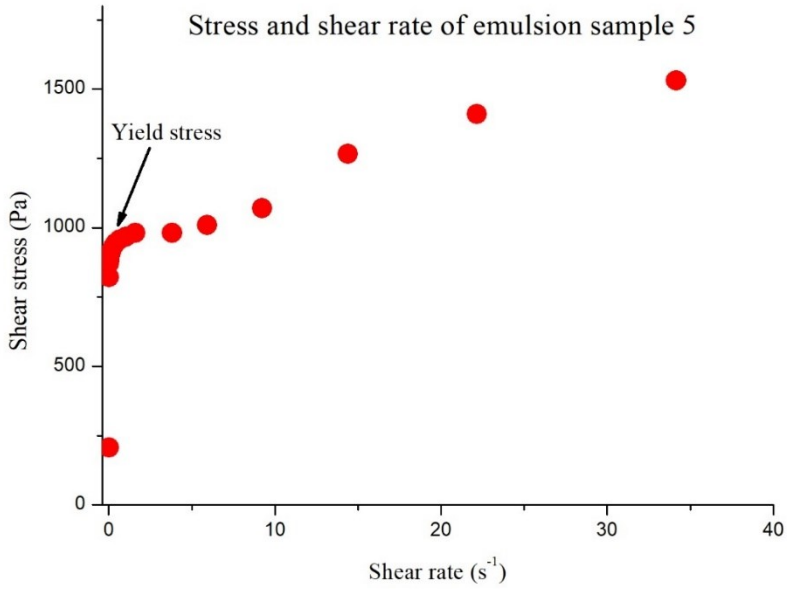
The yield stress of different samples can be obtained using shear stress *vs.* shear rate graphs, which is shown in Figure 45, when shear rate is close to 0 s^{-1}, the applied stress required to initiate flow is the yield stress (static yield stress).

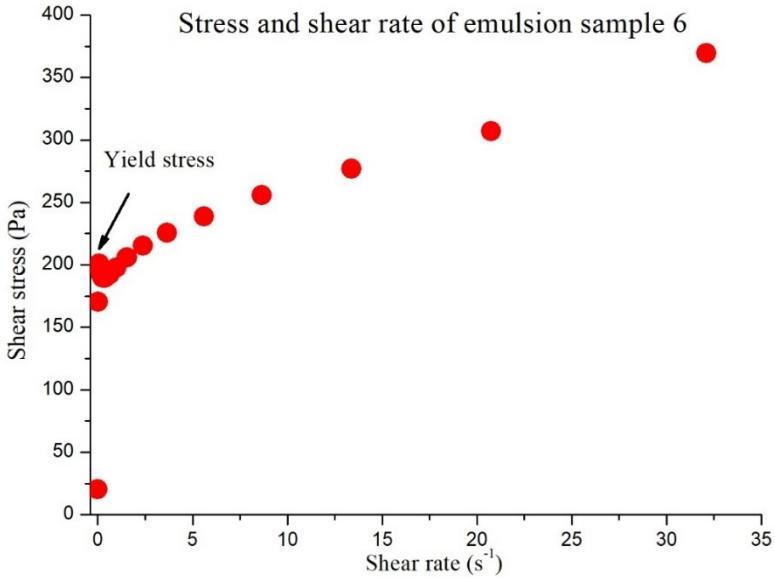

Stress and shear rate of emulsion sample 1
Yield stress
Shear stress (Pa)
Shear rate (s-1)
700
600
500
400
300
200
100
0
0
10
20
30
40

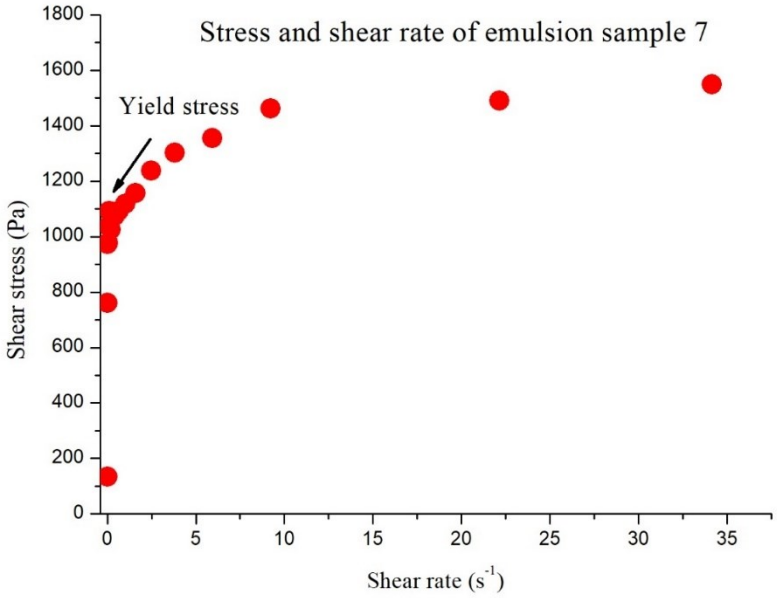

Stress and shear rate of emulsion sample 2
Yield stress
Shear stress (Pa)
Shear rate (s-1)
50
45
40
35
30
25
20
15
10
5
0
0
5
10
15
20
25

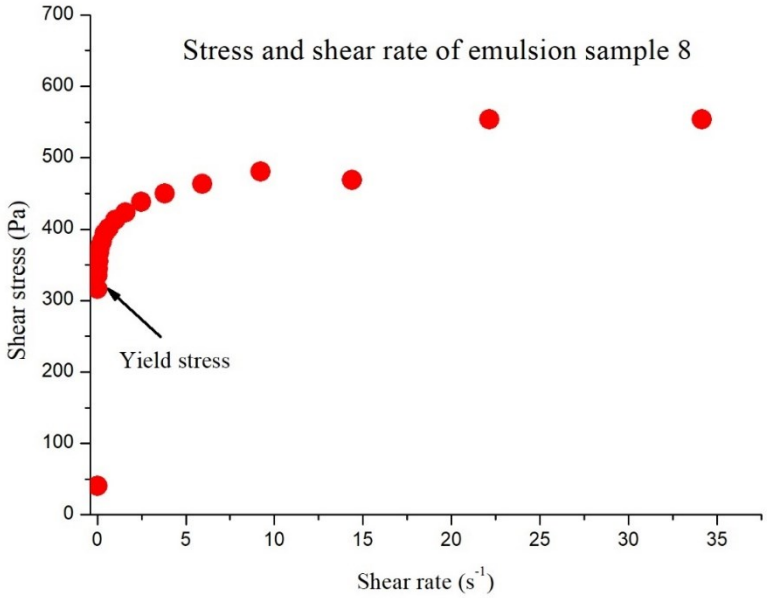

Stress and shear rate of emulsion sample 3
Yield stress
Shear stress (Pa)
Shear rate (s-1)
0
200
400
600
800
1000
1200
1400
0
20
40
60

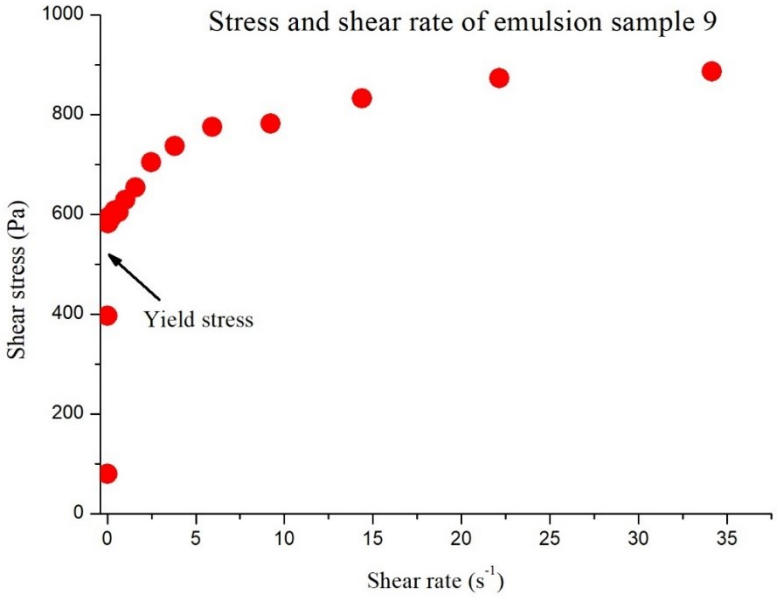

Stress and shear rate of emulsion sample 4
Yield stress
Shear stress (Pa)
Shear rate (s-1)
0
100
200
300
400
500
0
2
4
6
8
10
12
14
16
18

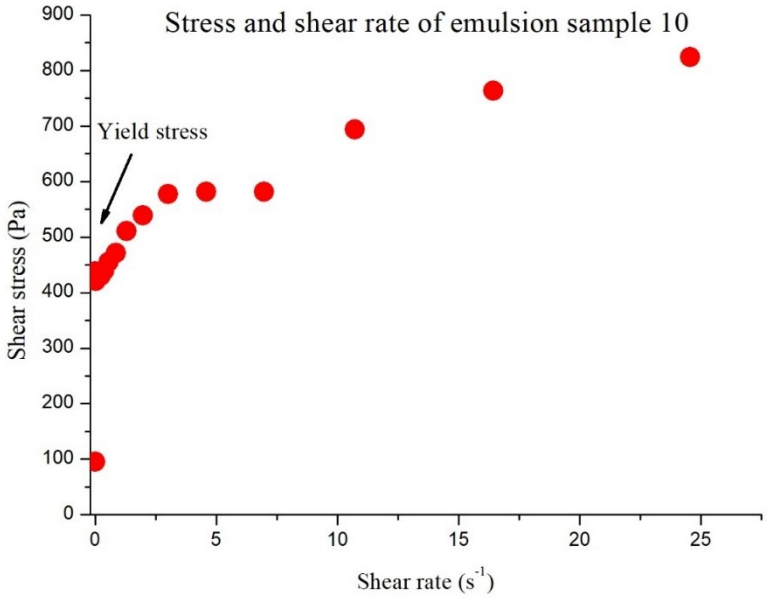

Stress and shear rate of emulsion sample 5
Yield stress
Shear stress (Pa)
Shear rate (s-1)
0
500
1000
1500
0
10
20
30
40


Stress and shear rate of emulsion sample 6
Yield stress
Shear stress (Pa)
Shear rate (s-1)
0
50
100
150
200
250
300
350
400
0
5
10
15
20
25
30
35


Stress and shear rate of emulsion sample 7
Yield stress
Shear stress (Pa)
Shear rate (s-1)
0
200
400
600
800
1000
1200
1400
1600
1800
0
5
10
15
20
25
30
35


Stress and shear rate of emulsion sample 8
Yield stress
Shear stress (Pa)
Shear rate (s-1)
0
100
200
300
400
500
600
700
0
5
10
15
20
25
30
35


Stress and shear rate of emulsion sample 9
Shear stress (Pa)
Shear rate (s-1)
Yield stress
0
200
400
600
800
1000
0
5
10
15
20
25
30
35


Stress and shear rate of emulsion sample 10
Shear stress (Pa)
Shear rate (s-1)
Yield stress
0
100
200
300
400
500
600
700
800
900
0
5
10
15
20
25

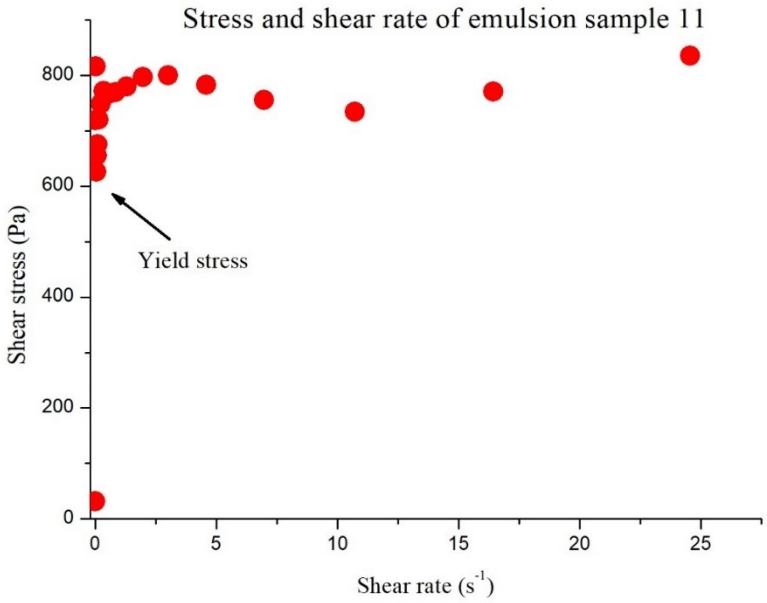
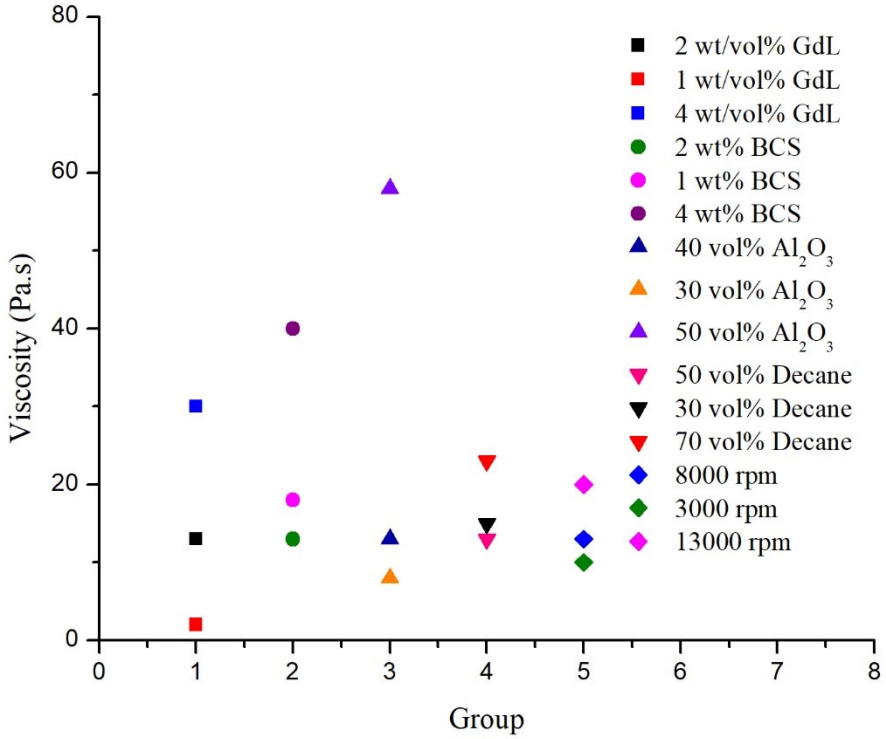
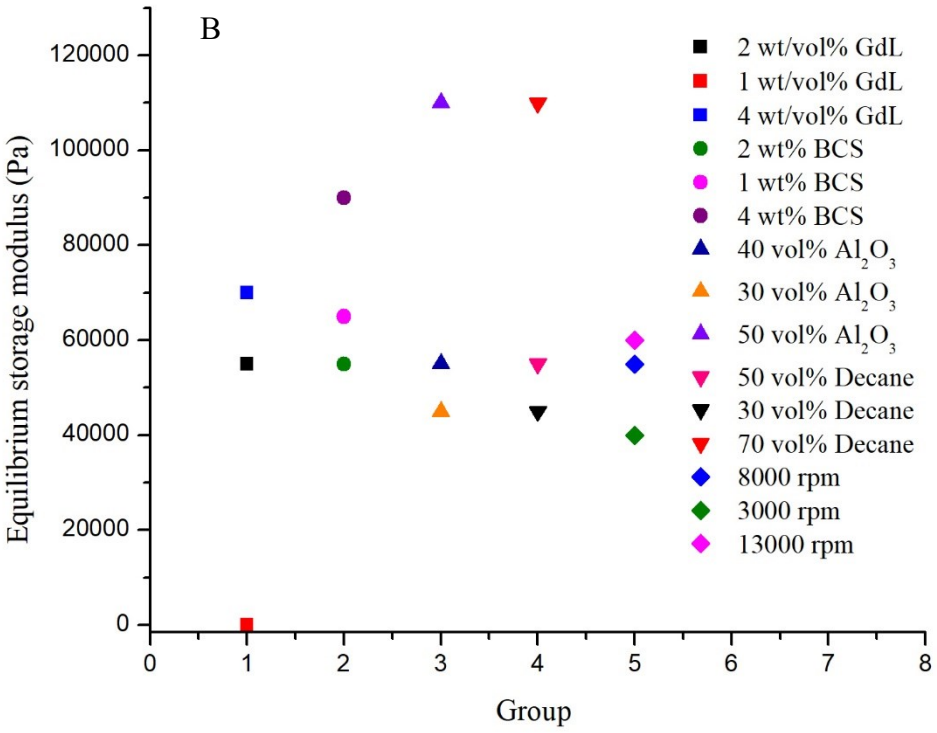


Figure 45. Shear rate and applied stress of emulsion samples.

A


Viscosity (Pa.s)
Group
2 wt/vol% GdL
1 wt/vol% GdL
4 wt/vol% GdL
2 wt% BCS
1 wt% BCS
4 wt% BCS
40 vol% Al2O3
30 vol% Al2O3
50 vol% Al2O3
50 vol% Decane
30 vol% Decane
70 vol% Decane
8000 rpm
3000 rpm
13000 rpm

B


Equilibrium storage modulus (Pa)
Group
2 wt/vol% GdL
1 wt/vol% GdL
4 wt/vol% GdL
2 wt% BCS
1 wt% BCS
4 wt% BCS
40 vol% Al2O3
30 vol% Al2O3
50 vol% Al2O3
50 vol% Decane
30 vol% Decane
70 vol% Decane
8000 rpm
3000 rpm
13000 rpm

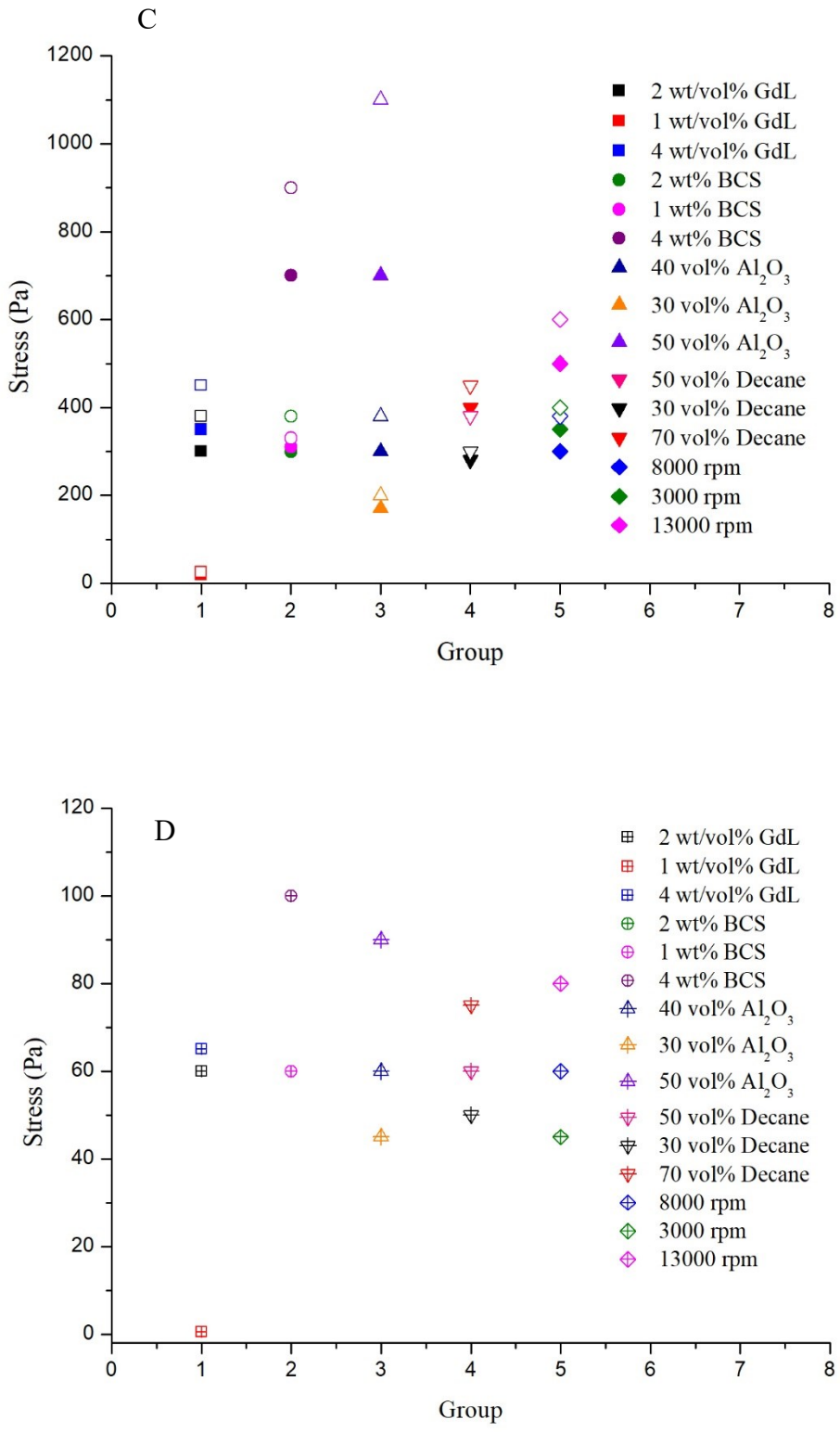


Figure 46. A) Viscosity at printing speed, B) equilibrium storage modulus, C) flow point and yield stress [The solid symbols are flow points gained from modulus cross point (Figure 44) and the open symbols are yield stress gained from shear stress *vs.* shear rate graphs (Figure 45)] and D) yield point of emulsions with different compositions.

As shown in Figure 46, all the factors influence the rheology of the emulsified slurries but some have a larger effect than others. The yield stress measured from shear stress *vs.* shear rate graphs is a bit higher than the flow point measured from modulus cross point. However, some authors call the flow point to yield stress as both are usually very similar and related to the stress need to make the ink flow.[20] The yield points are lower than the flow points and yield stress obviously (open symbols are higher than solid symbols for the same emulsions).

A flow transition index (FTI) gives an idea of the breaking behaviour of the pastes. FTI is a dimensionless index that can be calculated as flow point/yield point.[40] The calculated FTI for the emulsions are shown in Figure 47. The values of FTI for robocasting pastes are normally less than 20.[40] In this work, most of the emulsions have FTI values below 10 which means they are proper for robocasting, while sample 2 has a FTI value of ~40, indicating the network in this emulsion not as strong as other emulsions and this emulsion is not suitable for robocasting.

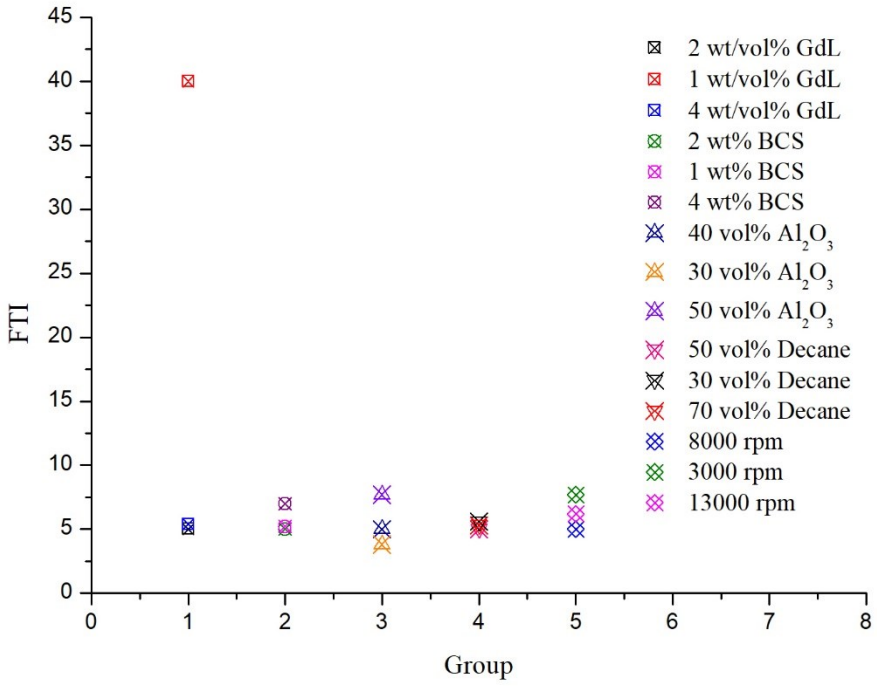


Figure 47. FTI of emulsions with different compositions.

The viscosity, equilibrium storage modulus, flow point, yield stress, yield point and FTI of the emulsion samples are summarised in Table 5.

Table 5. Rheological properties of emulsion samples.

Sample	Viscosity at 35 s^{-1}	Equilibrium storage modulus	Flow point	Yield stress	Yield point	FTI
1	13 Pa.s	5×10^4 Pa	300 Pa	380 Pa	60 Pa	5
2	2 Pa.s	0.01×10^4 Pa	20 Pa	25 Pa	0.5 Pa	40
3	30 Pa.s	7×10^4 Pa	350 Pa	450 Pa	65 Pa	5.4
4	18 Pa.s	6.5×10^4 Pa	310 Pa	330 Pa	60 Pa	5.2
5	40 Pa.s	9×10^4 Pa	700 Pa	900 Pa	100 Pa	7
6	8 Pa.s	4.5×10^4 Pa	170 Pa	200 Pa	45 Pa	3.8
7	58 Pa.s	11×10^4 Pa	700 Pa	1100 Pa	90 Pa	7.7
8	15 Pa.s	4.5×10^4 Pa	280 Pa	300 Pa	50 Pa	5.6
9	23 Pa.s	11×10^4 Pa	380 Pa	450 Pa	75 Pa	5.1
10	10 Pa.s	4×10^4 Pa	350 Pa	400 Pa	45 Pa	7.7
11	20 Pa.s	6×10^4 Pa	500 Pa	600 Pa	80 Pa	6.2

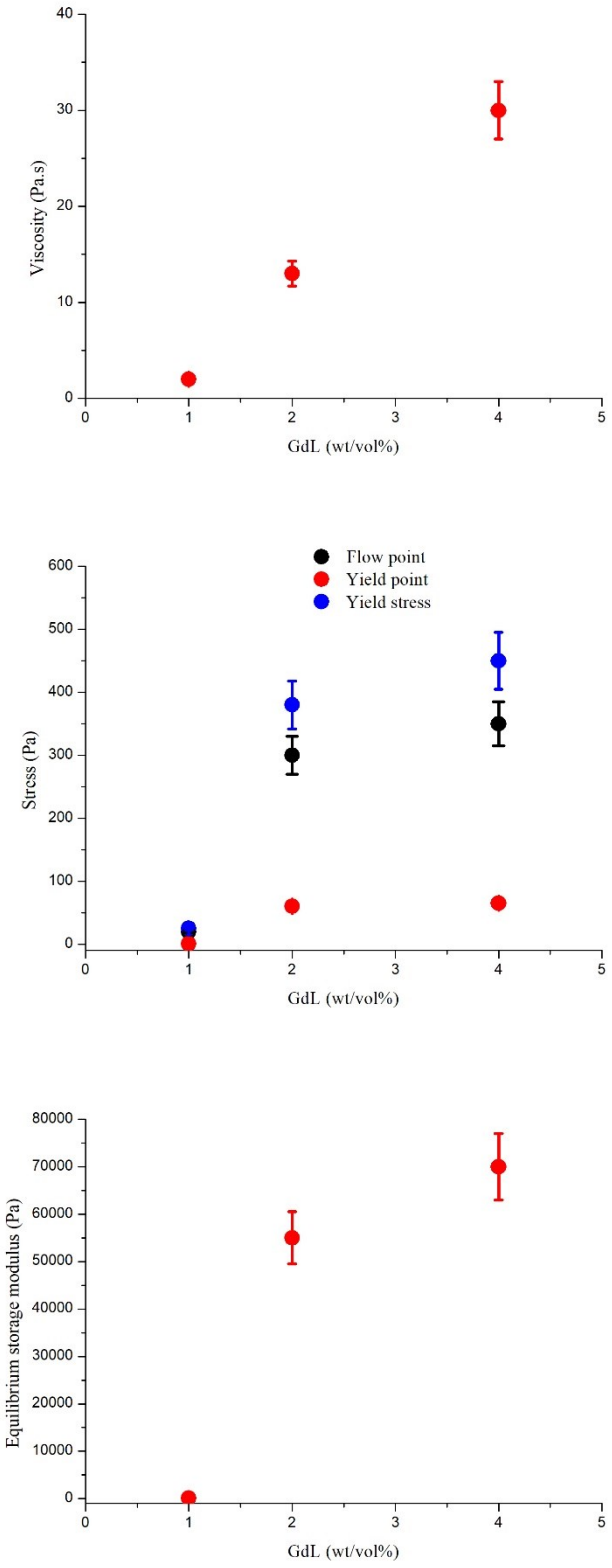


Figure 48. Viscosity, yield stress, yield point, flow point and equilibrium storage modulus of samples with different GδL concentration.

Figure 48 shows the influence of GδL concentration on the rheology, the measured samples have the same composition except the added GδL concentration (sample 1, 2 and 3). The data suggest that there is a minimum GδL concentration (above 1 wt/vol%) required to make the emulsion printable. The slurry with GδL concentration of 1 wt/vol% has a very low viscosity, yield stress, yield point, flow point and equilibrium storage modulus which is not suitable for printing. GδL decreases the pH of the emulsion in two steps, first it dissolves and then is hydrolysed into gluconic acid. When the pH is below the pKa of BCS (6.46), hydrogen bonds among the BCS molecules starts to establish. The amount of GδL should be enough (>1 wt/vol%) to promote bonding between BCS molecules and in the range from 1 wt/vol% to 4 wt/vol%, the more GδL added, the higher viscosity, yield stress, yield point, flow point and equilibrium storage modulus the slurry has.

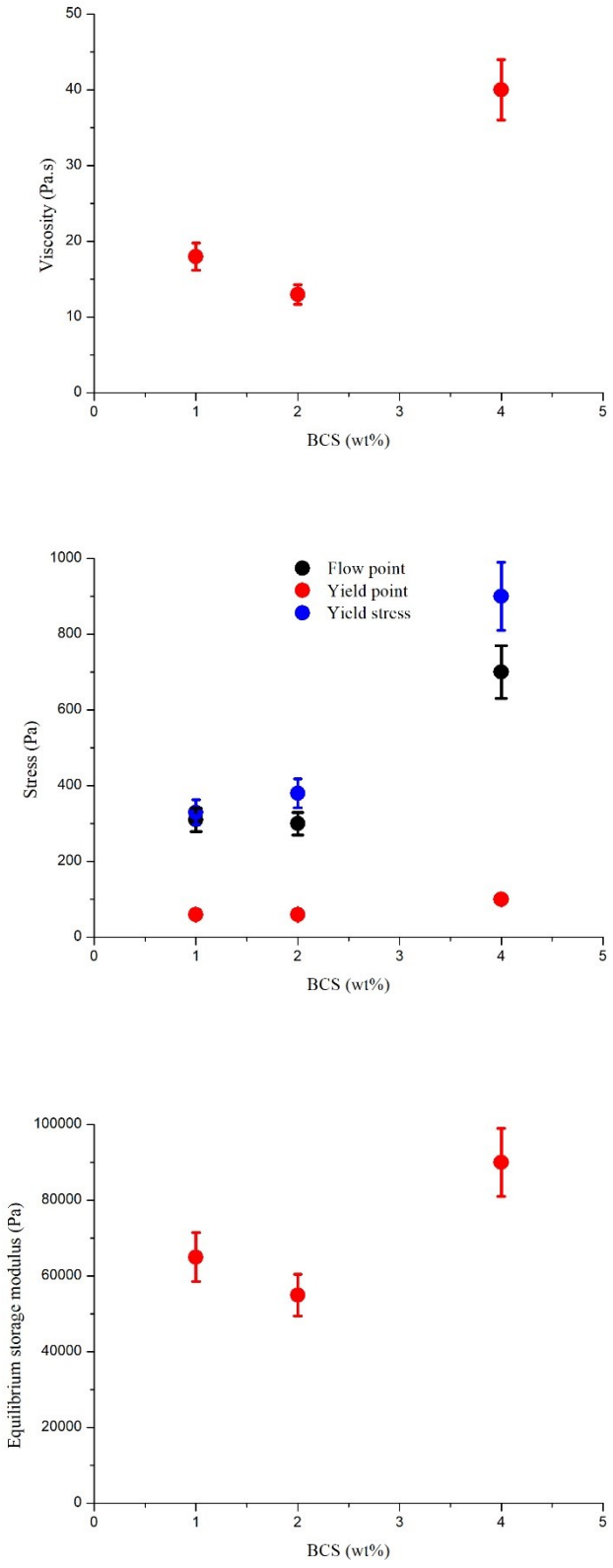


Figure 49. Viscosity, yield stress, yield point, flow point and equilibrium storage modulus of samples with different BCS concentration.

The effect of the BCS concentration is a bit more complex which is shown in Figure 49 (sample 1, 4 and 5). According to Garcia- Tuñon's study of Al_2O_3-BCS suspensions using the same alumina powders,[34] when the BCS concentration is lower than 2wt%, less than a monolayer of BCS molecules adsorb on the ceramics particles while if the BCS concentration is above 2 wt%, BCS multilayers will form and BCS may remain dissolved in the liquid. The results suggest that this excess BCS will increase the viscosity of the emulsion and the degree of interconnection increasing stiffness and yield stress. So, there is not much difference for samples prepared with BCS concentration below 2 wt%, but the samples prepared with BCS concentration of 4 wt% have much higher viscosity, yield stress, yield point, flow point and equilibrium storage modulus.

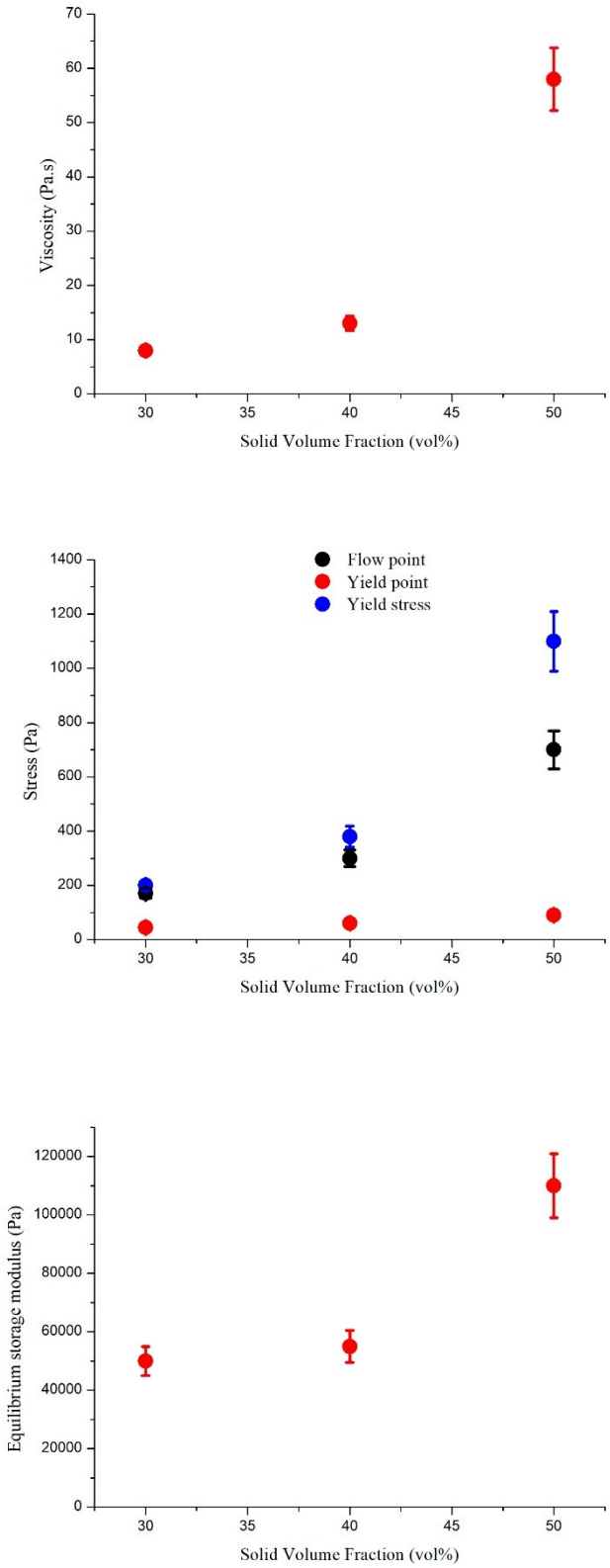


Figure 50. Viscosity, yield stress, yield point, flow point and equilibrium storage modulus of samples with different solid loading.

As it has been observed in other robocasting inks, increasing the solid loading in the water phase close to the packing limit has a large effect on the rheological properties which increasing viscosity, yield stress, yield point, flow point and equilibrium storage modulus (Figure 50) (sample 1, 6 and 7). There is a packing limit (theoretical maximum solid volume fraction) for the pastes which can be described using model:

$$\eta_r = (1 - \frac{\varphi}{\varphi_m})^{-K_H} \quad (18)$$

where η_r is the relative viscosity, φ is the volume fraction, φ_m is the theoretical maximum volume fraction and K_H is a hydrodynamic particle shape factor. The maximum volume fraction of solid is determined by the pastes system ranging from 0.07 to 0.65. [8, 20, 83] The calculated φ_m is ~0.6 and K_H is ~6.3 (Figure 51). In addition to viscosity, the other properties (yield stress, flow point and storage modulus) have similar curves with the solid volume fraction and the maximum volume fraction is ~0.6 as well.

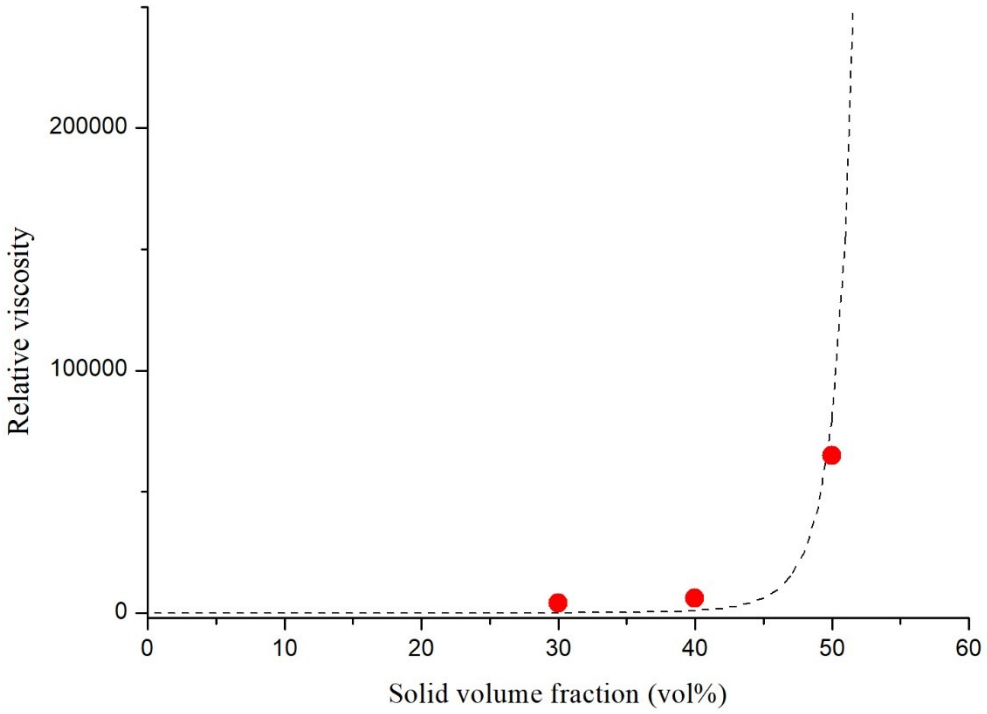


Figure 51. Plot of relative viscosity as a function of solid volume fraction.

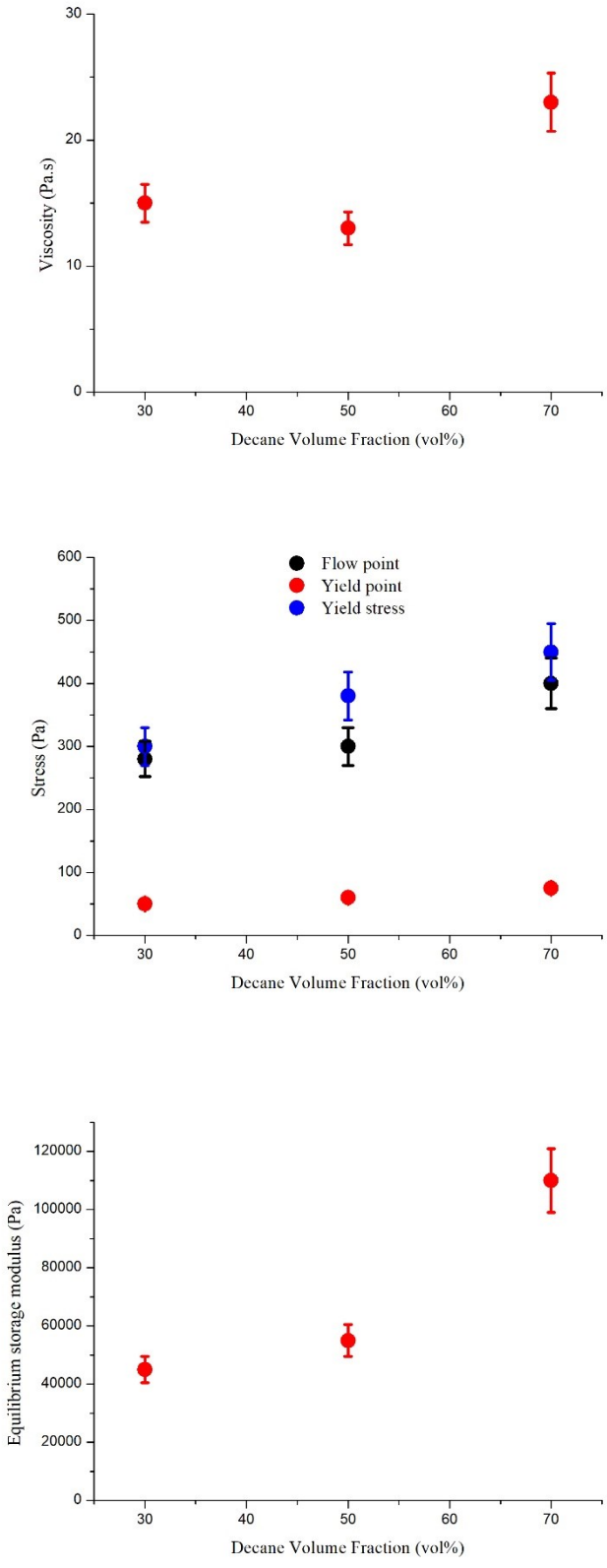


Figure 52. Viscosity, yield stress, yield point, flow point and equilibrium storage modulus of samples with different oil content.

Figure 52 shows the effect of oil content (sample 1, 8 and 9). The increasing of oil content increases the equilibrium storage modulus of the samples. The viscosity, yield stress, yield point and flow point start to increase when the oil content goes around 70 vol% which indicates the packing fraction for oil droplets is ~ 80 vol%. The packing fraction of oil droplets is higher than that for rigid particles as they can distort a bit and the size distribution is probably wider which favours packing. The yield point does not depend much on the particle contents or oil content as it mostly relates to the point in which plastic deformation starts (equilibrium storage modulus) and does not relate to flow. Equation 13 is used here as well to calculate the maximum oil volume fraction. The calculated K_H is ~4.9 and φ_m is ~0.8 (Figure 53).

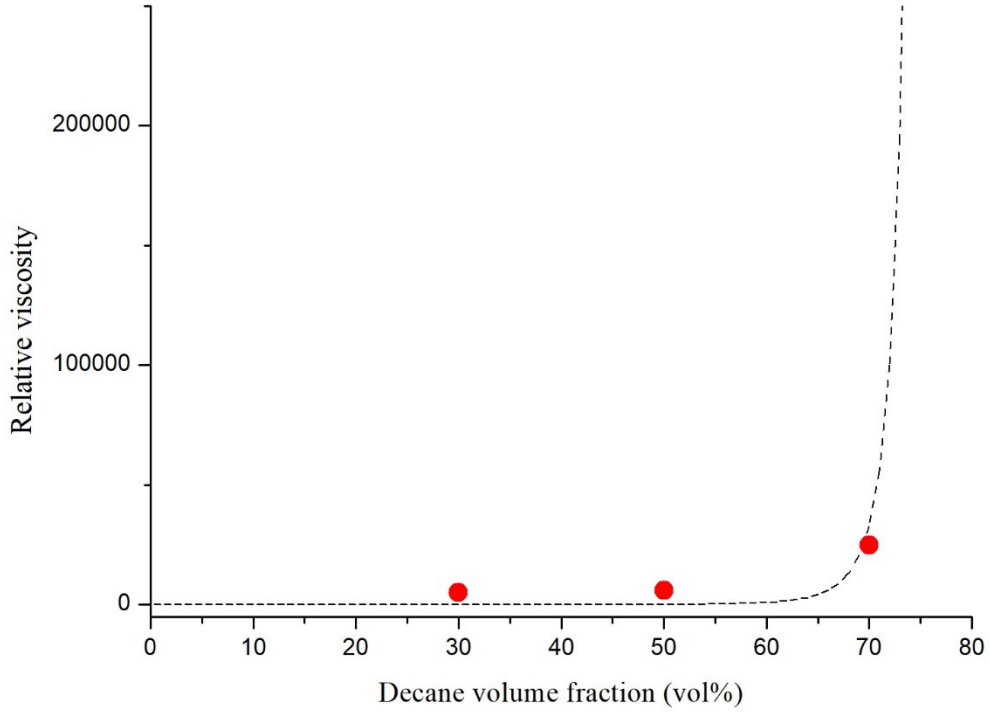


Figure 53. Plot of relative viscosity as a function of decane volume fraction.

Because the small number of experimental points, the fitting of the K_H and φ_m for solid and oil is an approximation. The oil packs better probably because these is a wider droplet sizes distribution than the ceramic particle size distribution and oil droplets are perhaps deformable to some extent.

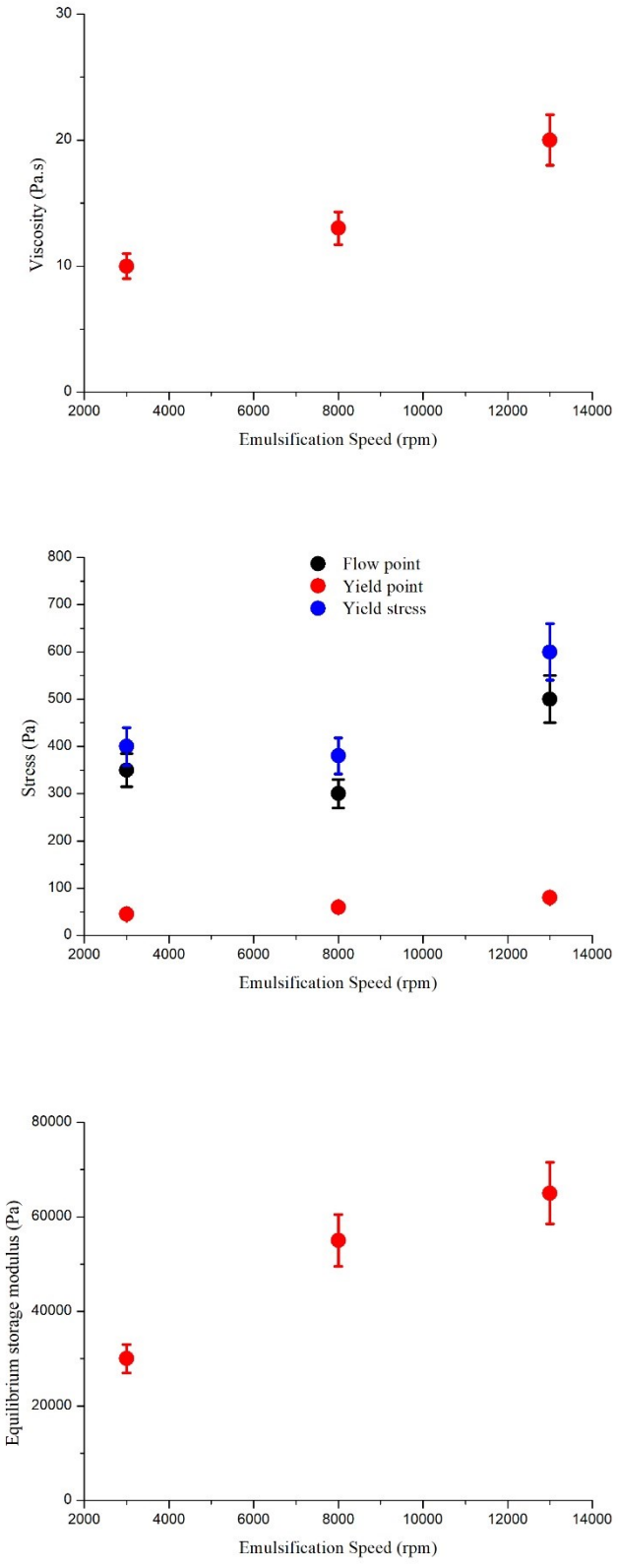


Figure 54. Viscosity, yield stress, yield point, flow point and equilibrium storage modulus of samples with different emulsification speed.

As can be seen in Figure 54 (sample 1, 10 and 11), a higher emulsification speed gives a higher viscosity, yield stress, yield point, flow point and equilibrium storage modulus of the emulsions. This is because the higher emulsification speed gives smaller droplets and therefore the increase of interfacial area between the water and oil that gives more interconnection among water, oil and particles. Another additional issue is the droplet size distribution. The more homogeneous droplet size distribution, the worse packing and therefore the lower packing limit. A good packing requires a wide particle distribution for smaller particles/droplets to fit between the larger ones.

Table 6. Rheological properties of emulsions/foams from different reports.

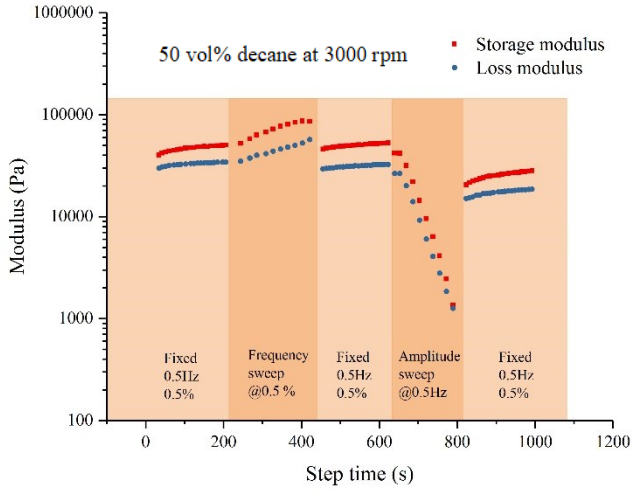
Researcher [Ref.]	Solid loading (in suspension)	Flow Points	Storage Modulus (G')
This work	30-50 vol% (50 vol% unprintable)	150-700 Pa	30-90 kPa
Sommer[45]	5 vol%	700 Pa	10 kPa
Minas[17]	30-50 vol%	58-660 Pa	1.6-100 kPa
Muth (Foam)[19]	20-60 vol%	30-100 Pa	4-80 kPa

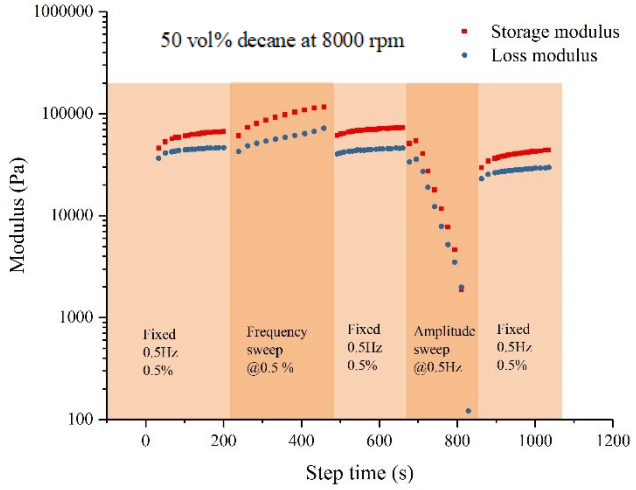
Table 6 gives a comparison between the rheology of the emulsions in this work and the rheology of emulsions/foams reported in other papers. The solid volume fraction is similar which has a limitation ~50 vol% except the foam gel reported by Muth which has a solid loading as high as 60 vol%. The flow point of the emulsions is also similar but the foam gel has a lower flow point. The storage modulus is various in different reports. The storage modulus is related to the particle network. In Sommer's report, the silica solid content is only ~10 wt% (~5 vol%) which is maybe the cause of low storage modulus. The variation of storage modulus in Minas' and Muth's report as well as the modulus in this work is large because the approaches used to create the particle networks results in different strength of the particle-particle interactions and therefore in different strength of the networks. Minas used different amount of PVA, Muth adjusted the pH of the emulsions which changes the particle network behaviour. In this work, the storage modulus is adjusted by changing the BCS concentration, GδL amount, solid loading, oil content and emulsification speed (droplet size).

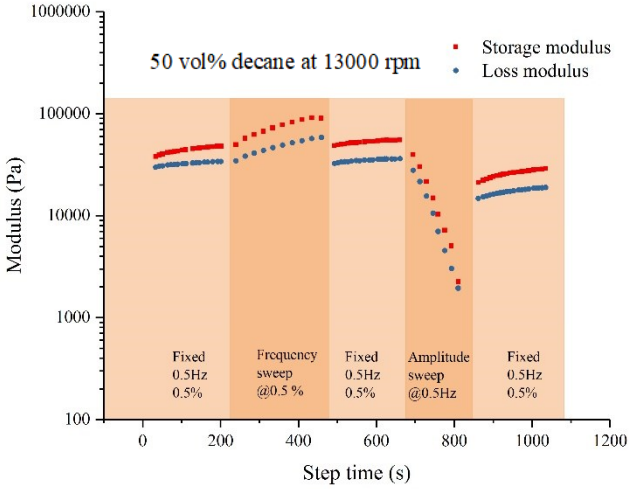
4.3.1.4 Rheology of samples with different oil content or stirring speed

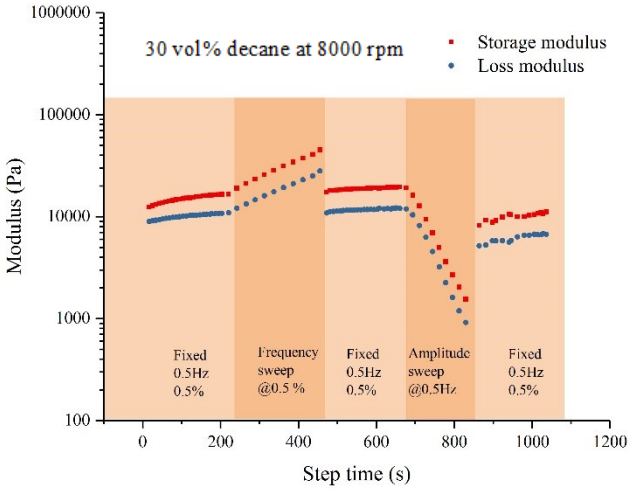
4.3.1.4.1 Evolution of viscoelastic fingerprints

In order to learn more about the stability of the inks, their response to varying conditions was assessed using a sequence of five oscillatory steps while monitoring the viscoelastic properties (G′, G). Another batch of samples are used here. All these samples are prepared with 40 vol% Al_2O_3 suspensions in water, 2 wt% BCS solutions and 2 wt/vol% GδL. The differences are the oil content and the stirring speed during emulsification (Figure 55).









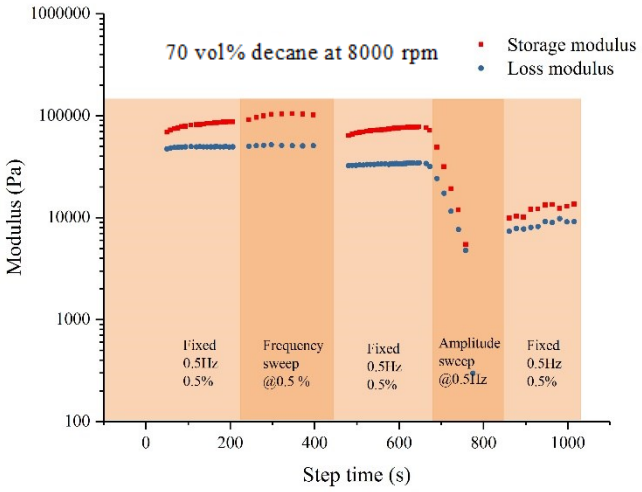


Figure 55. Oscillation sweeps for emulsified slurries.

All the slurries are stable under fixed sweep at 0.5 Hz and 0.5 % strain. Both the storage modulus and loss modulus increase slightly with increasing frequency (two parallel lines with the storage modulus above the loss modulus, which indicate the slurries have a gel-like response [30]). Both the storage modulus and loss modulus decrease with strain increasing while storage modulus decreases faster than loss modulus which means there is a point above which the loss modulus is larger than storage modulus.

There is not a significant variation in the storage and loss modulus between the first fixed step and the second one. However, they are significantly lower in the third fixed step, amplitude sweep, probably due to the coalescence of bubbles that partially "breaks" the emulsion during the amplitude sweep. The results show that a change in the frequency does not break the emulsion: the modulus recovers to the same value. Robocasting use a low printing speed (low strain rates from 25 to 70 s^{-1}) to produce green bodies that are not likely to cause droplet coalescence, thus the emulsions are suitable for robocasting.

During the frequency sweep, a fitting can be done using the model:

$$G = A\omega^n \tag{19}$$

where G is the storage modulus or loss modulus, A is a constant, ω is the frequency and n is a power-law exponent which can be used to describe the behaviour of the pastes.[30]

A degree of recovery is calculated using (storage modulus in the last step)/(storage modulus in the first step). The results of degree of recovery and calculated n are shown in Table 7.

Table 7. Degree of recovery of different emulsified slurries.

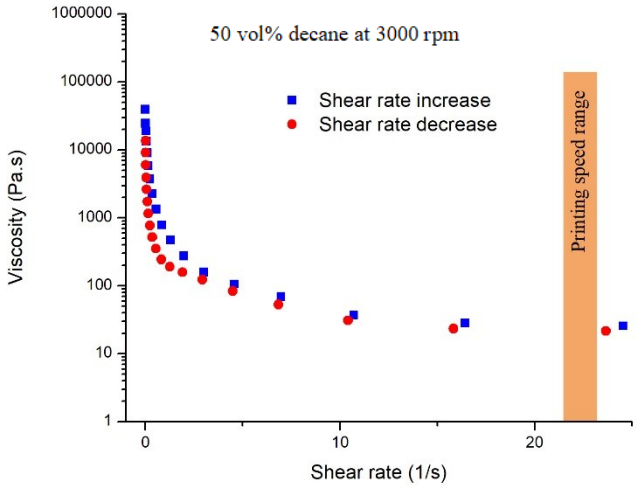
Sample	Degree of recovery	n
50 vol% decane at 3000 rpm	75 %	$n_{G'}$=0.17±0.02, $n_{G''}$=0.13±0.02
50 vol% decane at 8000 rpm	71 %	$n_{G'}$=0.18±0.03, $n_{G''}$=0.14±0.02
50 vol% decane at 13000 rpm	65 %	$n_{G'}$=0.19±0.03, $n_{G''}$=0.16±0.02
30 vol% decane at 8000 rpm	77 %	$n_{G'}$=0.21±0.02, $n_{G''}$=0.20±0.01
70 vol% decane at 8000 rpm	15 %	$n_{G'}$=0.04±0.02, $n_{G''}$=0.02±0.01

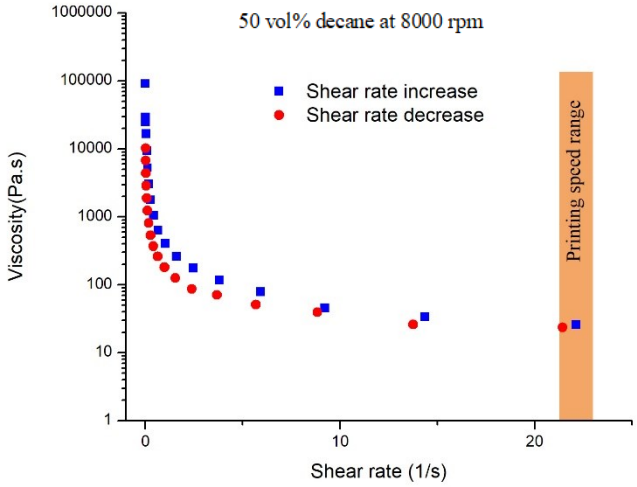
Most of the emulsions has a degree of recovery over 60 % except the emulsions with 70 vol% oil which has a much less degree of recovery that means this emulsion has significant oil coalescence during the measurement.

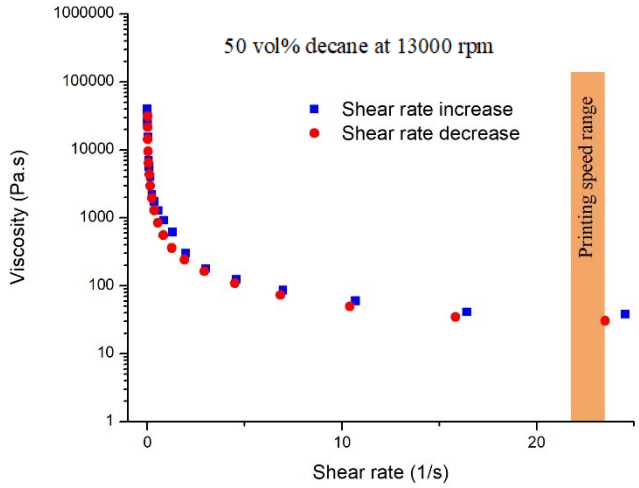
According to Lewis's report, typical gels should have a *n* between 0.3 and 0.7 and a lower *n* means a more solid like behaviour. The power-law exponent *n* ranges from 0.15 to 0.25 for most of the samples which are reasonable except the sample prepared with 70 vol% decane which has a *n* ~0.05 which means a more solid like behaviour maybe because the oil content is close to the packing limit (80 vol%) and the droplets are jammed. In addition, for 70 vol% decane paste, the storage modulus and loss modulus are more likely flat instead of increasing with increase of frequency which maybe due to the oil coalescence.

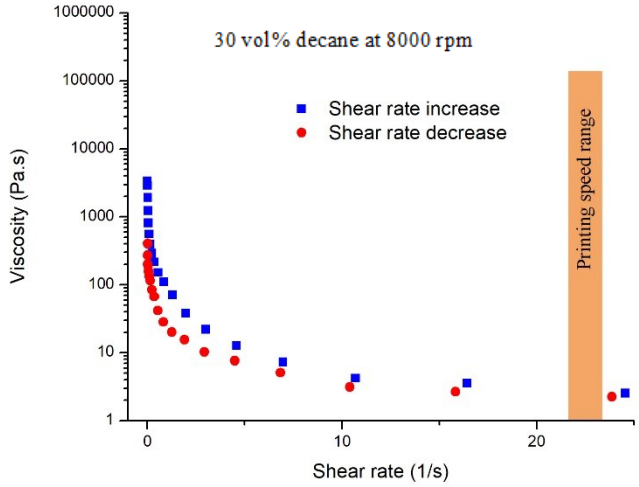
4.3.1.4.2 Hysteresis

Viscosity was measured using a shear rate cycle to assess if there was a measurable hysteresis (Figure 56). In all the emulsions the hysteresis is negligible suggesting that in the range of shear rates used in the measurement the emulsions are stable and so will be the inks during printing.


50 vol% decane at 3000 rpm
Shear rate increase
Shear rate decrease
Printing speed range
Viscosity (Pa.s)
Shear rate (1/s)
1000000
100000
10000
1000
100
10
1
0
10
20


50 vol% decane at 8000 rpm
Shear rate increase
Shear rate decrease
Printing speed range
Viscosity(Pa.s)
Shear rate (1/s)
1000000
100000
10000
1000
100
10
1
0
10
20





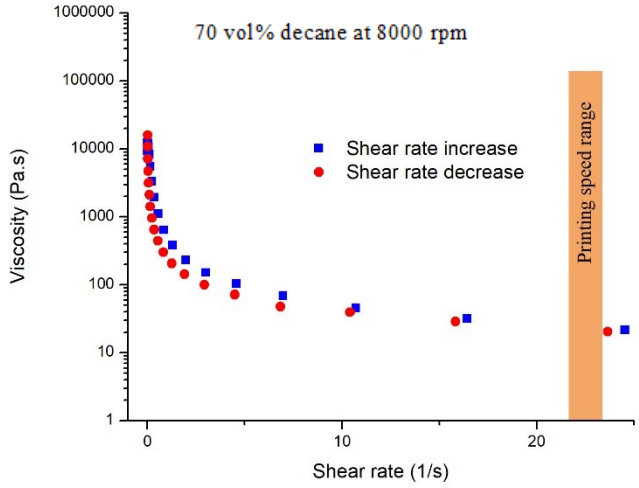
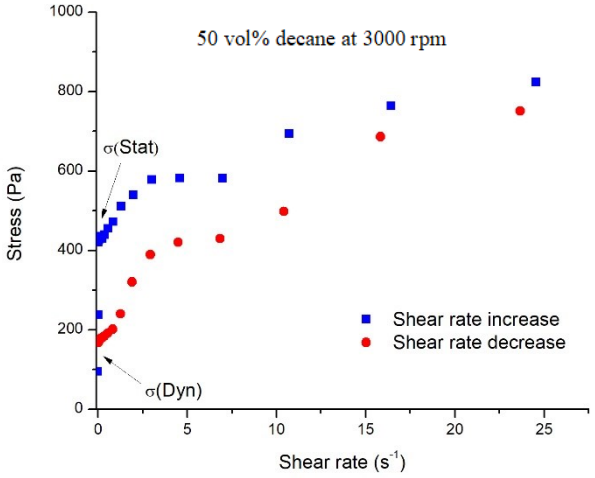
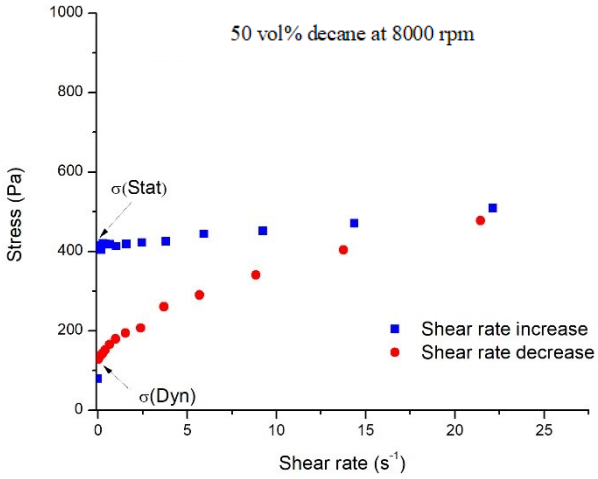


Figure 56. Hysteresis viscosity measurement of emulsions.

The hysteresis stress measurement of the samples is shown in Figure 57. All the samples have a time-dependent shear thinning property.





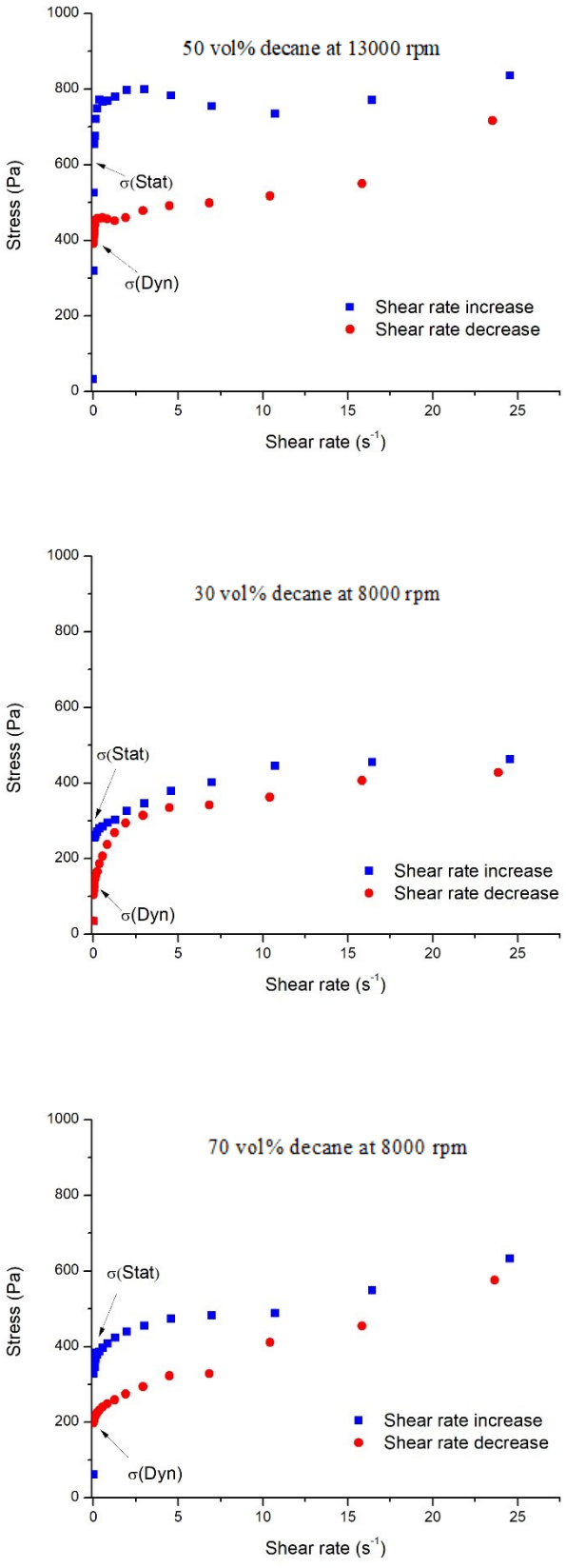
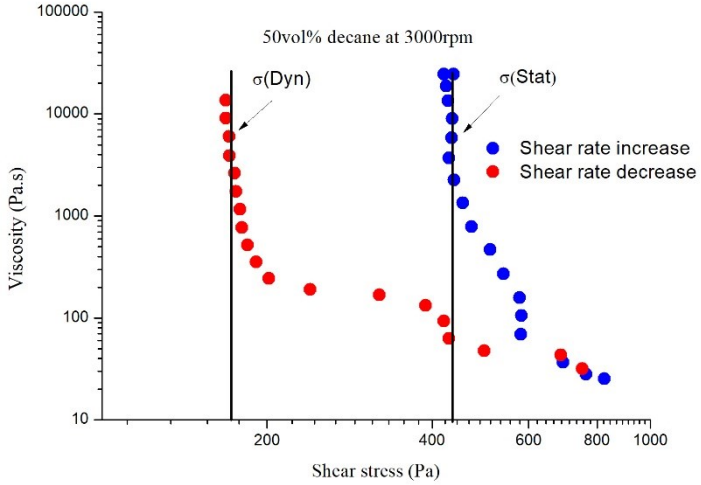
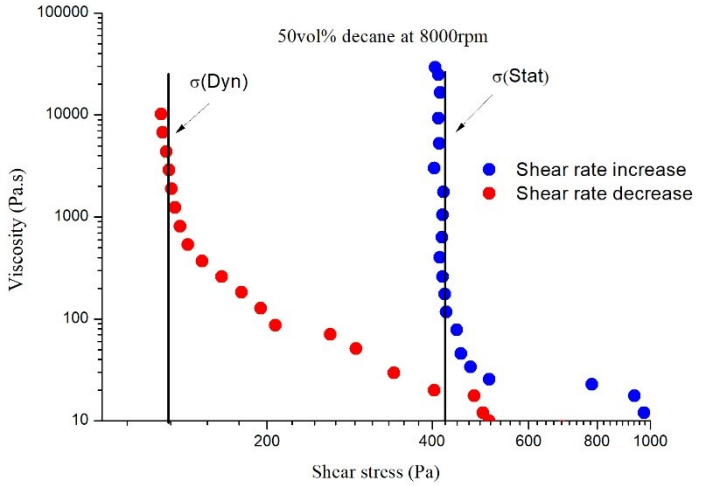


Figure 57. Hysteresis stress measurement of samples (the measurement of static yield stress is agreed with the results also shown in Figure 45).

The yield stress can be measured using viscosity *vs.* shear rate plot as well which is shown in Figure 58. The yield stress is the stress when the viscosity has a sharp decrease.[84]





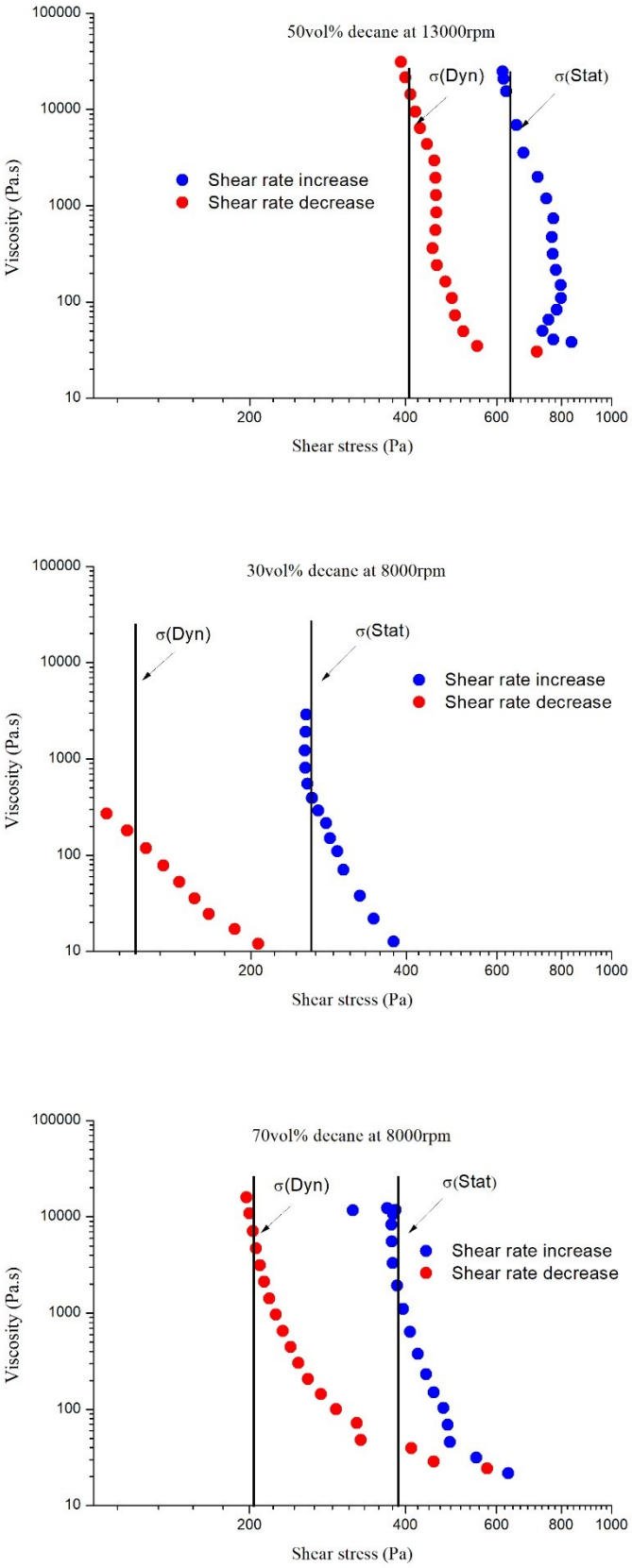


Figure 58. Viscosity *vs.* Shear rate of hysteresis measurement.

As expected, there is a difference between the yield stresses gained from increasing and decreasing of shear rate. We define the yield stress gained from shear rate increasing process as static yield stress σ_y^{Stat} and the yield stress gained from shear rate decreasing process as dynamic yield stress σ_y^{Dyn}. The yield stresses got form two described methods are similar. The σ_y^{Stat} , the σ_y^{Dyn} and the flow point of these samples are list in Table 8.

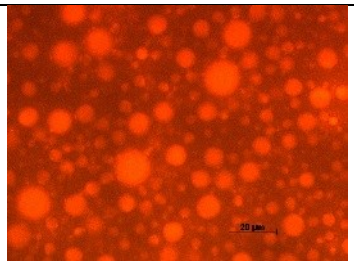
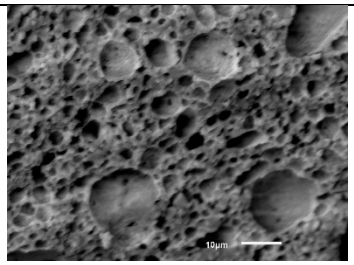
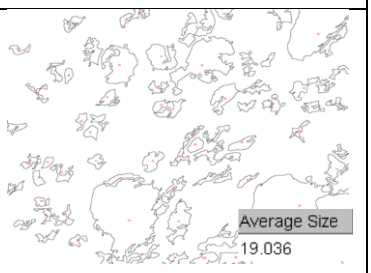
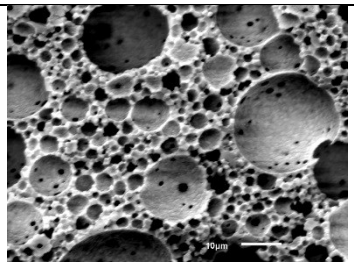
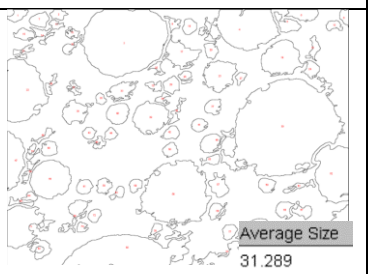
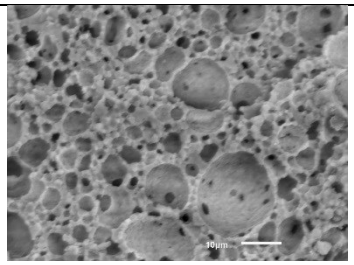
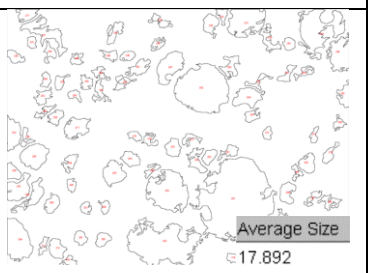
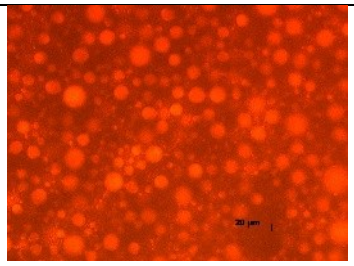
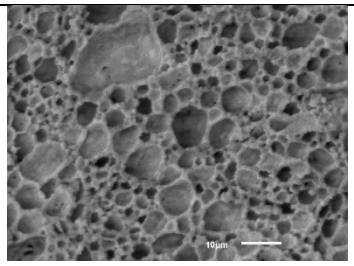
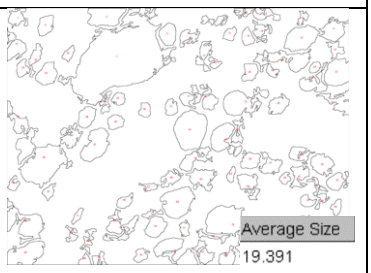
Table 8. σ_y^{Stat} , σ_y^{Dyn} and flow points of the selected emulsion samples.

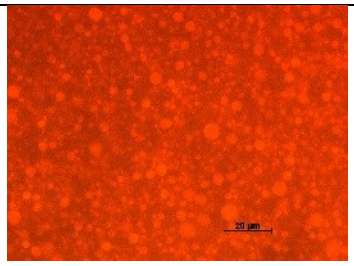
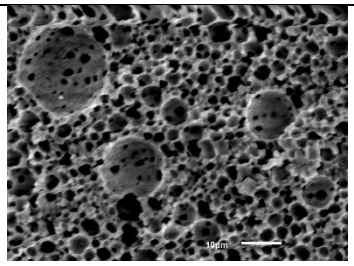
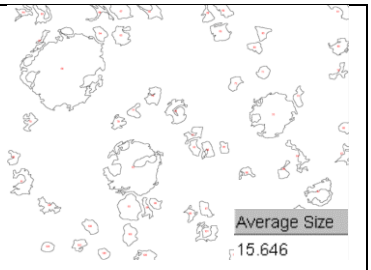
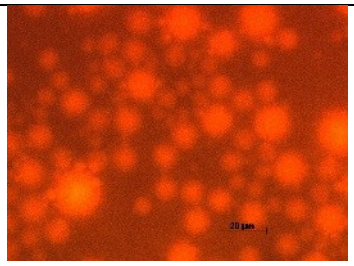
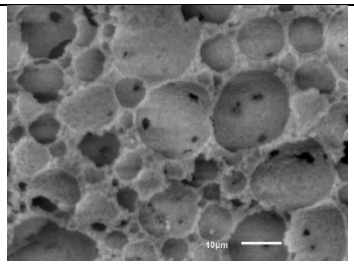
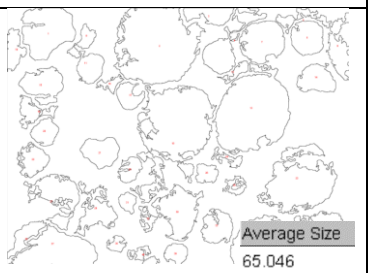
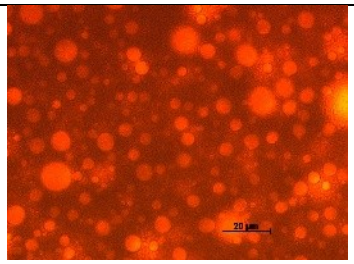
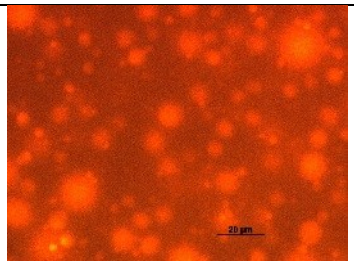
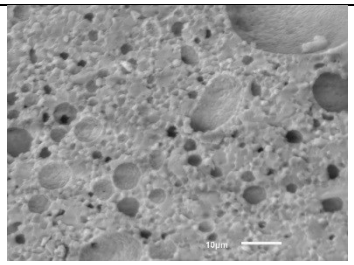
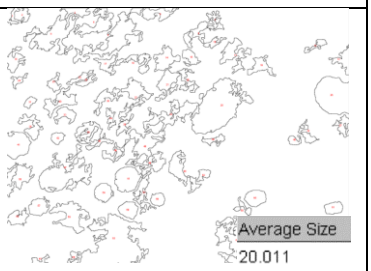
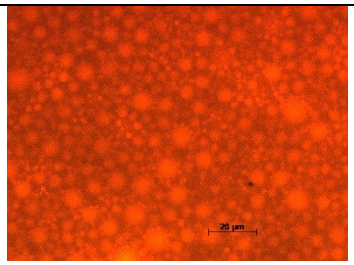
Sample ID	σ_y^{Stat}(Pa)	σ_y^{Dyn}(Pa)	Flow point (Pa)
1(50 vol% decane at 8000 rpm)	400	150	300
8(30 vol% decane at 8000 rpm)	300	<130	280
9(70 vol% decane at 8000 rpm)	390	200	380
10(50 vol% decane at 3000 rpm)	430	150	350
11(50 vol% decane at 13000rpm)	600	400	500

The static yield stress is normally higher than the dynamic yield stress because when the paste transfers from a solid state to a liquid state, the paste needs some extra stress to break the bonds among molecules to make it start to shear. As described in M'Barki's report, this measurement simulates the shear history of an ink during the printing. First, a stress is applied until the ink is extruded through the nozzle under a shear stress (σ_y^{Stat}). Once the ink is printed on the substrate, the stress relaxes to σ_y^{Dyn}.[25] Also, the static yield stress measured by shear stress *vs.* shear rate is normally a bit higher than the flow point measured by modulus crossover point.

4.3.2 Size of oil phase in emulsions and microstructure of printed emulsion samples

Rhodamine B were used to detect the oil droplets sizes and distribution in emulsions under optical microscopy. The oil phase and continuous phase in all the emulsion systems and the average emulsion droplet sizes are summarized in Figure 59.

ID	Suspension and average bubble size	Fracture surface	Average size of pores
1	 5.34±0.5 µm		 4.36±0.4 µm
2			 5.59±0.5 µm
3			 4.23±0.4 µm
4	 4.53±0.4 µm		 4.40±0.4 µm

5	 3.45±0.3 µm		 3.96±0.4 µm
6	 8.51±0.9 µm		 8.07±0.8 µm
7	 4.96±0.5 µm		
8	 4.73±0.5 µm		 4.47±0.4 µm
9	 4.05±0.4 µm		

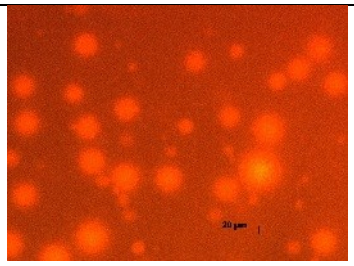
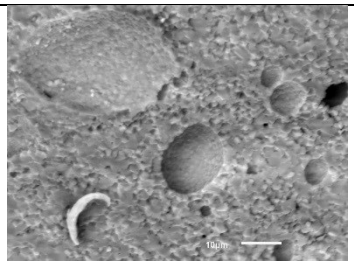
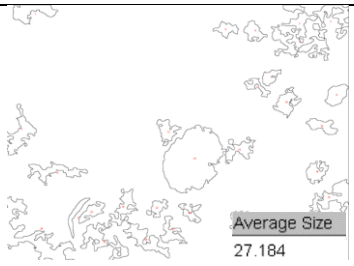
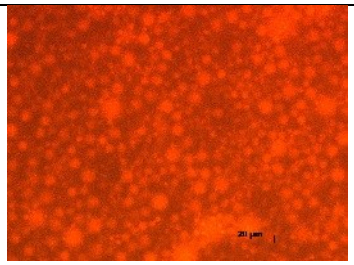
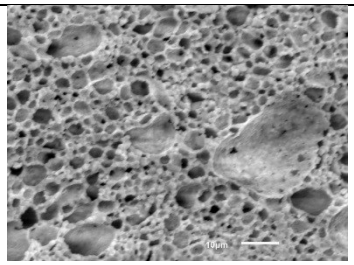
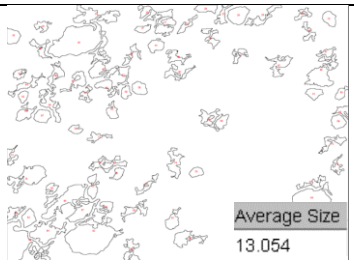
10	 7.12±0.7 μm		 5.21±0.5 μm
11	 3.87±0.4 μm		 3.61±0.4 μm
	30 μm	10 μm	10 μm

Figure 59. Microstructure and average size of bubbles in emulsions and pores of printed emulsion samples (sample 7 and 9 were not printable; sample 1, 2 and 3 start from the same suspension before adding GδL).

As shown in Figure 59, the microstructures of the sintered samples are mostly determined by the size and dispersion of the decane droplet in the emulsions (depending on the component of emulsions and the process of making emulsions). The average oil droplet size in an emulsion is normally slightly larger than the pore size of the sintered sample due to the shrinkage during drying and sintering. However, some sintered samples have few large pores which are significantly larger than the oil droplets in the emulsions due to droplet coalescence (e.g. Sample 2). Because of the set of thresholds for the Image J analysis, some smaller or larger pores may miss on the pictures. This may bias the calculated average pore sizes.

4.3.3 Printability of the emulsion-based inks

The printability of inks was mainly described by a range of yield stress and storage modulus. In Minas's research about the printing of emulsions, a printable ink should exhibit a yield stress over 200 Pa and a storage modulus over 2 kPa.[17] There are other criteria that can be used to show the printability of the inks.

4.3.3.1 Largest span that can be printed using the emulsion inks

For a printed spanning structure, a minimum storage G' is required which is expressed as:

$$G' \geq 1.4\rho g(\frac{L}{D})^4 D \tag{20}$$

where ρ is the density of the ink, L is the spanning distance and D is the diameter of the printed filament (nozzle size ~0.41×10^{-3} m). This equation is the requirement to ensure that a woodpile structure or any similar structure that has a filament span hanging like a bridge can be printed.[13, 85] So the largest span of a ink with a known storage modulus can be calculated

$$L \leq \sqrt[4]{\frac{G'D^3}{1.4\rho g}} \tag{21}$$

Table 9 shows the density and the largest span of different samples in which the density of the ink ρ_{ink} is calculated using equation

$$\rho_{ink} = \rho_{decane} * Vf_{decane} + \rho_{water} * Vf_{water} + \rho_{Al_2O_3} * Vf_{Al_2O_3} \tag{22}$$

where ρ_{decane}, ρ_{water} and $\rho_{Al_2O_3}$ are the density of pure decane (0.73 g/cm^3), water (1 g/cm^3) an Al_2O_3 (3.97 g/cm^3), Vf_{decane}, Vf_{water} and $Vf_{Al_2O_3}$ are the volume fraction of decane, water and Al_2O_3 in the emulsions. The calculated span is of the order of 3 to 4 mm which allows grids with decent span size to be printed.

Table 9. The density and largest span of different emulsion samples.

Sample ID	Equilibrium storage modulus (Pa)	Density (kg/m^3)	Largest span (m)
1	5×10^4	1459	3.71×10^{-3}
3	7×10^4	1459	3.94×10^{-3}
4	6.5×10^4	1459	3.87×10^{-3}
5	9×10^4	1459	4.20×10^{-3}
6	5×10^4	1310.5	3.72×10^{-3}
8	4.5×10^4	1750.6	3.37×10^{-3}
10	3×10^4	1459	3.19×10^{-3}
11	6.5×10^4	1459	3.87×10^{-3}

4.3.3.2 Criterion for a minimum yield stress, a maximum height of the emulsion inks

As described in Chan's reports, the minimum yield stress for a printable ink in his reports(flow points in this work as the value is the cross over point between modulus) τ_{fp} is related to the gravity, suspension surface tension and printed part's height which is written as:[85]

$$\tau_{fp} \geq \gamma D^{-1} + \rho g h \tag{23}$$

where γ is the suspension's surface tension, D is the nozzle diameter (0.41×10^{-3} m), ρ is the density of the ink, g is the gravitational acceleration (9.8 m/s^2), h is the printed part's height (3×10^{-3} m). However, the surface tension of the suspension was not measured in this work. Here, a first approximation is made using surface tension of water (72 dyn/cm~72×10^{-3} N/m) instead of that of the suspension. This equation shows that a printed bar or any part should be strong enough (the yield stress or flow point is high enough) so it will not distort neither by the force of gravity under its own weight (tend to make the part slump) or by the capillary forces (tend to make the part become a sphere to reduce the surface and therefore the surface energy of the system).

The maximum printable height h_{max} can also be calculated using the estimation:[25]

$$h_{max} = \frac{\sigma_y^{Dyn}}{\rho g} \tag{24}$$

where ρ is the density of the ink, g is the gravitational acceleration.

Two dimensionless numbers Ξ and Ξ_γ can be used to describe the printability of the pastes.[25]

$$\Xi = \frac{\sigma_y^{Dyn}}{\gamma D^{-1} + \rho g h} \tag{25.a}$$

$$\Xi_\gamma = \frac{\sigma_y^{Dyn}}{\gamma D^{-1}} \tag{25.b}$$

where γ is the suspension's surface tension, D is the nozzle diameter, ρ is the density of the ink, g is the gravitational acceleration, h is the printed part's height. An approximation is made here as well for the surface tension of the samples using surface tension of water.

There are two forces that try to distort the printed parts. One is the gravity and the other one is the capillary forces that try to minimize the total surface. The two dimensionless numbers Ξ and Ξ_γ tell the relationship between the strength of the printed parts and these forces.

The results of minimum flow point, h_{max}, Ξ and Ξ_{γ} are shown in Table 10.

Table 10. Minimum τ_{fp}, h_{max}, Ξ and Ξ_{γ} of different emulsified slurries.

Composition	Variable		Minimum τ_{fp} (Pa)	h_{max} (mm)	Ξ	Ξ_{γ}
Decane: 50 vol% Solid: 40 vol% BCS: 2 wt% Stirring: 8000 rpm	GδL: wt/vol%	1	223	0.7	0.04	0.06
		2	223	12.6	0.81	1.03
		4	223	16.1	1.03	1.31
GδL: 2wt/vol% Decane: 50 vol% Solid: 40 vol% Stirring: 8000 rpm	BCS: wt%	1	223	11.9	0.76	0.98
		2	223	12.6	0.81	1.03
		4	223	35.0	2.24	2.85
GδL: 2wt/vol% Decane: 50 vol% BCS: 2 wt% Stirring: 8000 rpm	Solid: vol%	30	219	7.8	0.51	0.57
		40	223	12.6	0.81	1.03
GδL: 2wt/vol% Solid: 40 vol% BCS: 2 wt% Stirring: 8000 rpm	Decane: vol%	30	231	9.3	0.69	0.91
		50	223	12.6	0.81	1.03
GδL: 2wt/vol% Decane: 50 vol% Solid: 40 vol% BCS: 2 wt%	Speed: rpm	3000	223	10.5	0.67	0.85
		8000	223	12.6	0.81	1.03
		13000	223	21.0	1.35	1.71

The calculated minimum flow point for most of the slurries is 223 Pa (219 Pa for sample 6 and 231 for sample 8). Most of the printable emulsions in this work have the flow point that obey this criterion. The maximum height for these pastes ranging from 7.8 to 35 mm except sample 2 which is only 0.7 mm. This means the slump occurs when the second layer is printed for sample 2.

Most of the slurries have a value of Ξ over 0.5 and the Ξ_γ is slightly larger than Ξ. When comparing these data with those in M'Barki's report using a similar nozzle size of 500 μm, sample 2 is in the slumping area, sample 6 has some shape deformation (about 20 %) and other samples are in the printable area.[25]

4.3.3.3 Criterion about the relationship between storage modulus and flow point

According to Chan's report, slumping is avoided when the storage modulus and flow point exceed a critical value and the relationship between the storage modulus and flow point to predict the slumping of the emulsions is:

$$G' = \frac{C_1}{\tau_{fp}} \tag{26}$$

where C_1 is a constant (5×10^6 in Chan's research[85]). Figure 60 shows the storage modulus and flow points of all the emulsion samples in this work as well as other printable inks that reported in other papers to see if these inks follow Chan's criteria. Most of the inks follow the criteria except two reported by Minas[17] and Muth[19] which are slight below the C_1 curve. Sample 2 in this work which is unprintable is at the left bottom corner that is far away from the C_1 line.

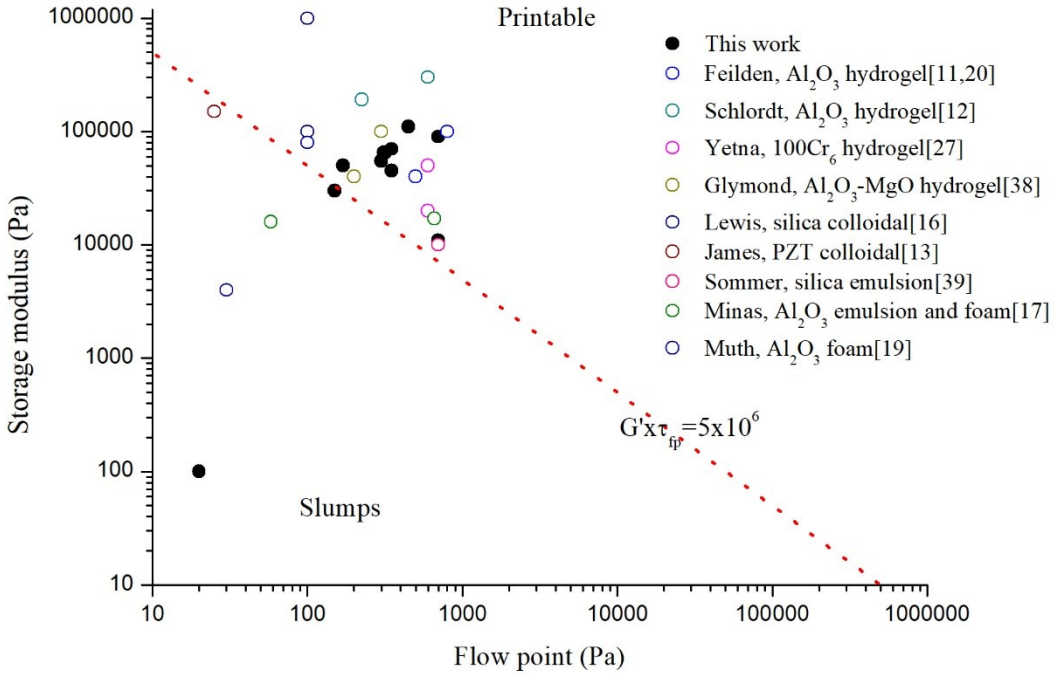


Figure 60. Storage modulus *vs.* Flow point of differentsch inks.

4.3.3.4 Shear stress profile of the inks in the nozzle during printing

During the extrusion of the inks through nozzles, a shear stress profile characterises the flow of the inks which can be described using equation

$$\tau_r = \frac{r\Delta P}{2l} \tag{27}$$

where τ_r is the radial shear stress, r is the radial position within the nozzle, ΔP is the pressure gradient, l is the nozzle length.[13, 39] Figure 61 shows the shear stress profile of the inks passing through a 410 µm cylindrical nozzle at a printing speed of 6 mm/s. As the nozzle used here is conical nozzle instead of straight steel nozzle, the nozzle length used in the calculation is 0.1 mm which is not a precise value but can give an indication of using straight nozzles to give an idea of the problems and values in this system. The shear rate of the inks near the nozzle wall at 6 mm/s through the 410 µm nozzle is calculated using equation 12 as 35 s^{-1}.

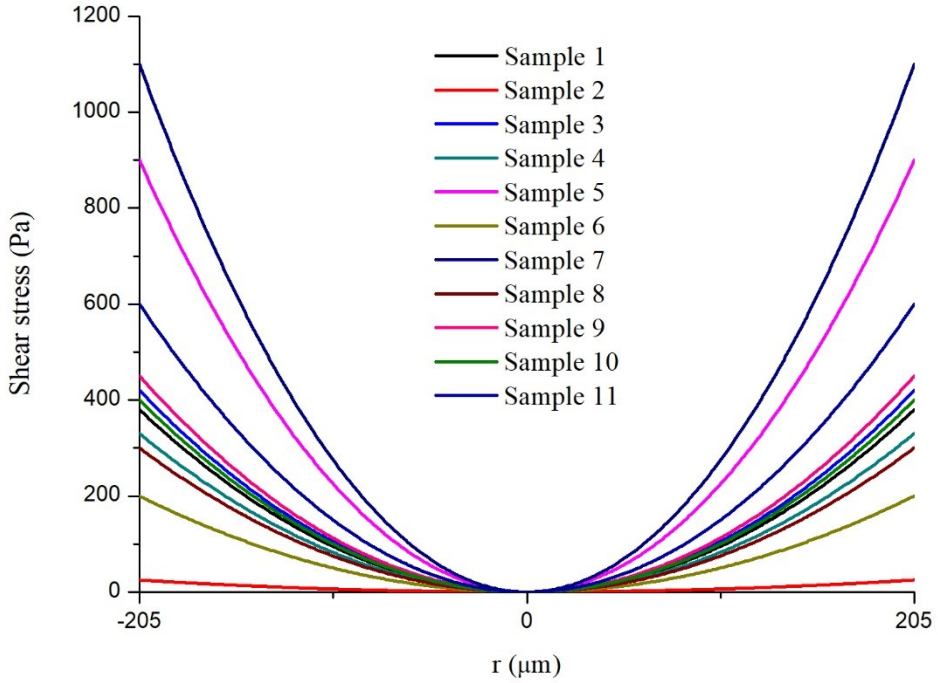


Figure 61. Shear stress profile of emulsion samples extruded through a 410 μm nozzle.

Because of the exist of shear stress gradient, oil droplets occasionally drip down during printing which means droplet coalescence occurs and these oil droplets do not remain in the bulk of the emulsified slurries. Figure 62 shows mechanism of shear stress induced loss of organisation of the emulsions during printing (in a straight nozzle as well). When the emulsion starts to flow, the shear stress in the nozzle has a gradient that at the nozzle centre, the shear rate is 0 (r=0 μm, τ_r=0 Pa) and at the wall of the nozzle, the shear rate is the maximum (r=205 μm, τ_r=$\tau_{r\,\max}$). During the printing, the inks near the nozzle wall have more applied shear stress which disrupts the oil droplets and eventually results in oil droplet coalescence. When the emulsion ink is extruded out, the large oil droplets come from droplet coalescence are not stabilised by the emulsion network and could lead to large pores on the sample surface (defects).

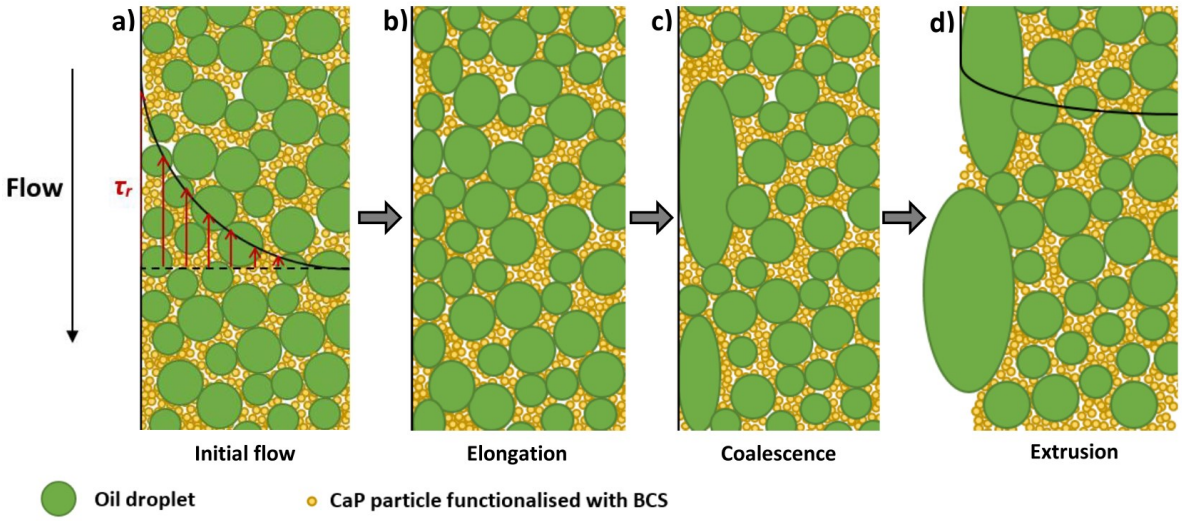


Figure 62. The loss of organisation of emulsions during printing. (a) Initial emulsion structure in the nozzle when the emulsion starts to flow. (b) Oil droplet disruption due to the high shear stress near the nozzle wall. (c) Oil droplet structure breakdown causes oil droplet coalescence. (d) The formation of large oil droplets on the surface of extruded filaments. Reproduced with permission from[39]

4.3.4 Printed Samples with Different emulsion-based inks

Examples of printed bars using different emulsions are shown in Figure 63. Samples 7 and 9 could not be printed due to their high viscosity and yield stress that demanded very large pressures for extrusion. On the other side of the spectrum, sample 2 did not hold its shape after printing, probably due to its low flow point when compared with the surface tension[25]. In this case the capillary forces can deform the printed bar and cause the emulsion to spread on the substrate. This is in agreement with the calculations summarized in Table 10 and the low value of Ξ and Ξ_γ for this emulsion. All the other emulsions can be used to print bars that retain their shapes.

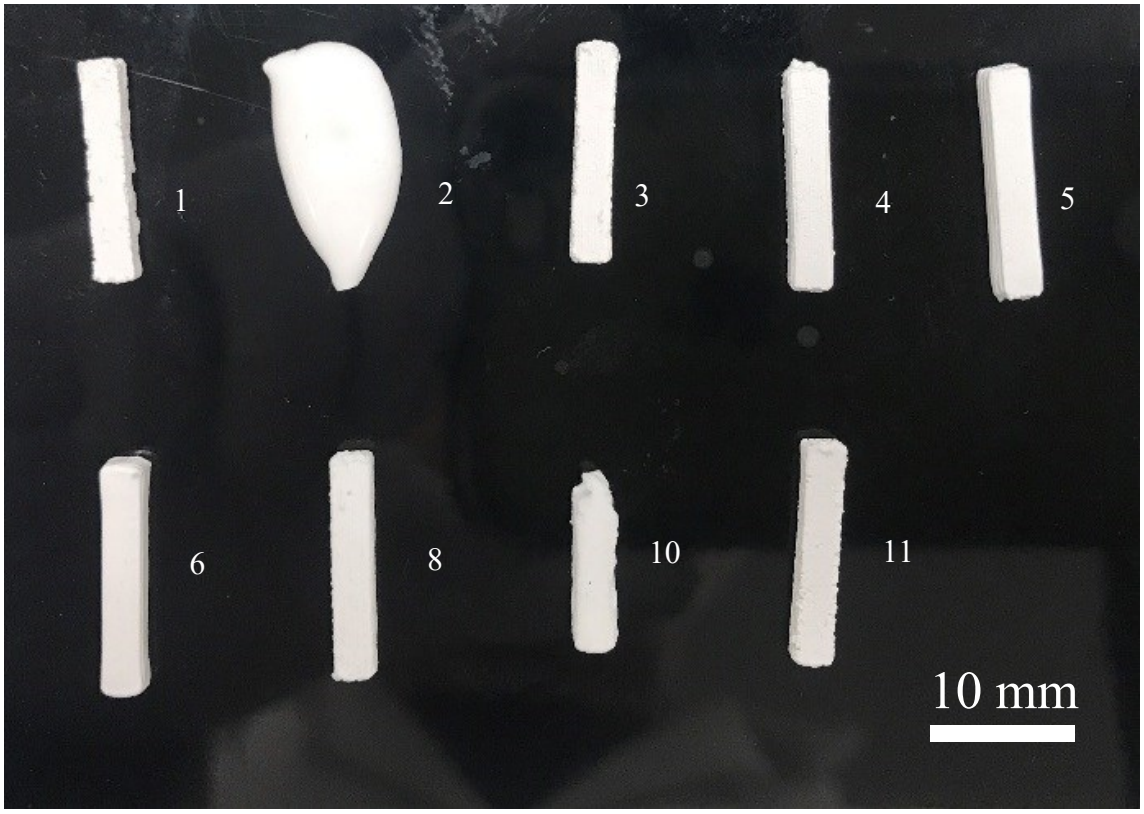


Figure 63. Sintered printed emulsion samples.

4.3.5 Microstructure and Strength of the printed samples

The density, porosity and calculated strength of printed samples are summarized in Table 11. Three specimens of each sample are tested except sample 2 which only have one specimen tested. The results show that, as expected, decreasing the solid loading in water decreases the final density. A higher solid loading gives a higher density of the emulsion and finally leads to a higher sample density. In contrast, a higher decane content reduces the emulsion density and results in a lower final sample density. A higher stirring speed creates smaller decane droplets in the emulsion which stabilises the emulsion and reduces the formation and loss of decane droplets during printing and hence gives the samples a lower density. Despite the fact that Sample 2 did not retain its shape, the printed parts were cut into a small bar to provide values for comparison.

Table 11. Density and Porosity of emulsion samples. Although standard sample 2 bars cannot be printed, a small bar was cut from the extruded paste for the measurement.

Sample ID	1	2	3	4	5	6	8	10	11
Density (g/cm^3)	2.44 ±0.07	1.68	2.15 ±0.16	2.04 ±0.03	1.79 ±0.11	1.61 ±0.06	3.09 ±0.04	3.55 ±0.05	2.26 ±0.09
Porosity (%)	38.5 ±1.8	57.7	45.8 ±4.1	48.6 ±0.8	54.9 ±2.8	59.4 ±1.5	22.2 ±1.0	10.6 ±1.3	43.1 ±1.5
Strength (MPa)	93.8 ±34.7	54.1	92.4 ±8.4	91.9 ±0.4	83.7 ±8.9	68.5 ±14.9	174.4 ±25.1	187.4 ±59.3	74.1 ±10.6

As expected, the samples exhibit a gradual brittle failure in the bending tests as can usually be observed in porous ceramics (Figure 64). Drops in the stress/strain curve are due to fracture of isolated ceramic walls while the rest of the sample can still hold load. The strengths (obtained from the first major fracture in the displacement- stress curve) decreases with the increase of the porosity (Figure 65).

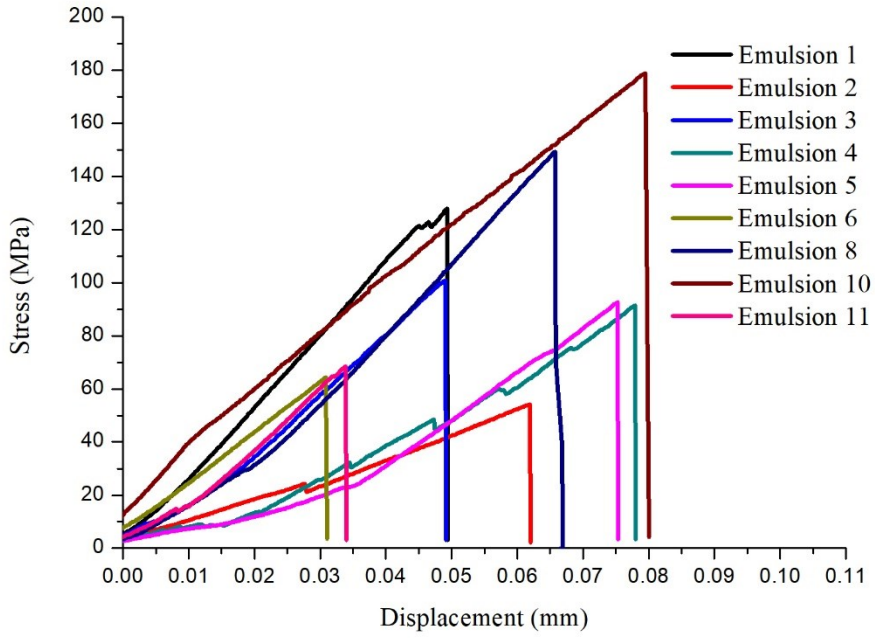


Figure 64. Stress applied on the representative specimen during three-point bending test.

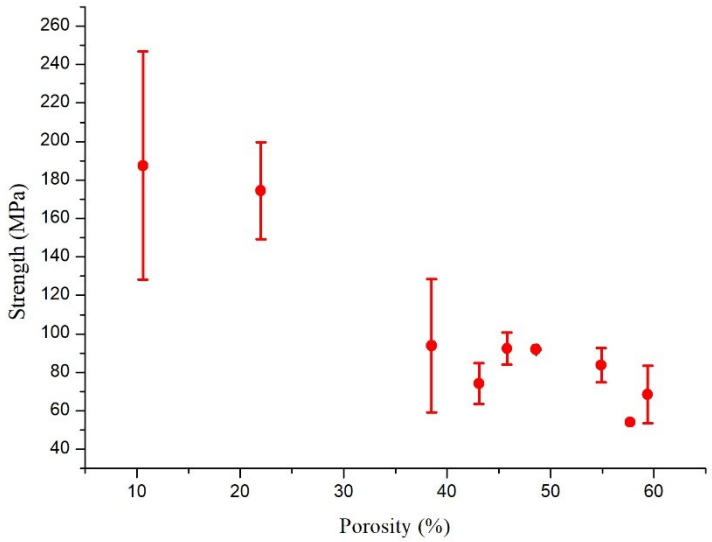


Figure 65. Porosity *vs.* bending strength of the sintered emulsion samples.

A power fitting of the relationship between the strength σ and the relative density ρ_{re} can be done using the model:

$$\sigma = A * {\rho_{re}}^{n} \tag{28}$$

Figure 66 shows the results of fitting of the emulsion samples. The fitting has a n ~1.5 which is in consistent with what is reported in Gibson's report for ceramic foams.[86]

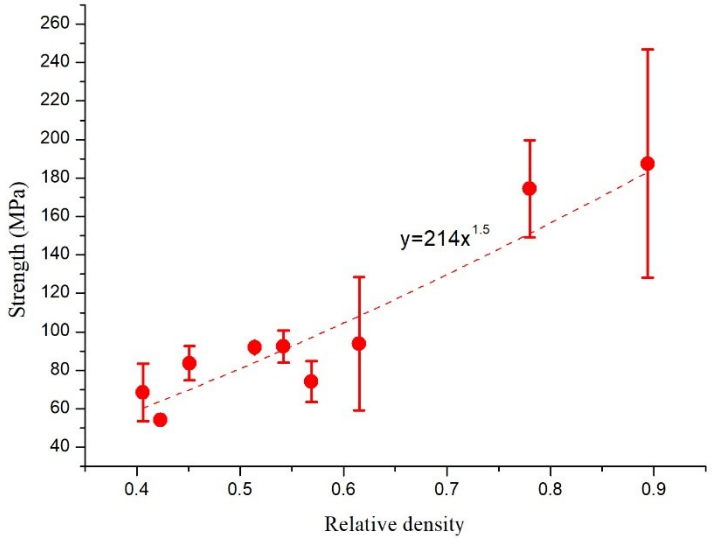


Figure 66. Relative density *vs.* bending strength of the sintered emulsion samples.

The strength of the sintered samples in this work is compared with the other reported emulsion/foam samples in Table 12 and Figure 67. As can been seen in Figure 67, the porous ceramics prepared using alumina emulsion in this work have similar strength as other reported ceramics no matter which type of fabrication technology used.

Table 12. Strength of porous ceramics (mostly robocasting and gel-casting with emulsions/foams) from different reports.

Researcher [Ref.]	Strength (MPa)
This work	70-200 (Robocasting, alumina emulsions, 3-point bending, 10-60 % porosity)
Minas[17]	1-100 (Robocasting, alumina emulsions and foams, compressive strength, 50-90 % porosity)
Garcia-Tunon[34]	40-80 (Gel-casting, alumina emulsions, 3-point bending, 50 % porosity)
Costa Machado[18]	10-20 (Robocasting, β-TCP /HA emulsions, compressive strength, 60-80 % porosity)
Zhang[87]	1-30 (Robocasting, boehmite foams, compressive strength, 75-95 % porosity)
Ostrowski[88]	30-200 (Free sintered and hot pressed, porous alumina ceramic, 4-point bending, 20-40 % porosity)
Mao[89]	10-50 (Gel-casting, alumina foams, flexural strength, 65-85 % porosity)
Chakravarty [90]	20-400 (Spark plasma sintering, porous alumina ceramic, biaxial bending test, 20-60 % porosity)
Ferraro[91]	35 (Gel-casting, SiC emulsions, 4-point bending, 55 % porosity)

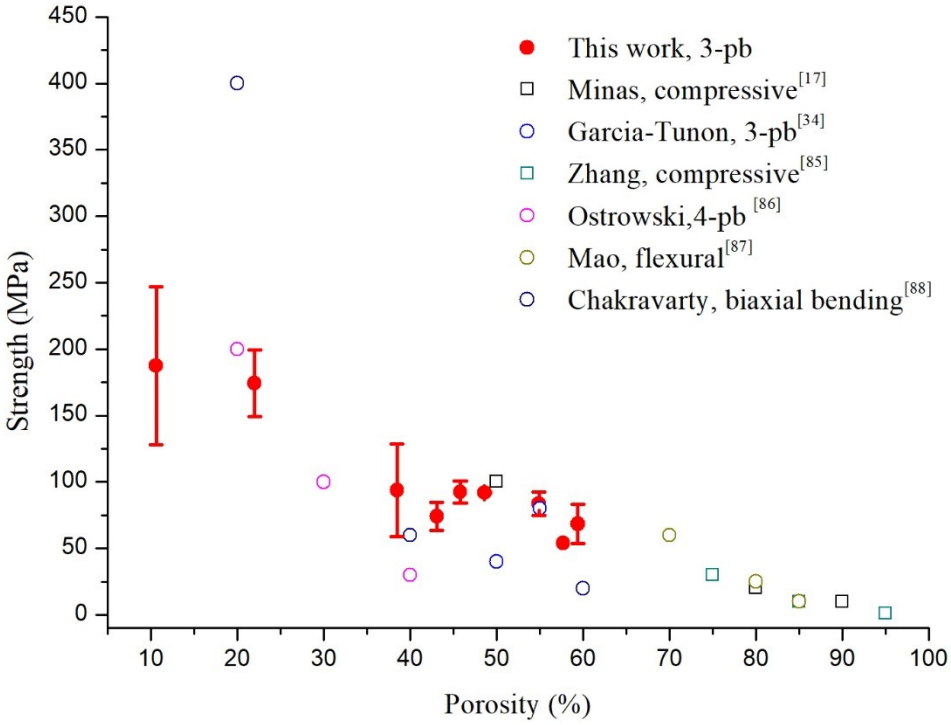


Figure 67. Comparison of strength of porous alumina ceramics.

4.4. Conclusion

The functionalization of ceramic particles with a pH responsive block copolymer surfactant can be used to formulate inks with the viscoelastic response required for the additive manufacturing of microporous alumina ceramics using robotic assisted deposition. In particular they exhibit a shear thinning behaviour and, for the printable emulsions, the yield stresses and storage modulus are large enough to overcome the gravitational and capillary forces and avoid deformation of the printed parts. The emulsions are stable and there is only limited droplet coalescence during printing.

The rheological properties of the emulsion-based inks for robocasting are affected by the solid loading of the suspension, the volume percentage of oil phase, the concentration of the BCS solution, the amount of pH trigger and the stirring speed during the emulsification. In general, the viscosity, yield stress and the equilibrium storage modulus of the emulsified inks increase with the increase of all these factors.

The average micropore size (between 4 and 9 μm according to Figure 59) in the final sintered ceramics can be manipulated by changing the solid loading or stirring speed. The total porosity can be varied by changing the amount of the oil phase and the stirring speed during emulsification. The BCS concentration and GδL added in the emulsions are used to adjust their rheology and make them suitable for robocasting. By combining all these factors, a desirable microstructure of the ceramic can be achieved. The printed porous ceramics have porosities from 10 to 60 % with a decreasing bending strength from 200 MPa to 80 MPa which is similar as other reported alumina porous ceramics fabricated using different techniques.

Robocasting has been proved to print porous ceramic parts with designed porous structure. In order to fabricate products with more complex structure, a core/shell structure may be robocasted using different inks.

Chapter 5: Core/shell structural ceramic composites

5.1 Introduction

It is a general knowledge that ceramics have high stiffness and low toughness as well. Robocasting is a promising technology to fabricate ceramic parts with complex shapes. However, work focuses mostly on printing monolithic ceramics which gives no improvement to the fracture resistance of the final products. The objective of this section is to fabricate metal/ceramic composites in which a ceramic matrix is reinforced by continuous metallic fibres. To reach this goal, filaments with a novel core/shell structure were prepared by co-extruding an Al_2O_3 and a stainless-steel ink through a single nozzle using a robocaster. The interface between the core and the shell can also be manipulated by extruding a more complex filament with a thin layer between them. In this case we have chosen an ink containing a mixture of graphite and Al_2O_3 to create a porous, weak interface between the Al_2O_3 matrix and the steel fibre.

Several researches have built core/shell structures, some of them used polymeric materials with complex, concentric extrusion nozzles[74], and some of them use short fibres as reinforcement[75]. However, long fibres are preferred to provide toughness as long fibres give more fracture resistance than short ones as they can enhance the contributions of bridging of fibre pull-out.[92] The approach described here provides a simple way to fabricate long continuous fibres inside the ceramic matrix by using inks based on thermally reversible hydrogels to build printing cartridges with a core -hell structure. These cartridges can be extruded through a thin nozzle to print macroscopic parts while retaining their core-shell structure.

The rheology of the printing pastes is one of the most important factors for successful robocasting. The rheology of different inks was studied to make it possible to co-extrude them simultaneously. The microstructure and phases presented in the material where analysed using X-ray diffraction (XRD) as well as optical microscopy and SEM-EDS. In particular, these techniques were used to assess the shape and continuity of the steel fibres as well as to characterize the steel-alumina interface in order to identify possible reactions between the different materials during sintering. The mechanical properties of sintered dense samples and grids were determined to understand how the steel fibres reinforce the ceramic products and to identify the key factors which may affect the properties. Hardness, tensile (in situ in the SEM using dog-bone samples) as well as three-point and four-point bending tests (ex situ and in situ in the SEM) were performed in dense samples and the strength of grids was tested in compression.

5.2 Results

5.2.1 Rheology Property of the hydrogel inks

5.2.1.1 Effect of Pluronic concentration on liquid-gel temperature transition

Temperature ramp tests were done on Pluronic solutions with concentrations from 15 wt% to 40 wt% to find suitable Pluronic concentrations for robocasting. According to Figure 68, the 15 wt% Pluronic solution does not exhibit a liquid-gel transformation between 0 ℃ to 40 ℃. For other Pluronic solutions, the liquid-gel transformation temperature decreases with increasing Pluronic concentration. The proper concentration range for robocasting is from 20 wt% to 30 wt% which shows liquid-gel transformation temperatures ranging from 15 ℃ to 25 ℃ which are suitably close to the room temperature.

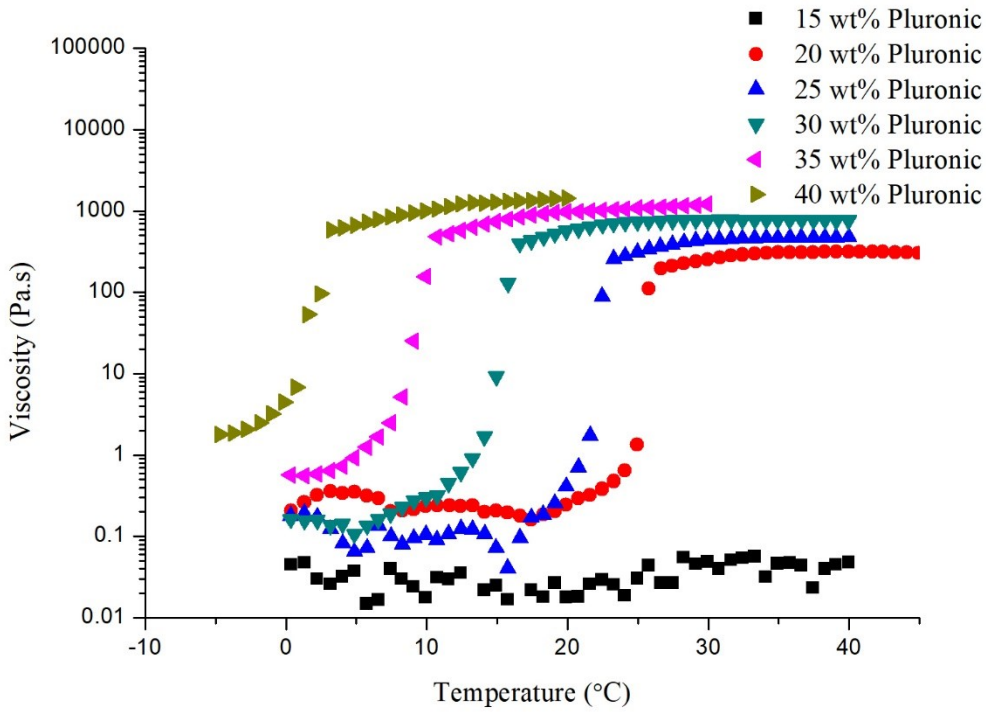


Figure 68. Temperature ramp of solutions with different Pluronic concentration.

5.2.1.2 Effect of alumina concentration on liquid-gel temperature transition

Temperature ramp tests were also done on inks with a constant Pluronic concentration (25 wt%) but with different solid loadings (Al_2O_3 from 25 vol% to 40 vol%) to quantify the influence of the solid loading on the viscosity and liquid-gel transformation temperature (Figure 69). The graph shows that the solid content has an effect on viscosity (higher solid content, higher viscosity) but not a big effect on liquid-gel transformation temperature (~20 ℃ for all inks).

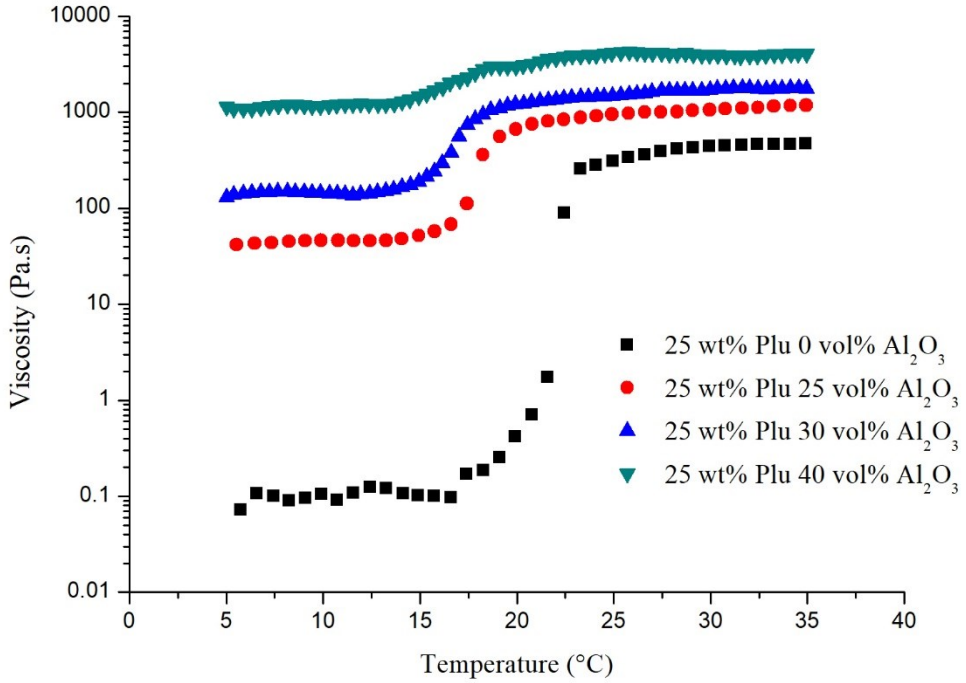


Figure 69. Temperature ramp of pastes prepared with a 25wt% Pluronic solution but different solid loadings.

5.2.1.3 Properties of different inks

5.2.1.3.1 Properties of alumina inks

The rheology properties of Al_2O_3 inks with different solid concentration (prepared with 25 wt% Pluronic solution) is shown in Figure 70 and Figure 71.

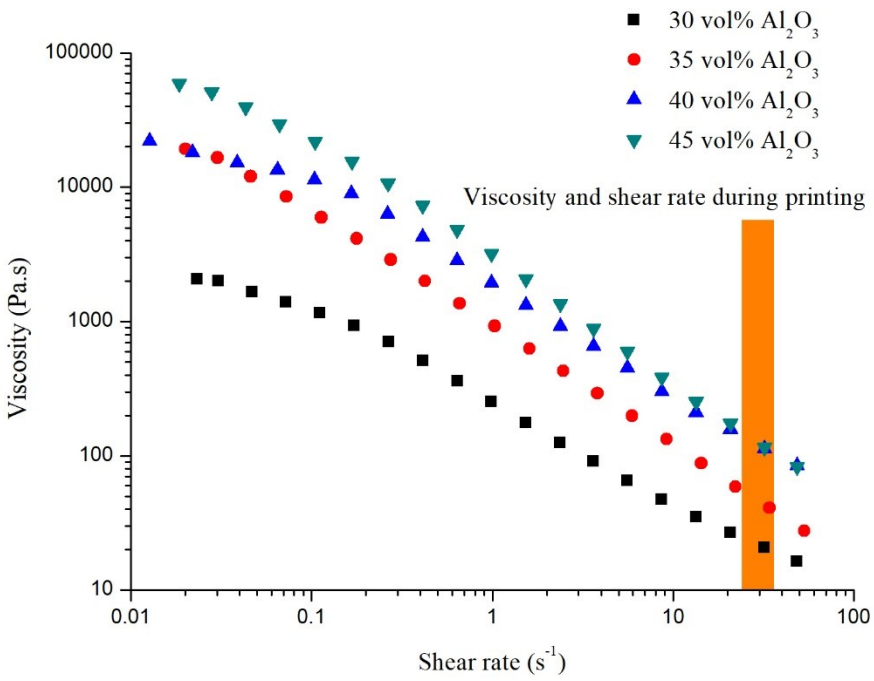


Figure 70. Flow ramp of inks with Al_2O_3 concentration from 30 vol% to 45 vol%. (Colour band is the viscosity and shear rate during printing and Pluronic concentration is 25 wt% here)

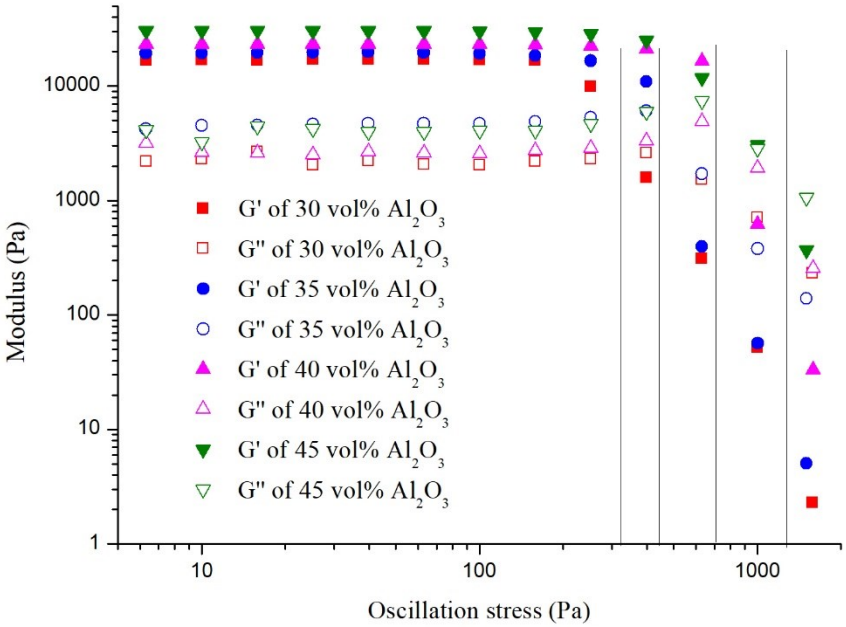


Figure 71. Oscillation amplitude sweep of inks with Al_2O_3 concentration from 30 vol% to 45 vol% (The lines indicate the flow point of the 30 vol%, 35 vol%, 40 vol%, 45 vol% from left to right respectively).

The increasing of solid loading increases the viscosity, flow point and equilibrium storage modulus of the inks. Figure 72 gives the relationship between the viscosity and solid content at a fixed shear rate (~35 s^{-1}). The viscosity seems to grow linear with the solid concentration.

The relationship appears linear instead of following KD model (Equation 13) because the range is relatively short (30-45 vol%). In Feilden's report the dependence for a similar ink composition is linear in this range of concentrations as well.[20]

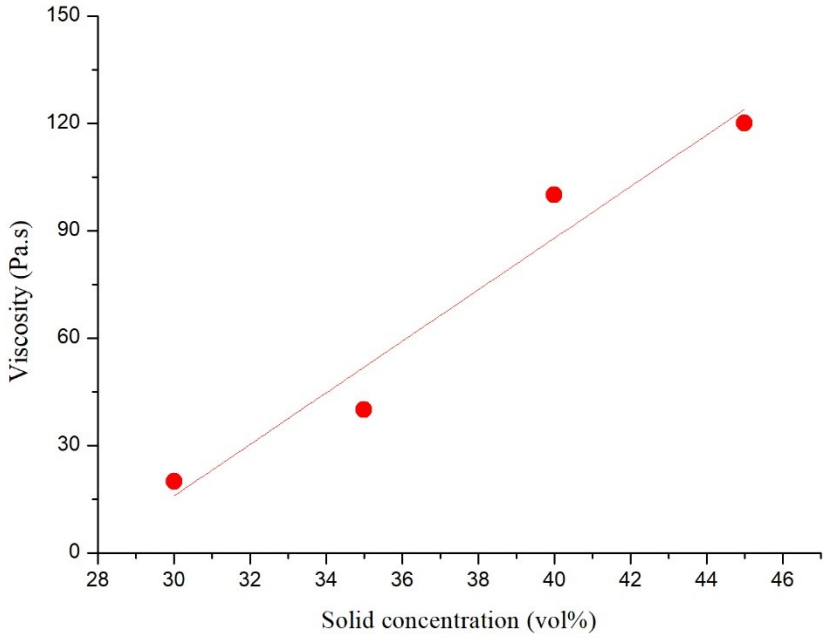


Figure 72. Relationship between viscosity and solid concentration at a shear rate of 35 s^{-1}.

Figure 73 gives an example of calculating the viscosity parameter (K) and shear thinning coefficient (n). As the yield stress τ_y is similar as the flow point τ_{fp}, a first estimation is done by replacing the yield stress with the flow point in Herschel-Bulkley model. This is a plot of $ln(\tau - \tau_{fp})$ *vs.* $ln(\dot{\gamma})$ of 35 vol% Al_2O_3 ink. The slope for this particular case is 0.20 which means that this is the value of n for this ink. The intercept is 6.16 which is equal to ln(K), so the K for this ink is 473.4 $Pa.s^n$. The calculated n and K for inks with different solid loading is shown in Figure 74 and Figure 75.

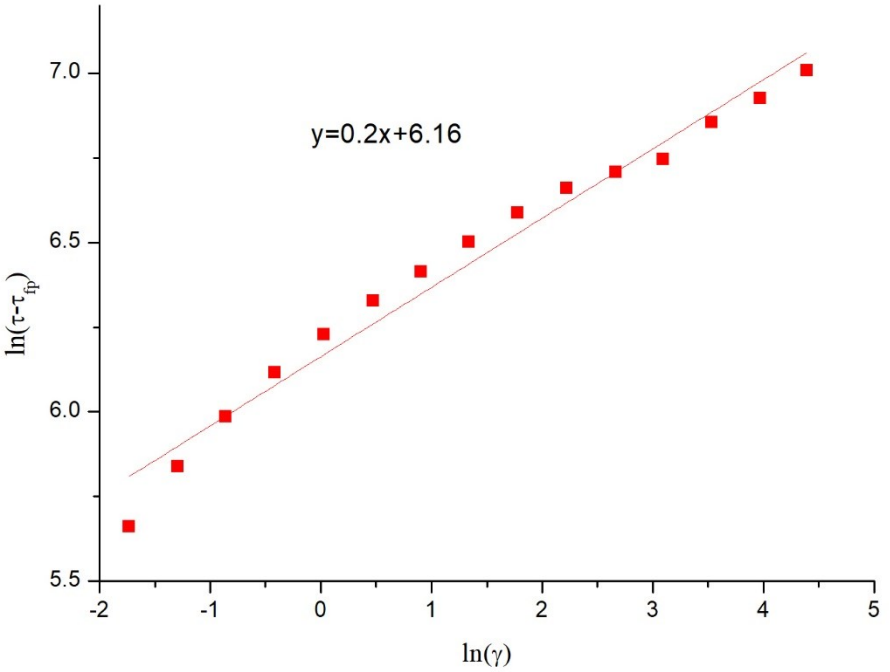


Figure 73. Example of calculation of *n* and *K* using 35 vol% Al_2O_3 ink.

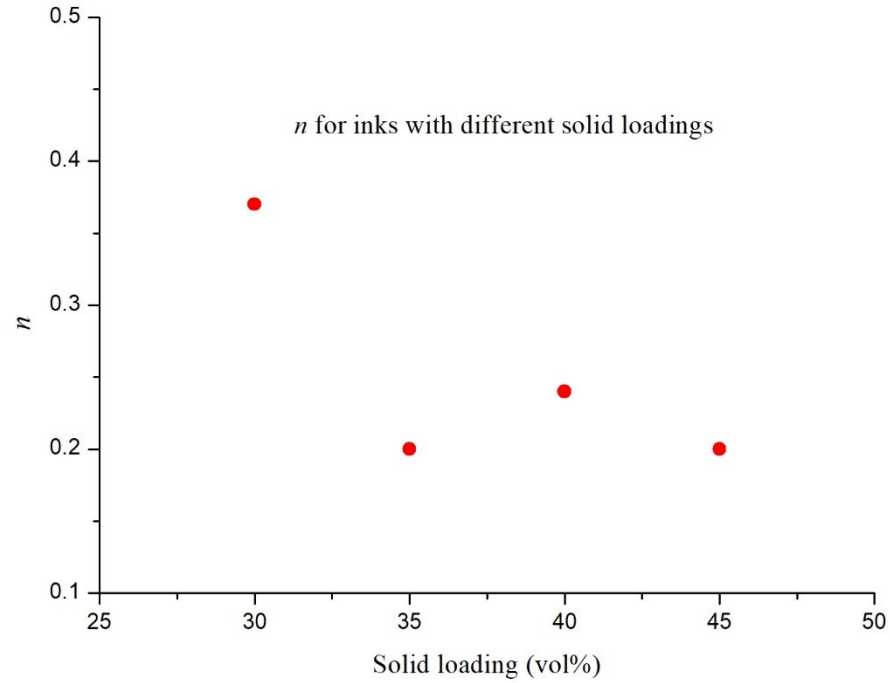


Figure 74. *n* of inks with different solid loading.

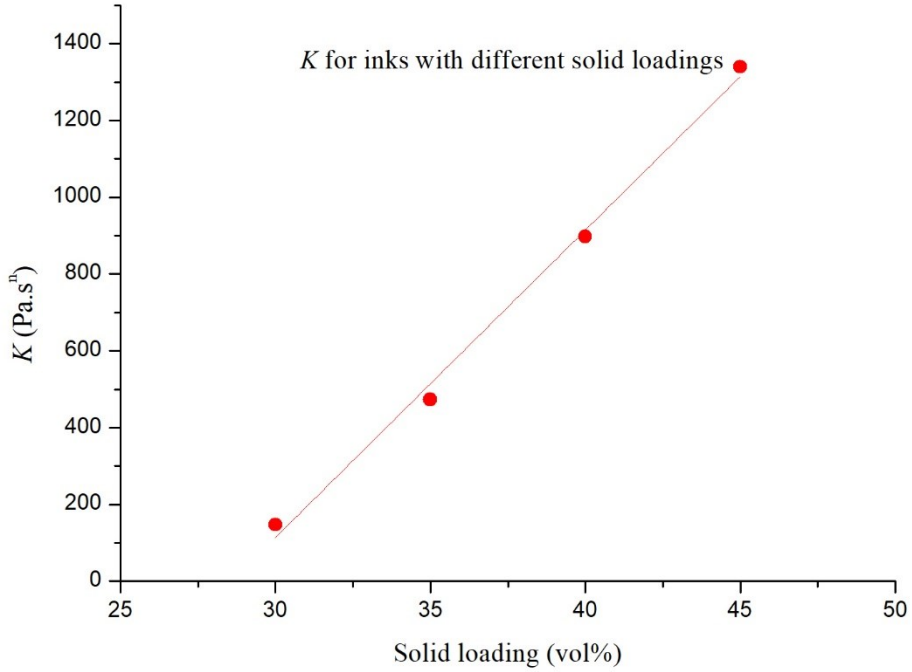


Figure 75. *K* of inks with different solid loading.

The *n* for these inks has a range from 0.2 to 0.4 and the n seems be high for low solid concentration and then remains constant. The value of *K* has a linear increasing with the increasing of solid loading which means the increasing of viscosity.

5.2.1.3.2 Properties of C-alumina inks

Figures 76, 77 and 78 give the rheology property of C-Al_2O_3 ink used as the interface ink. This kind of ink has a similar rheology property as the 35 vol% Al_2O_3 ink. This ink has a shear thinning behaviour with K= 469 Pa.s^n, n=0.2, yield point=150 Pa, flow point=450 Pa, equilibrium storage modulus=24000 Pa and viscosity at 35 s^{-1}=60 Pa.

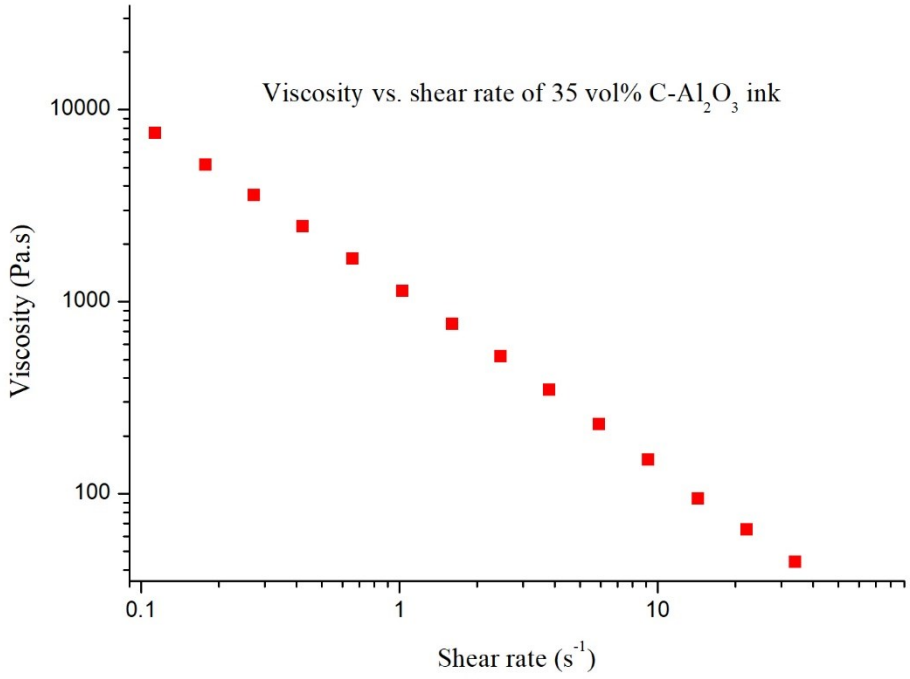


Figure 76. Flow ramp of 35 vol% C-Al_2O_3 ink.

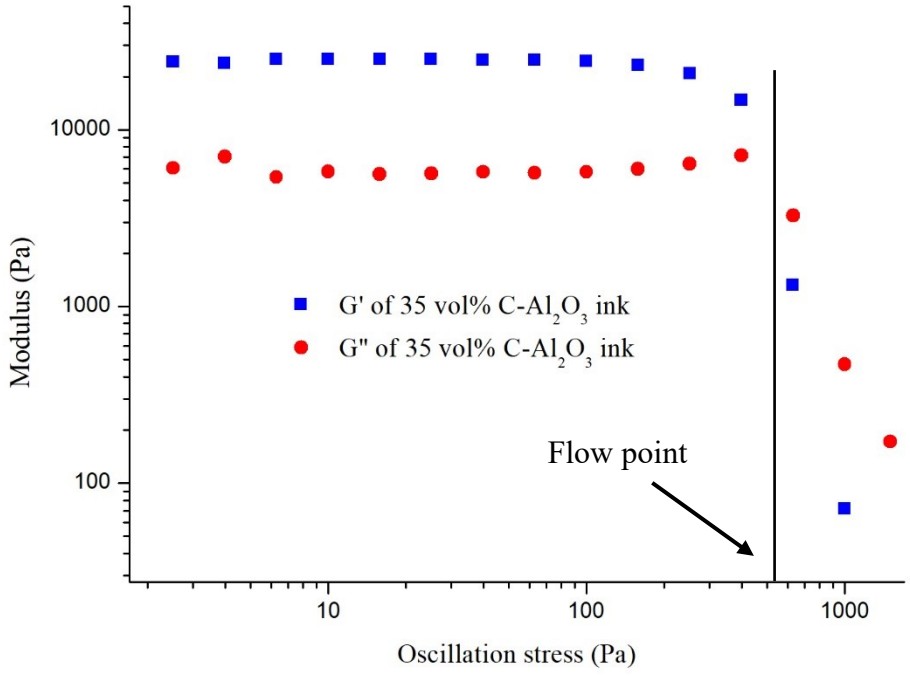


Figure 77. Oscillation amplitude sweep of 35 vol% C-Al_2O_3 ink.

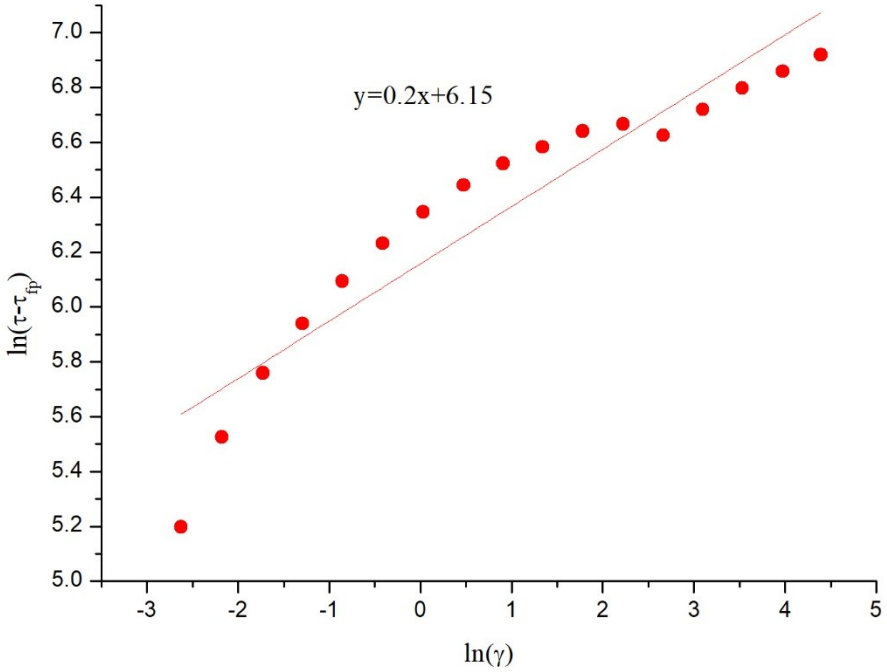


Figure 78. $ln(\tau - \tau_{fp})$ *vs.* $ln(\dot{\gamma})$ of 35 vol% C-Al_2O_3 ink.

5.2.1.3.3 Properties of iron oxide inks

Iron oxide inks prepared with 25 wt% Pluronic solution with a solid concentration of 25 and 35 vol% were firstly used as the core ink for core/shell structures. The aim was to use it as a precursor for iron (after reduction during sintering in vacuum or reducing H_2 environment). The rheology of Fe_2O_3 inks is summarized in Figures 79, 80 and 81. The 25 vol% Fe_2O_3 ink has K= 97 Pa.s^n, n=0.29, yield point=20 Pa, flow point=100 Pa, equilibrium storage modulus=11000 Pa and viscosity at 35 s^{-1}=10 Pa which is quite different from the rheology of 35 vol% Al_2O_3 ink. Although the rheology property of the 35 vol% Fe_2O_3 ink matches with the rheology of 35 vol% Al_2O_3 ink (K= 780 Pa.s^n, n=0.22, yield point=80 Pa, flow point=400 Pa, equilibrium storage modulus=25000 Pa and viscosity at 35 s^{-1}=100 Pa), the reduction of the Fe_2O_3 was not a success. As shown in Figure 82, the Fe_2O_3 parts seems be not fully reduced into iron (no metallic cores) thus cannot form long iron fibres in the structure.

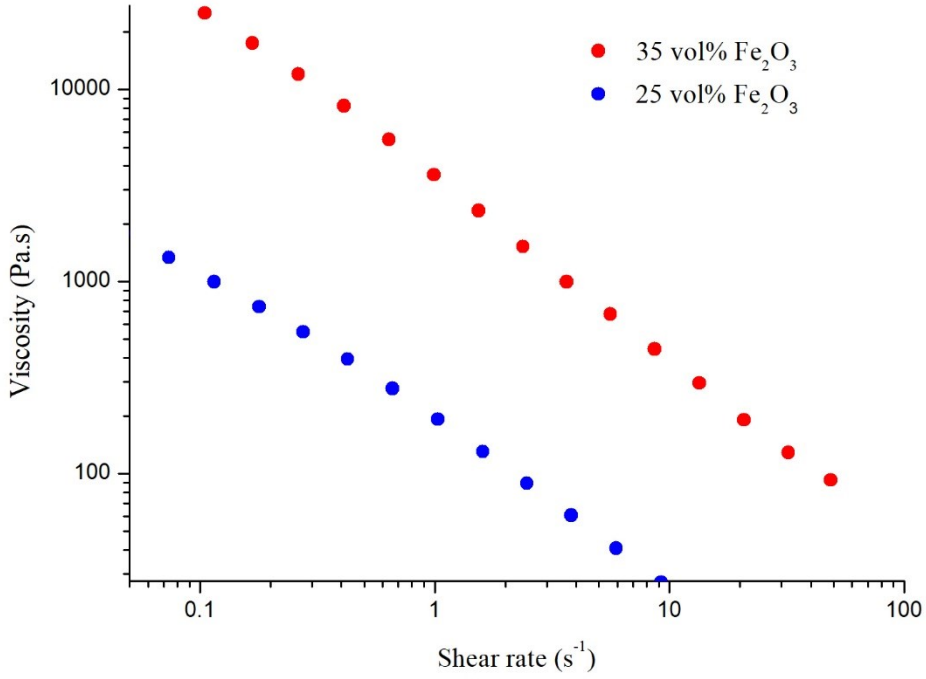


Figure 79. Flow ramp of 25 vol% and 35 vol% Fe_2O_3 ink.

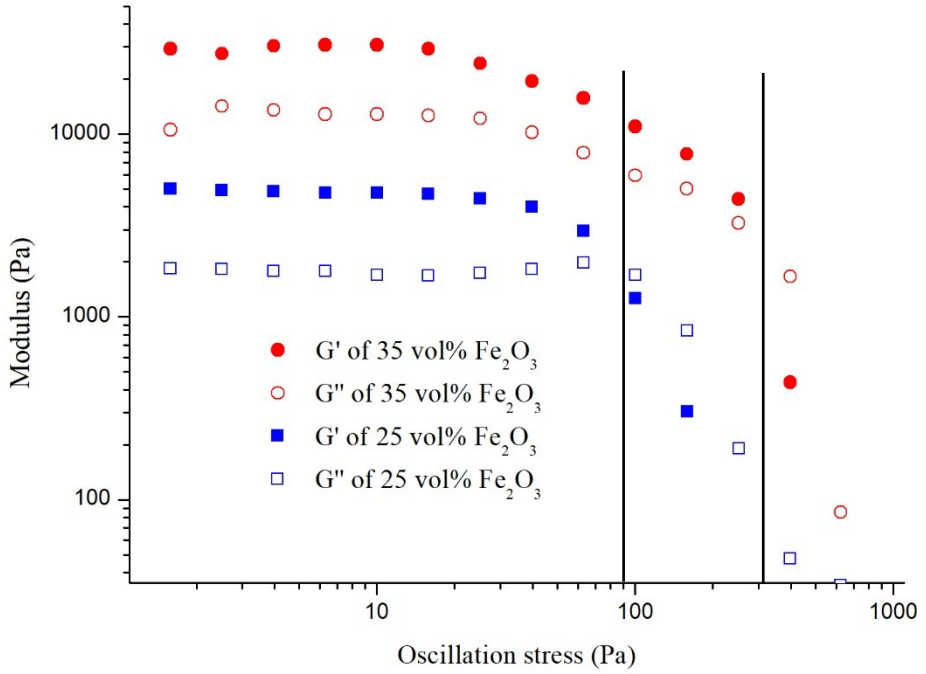


Figure 80. Oscillation amplitude sweep of 25 vol% and 35 vol% Fe_2O_3 ink (The lines indicate the flow point of the 25 vol% and 35 vol% Fe_2O_3 from left to right respectively).

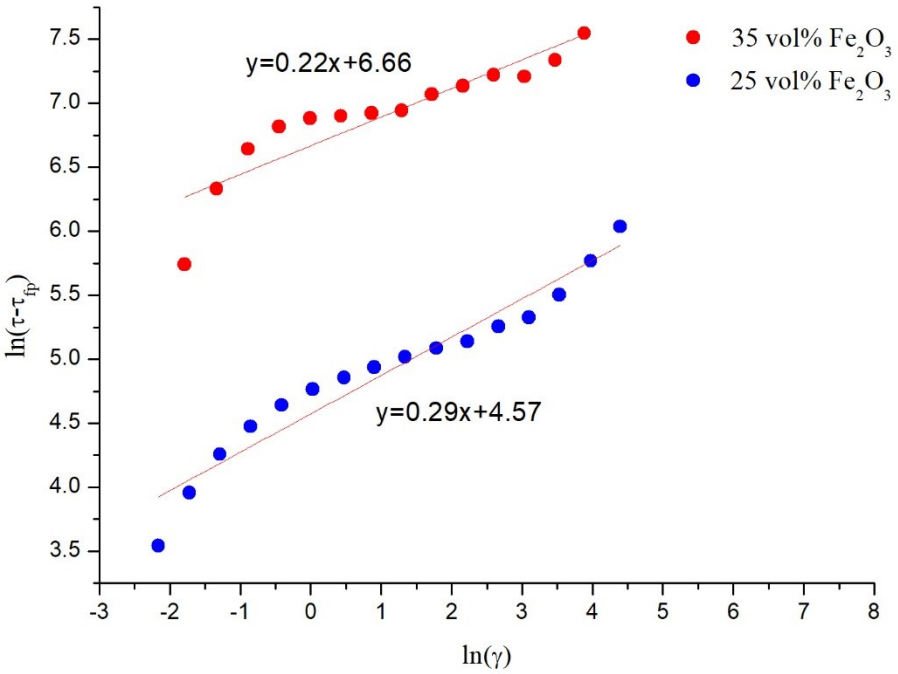


Figure 81. $ln(\tau - \tau_{fp})$ *vs.* $ln(\dot{\gamma})$ **of 35 vol% Fe_2O_3 ink.**

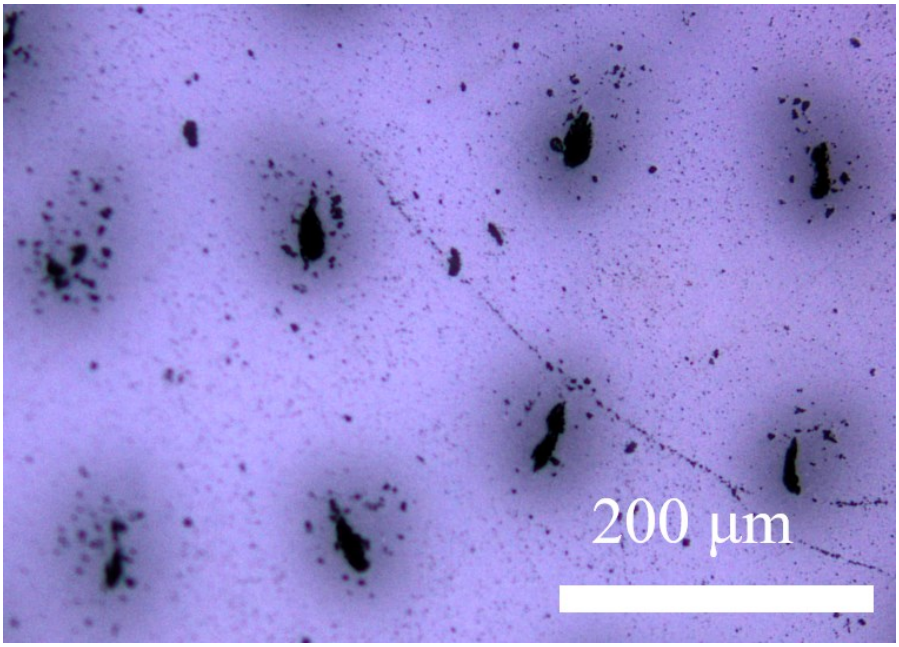


Figure 82. Optical microscopy of cross section of composite samples printed core/shell Fe_2O_3/Al_2O_3 filaments (Sintered in vacuum at 1550 °C and the dark holes indicate the Fe_2O_3 cores).

5.2.1.3.4 Properties of iron and steel inks

After the failure of iron oxide inks, inks prepared using iron powders and stainless-steel powders were chosen as the core inks. The rheology of the iron and steel inks is summarized in Figures 83, 84 and 85. However, the samples prepared with iron inks got oxidised during drying in air. Finally, the core/shell structural composites used steel inks as the core inks. There is a problem with the 35 vol% steel ink that although it is printable, it does not flow even if put it in an ice bath to keep it at 0 °C, so it cannot fill the core during manufacturing the core/shell syringes. Hence, the co-extrusion process used 30 vol% steel ink as the core ink. These three inks are all shear thinning with K= 106 Pa.s^n, n=0.35, yield point=120 Pa, flow point=450 Pa, equilibrium storage modulus=20000 Pa and viscosity at 35 s^{-1}=50 Pa for 30 vol% steel ink; K= 392 Pa.s^n, n=0.44, yield point=200 Pa, flow point=600 Pa, equilibrium storage modulus=30000 Pa and viscosity at 35 s^{-1}=60 Pa for 35 vol% steel ink; K= 279 Pa.s^n, n=0.44, yield point=100 Pa, flow point=350 Pa, equilibrium storage modulus=24000 Pa and viscosity at 35 s^{-1}=55 Pa for 35 vol% iron ink.

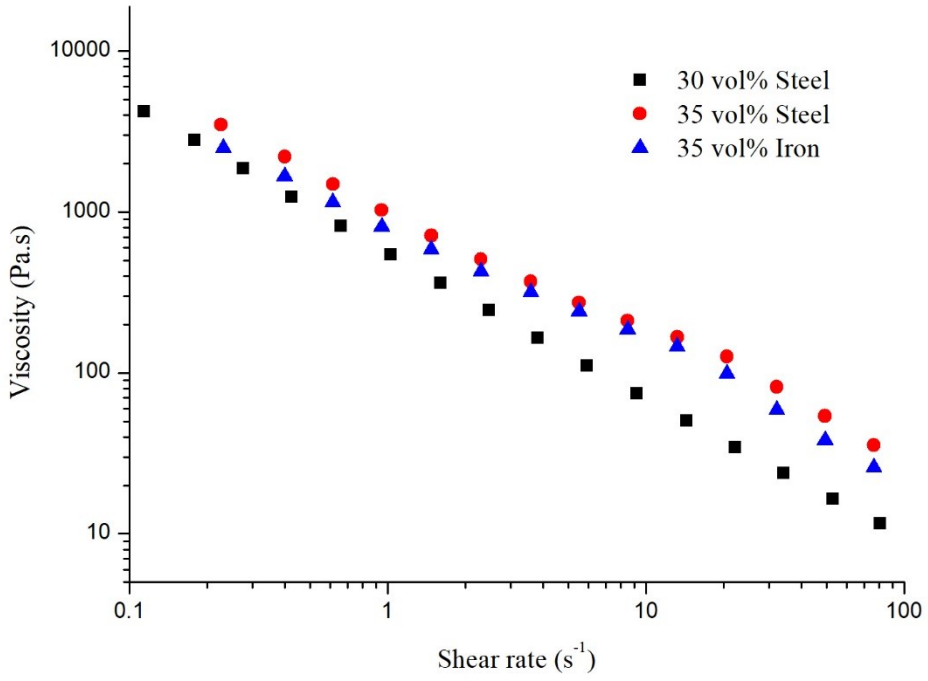


Figure 83. Flow ramp of different steel and iron ink.

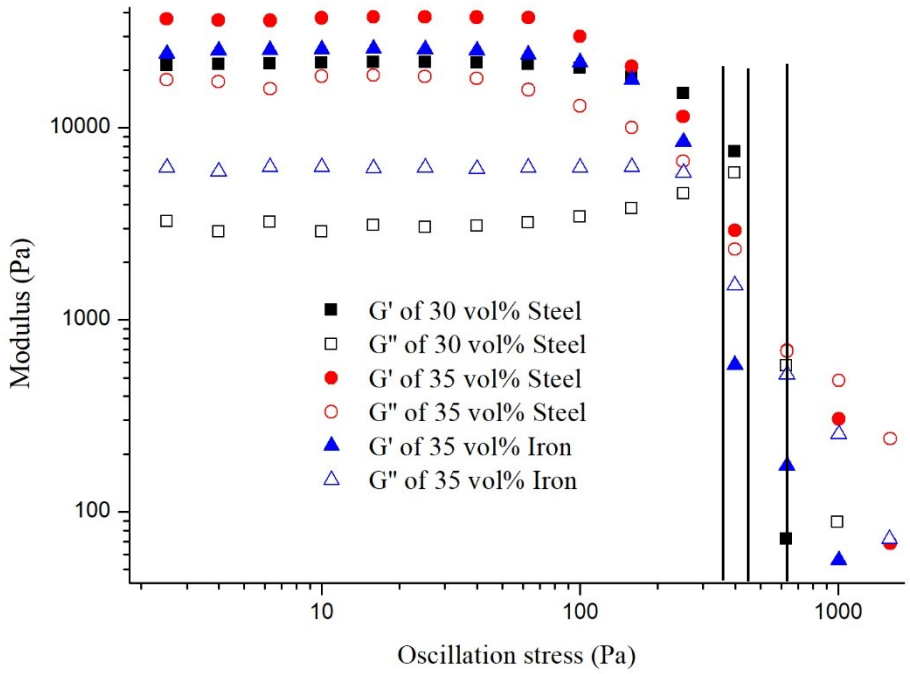


Figure 84. Oscillation amplitude sweep of different steel and iron ink (The lines indicate the flow point of the 35 vol% Iron, 30 vol% Steel, 35 vol% Steel from left to right respectively).

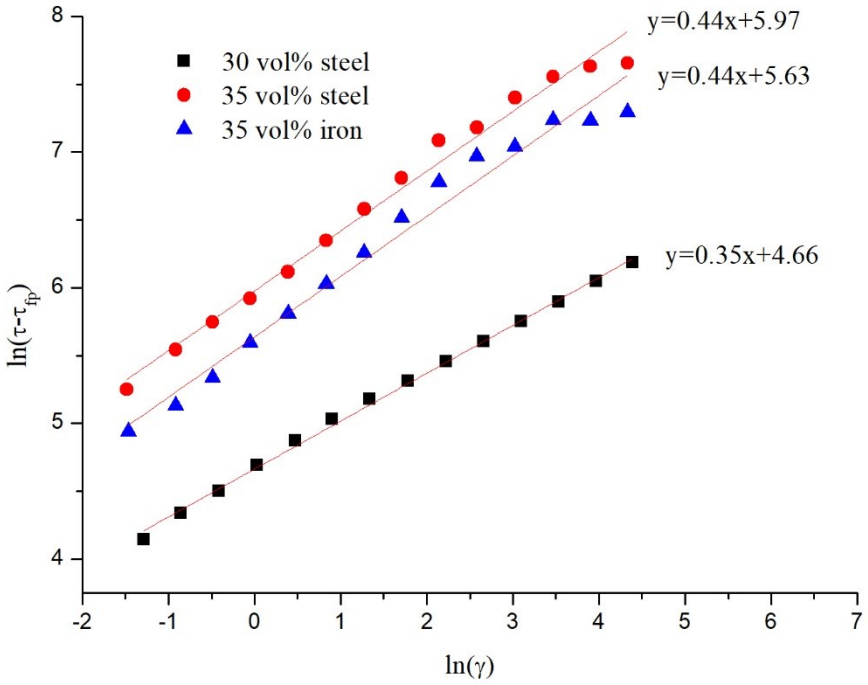


Figure 85. $ln(\tau - \tau_{fp})$ *vs.* $ln(\dot{\gamma})$ of different steel and iron ink

5.2.1.3.5 Property of three inks for co-extrusion

5.2.1.3.5.1 Flow ramp

A printable ink should be shear thinning which has a decrease of viscosity with an increase of shear rate. Figure 86 shows the shear thinning behaviour of three different inks used for core/shell structure. These three inks have similar viscosity at a same shear rate which makes it possible for them to be co-extruded.

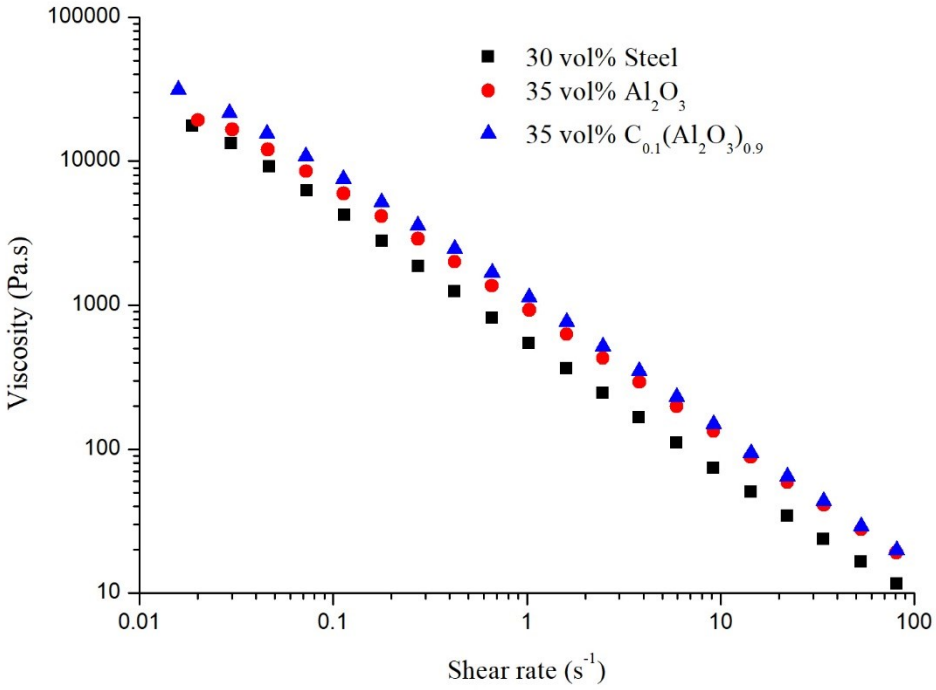


Figure 86. Flow ramp of three different inks

5.2.1.3.5.2 Oscillation amplitude sweep

The oscillation amplitude sweep test gives a visible change of the storage modulus (G') and loss modulus(G'') with the change of the oscillation stress which is shown in Figure 87. When the applied stress is low, G' is higher than G'' which means the ink has a solid like behaviour while when the applied stress is high enough, G'' is higher than G', the ink response is liquid-like. The cross point of the G' curve and the G'' curve indicates the flow point of the ink. The three inks used here have similar flow point ~400 Pa (so as the yield stress) and yield point ~200 Pa which gives it possibility to co-extrude them.

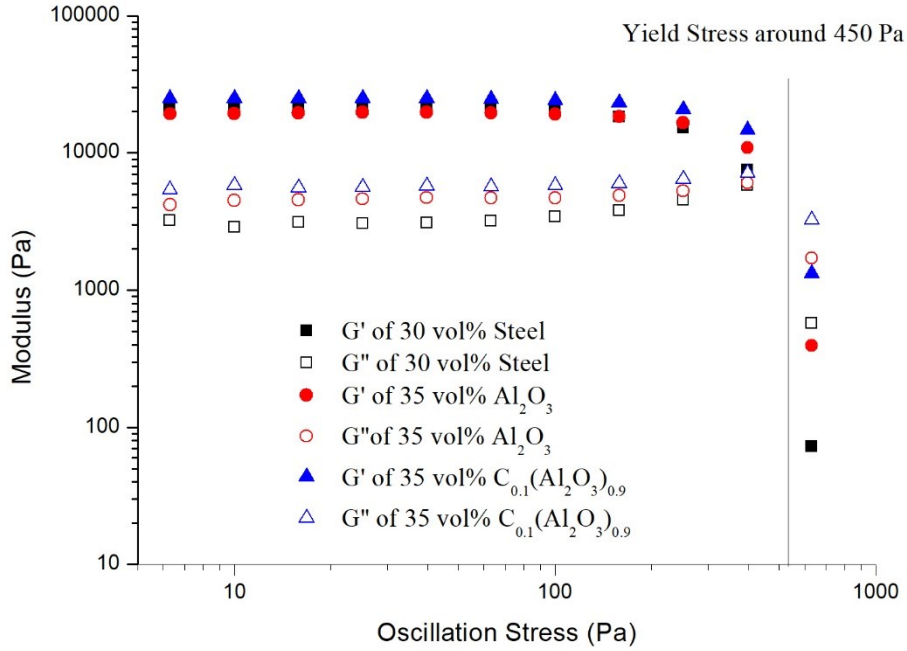


Figure 87. Oscillation amplitude sweep of different inks

5.2.2 Structural characterization

5.2.2.1 Shrinkage of the printed samples

The printed samples are shown in Figure 36. Assuming that the shrinkage was isotropic, the longitudinal shrinkage of the samples is calculated using the bar shaped samples (Figure 36 B). These samples are designed as 35×3×3 mm during printing. The shrinkage of the samples during drying and sintering was measured. The original printed samples have an average length of 35 mm. Dried bars which are then dealt with CIP have an average length of 30.5 mm after CIP and the average length of the sintered bars is 26.5 mm. Thus, the calculated average drying shrinkage of the samples is 12.86 % and the average sintering shrinkage of the samples is 24.29 % (assuming that shrinkage is homogeneous).

5.2.2.2 SEM analysis

Figure 88 shows the fracture surfaces and polished cross sections of sintered Al_2O_3 and composites printed with core/shell steel/Al_2O_3 filaments. Cross sections of bars printed with one core filaments that have undergone cold isostatic pressing are compared to those that have not been pressed. The main observations in Figure 88 are:

-There is a clear distortion of the metallic cores in the sintered samples. These cores become "flatter."

-The dimensions of the flattened cores are of the order of 200×50 mm.

-The interface between the steel fibres and the alumina matrix is sharp (no reaction products or porosity are visible in the polished cross sections) but rough at the microscopic level.

-There is significant plastic deformation of the metallic fibres in the fracture surfaces.

-Large pores remain in the sample that did not undergo CIP.

-The C-Alumina ink successfully created a porous interface between the steel and the dense alumina matrix with a thickness of around 50 mm.

-In the 2-core system one of the metallic fibres always seem to be much wider than the other.

-In the 3-core system some of the fibres may be merging.

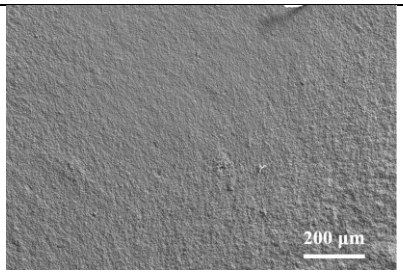
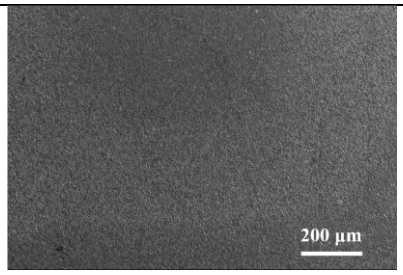
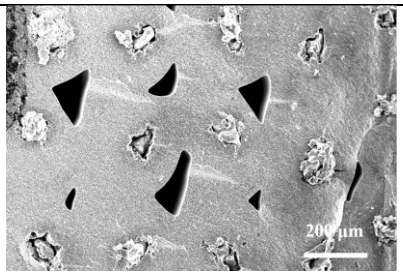
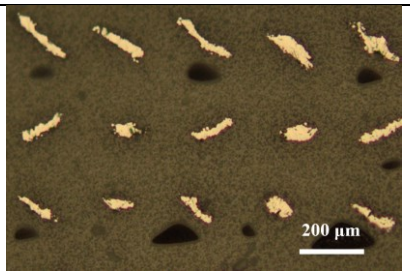
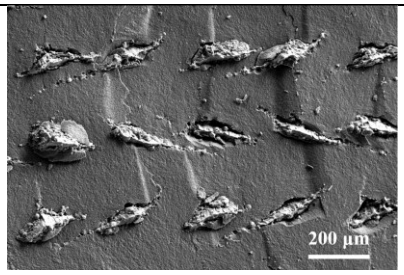
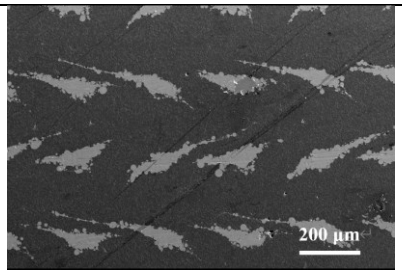
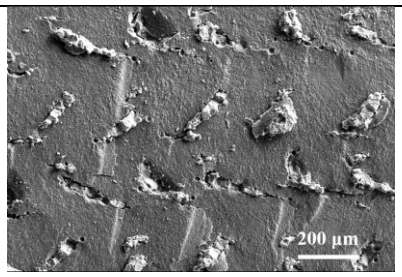
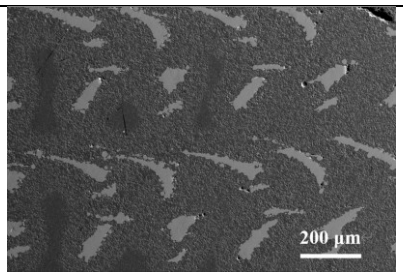
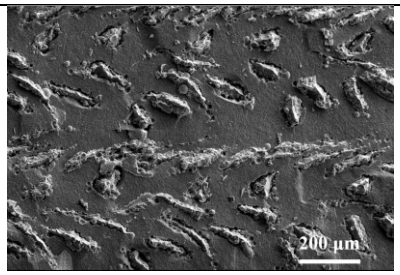
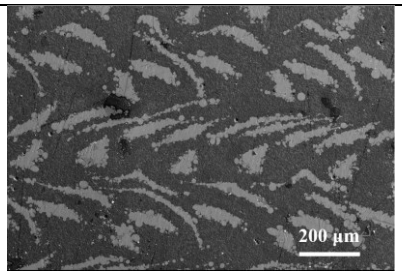
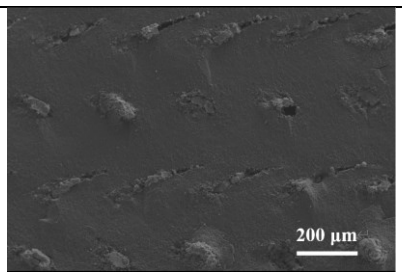
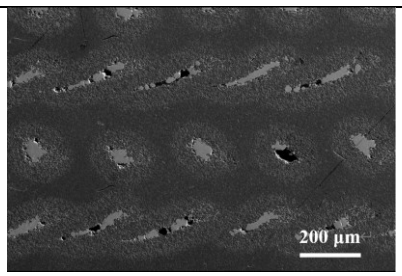
Sample	Fracture surface	Polished surface
Al_2O_3		
1-core without CIP		
1-core		
2-core		
3-core		
C-interface		

Figure 88. Unpolished and polished cross section of pure Al_2O_3 bars and core/shell bars.

Because the fibres are not circular in the bar shaped samples. Grid samples are prepared and the SEM graphs of the polished cross section of the grids are shown in Figure 89.

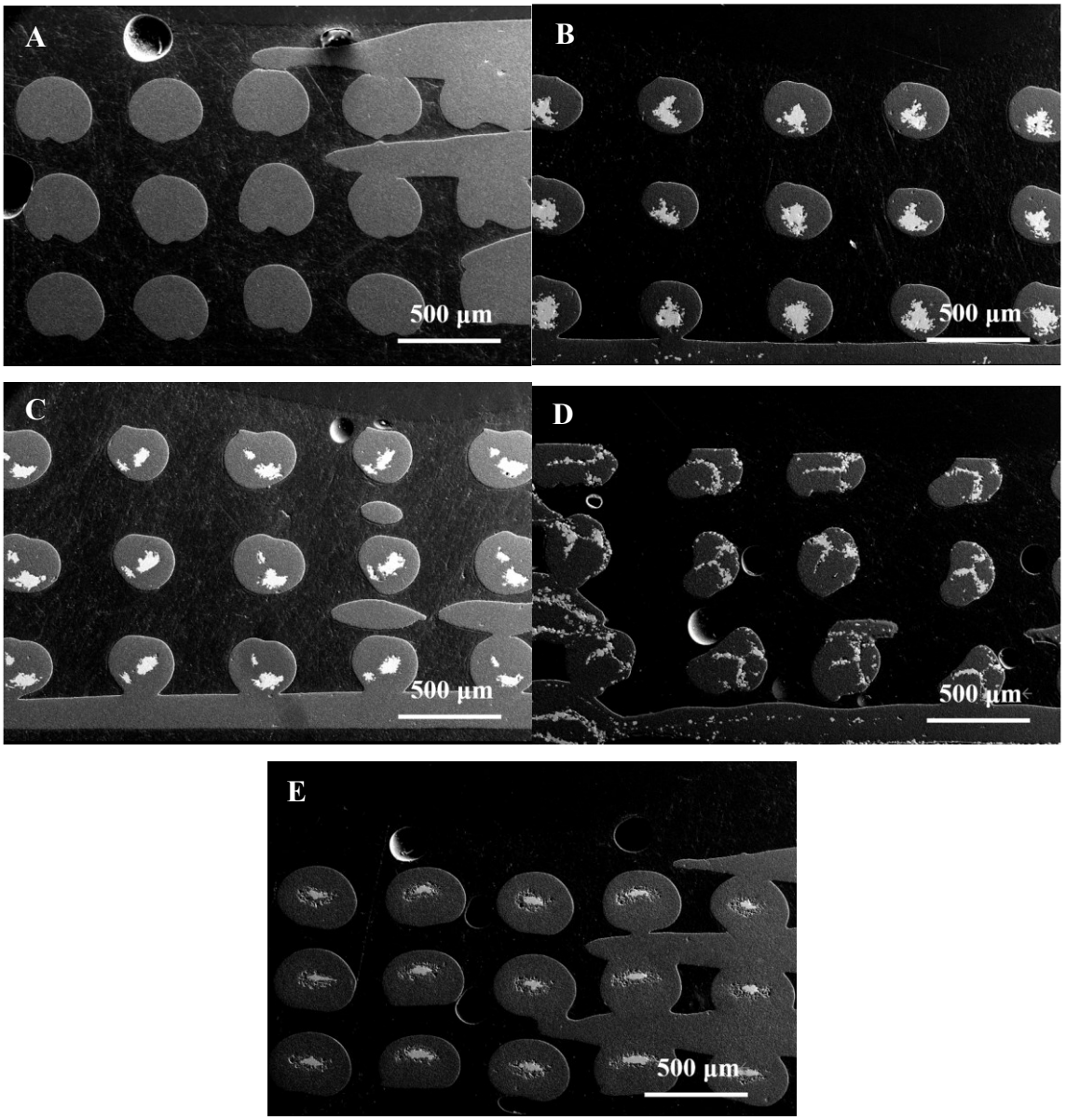


Figure 89. Polished cross section of grid samples: A) Al_2O_3; B) 1-core; C) 2-core; D) 3-core; E) C-interface.

As can be observed in Figure 89, all the sintered filaments have a diameter ~250 mm. The diameter of the steel fibres is of order of 100 mm for 1-core samples while for 2-core samples, one of the fibres is much thicker than the other (one is ~50 mm and another is ~20 mm). The shape of the steel fibres in 3-core sample is much less defined and there seems to be some merging. Similar as for the dense bars, the C-Al_2O_3 interfacial layer results in a porous interface ~50 mm thick. Comparing with the SEM figures of 1-core, 2-core and C-interface bars, the

cross sections of 1-core, 2-core and C-interface grids show that the steel fibres are rounder than those in the bar shaped samples.

5.2.2.3 Volume fraction of steel in the core/shell structure

The volume fraction of stainless steel in the samples were obtained by comparing the area of the Al_2O_3 and steel in the polished surface SEM figures using ImageJ (Figure 90). The value of the area (%) is recognised as the volume fraction of the steel in the samples. The volume fraction oscillates between 7 % for the porous interface sample and 15-22 % for the others.

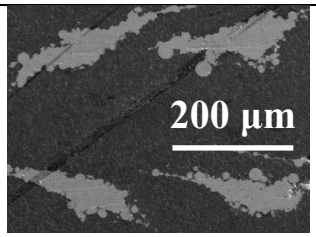
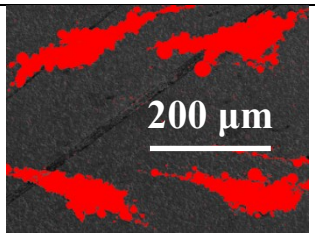
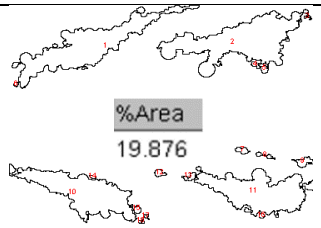
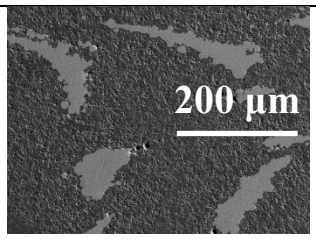
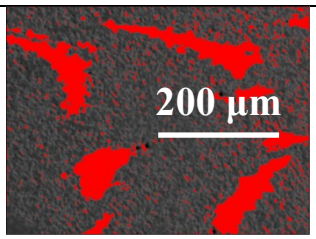
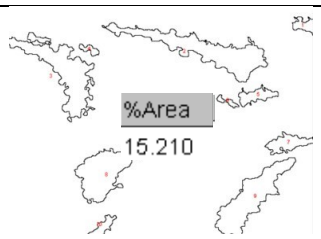
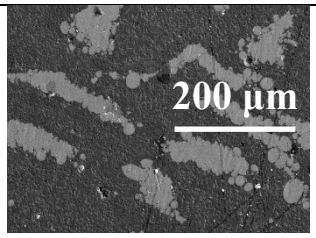
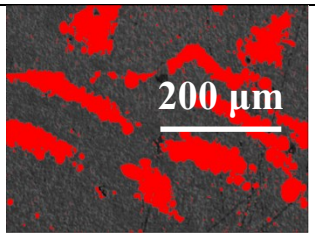
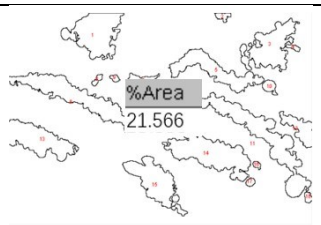
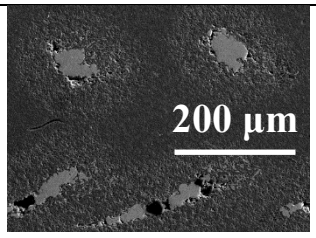
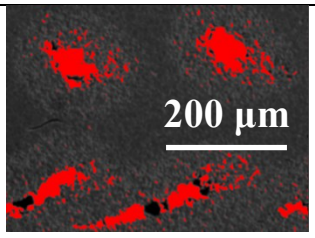
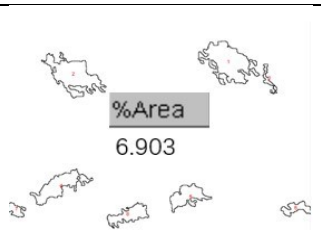
Sample	Original image	Threshold image	Area (%)
1-core			
2-core			
3-core			
C-interface			

Figure 90. Image J analyse of the volume fraction of the steel in the core/shell structure

5.2.2.4 Density and porosity

A theoretical Al_2O_3 and steel volume fraction is calculated using the dimensions of the syringe (diameter of 15.6 mm) and spacers (diameter of 4.5 and 8 mm) during the preparation of the printing cartridges. First, a theoretical steel volume fraction $(V_f^S)_{\text{theoretical}}$ of printed samples is calculated as:

$$(V_f^S)_{theoretical} = \frac{n\pi r^2 V_S}{(\pi R^2 - n\pi r^2)V_A + n\pi r^2 V_S} \tag{29}$$

where n is the number of cores, r is the radius of the spacer, R is the radius of the syringe, V_S is the volume fraction of steel in the ink (0.3) and V_A is the volume fraction of alumina in the ink (0.35). Then the theoretical Al_2O_3 volume fraction $(V_f^A)_{theoretical}$ can be calculated using:

$$(V_f^A)_{theoretical} = 1 - (V_f^S)_{theoretical} \tag{30}$$

The real Al_2O_3 volume fraction $(V_f^A)_{real}$ is calculated using the real steel volume fraction $(V_f^S)_{real}$ gained from the ImageJ analysis shown in Figure 90 (assuming the alumina matrix is dense):

$$(V_f^A)_{real} = 1 - (V_f^S)_{real} \tag{31}$$

The real density ρ_{real} of these samples were measured by the Archimedes method (Equation 6). The $\rho_{theoretical}$ of a dense core/shell sample was calculated using the equation:

$$\rho_{theoretical} = \rho_{steel}(V_f^S)_{theoretical} + \rho_{Al_2O_3}(V_f^A)_{theoretical} \tag{32}$$

where $\rho_{Al_2O_3}$ is the density of pure Al_2O_3 (3.97 g/cm^3), ρ_{steel} is the density of pure steel (7.75 g/cm^3).

The core size differentiation during printing and sintering can be described by a relationship between theoretical and real steel volume fraction:

$$Ratio = (V_f^S)_{theoretical}/(V_f^S)_{real} \tag{33}$$

The Al_2O_3 and steel theoretical and real volume fraction, density, porosity and the ratio of theoretical and real steel volume fraction of different samples were listed in Table 13. The porosity of the samples is calculated using equation 7.

Table 13. Al_2O_3 and steel volume fraction, density, ratio and porosity of different samples.

Sample	ρ_{real}(g/cm^3)	$\rho_{theoretical}$ (g/cm^3)	$(V_f^s)_{real}$	$(V_f^s)_{theoretical}$	Ratio	Porosity
Al_2O_3	3.67±0.05	3.97	-	-	-	7.6 %
1-core	4.48±0.07	4.85	0.199±0.015	0.234	1.176	7.6 %
2-core	4.27±0.06	4.52	0.142±0.012	0.146	1.028	5.5 %
3-core	4.63±0.07	4.81	0.216±0.017	0.222	1.027	3.7 %
C-interface	3.76±0.05	4.24	0.069±0.008	0.072	1.043	11.3 %

The porosity of the samples is about 4 to 8 % except for the C-Interface sample which has a higher porosity (~11 %) due to the porous interface. The Ratios of core-shell samples are close to 1 which means these samples do not have large core size differentiation.

5.2.2.5 Analysis of interface between the fibre and the alumina about the possible reactions

5.2.2.5.1 X-ray diffraction (XRD)

X-ray diffraction was done on powders obtained from the sintered samples after grinding with an agate mortar. The Al_2O_3 matrix was ground into fine powder but most of the steel fibres deform plastically and do not break (Figure 91).

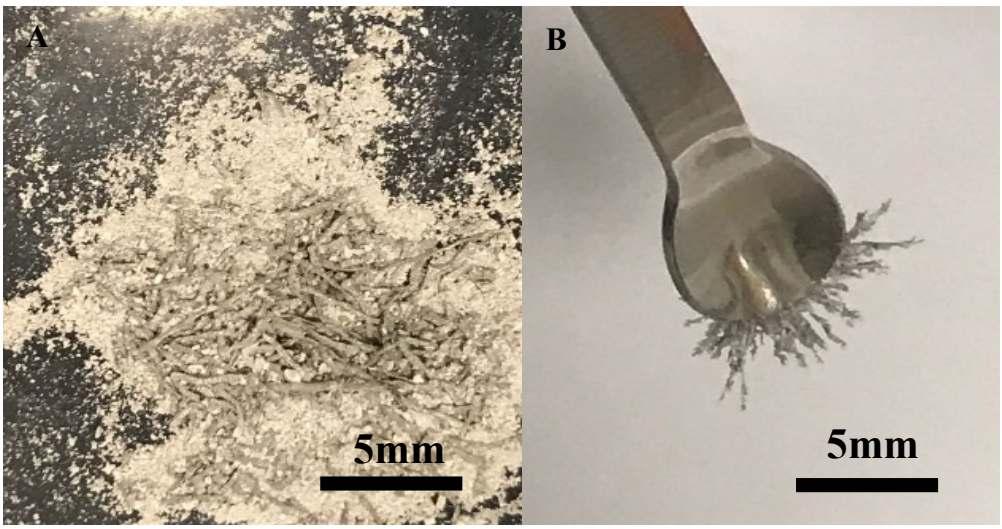


Figure 91. Photographs of A) ground 1 core sample; B) the steel fibres which can be separated using a magnet.

The measured XRD patterns are shown in Figure 92.

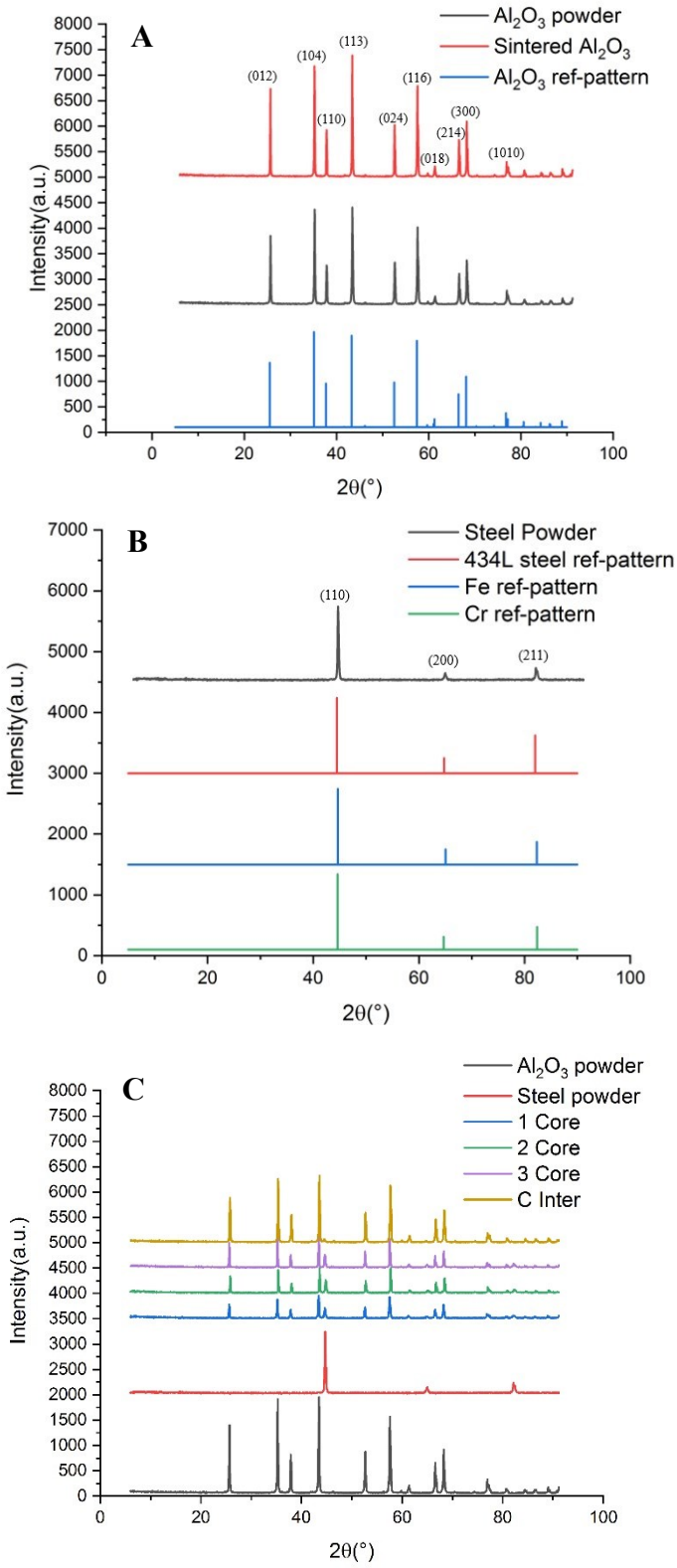


Figure 92. XRD pattern of A) Al_2O_3 matrix; B) Steel fibres; C) samples with different components.

5.2.2.5.2 SEM-EDS map results

The SEM-EDS map tests were done on the core/shell samples. The results are shown from Figure 93 to Figure 97.

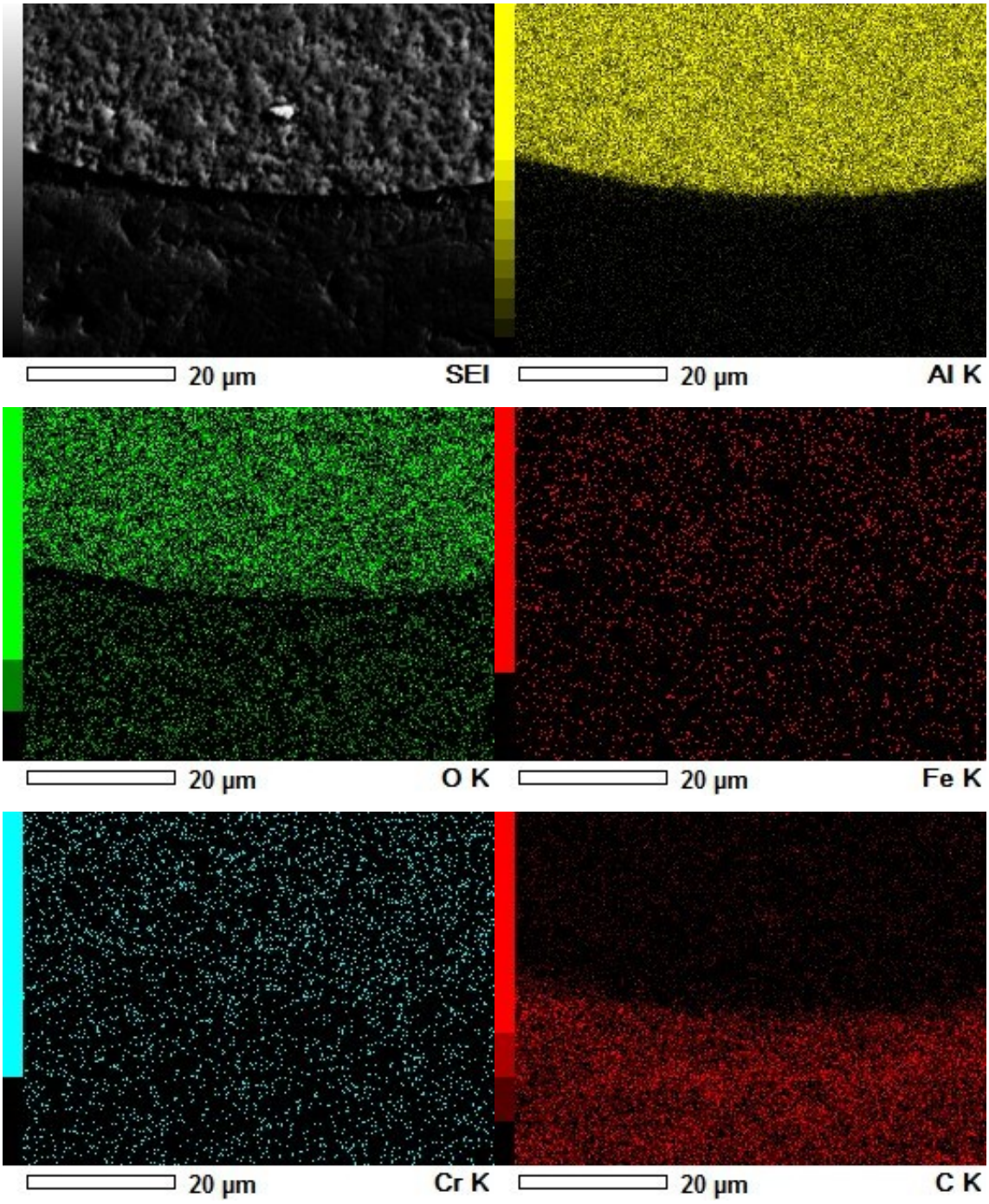


Figure 93. SEM-EDS map results of an Al_2O_3 grid sample (bottom part is epoxy resin).

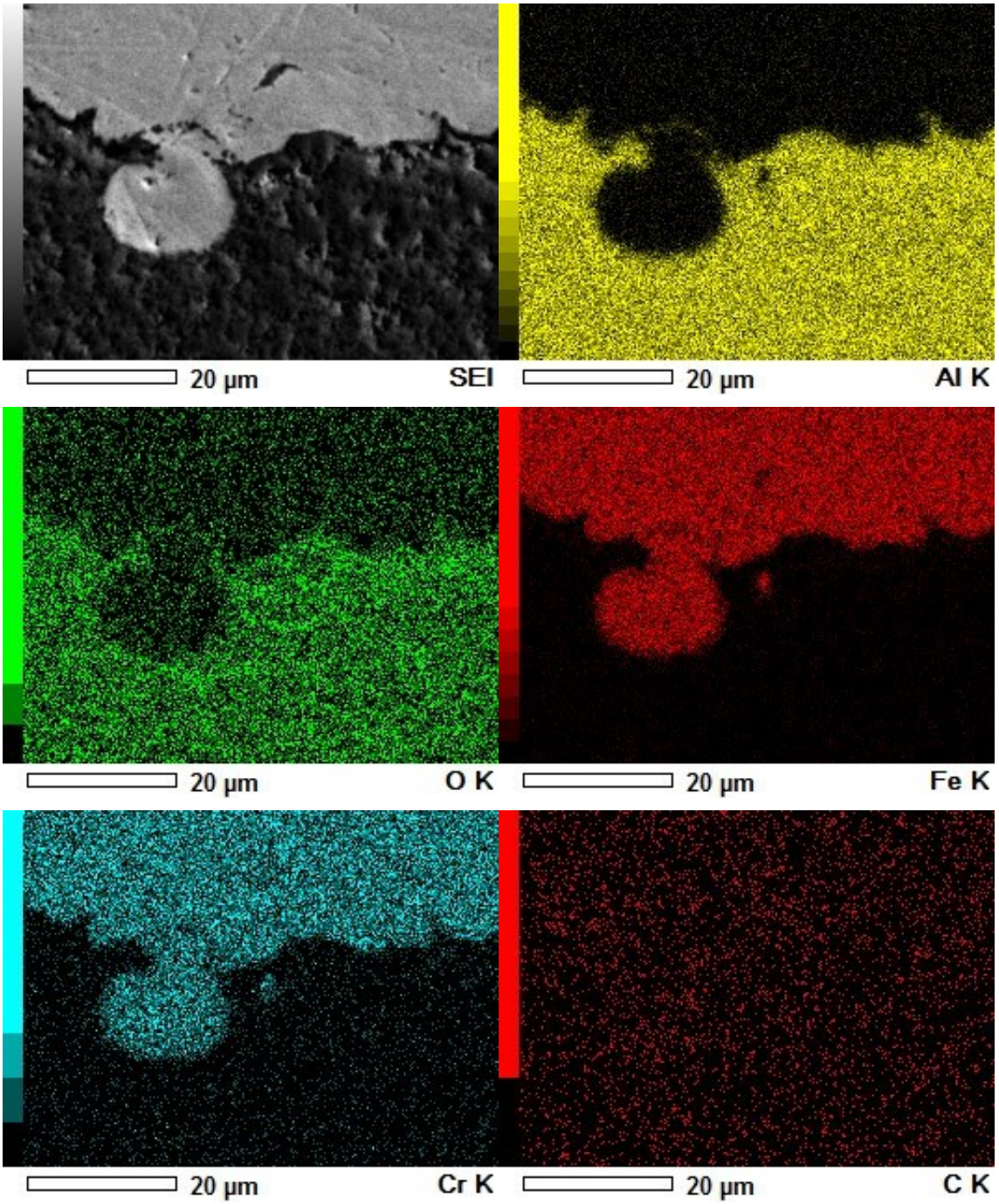


Figure 94. SEM-EDS map results of a 1-core grid sample.

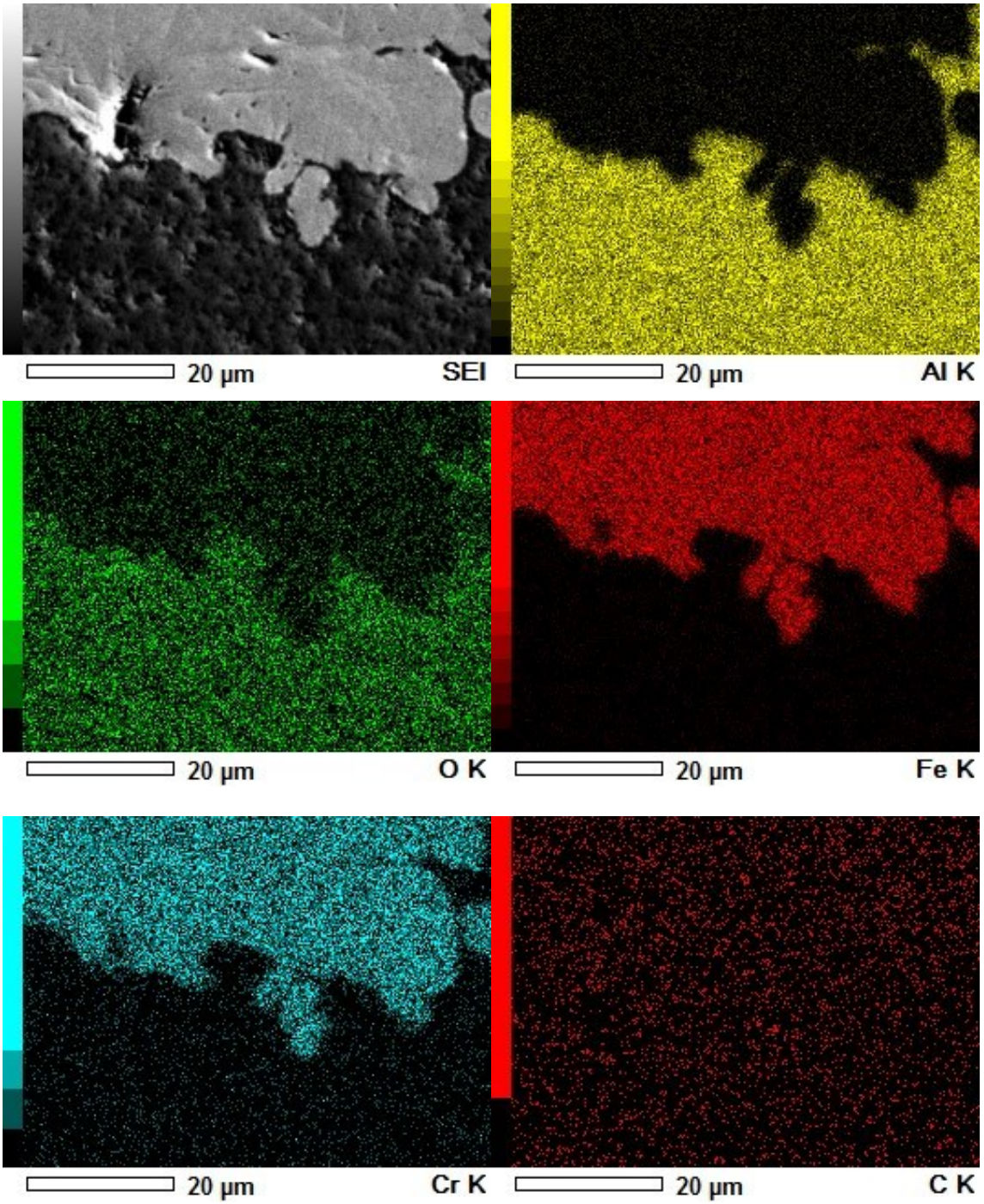


Figure 95. SEM-EDS map results of a 2-core grid sample.

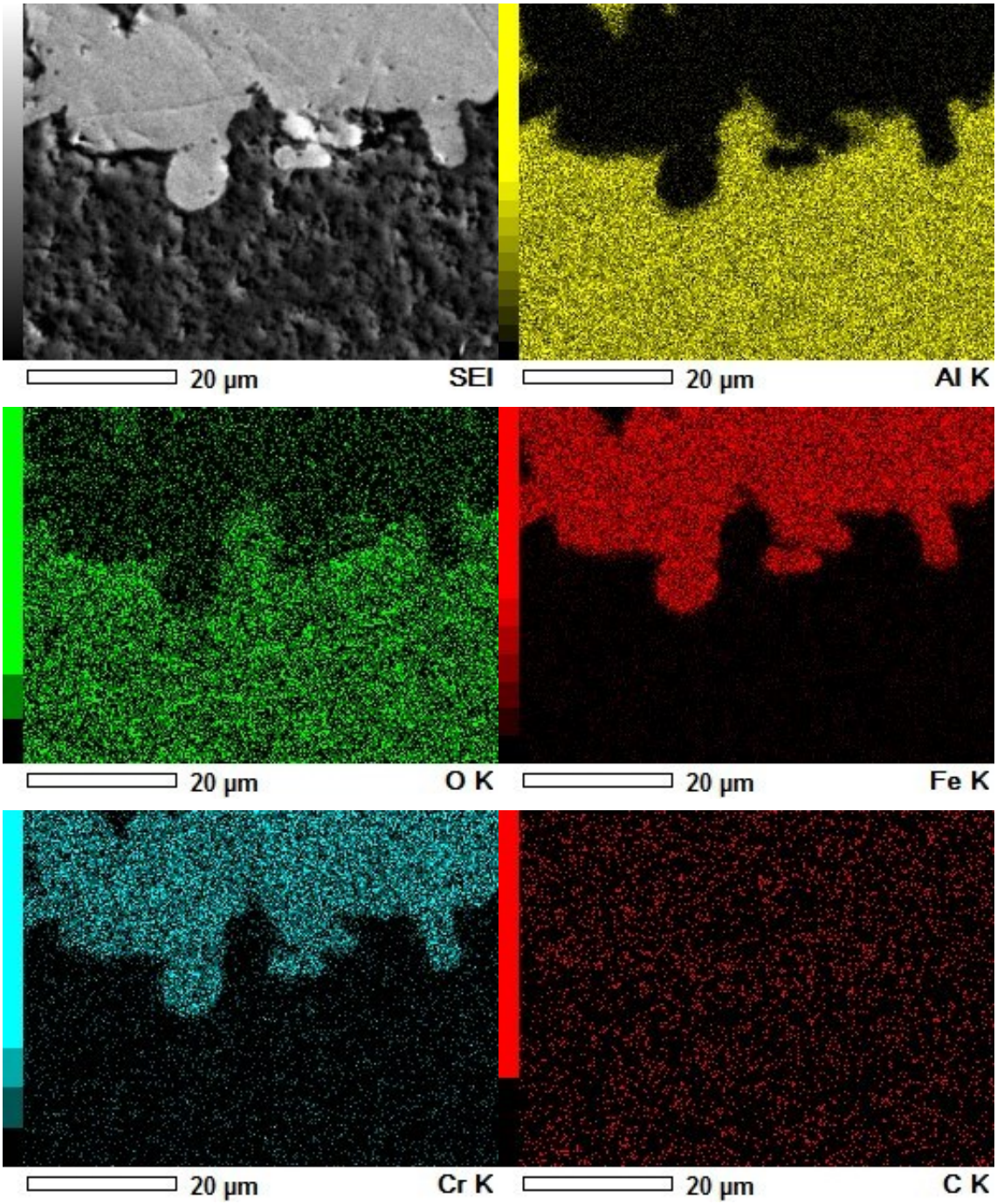


Figure 96. SEM-EDS map results of a 3-core grid sample.

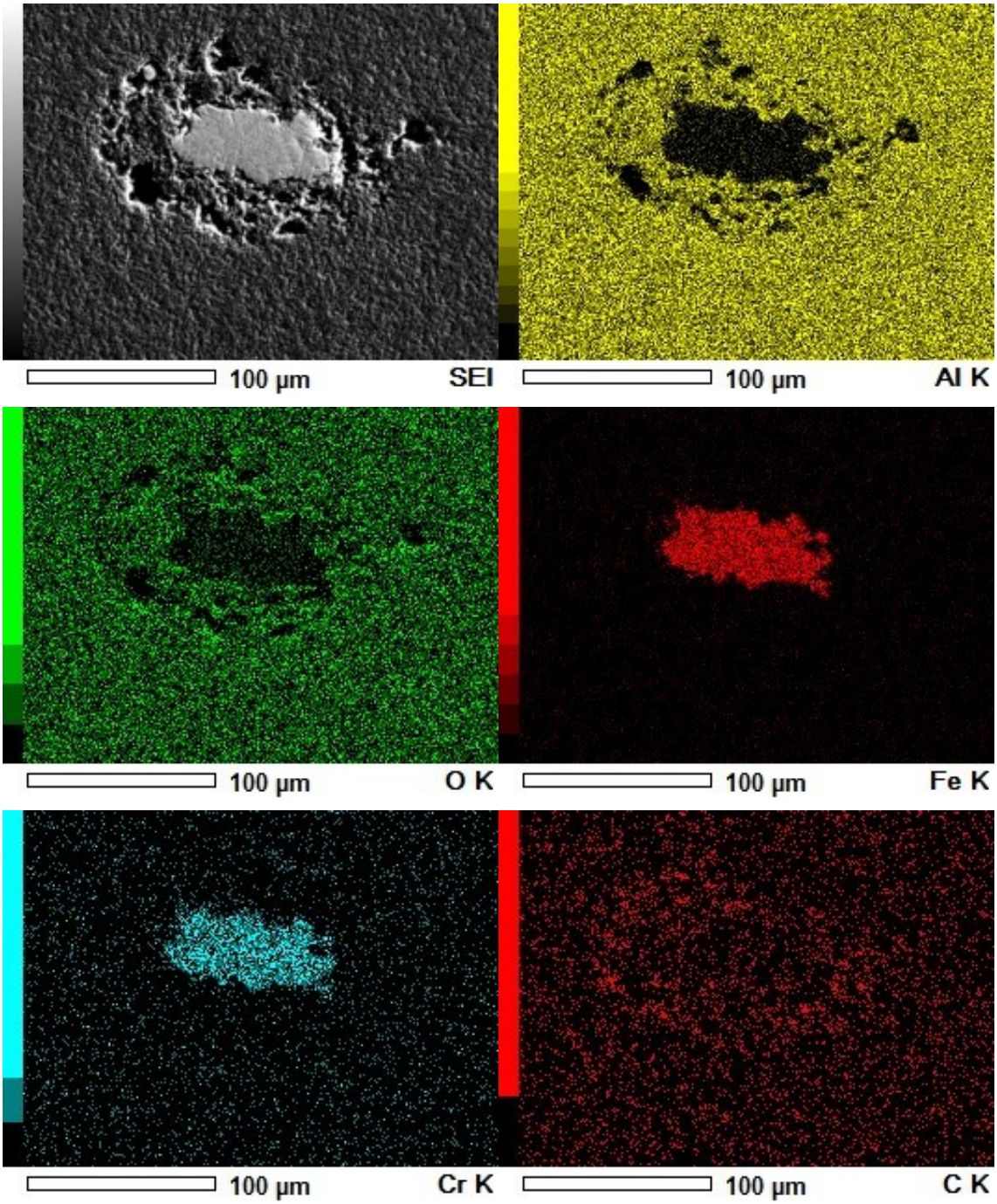


Figure 97. SEM-EDS map results of a C-interface grid sample.

It can be observed from the figures that there are no reactions at the interface, there is no mixing of the steel and alumina inks during extrusion, and the interfaces are rough at the microscopic scale.

The carbon shown in Figure 93 is because of the embedding (Epoxy resin). The carbon shown in Figure 94 to 96 may be some carbon residue from the Pluronic due to the firing in vacuum.

The carbon ring shown in Figure 97 may be the additional carbon residue from the graphite in the porous region after firing in vacuum.

5.2.3 Mechanical testing

Three specimens of each single filament sample were used to do the in-situ 3-point bending test. Each grid sample was undertaken compression test using 3 specimens. Each unnotched core/shell sample (polished or not polished) was undertaken 4-point bending test using 5 specimens. Three specimens of each notched sample were used to do the conventional 3-point bending test while another three specimens were used to do the in-situ 3-point bending test. Due to the hardness of preparing dog-bone shaped samples. Only one specimen of each dog-bone sample was used to do the tensile test.

5.2.3.1 Single fibre mechanical testing

In-situ three-point bending tests were done on single filament samples. The stress σ_f was calculated by equation

$$\sigma_f = \frac{FL}{\pi R^3} \tag{13}$$

where F is the applied force, L is the support span, R is the radius of the filament.

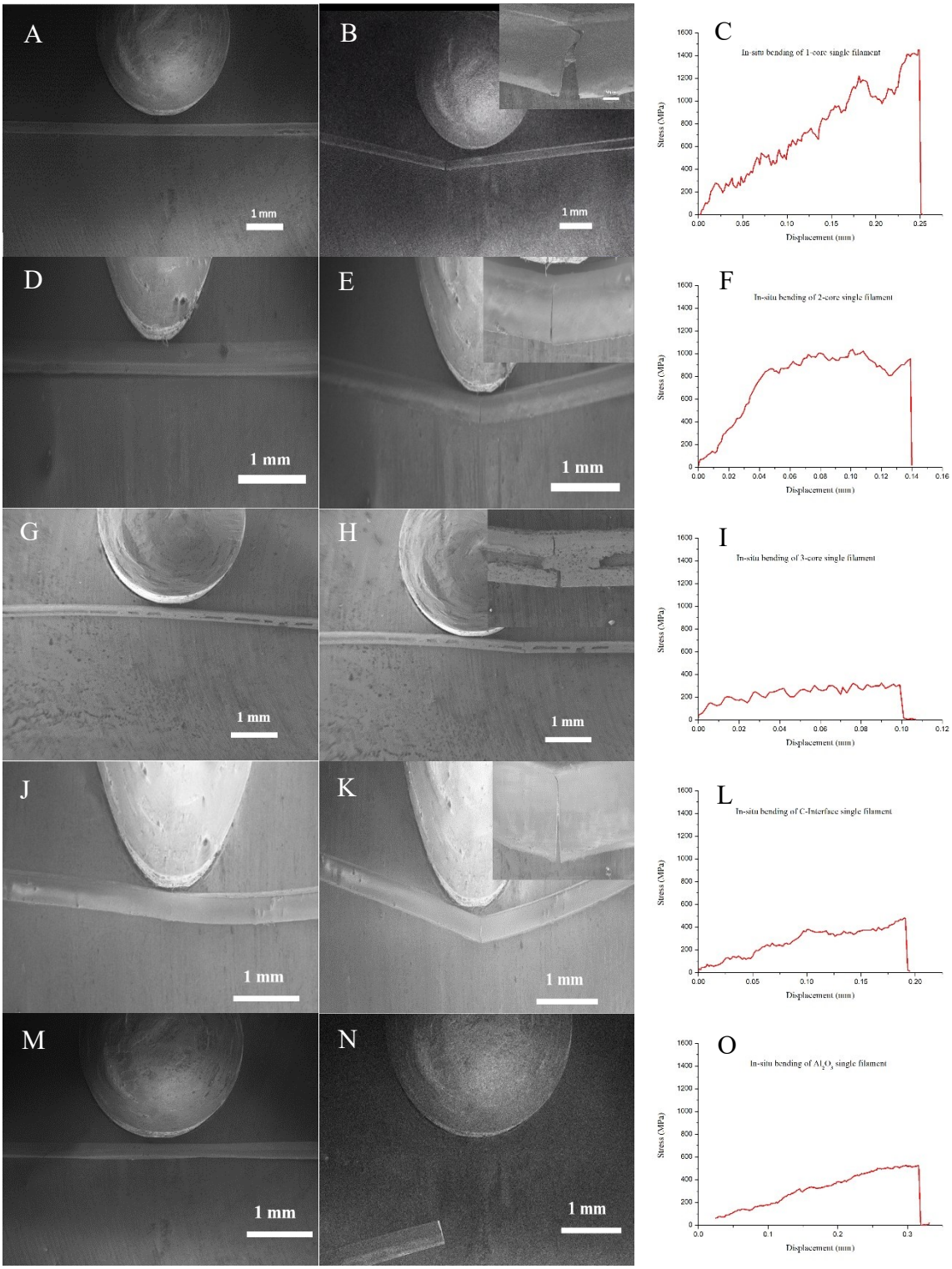


Figure 98. A-B) a 1-core single filament before and after bending test; C) Displacement-Stress curve of the 1-core single filament during bending; D-E) a 2-core single filament before and after bending test; F) Displacement-Stress curve of the 2-core single filament during bending; G-H) a 3-core single filament before and after bending test; I) Displacement-Stress curve of the 3-core single filament during bending; J-K) a C-interface single filament before and after bending test; L) Displacement-Stress curve of the C-interface single filament during bending; M-N) an Al_2O_3 single filament before and after bending test; O) Displacement-Stress curve of the Al_2O_3 single filament during bending.

Figure 98 shows the behaviour of the single filament before and after the bending test as well as the displacement-stress curve. The steel fibres inside core/shell single filaments deform but do not fracture, preventing the filaments from breaking into two separate parts when the ceramic shell breaks. The average strength of the samples gained from the displacement-stress curves is list in Table 14. 1-core and 2-core single filaments are stronger than pure Al_2O_3 single filaments, while 3-core and C-interface single filaments are weaker.

Table 14. Average strength of different single filaments

Sample	Average strength (MPa)
Al_2O_3	400±150
1-Core	850±350
2-Core	700±200
3-Core	300±100
C-Interface	300±100

5.2.3.2 Strength and fracture of grids

Grids were prepared for compression tests. Figure 99 gives a comparison between brittle samples (Al_2O_3) and tough samples (1-core). The stress-deformation curve is shown in Figure 100. The compressive stress σ_e was calculated by equation

$$\sigma_e = \frac{F}{A_0} \tag{12}$$

where F is the applied force and A_0 is the surface area of the top/bottom.

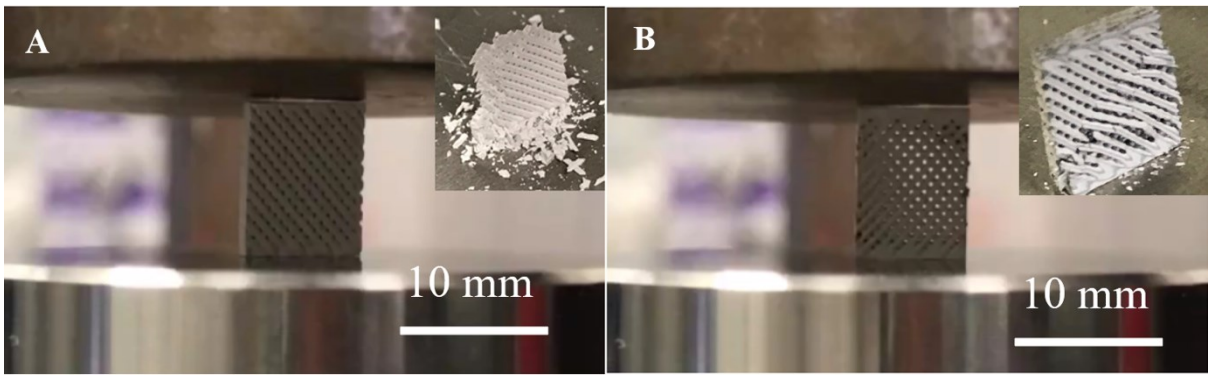


Figure 99. A) Compression test of an Al_2O_3 grid (breaking with steps); B) Compression test of a 1-core steel/Al_2O_3 grid (steel filaments hold the grid together by bending).

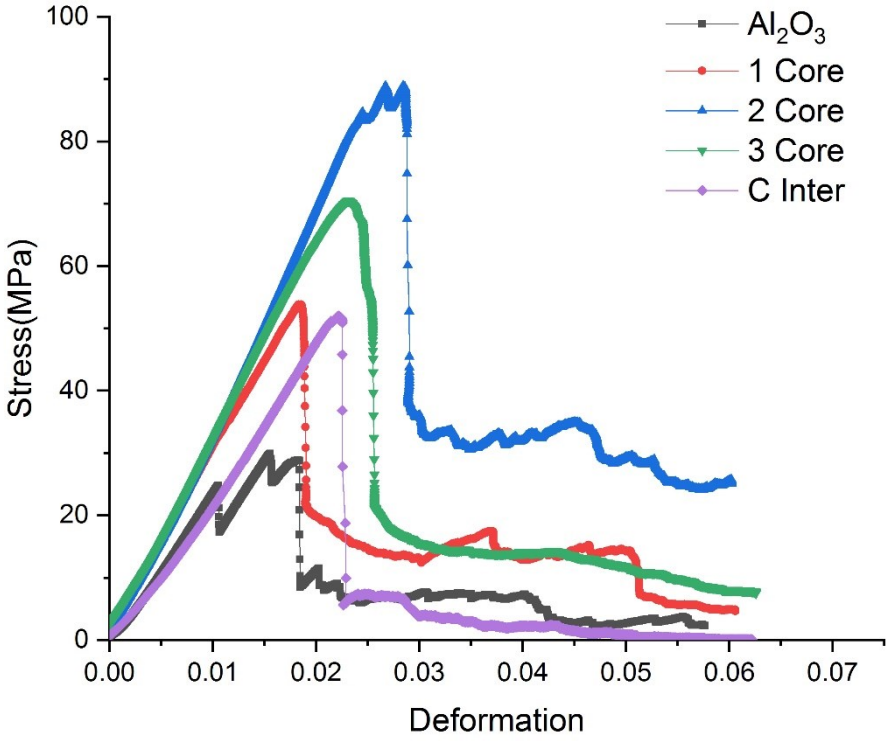


Figure 100. Deformation-stress curves of grids with different components.

The introduction of steel cores strengthens the samples. The Al_2O_3 ceramic gird breaks with steps that correspond to the individual brittle fracture of single struts. The grids made with steel cores fail by buckling of the struts and they are able to hold a residual load after failure (with the exception of the one with porous C interface). Within the number of samples tested, the results suggest that samples with 2 and 3 cores are stronger.

5.2.3.3 Strength of polished and un-polished bars

5.2.3.3.1 Four-point bending test of bar shaped samples

Strengths of bars with polished and unpolished tensile faces were measured by 4-point bending test (Figure 34 A). The support span was 20 mm, the loading span was 10 mm, the test speed was 0.2 mm/min. The equation for the flexural stress σ_f and the strain ε here are

$$\sigma_f = \frac{3F(L-L_l)}{2bd^2} \tag{9}$$

$$\varepsilon = \frac{48Dd}{11L^2} \tag{10}$$

where L is the support span, L_l is the loading span, F is the applied force, b is the width and d is the thickness. Figure 101 is the strain-stress curves of different polished and unpolished samples. The Al_2O_3 bar and the C Interface bar show brittle behaviour while other samples have a gradual failure that may indicate a relatively high toughness.

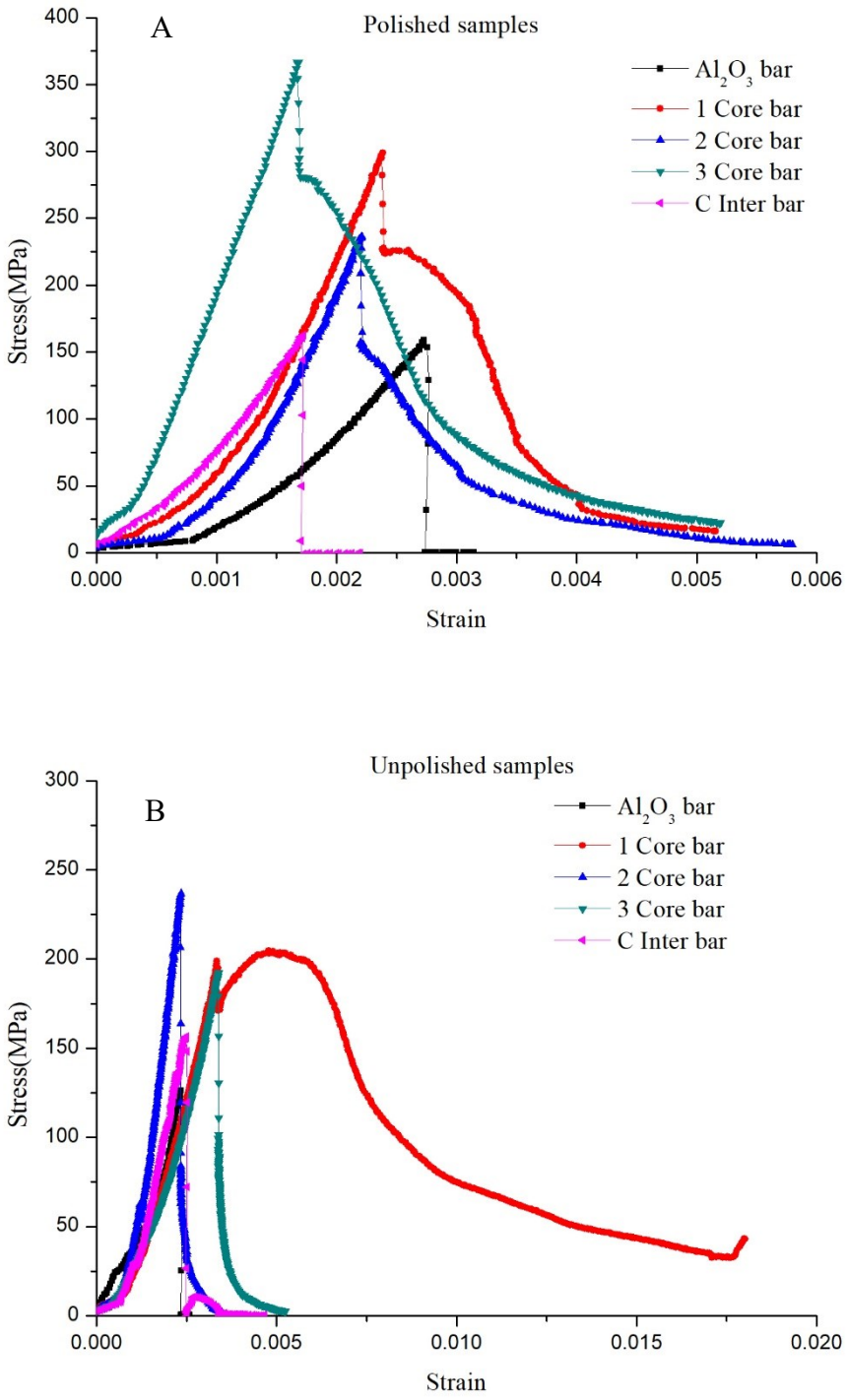


Figure 101. Strain-stress of A) polished and B) unpolished samples.

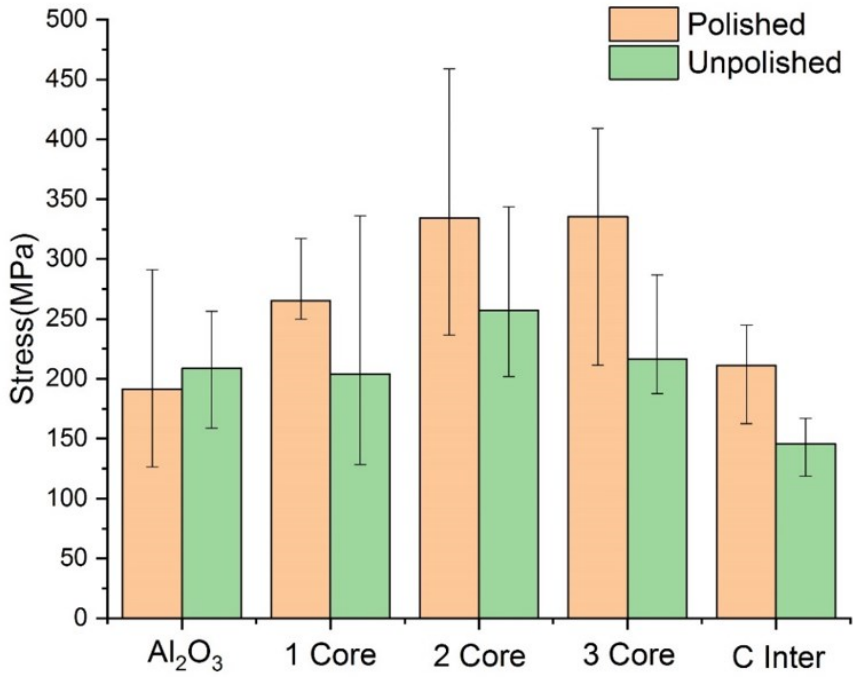


Figure 102. Strengths of different samples.

Figure 102 shows the average strengths of polished and unpolished samples. There is no statistically significant difference of the strengths between samples. The samples have average strengths ranging from 150 MPa to 350 MPa and all the samples have an overlap of the strengths considering the error bars. The polished samples are stronger than unpolished ones as there are few defects on the sample tensile surfaces after being polished.

5.2.3.3.2 Three-point bending test of SENB samples

The three-point bending tests were done on SENB samples with a support span of 15mm and a test speed of 5 μm/min. A Linear Variable Differential Transformer (LVDT) was used here to accurately measure displacement during the tests (Figure 34 B).

Continuous tests were done to compare the behaviours of different samples during bending. Because the samples are SENB samples instead of bars, the stress calculated here is not the real stress during bending but gives a reference value of the pressure applied on the sample during bending test. The equation 8 is used here to calculate the stress σ_f:

$$\sigma_f = \frac{3FL}{2bd^2} \tag{8}$$

where F is the applied force, L is the support span, b is the width, d is the thickness of the rectangular cross section.

Figure 103 A shows the relationship between the force and the displacement measured by LVDT and Figure 103 B gives the stress-strain curve of the samples. The strain ε is calculated using the equation

$$\varepsilon = \frac{6Dd}{L^2} \tag{11}$$

Where D is the displacement, d is the sample thickness and L is the support span.

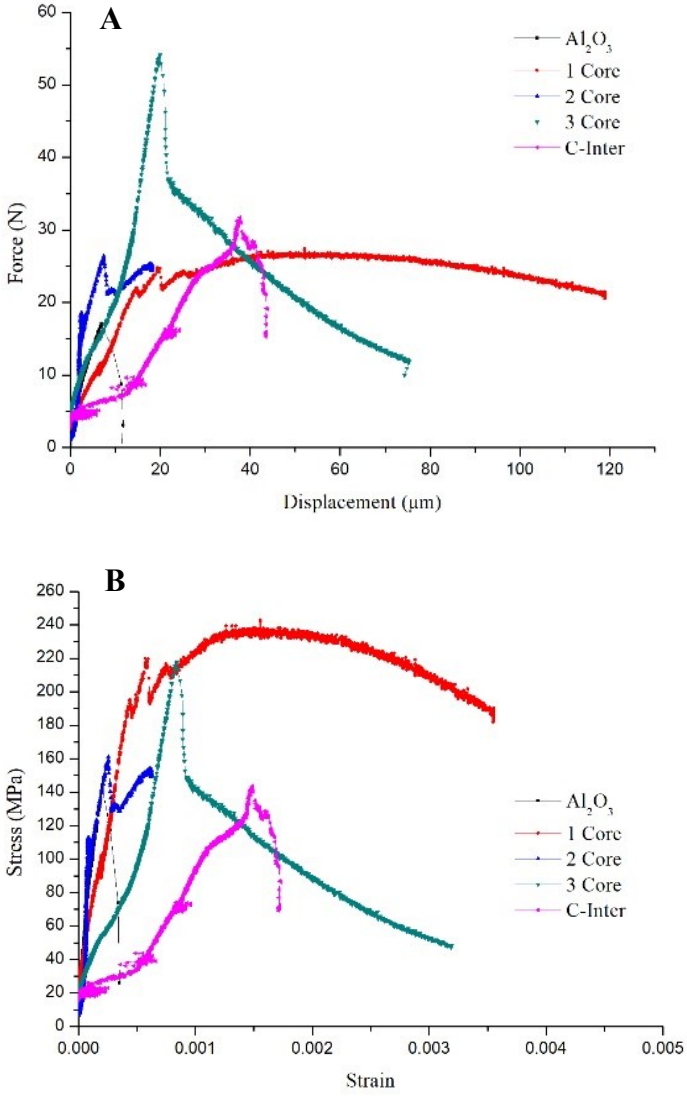


Figure 103. A) continuous Displacement-force curves of SENB samples; B) Continuous Strain-stress curves of SENB samples.

Similar to four point bending, the Al_2O_3 sample and the C Interface sample are brittle during bending while other samples show non-fragile behaviour.

In-situ three-point bending tests were also done under SEM using SENB samples. The test speed was set at 0.1 mm/min (Figure 104).

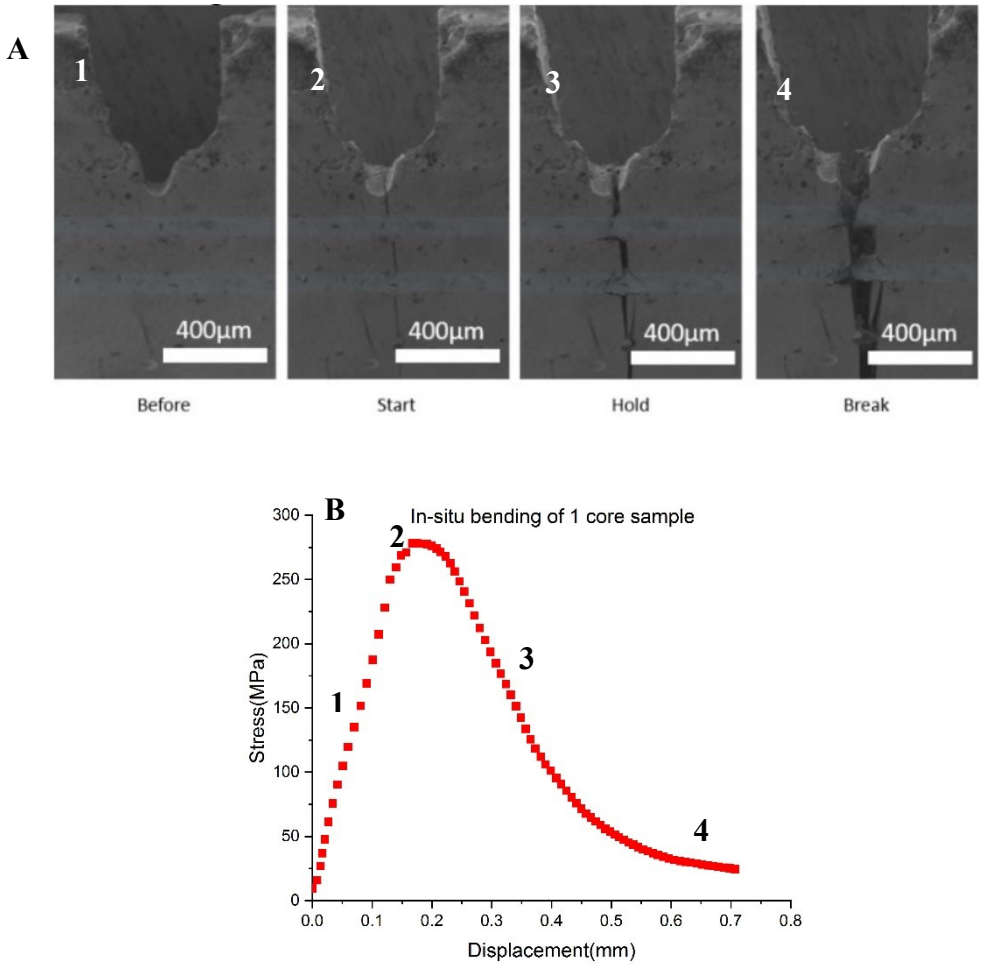


Figure 104. A) SEM graphs of a 1 core SENB bar under in-situ bending test; B) Displacement-stress curve of the 1 core sample during the bending

The tests illustrate how the steel fibres work during bending. First, the matrix cracks but these cracks may be bridged by the metallic fibres as the stress go on increasing after the first crack. When the force increases, the crack grows and the steel fibres start to deform plastically. Finally, the steel fibres break as well.

5.2.3.4 In-situ Tensile test of dog-bone samples

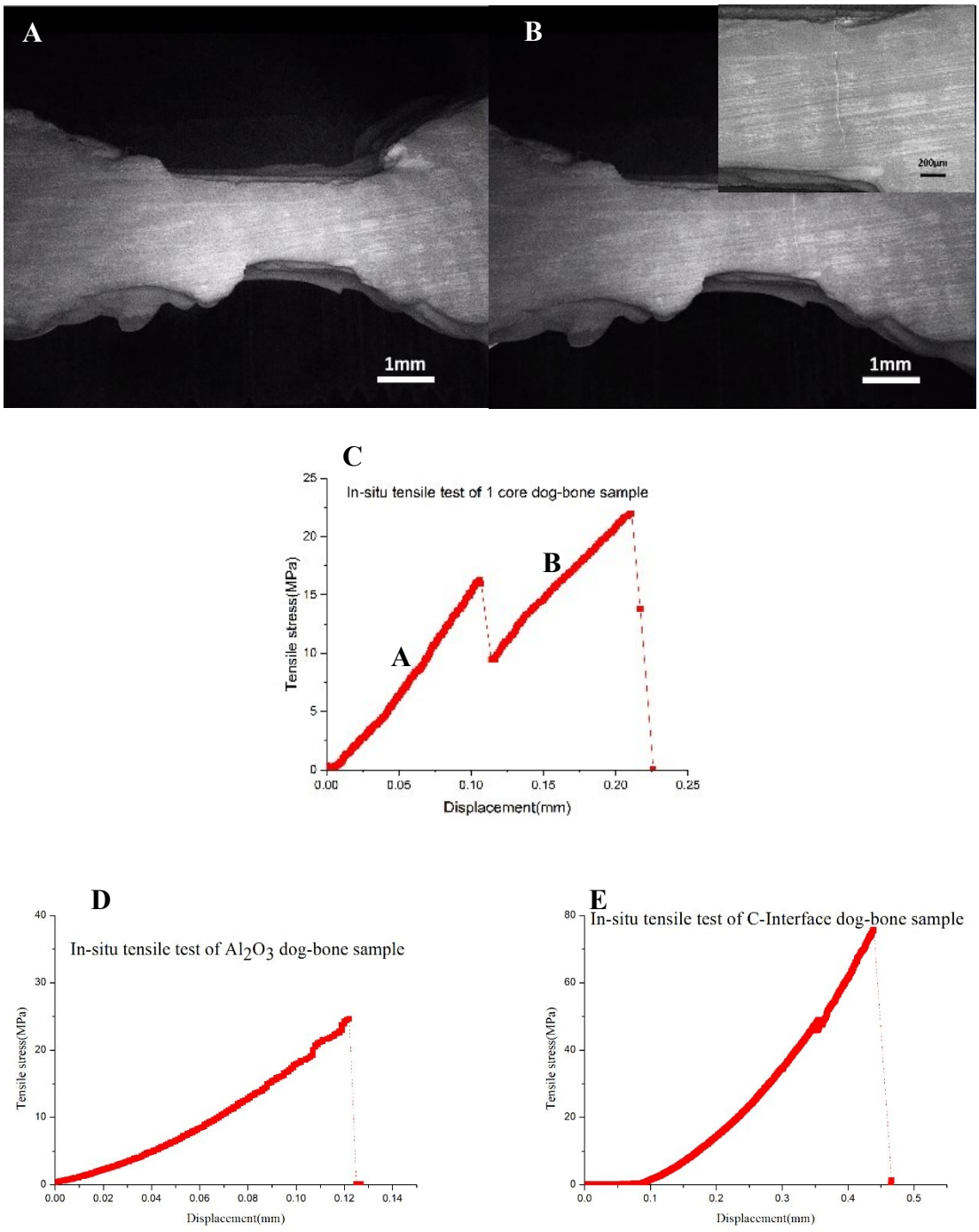


Figure 105. A) Before cracking; B) after cracking; C) Displacement-Stress curve of a 1 core dog-bone sample; D) Displacement-Stress curve of an Al_2O_3 dog-bone sample; E) Displacement-Stress curve of a C-Interface dog-bone sample.

In-situ tensile test were conducted using dog-bone samples (Al_2O_3, 1-core and C-interface). Both Al_2O_3 and C-Interface samples were brittle and they break suddenly after the tensile stress reaches to the highest point. For the 1-core sample (Figure 105 A, B and C), first, there is a

drop in load as a crack form in the matrix but the sample still did not break in two. Instead, the stress decreased a bit after cracking but it went on to increase as the displacement increased. Finally, the part breaks like a brittle sample. The tensile stress σ_b was calculated by equation

$$\sigma_b = \frac{F}{S_0} \tag{14}$$

where F is the applied force and S_0 is the area of the rectangular cross section. The tensile strength of alumina and core/shell composites are shown in Table 15.

Table 15. Tensile strength of dog-bone samples.

Sample	Tensile strength
Alumina	25 MPa
1-core sample	22 MPa
C-Inter sample	75 MPa

5.2.3.5 Fracture toughness (K_{IC})

The fracture toughness(K_{IC}) of the SENB samples were also calculated using equation[93]

$$K_{IC} = \frac{3PS}{2BW^{\frac{3}{2}}} * \left(\frac{a}{W}\right)^{\frac{1}{2}} * \frac{1.99-\frac{a}{W}*(1-\frac{a}{W})(2.15-3.93\frac{a}{W}+2.7(\frac{a}{W})^2)}{(1+2\frac{a}{W})(1-\frac{a}{W})^{3/2}} \tag{34}$$

where P is the applied load, S is the span, B is the width of the specimen, W is the thickness of the specimen, α is the crack length. The applied loads used to calculate the K_{IC} are the forces in Figure 103 A at which the slope of the displacement force curve stops being linear. It can be observed that adding of the steel long fibres in the alumina matrix increases the fracture toughness of the materials (Figure 106).

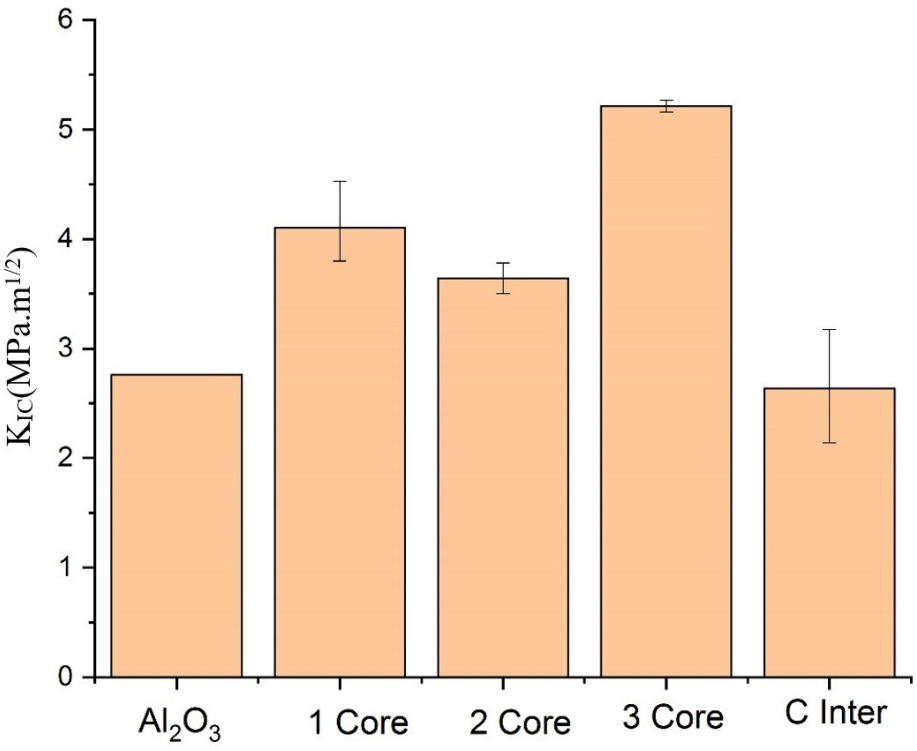


Figure 106. K_{IC} of different SENB samples

5.2.3.6 Work of fracture

Fracture energy, also known as work of fracture γ_{WOF} was caluclated by the equation

$$\gamma_{WOF} = \frac{W}{2A_{CS}} \tag{35}$$

where W is the total energy input of the fracture process, A_{CS} is the area of the fracture surface. The energy input is calculated by the equation

$$W = \int P d\delta \tag{36}$$

where P is the applied load and the $d\delta$ is the change of the displacement of the sample (Figure 107). The value of the W is the area below the load-displacement curve.[94]

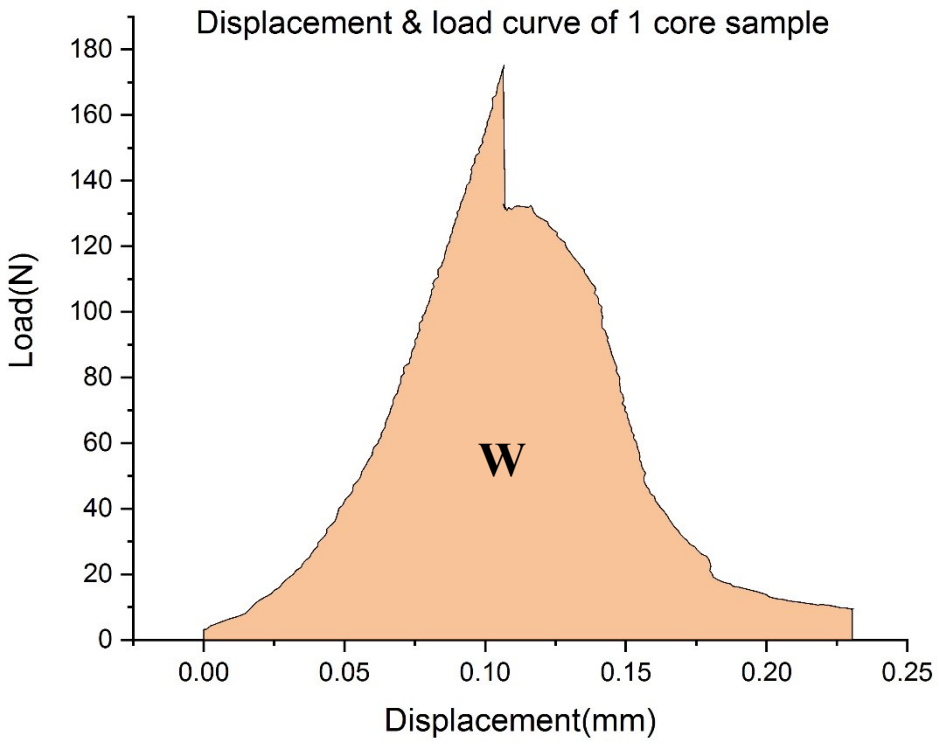


Figure 107. The displacement-load curve which gives the energy input during fracture process of a 1-core bar sample.

Works of fracture of the SENB samples were calculated by equations 34 & 35. The results are shown in Figure 108. In principle, the work of fracture can not be measured on brittle samples (Al_2O_3 and C Interface). For these samples, the area under the displacement-load curves is an upper limit for the work of fracture (the real work of fracture should be lower than the area).[95] 1-core and 3-core samples have similar works of fracture around 1500 J/m^2 while samples with 2 cores have lower work of fracture about 800 J/m^2.

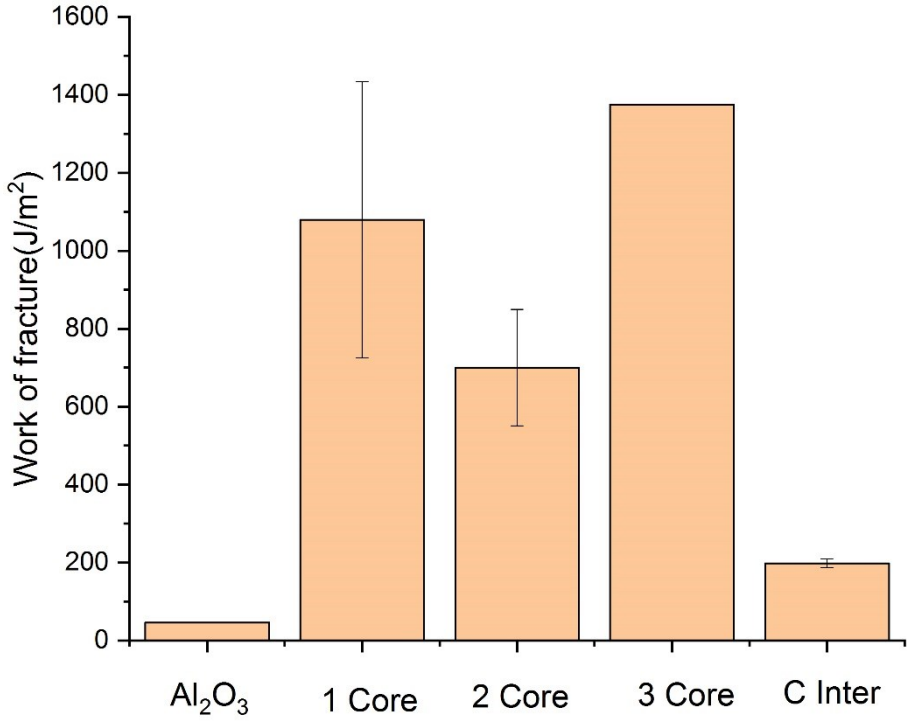


Figure 108. Work of fracture of different SENB samples.

For comparison, we have calculated works of fracture in unnotched polished and unpolished samples (Figure 109). The upper limit of work of fracture for Al_2O_3 samples and the C Interface samples is around 500 J/m^2. 2-core samples have an average work of fracture about 800 J/m^2. 1-core and 3-core samples have similar work of fracture around 1200 J/m^2 among which the highest one reaches to 2000 J/m^2.

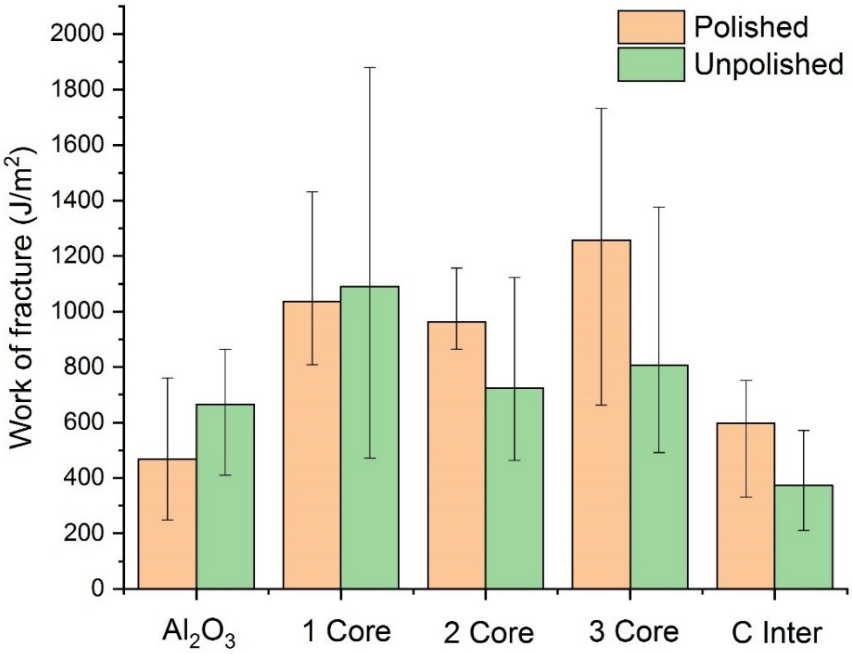


Figure 109. Work of fracture of different samples.

5.2.3.7 Cyclic three-point bending tests

Cyclic three-point bending tests were done on SENB samples as well (except Al_2O_3 samples which are brittle). This kind of test was operated by loading-unloading cycles during the bending period. Figure 110 gives an example of how the stress-displacement (measured with a LVDT) curves and strain-stress curves look like during the cyclic tests.

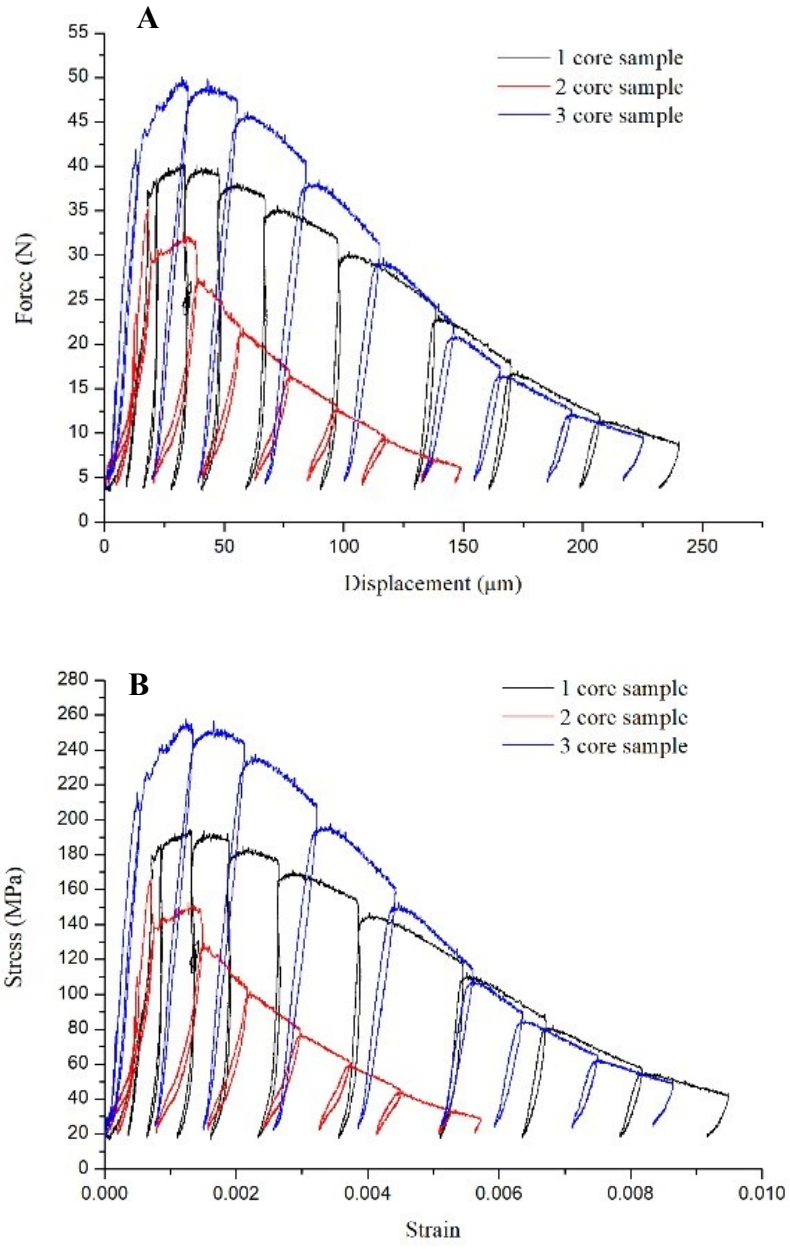


Figure 110. A) Cyclic Displacement-force curves of SENB samples; B) Cyclic Strain-stress curves of SENB samples

The slopes of stress-strain curves were calculated to estimate the elastic-plastic behaviour of the samples during bending. The C-Interface samples broke directly so the cyclic test could not be performed with these samples.

The slopes of the samples are shown in Figure 111 for displacement-force curves and strain-stress curves separately. From these figures, the slope decreases noticeably with the increasing number of cycles. The slope of loading is a bit larger than unloading during the same cycle.

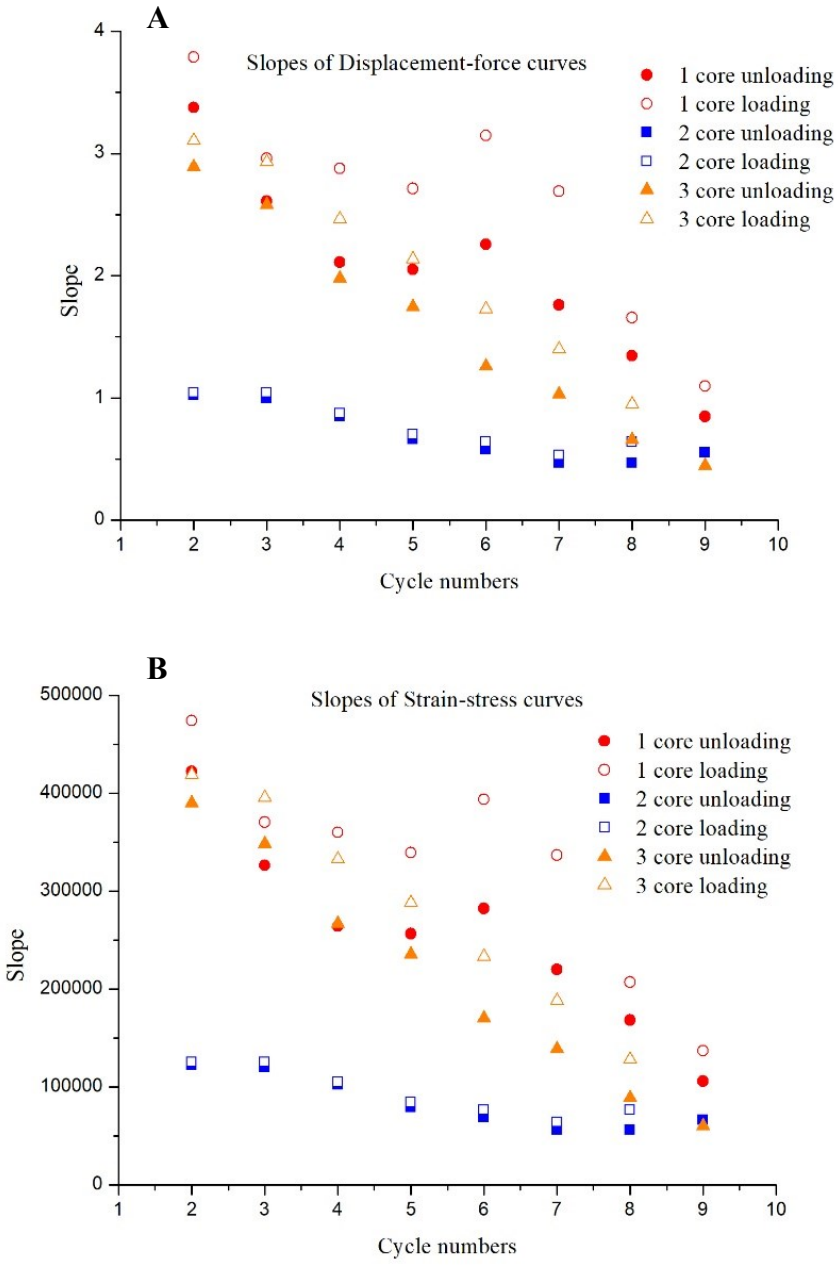


Figure 111. A) Slopes of Displacement-force curves of SENB samples; B) Slopes of Strain-stress curves of SENB samples.

5.3 Discussion

5.3.1 Factors that affect the liquid-gel transition

Figure 112 summarizes the liquid-gel transition temperature of solutions with different Pluronic concentration. The copolymers (PEO-PPO-PEO) exist as molecules when the temperature or the Pluronic concentration is low which makes the solution a liquid-like behaviour. However, a liquid-gel transition occurs when the temperature or Pluronic concentration keep increasing and thermodynamically stable micelles are formed which results in an increase viscosity. The polarity of ethylene oxide (EO) and propylene oxide (PO) segments decreases with the increasing of temperature which leads to the micellization process. Hence, the PPO content affects the critical micellization temperature: a higher PPO content makes the micellization temperature lower.[29]

Figure 68 shows that the solid loading of the paste does not influence significantly the liquid-gel transformation temperature (The liquid-gel transformation occurs from 17 to 23 ℃). In hydrogel pastes prepared with Pluronic solutions, the majority of the strength come from the hydrogel, not the ceramic particles. [20] The copolymers simply act as carriers of ceramic particles so the liquid-gel transition temperature is mainly determined by the Pluronic concentration and the solid loading does not has obvious effects on the liquid-gel temperature. However, increasing of the solid loading increases the viscosity of the pastes as expected.

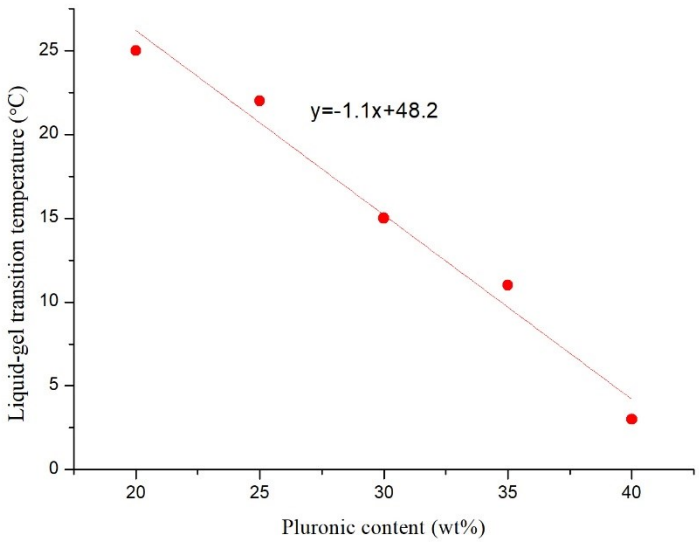


Figure 112. Liquid-gel transition temperature of solutions with different Pluronic concentration (the empirical liner fitting is valid from 20 to 40 wt%).

5.3.2 Rheological property of different inks.

Table 16 summarizes the rheological properties of the hydrogel inks used in this work. The maximum span that can be printed in a grid without deformation is calculated using the storage modulus as described in equation 16 ($L \leq \sqrt[4]{G'D^3/1.4\rho g}$). The maximum height that can be printed with these inks is calculated using equation 19 ($h_{max} = \sigma_y^{Dyn}/\rho g$). All these inks can be printed individually. The shear thinning coefficient (n) is between 0.2 and 0.45, viscosity parameter (K) is from 100 to 1350 Pa.s^n which is mainly depended on the solid loading. These inks have a flow point ranging from 350 (250 for pure Pluronic solution, 100 for 25 vol% Fe_2O_3 ink) to 1000 Pa and the equilibrium storage modulus is from 17000 (13000 Pa for pure Pluronic solution, 11000 Pa for 25 vol% Fe_2O_3 ink) to 30000 Pa.

One important point is that the steel inks are stable. Despite the high density of the steel and the relatively large particle size, these inks do not sediment. This may be an advantage of the hydrogel inks *vs.* colloidal inks as the particles are immersed in a hydrogel but the colloidal inks are based on the interactions of the particles in water where some degree of sedimentation can occur.

Comparing with other inks for robocasting shown in Table 2, the inks used here has a similar n and K as hydrogel inks reported by Feilden[20], but the n is much smaller and K is much higher than that of the colloidal ink (using lead zirconate titanate) reported by Smay[13]. The flow point of the hydrogel inks in this work is similar as other reported hydrogel inks but the equilibrium storage modulus is somewhat smaller maybe because of the usage of Dolapix as dispersant that will reduce particle aggregation. The printing viscosities of these inks are similar as those reported for other robocasting inks.[11-13, 16, 17, 19, 20, 28, 44, 45]

Table 16. Rheology of hydrogels used in this work (25 wt% Pluronic at 25 ℃).

Powder	Solid loading	Shear thinning coefficient (n)	Viscosity parameter (K)	Flow point (τ_{fp})	Equilibrium storage Modulus (G'_{eq})	Viscosity at 35 s^{-1}	Maximum span in a grid	Maximum height
no[20]	0	0.22	550 $Pa.s^n$	250 Pa	1.3×10^4 Pa	5 Pa.s	2.84 mm	25.5 mm
Al_2O_3	30	0.37	147 $Pa.s^n$	350 Pa	1.7×10^4 Pa	20 Pa.s	2.59 mm	18.9 mm
	35	0.2	473 $Pa.s^n$	450 Pa	2×10^4 Pa	40 Pa.s	2.65 mm	22.5 mm
	40	0.24	898 $Pa.s^n$	700 Pa	2.3×10^4 Pa	100 Pa.s	2.70 mm	32.6 mm
	45	0.2	1350 $Pa.s^n$	1000 Pa	3×10^4 Pa	120 Pa.s	2.83 mm	43.7 mm
C-Al_2O_3	35	0.2	469 $Pa.s^n$	450 Pa	2.4×10^4 Pa	600 Pa.s	2.80 mm	23.2 mm
Fe_2O_3	25	0.29	97 $Pa.s^n$	100 Pa	1.1×10^4 Pa	10 Pa.s	2.28 mm	4.9 mm
	35	0.22	780 $Pa.s^n$	400 Pa	2.5×10^4 Pa	100 Pa.s	2.67 mm	16.4 mm
Iron	35	0.44	279 $Pa.s^n$	350 Pa	2.4×10^4 Pa	550 Pa.s	2.44 mm	10.6 mm
Steel	30	0.35	106 $Pa.s^n$	450 Pa	2×10^4 Pa	50 Pa.s	2.40 mm	15.2 mm
	35	0.44	392 $Pa.s^n$	600 Pa	3×10^4 Pa	60 Pa.s	2.59 mm	18.2 mm

As the Pluronic concentration used for all inks is the same (25 wt%), the Pluronic is mostly used to dictate the transition temperature.

As expected, the solid loading has strong influence on the rheology. Take the alumina inks with different solid loading for an example, the viscosity, flow point and equilibrium storage modulus increase with the increasing of alumina concentration. For the alumina inks, the shear thinning coefficient is more or less constant (~0.2) except for the ink with lower solid content. One possible reason is that when the solid concentration starts to go down, the suspension becomes more 'Newtonian'. As steel and iron powders are rounder than alumina powders and round shape could facilitate flow[78], the steel and iron inks have higher n than alumina inks (more Newtonian).

5.3.3 Printability of the hydrogel inks

The printability of the inks is analysed using Chan's criterion ($G' = C_1/\tau_{fp}$, C_1 is a constant ~5×10^6) using the relationship between storage modulus and yield stress.[85] Figure 113 shows the plot of all the hydrogel inks in this work. Most inks follow this criterion which means these

inks are printable in principle. The pure 25 wt% Pluronic solution and 25 vol% Fe_2O_3 ink do not follow the criterion which means that it may not be able to be printed.

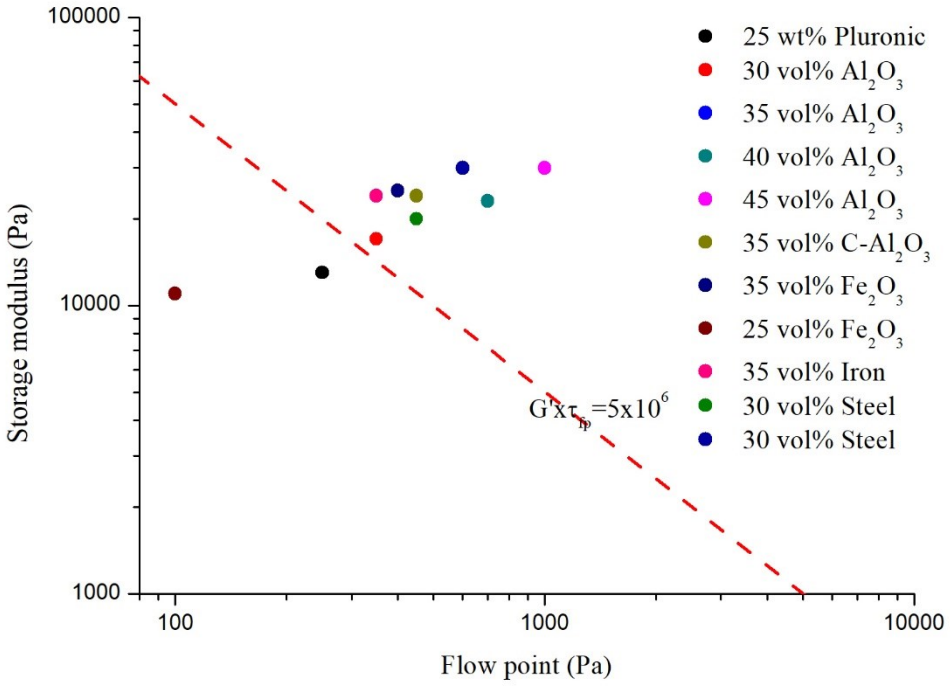


Figure 113. Storage modulus *vs.* Flow point of different hydrogel inks.

5.3.4 The shear stress profile of the inks across the nozzle during printing

The shear stress profile of different inks described using equation 22 is shown in Figure 114. The nozzle diameter used here is 410 μm and the printing speed is 6 mm/s, thus the shear rate is 35 s^{-1} according to equation. As the nozzle used here is conical one instead of straight one, an indication of using straight nozzles (0.1 mm) is applied here. As the inks for core/shell co-extruding have similar viscosity, flow point and storage modulus, the inks in one syringe can be recognised as a homogeneous ink. The core part (-100 μm<r<100 μm) is fully inside low shear stress region (<200 Pa) which indicates the core ink does not have significant deformation during printing.

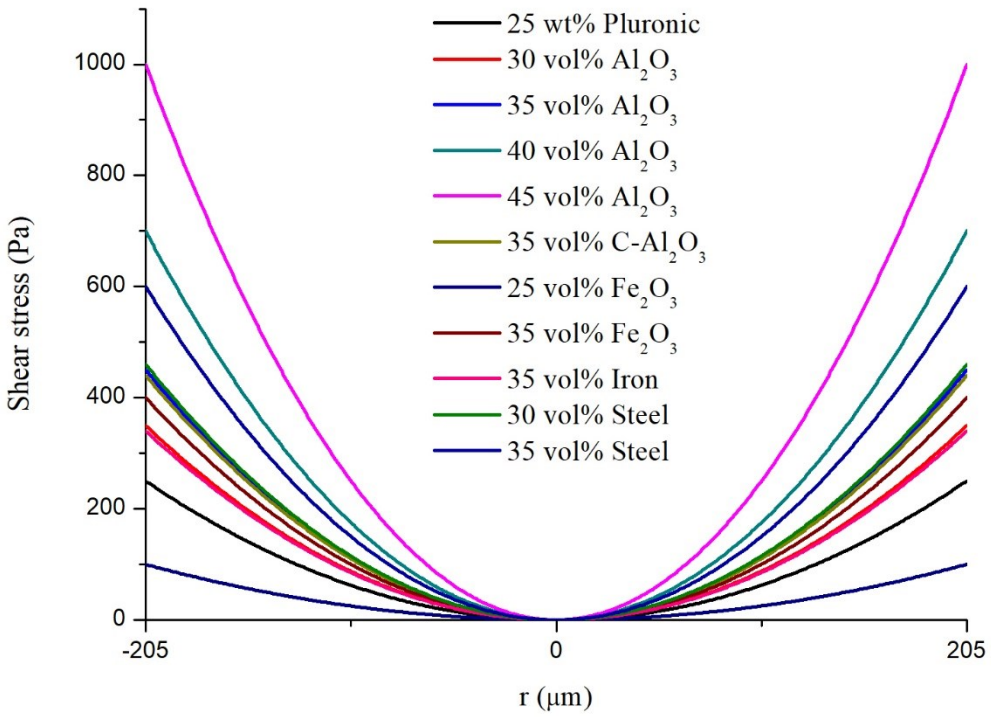


Figure 114. Shear stress profile of hydrogel inks extruded through a 410 μm nozzle.

5.3.5 Rheology of inks not suitable for co-extruding

When the rheology of the inks not match, the inks are not suitable for co-extruding. The ink with lower viscosity, yield stress, storage modulus would be extruded out first.

The rheology of two un-matched Pluronic based inks (40 vol% Al_2O_3 and 25 vol% Fe_2O_3 dispersed with 2 wt% Dolapix) is shown in Figure 115. These two inks have different viscosity at a same shear rate and the Fe_2O_3 ink has a lower flow point (90 Pa) than the Al_2O_3 ink (400 Pa).

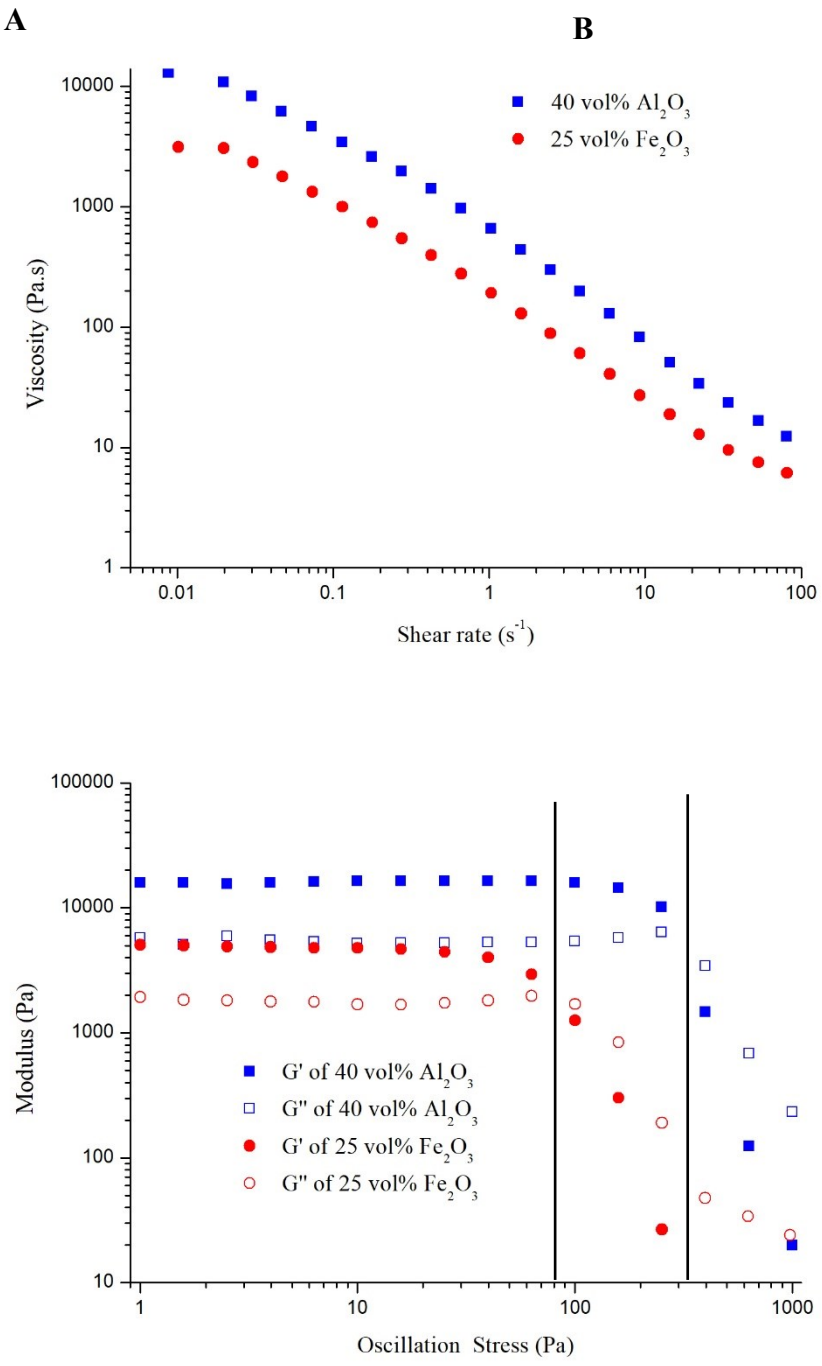


Figure 115. (A) Flow ramp and (B) Oscillation amplitude ramp of 40 vol% Al_2O_3 and 25 vol% Fe_2O_3 inks (two lines indicate the flow points of 25 vol% Fe_2O_3 and 40 vol% Al_2O_3, respectively).

The core/shell ink loaded in the syringe and the cross section of the printed sample are shown in Figure 116. There is a perfect core/shell cross section before printing (Figure 116 A) but the cross section of the printed sample shows how the arrangements has been lost (Figure 116 B). The Fe_2O_3 ink with more flowability is extruded out first while the Al_2O_3 ink cannot be co-extruded to create a continuous fibre with a regular arrangement.

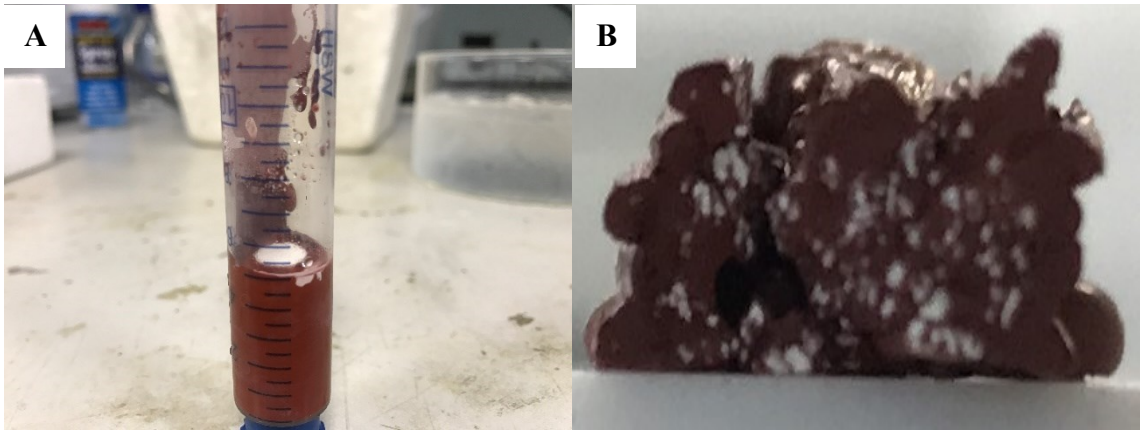


Figure 116. A) A syringe with a perfect Al_2O_3/Fe_2O_3 core/shell loading; B) The cross section of the printed Al_2O_3/Fe_2O_3 core/shell sample

When the rheology of the inks matches, their flow is homogeneous through the nozzles, thus there is no significant deformation during the movement from the syringes to the nozzles and the final co-extrusion on the substrate.

5.3.6 Structure characterization of the core/shell samples

5.3.6.1 Microstructure

As shown in Figures 88 and 89, in the grids the cross section of the steel fibre is relatively isotropic (circular) but in the bars there is significant distortion. This is probably due to the pressure on the extruded line against the base during printing. In addition, the CIP process may create additional distortion. However, CIP gives a significant densification to the samples and closes large defects (Figure 88). Before pressing large pores can remain between printed lines due to limited packing and deformation against the printed part. From the cross-section surface of the core-shell samples, the steel fibres can be easily distinguished. Plastic deformation of the steel fibres during bending can also be observed on the fracture surfaces. The formation of a porous interphase between the steel and the alumina can be clearly observed. The porosity is generated due to C burning out during sintering.

In the grids most of the steel core parts roughly keep their circular shape except the 3-core sample (Figure 89 D). Pressure given by the nearby filaments during printing of grids is much lower than that for the bars and therefore there is less deformation. In the case of the samples with three cores it is possible that the separation between cores is too small and they enter in contact partially during printing. As for the dense bars the use of a C-Al_2O_3 interlayer resulted in the formation of a porous interphase (~50 mm thick) between the steel and the alumina (Figure 89 E).

5.3.6.2 Steel volume fraction, density and porosity

The real steel volume fraction is slightly lower than the calculated theoretical volume fraction using dimensions of the spacers and the syringe. This is in anticipation as the method using Image J to calculate the volume fraction does not take the microporosity in the alumina matrix into consideration, so the real volume fraction = area of steel/ (area of alumina + area of pores in alumina). After the drying and sintering, the steel fibres are denser than Al_2O_3 matrix.

The remaining porosity in the samples ranges between 5 to 8 %. This value is relatively high. However, it is consistent with the sintering temperature. The samples were sintered at 1400 ℃ which is 100-150 ℃ lower than typically used with this type of alumina. This temperature was selected to avoid melting of the steel (430L stainless steel has a melting point between 1425 to 1450 ℃). As a result, the Al_2O_3 matrix were not fully sintered. For the C-interface samples, the higher porosity results from the burnt out of the graphite during sintering that generated a porous Al_2O_3-Steel interphase as intended. When the sintering temperature is higher than the melting point of the steel, some of the melted steel may come to the sample's surface form its core position and form steel drops on the sample surface (Figure 117). This is probably due to poor wetting of the steel on alumina. The contact angle of Fe-Cr liquids with similar Cr content as 430L steel on alumina is very high (above 140°)[96]. This is the reason why the steel should not be melted as shown in figure because the high contact angle make it sweat away from alumina.

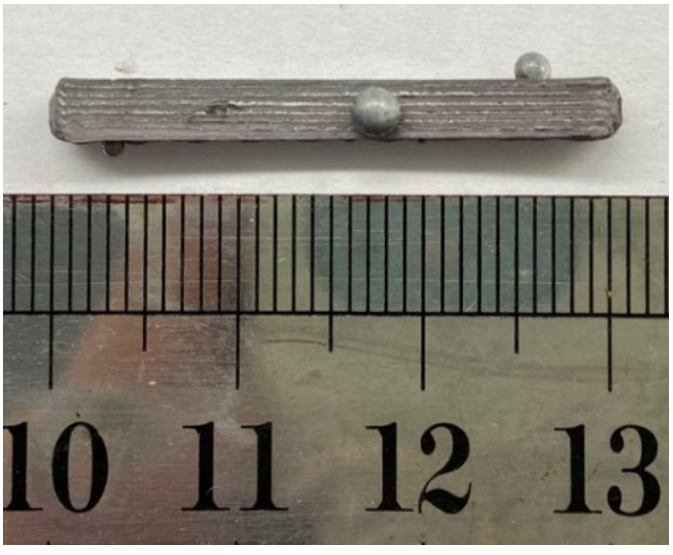


Figure 117. Photograph of a 1-core sample sintered at 1550 ℃ with steel drops on the sample surface.

5.3.6.3 Analysis of interface reactions

According to the XRD and the SEM-EDS analysis, the steel did not react with the Al_2O_3 or the graphite during sintering. No additional phases could be detected using any of the techniques. The reference pattern for steel used here is 434L steel instead of 430L steel because there is no reference pattern for 430L in the database. The only difference between these two steels is that 434L steel has over 1 % Mn while 430L steel does not. The steel peaks in the XRD analysis of the C-interface sample pattern are harder to identify because of the lower volume fraction of the steel in this sample (lower than 10 vol%).

Under the conditions used in this work, no reaction is expected between Fe and Al_2O_3[97] or between Cr and Al_2O_3[98]. In addition, as shown in an Ellingham diagram in Figure 118[99], neither iron nor chromium are expected to reduce Al_2O_3. Regarding the reactions with graphite, it seems that the amount of graphite is small and it is probably eliminated from the sample before any carbides can form.

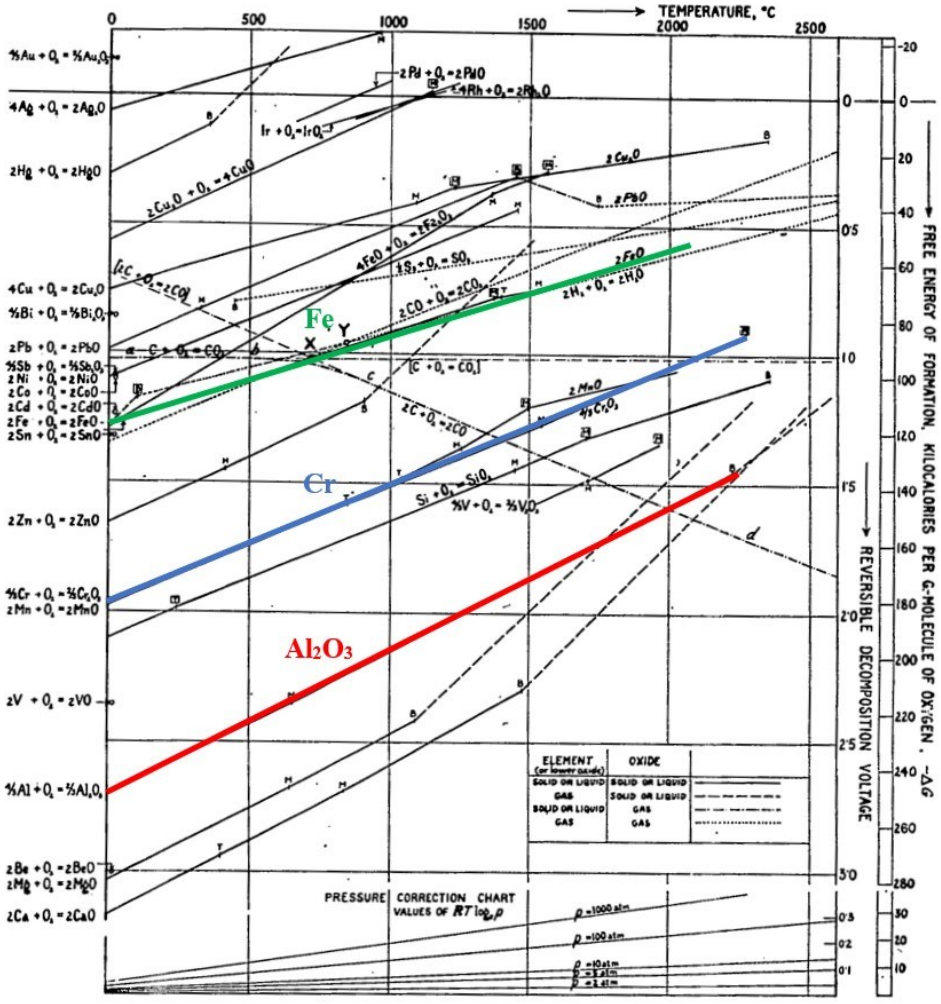


Figure 118. Ellingham Diagram. Reproduced with permission from[99]

5.3.7 Mechanical tests

5.3.7.1 Thermal residual stress in the samples

When the samples cool down from the sintering temperature, thermal residual stresses develop because of the difference of the coefficient of thermal expansion between the fibres and the matrix. This is an important factor that may influence the mechanical properties of the fibre reinforced composites. The structure of core/shell cylinders can be simplified as shown in Figure 119. This structure can be used to develop a simple analytic model to calculate the thermal residual stress in the fibres and the matrix.[100, 101] This calculation is under the limitations that it is a purely elastic calculation and the properties of the materials are constant in the whole range of temperature.

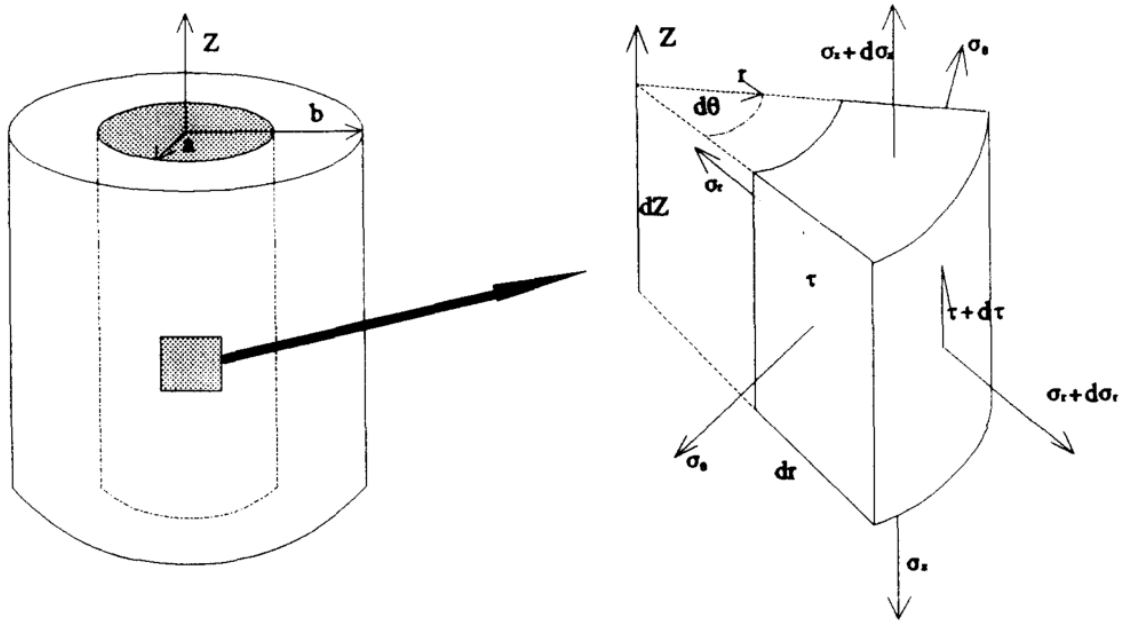


Figure 119. A concentric cylinder with core/shell structure and stress on a piece of the structure. Reproduced with permission from[100]

First, the Hooke's equations are the constitutive equations which show the stress, strain and temperature changes in the materials:

$$\varepsilon_r = \frac{\sigma_r - \nu(\sigma_\theta + \sigma_z)}{E} + \alpha_r \Delta T \qquad (37\ a)$$

$$\varepsilon_\theta = \frac{\sigma_\theta - \nu(\sigma_r + \sigma_z)}{E} + \alpha_\theta \Delta T \qquad (37\ b)$$

$$\varepsilon_z = \frac{\sigma_z - \nu(\sigma_r + \sigma_\theta)}{E} + \alpha_z \Delta T \qquad (37\ c)$$

where ε_r is the radial strain, ε_θ is the tangential strain, ε_z is the axial strain, σ_r is the radial stress, σ_θ is the tangential stress, σ_z is the axial stress, v is the Poisson's ratio of the material, E is the elastic modulus of the material, α_r is the radial coefficient of thermal expansion, α_θ is the tangential coefficient of thermal expansion, α_z is the axial coefficient of thermal expansion and ΔT is the temperature difference during cooling (-1400 ℃ in this work). The equations can be rewritten into the stress mode when the material has an isotropic thermal expansion which means α_r=α_θ=α_z=α:

$$\sigma_r = (\lambda + 2G)\varepsilon_r + \lambda\varepsilon_\theta + \lambda\varepsilon_z - (3\lambda + 2G)\alpha\Delta T \quad (38\ a)$$

$$\sigma_\theta = (\lambda + 2G)\varepsilon_\theta + \lambda\varepsilon_r + \lambda\varepsilon_z - (3\lambda + 2G)\alpha\Delta T \quad (38\ b)$$

$$\sigma_z = (\lambda + 2G)\varepsilon_z + \lambda\varepsilon_r + \lambda\varepsilon_\theta - (3\lambda + 2G)\alpha\Delta T \quad (38\ c)$$

where

$$\lambda = \frac{Ev}{(v+1)(1-2v)} \quad (39\ a)$$

$$G = \frac{E}{2(1+v)} \quad (39\ b)$$

Given a radial displacement of *u*, the strain can be described as:

$$\varepsilon_r = \frac{d_u}{d_r} \quad (40\ a)$$

$$\varepsilon_\theta = \frac{u}{r} \quad (40\ b)$$

$$\varepsilon_z = constant \quad (40\ c)$$

As the shearing stress of cylindrical symmetry must be 0, the stress should follow the equilibrium equation:

$$\frac{d\sigma_r}{dr} + \frac{(\sigma_r - \sigma_\theta)}{r} = 0 \quad (41)$$

the second-order differential equation in terms of *u* and *r* is:

$$\frac{d^2u}{dr^2} + \left(\frac{1}{r}\right)\frac{du}{dr} - \frac{u}{r^2} = 0 \quad (42)$$

gives a solution of *u* as:

$$u = C_1 r + \frac{C_2}{r} \quad (43)$$

where C_1 and C_2 are constants determined by boundary conditions:

1) $\sigma_{rm} = 0$ at $r = R_m$

2) $\sigma_{rf} = \sigma_{rm}$ at $r = R_f$

3) $\varepsilon_{zf} = \varepsilon_{zm}$ at $r = R_f$

4) $\varepsilon_{\theta f} = \varepsilon_{\theta m}$ at $r = R_f$

5) $\sigma_{zf} \times V_f + \sigma_{zm} \times (1 - V_f) = 0$

where σ_{rm} is the radial stress of matrix, σ_{rf} is the radial stress of fibre, σ_{zm} is the axial stress of matrix, σ_{zf} is the axial stress of fibre, ε_{zm} is the axial strain of matrix, ε_{zf} is the axial strain of fibre, $\varepsilon_{\theta m}$ is the tangential strain of matrix, $\varepsilon_{\theta f}$ is the tangential strain of fibre, R_m is the radius of matrix, R_f is the radius of fibre, V_f is the volume fraction of fibres.

The final expressions for stresses in the fibre and the matrix can be solved as:

$$\sigma_{rf} = (T_{1f} + T_{2f})(\alpha_m - \alpha_f)\Delta T \quad (44\text{ a})$$

$$\sigma_{\theta f} = \sigma_{rf} \quad (44\text{ b})$$

$$\sigma_{zf} = (T_1 + T_2)(\alpha_m - \alpha_f)\delta\Delta T \quad (44\text{ c})$$

and

$$\sigma_{rm} = (T_{1m} + T_{2m})\big(\alpha_m - \alpha_f\big)\delta_r\Delta T \quad (45\text{ a})$$

$$\sigma_{\theta m} = (T_{1m} + T_{2m})\big(\alpha_m - \alpha_f\big)\delta_\theta\Delta T \quad (45\text{ b})$$

$$\sigma_{zm} = (T_1 + T_2)(\alpha_m - \alpha_f)\Delta T \quad (45\text{ c})$$

where

$$\delta = (1 - \frac{R_m^2}{R_f^2}) \quad (46\text{ a})$$

$$\delta_r = (1 - \frac{R_m^2}{r^2}) \quad (46\text{ b})$$

$$\delta_\theta = (1 + \frac{R_m^2}{r^2}) \quad (46\text{ c})$$

and

$$T_1 = \frac{(\frac{E_f q_1 \nu_f}{\lambda_1} + E_f)}{\lambda_3} \quad (47\text{ a})$$

$$T_2 = \frac{E_f q_1}{\lambda_1 \lambda_3} \quad (47\text{ b})$$

$$T_{1m} = \frac{\lambda_2 T_1}{\lambda_1} + \frac{\nu_f}{\lambda_1} \quad (47\text{ c})$$

$$T_{2m} = \frac{\lambda_2 T_2}{\lambda_1} + \frac{1}{\lambda_1} \quad (47\text{ d})$$

$$T_{1f} = \delta T_{1m} \quad (47\text{ e})$$

$$T_{2f} = \delta T_{2m} \quad (47\text{ f})$$

where the additional parameters are defined as:

$$q_1 = \frac{2\nu_f \delta}{E_f} - \frac{2\nu_m}{E_m} \quad (48\text{ a})$$

$$\lambda_1 = \frac{(1-\nu_f)\delta}{E_f} - \frac{1-\nu_m}{E_m} - \frac{(1+\nu_m)R_m^2}{E_m R_f^2} \quad (48\text{ b})$$

$$\lambda_2 = \frac{(\nu_f - \nu_m)}{E_m} \quad (48\text{ c})$$

$$\lambda_3 = \delta - \frac{E_f q_1 \lambda_2}{\lambda_1} - \frac{E_f}{E_m} \quad (48\text{ d})$$

The elastic modulus, Poisson ratio and coefficient of thermal expansion of Al_2O_3 and steel are shown in Table 17 and the calculated stresses for the 1-core sample with a ΔT of -1400 ℃ are shown in Table 18. For 1-core sample, as the alumina shell is ~5 % porosity, the Elastic modulus used here (330 GPa) is ~95 % of the reported value (350 GPa[102]) which is for a dense alumina.[103]

Table 17. Elastic modulus, Poisson ratio and coefficient of thermal expansion of Al_2O_3 and steel.

Material	Elastic modulus (GPa)	Poisson ratio	Thermal expansion coefficient (1/℃)
Al_2O_3	330	0.2	7.2×10^{-6}
Steel	200	0.3	15×10^{-6}

Table 18. Thermal residual stresses in the core/shell samples

Sample	Radial stress of matrix (σ_{rm}, GPa)	Radial stress of fibre (σ_{rf}, GPa)	Tangential stress of matrix ($\sigma_{\theta m}$,GPa)	Tangential stress of fibre ($\sigma_{\theta f}$, GPa)	Axial stress of matrix (σ_{zm}, GPa)	Axial stress of fibre (σ_{zf}, GPa)
1-core	$0.32(\frac{125^2}{r^2}-1)$	1.69	$-0.32(\frac{125^2}{r^2}+1)$	1.69	-0.56	2.94

The radial stress and tangential stress of matrix is related to the position inside the sample (r). The r is from 50 to 125 μm (radius of the sintered core and sintered shell of 1-core sample) for a 1-core sample. The radial stress of matrix at the interface (50 μm) is 1.69 GPa. The tangential stresses of matrix at the interface (50 μm) is -2.32 GPa. The negative value for the tangential and axial stress of matrix indicates that the stress inside the matrix is in the opposite direction as that inside the fibres.

However, this is just an elastic calculation. This calculation is suggested to overestimate stresses by a couple of factors:

-The properties of the steel are not constant on the range of temperatures. The Young's modulus of steels go down very fast with temperature.[104, 105] The thermal expansion coefficient increases with the increasing of temperature.[106]

-According to the calculations and Tresca criterium, the difference between two of the principal stresses (axial stress minus radial stress or tangential stress which is ~1 GPa here) is higher than the shear yield stress which can be taken as half of the yield stress in tension. So there is a limit of how much residual stress you can have with metallic fibres (or matrix).

Two assumptions are made here. One is that the R_m is the radius of a single filament without considering interaction between the stress fields around different fibres. Another one is that the fibres are cylindrical.

From the results of the thermal residual stress in the composites, several conclusions can be made:

-Fibres will be in tension and matrix has tensile radial stress but compressive tangential and axial stresses.

-The stresses are going to be significant so they can explain some of the trends observed in the strength measurements.

5.3.7.2 Three-point bending test of single filaments

Although the displacement-stress curve shows a brittle-like behaviour after the crack occurs for all the single filaments, the steel fibres hold the filament to prevent it from totally breaking away (Figure 98). The reason for the sharp decrease of the stress is because during this test the filament loses contact with the pins after breaking which gives no force to the pins any more. The strength calculated here is about 4 times of that calculated by using bar samples maybe due to the less defects in the smaller single filament samples. However, the 3-core single filament has a much lower strength as we expected. The possible reason is that some of the steel fibres are not inside the composite structure but on the surface, which can be seen in Figure 98 G-H. That creates large defects on the surface leading to a decrease in the strength.

5.3.7.3 Compressive measurement of grids

As can be seen in Figure 99 A and Figure 100, the Al_2O_3 sample and C-Interface sample have brittle compressive behaviour. The compressive stress drops down to 0 MPa once they are broken while for other core/shell samples, the steel fibres in the structures buckle but can still partially support the structure after the cracking of the ceramic shell which results in a plateau of the stress after the drop of the stress. This result is consistent with the behaviour of different single filaments. The compressive strengths of the core/shell samples range from 60 to 100 MPa.

Some papers have reported the compressive strength of robocasted grids. Miranda printed HA/β-TCP grids with a filament diameter ~250 μm and a road width ~400 μm (in plane line spacing from centre to centre). The compressive strength of HA samples is ~50 MPa and of β-TCP is ~15 MPa. Miranda compressed the grids in z-direction of printing which means that the individual struts failed because they are compressed or bent whereas in this work, the grids are compressed in x-y orientation where the struts are buckled during compression.[107]

By comparing the compressive strength of the samples in this work and in Miranda's paper, the compressive strength depends on the test orientation, the ceramic materials and the structure of the grids.

5.3.7.4 Mechanical property of bar shaped samples

5.3.7.4.1 Strength of different bar shaped samples

The bending strength of the bars can be seen in Figure 101, 102 and 103. There is no significant difference among the bar shaped samples. The bending strength of the Al_2O_3 sample is ~200 MPa which is lower than strengths often reported for conventional Al_2O_3 ceramic (~250-350

MPa)[108]. This is probably due to the limited densification that results from the relatively low sintering temperature. Although the C-Interface sample has steel fibres in the structure, the low steel volume fraction and high porosity (>10 %) results in a low strength and a brittle facture behaviour. The core/shell samples without interface have higher steel volume fraction and therefore they exhibit a gradual fracture (stable crack growth shown in Figure 104).

During the tensile test of 1-core dog-bone sample, it seems the steel fibres give some reinforcement to avoid the sample from breaking into two parts (Figure 105 A, B). There is a drop in load due to fracture of the matrix but the fibres are able to hold the structure together and the load increases again as the displacement increases until the final fracture. However, the test speed here was 0.1 mm/min which maybe a bit fast. The reinforcement behaviour maybe more obvious if the test speed could be slower.

The critical defect size *a* of purely brittle ceramic materials can be analysed using the Griffith/Irwin failure criterion between fracture toughness (K_{IC}) and the strength (σ):

$$K_{IC} = Y\sigma(\pi a)^{1/2} \tag{49}$$

Where Y is a geometric factor (~1).[109] Taking the alumina samples as an example, the strengths for the single filament is 400 MPa, for the bar is 200 MPa and for the dog bone is 25 MPa, the calculated defect sizes are 10, 50 and 3000 μm respectively (K_{IC}=2.5 MPa.m$^{1/2}$). Because of the low sintering temperature (1400 °C), the samples are not fully dense, thus there should be some micro pores in the structures. The calculated defect sizes agree with the fact especially for the bending test samples (single filaments and bars).

However, the defect size of dog-bone sample is too big (~mm). According to Weibull, the strength is expected to go down with volume/surface tested (depending if the critical flaw is in the volume or the surface). The larger the volume of the sample, the more likely a critical flaw will be found. When the strength is controlled by volume flaws, the relationship between strength and volume tested can be written as:

$$\sigma_1 V_1^{1/m} = \sigma_2 V_2^{1/m} \tag{50}$$

where σ is the strength, *V* is the volume of the sample and m is the Weibull modulus. However, even considering that the volume/surface is much bigger in tension, the strengths are too low and the critical defects are too big. One possibility is that the alignment is not good and there is some degree of bending. Another reason is that these are a bit more complex samples to print and some big defects (~mm) are already present (Figure 120).

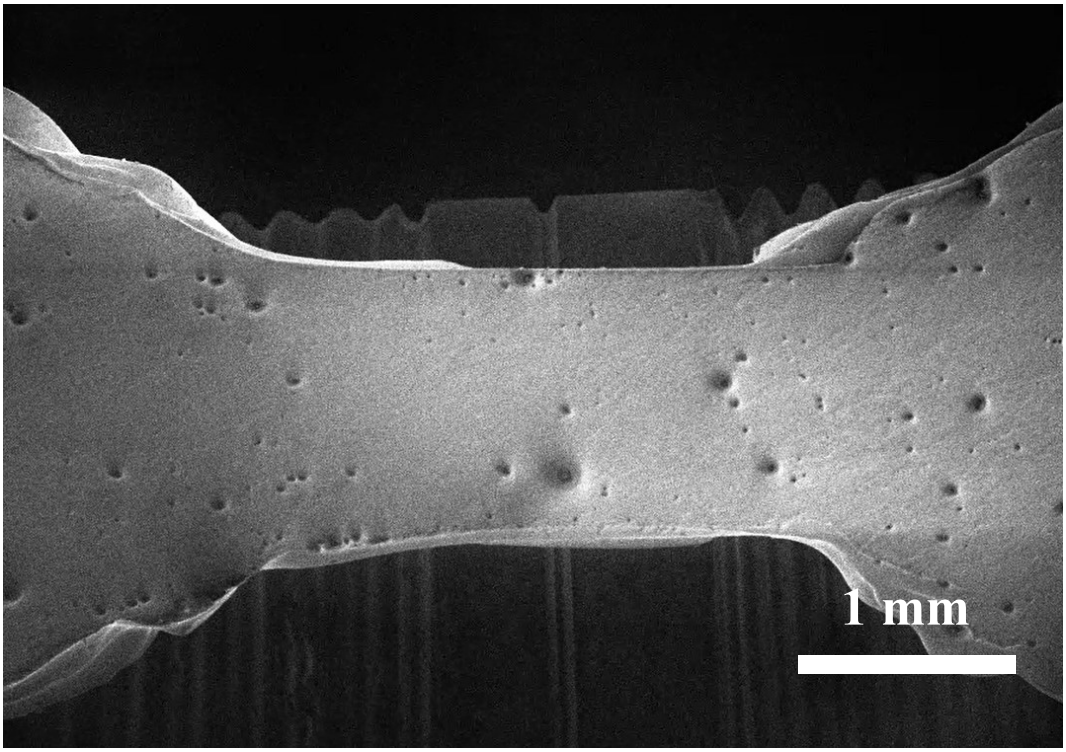


Figure 120. Polished surface of an alumina dog-bone sample.

The bending strengths of the single filaments are already higher probably due to the small defect size. In the bars, failure will start in the ceramic matrix in the tensile face. The presence of the steel fibres may have two effects, there will be residual compressive stresses in the matrix that work against the applied tensile stresses and in addition there may be less volume defects as the steel densifies well during sintering.

During the tensile test of the bars, the SEM (Figure 105 A, B) shows that the alumina matrix cracks but the fibres are still holding the samples so the strength should be something of the order of $f \times \sigma_f$ where f is the volume fraction of fibres from 0.1 to 0.25. Also, the stress-strain curve (Figure 105 C) agrees in that this is what is happening. The fracture surfaces of the samples (Figure 88) show that there is practically no fibre delamination. Assuming the fibres ultimate strengths of the order of 500 MPa, then the strengths should be of the order of 50-100 MPa. This is a bit higher than the calculated values as there are large defects in the samples and there are relatively large tensile residual stresses in the fibres.

Regarding the tensile test shown in Figure 105 C, the shape of the curve is what can be expected following the Aveston-Cooper-Kelly model.[110]. In an ideal ceramic composite with reinforcing metallic fibres a small dip or plateau can be expected in the tensile stress-strain curves when the matrix breaks (Figure 121). A bigger dip is observed in the tests of the dog-

bone samples but this is probably due to the way the sample is held (not griped but resting on the pins). This means when the matrix breaks there may be a bit of rearrangement. This result shows that it is possible to combine additive manufacturing and the core-shell filaments developed here to fabricate fibre-reinforced composites with an ideal behaviour.

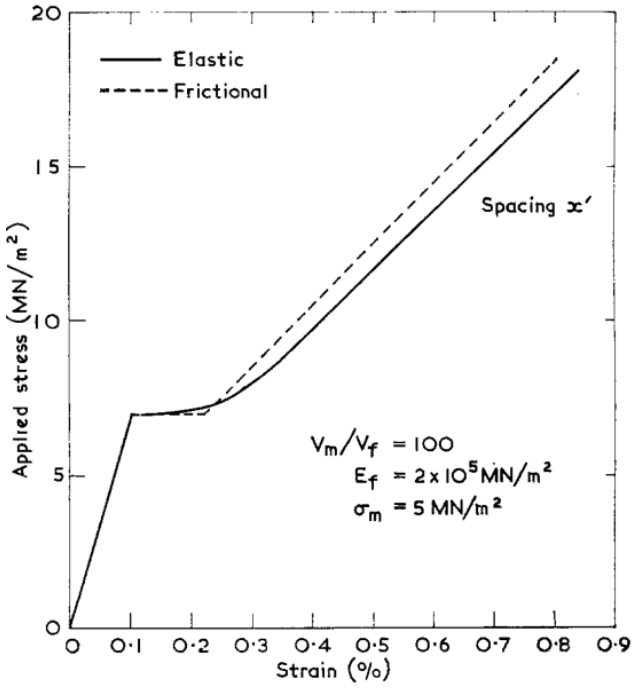


Figure 121. The stress-strain curve of a cement reinforced with long steel fibres. Reproduced with permission from[110]

5.3.7.4.2 Fracture behaviour of the bar shaped samples

The calculated fracture toughness (K_{IC}) of SENB samples are shown in Figure 106. The value of K_{IC} is in proportion with the steel content (3-core >1-core>2-core>C-Interface>Al_2O_3). The works of fracture (γ_{WOF}) describe the required amount of energy to break off a sample. As shown in Figure 108, the calculated works of fracture are consistent with the fracture toughness. Table 19 shows a comparison of K_{IC}, γ_{WOF} and strength between the samples in this work and other reported ceramic-metal composites.

Table 19. Fracture toughness, works of fracture and strengths of different composites.

Researcher [Ref.]	Material	K_{IC} (MPa.m$^{1/2}$)	γ_{WOF} (KJ/m^2)	Strength (MPa)
This work	Steel in Al_2O_3 (10~25 vol%)	3.8~5.5	1~2	200-450
Hoffman[111]	Al in Al_2O_3 (13 vol%)	4~7	100~140	160
Pemberton[112]	Steel in Al_2O_3 (5~15 vol%)	-	2~25	-
Ferraro[113]	Al-4Mg in Al_2O_3 (65~80 vol%)	14.5~15.5	3~6	400-600

So, the variation of the K_{IC} in this work is not large with all the samples have a K_{IC} close to the alumina value. Since the crack of the core/shell samples starts in the matrix, it is difficult to measure exactly in the curve when the crack starts. In addition, the small increase in the measured K_{IC} may be caused by the residual compressive stresses in the matrix. The fracture toughness of ceramic matrices reinforced with metallic fibres/laminates vary in different reports as people used different metal, different reinforcement type (fibres or laminates) and different metal volume fraction. Hoffman [111] used aluminium fibres in the alumina matrix (13 vol%) and the K_{IC} is similar to the one of the matrix as well. Ferraro [113] used freeze drying to produce the composites with metal/ceramic laminates. The samples in his work have a metal volume fraction over 65 vol% which give the composites a relative high fracture toughness. Pemberton's matrix [112] is not fully sintered alumina but something like a cement as the matrix is only consolidate at 450 ℃. For that reason, their works of fracture are a bit higher than the core/shell composites in this work because the weak matrix make the contribution from delamination significant.

The work of fracture of pure alumina ceramic cannot be measured using the area under displacement-load curve as the fracture is brittle and therefore the area overestimates the work of fracture. However, because it is brittle, an estimate on the work of fracture can be get by calculating G_C critical strain energy release rate that is

$$G_C = {K_{IC}}^2/E \tag{51}$$

Where K_{IC} is the critical stress concentration and E is Young's modulus. In this case, K_{IC} is 3 MPa.m$^{1/2}$ and E is 350 GPa[102], the G_C is around 25 J/m^2. By adding the fibres, the work of fracture is increased by an order of magnitude (Figure 122).

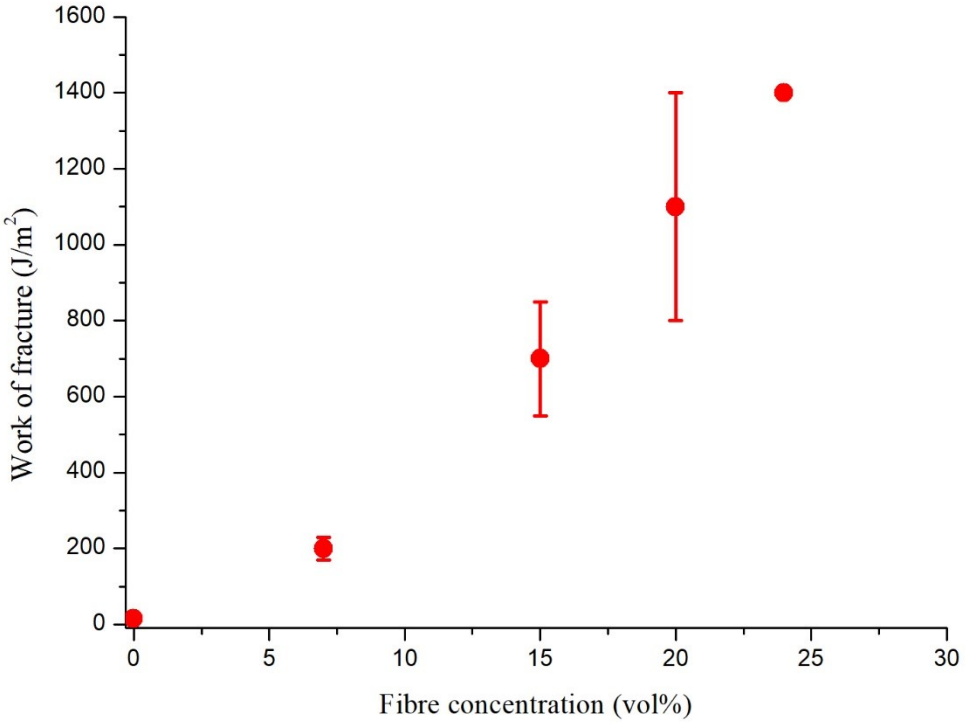


Figure 122. Work of fracture of the samples with different experimental fibre concentration.

5.3.7.4.3 Predicted work of fracture calculated using work of deformation

Assuming the work of fracture of the matrix is negligible, the degree of delamination is very limited and therefore the contribution of delamination is very small. The work of fracture is determined by the deformation and rupture of the steel fibres. In the absences of substantial delamination, the expected work of fracture, γ_{Wof}, could be calculated using Clyne's model

$$\gamma_{Wof} = \frac{V_f s_f R W_f}{\varepsilon_*} \tag{52}$$

where V_f is the volume fraction of the fibre, s_f is the fibre deformation aspect ratio, R is the radius of the fibre, W_f is the work of deformation of the fibre and ε_* is the fibre strain to failure.[112] The model assumes that the main contribution to the work of fracture is the deformation of the metallic fibres. The work of deformation and fibre strain to failure of 430 stainless steel can be approximated from the stress-strain curve shown in Figure 123 which is ~120 MPa (MJ/m^3) and ~0.25 at 23 °C.[114] The fibre deformation aspect ratio is ~1 as there is almost no delamination in the system and the length of fibre protruding/deformation is very small according to the SEM pictures. The fibre radius can be assumed as 50 μm for 1-core

samples and 25 μm for 2-core, 3-core and C-Interface samples. The predicted work of fracture of the core/shell samples are shown in Table 20.

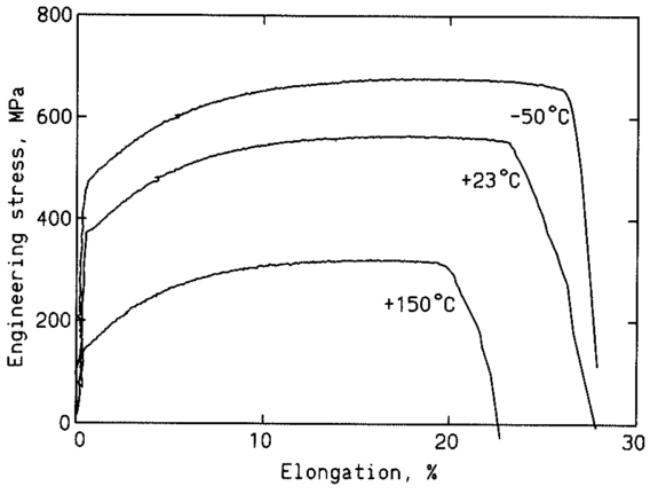


Figure 123. Strain-stress curves of 430 stainless steel at different temperature. Adapted with permission from[114]

Table 20. Predicted work of fracture of different samples

Sample	Predicted work of fracture (KJ/m^2)	Experimental work of fracture (KJ/m^2)
1-core	4.8	1.2
2-core	1.8	0.7
3-core	2.6	1.4
C-Inter	0.8	0.2

The predicted value of work of fracture is a bit larger than the measured value. One possibility is that the fibres are flat instead of typical circular which may decrease the work of fracture of the composites. Another possibility is that the fibre work of deformation is calculated from a graph for bulk steel not from the actual fibre. The fibre deformation aspect ratio is also an approximation taken from the images of fracture surfaces.

This model tells that the more steel in the composites the more work of deformation and therefore the higher work of fracture can be observed.

5.3.7.5 Variation of strength with fibre content

5.3.7.5.1 Flexural strength

The flexural strength *vs.* fibre content is shown in Figure 124. Although there is no significant difference of the strength shown in Figure 102, there may be some relationships between the strength and the fibre content. When the volume fraction of fibres is lower than a minimum volume fraction (~ 0.1 according to Figure 124), the fibres do not give obvious influence on the flexural strength of the composites. However, when the fibre volume fraction is larger than the minimum volume fraction, the increasing of fibre content results in a slight increase of flexural strength. The possible reason may be less porosity of steel fibres or more residual compressive stresses in the matrix.

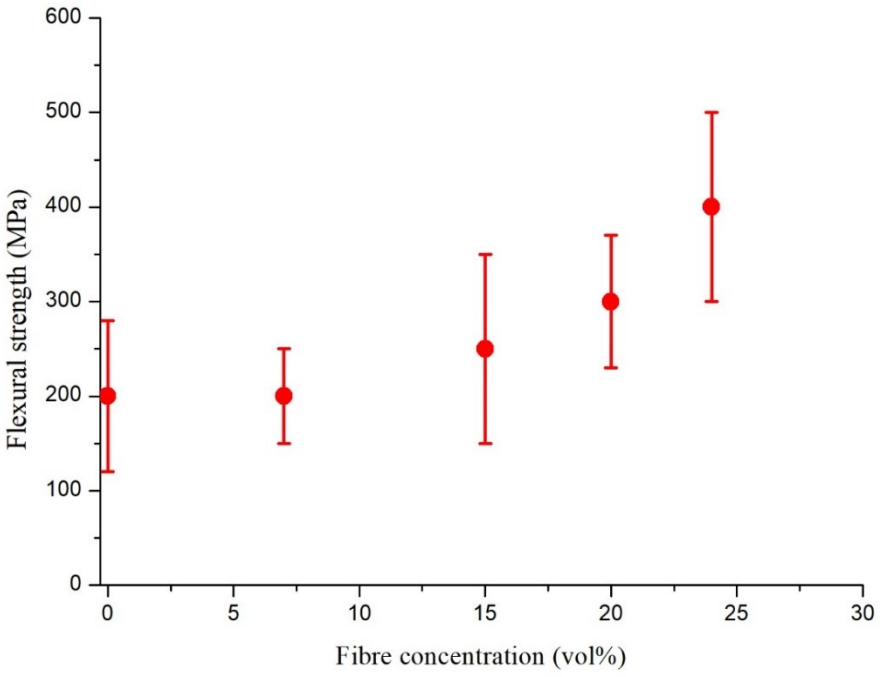


Figure 124. Flexural strength *vs.* experimental fibre content of the core/shell samples (An average value of polished and unpolished samples is used here as they are similar).

5.3.7.5.2 Tensile strength

The tensile strength of an Al_2O_3 dog-bone sample is shown in Figure 105 D. The tensile strength of the sample is 25 MPa which is much lower than reported tensile strength for dense thin flat alumina ceramic (~150 MPa)[115]. The tensile strength of 1-core sample is only 22 MPa as shown in Figure 105 C. However, the C-Interface sample seems to have a much higher tensile strength ~ 75 MPa (Figure 105 E) maybe because of the lower residual stress. The

relationship of the tensile strength and the fibre concentration cannot be obtained here. However only few samples were tested (one of each type) and there is probably a relatively large variability of tensile strengths and defects sizes in the 3D printed dog bones. The strength for the pure alumina suggests a relatively large defect size (consistent to some extent with the SEM images, Figure 120).

The tensile strength of 430L stainless steel is reported as 480 MPa.[116, 117] As the matrix breaks first and the fibre hold the sample together (only one crack is observed before breaking in this test). If the fibres are the ones holding the load, a simple rule for tensile strength (σ_c) of this fibre composite can be written as:

$$\sigma_c = \sigma_f v_f \tag{53}$$

where σ_f is the tensile strength of fibre and v_f is the volume fraction of fibre.[118] However, the predicted tensile strength is larger than the measured strength (~100 MPa for a steel strength of 480 MPa and steel volume fraction of 0.2). One possible reason is that the sintered fibre may be weaker than the bulk steel as reported. [116, 117] Another one is that there are tensile stresses in the fibres.

Equation 53 is valid when the matrix fails first and there is enough fibre concentration so that the fibres are able to hold the sample after the matrix fails. This seems to agree with the shape of the stress-displacement curve (Figure 105 C) and the in-situ observations in the SEM (Figure 105 A and B). However, it does not agree with the fact that the sample with the C-interface (that have less steel) is stronger or the observation that the strength of the alumina sample is very similar to the strength of the sample with fibres (1-core). As only very few samples have been tested, the results are preliminary. The strengths may be influenced by an inhomogeneous defect distribution from sample to sample and the effects of residual stresses are not considered. More testing will be needed to fully assess the validity of equation 53 to describe the tensile response of the composites.

5.3.8 Cyclic three-point bending tests

As can be observed in Figure 111, the decrease of the loading-unloading slopes during cyclic tests with the increasing number of cycles is related to increasing plastic deformation during bending. As the plastic deformation of fibres increases, the compliance of the sample increases and therefore the slope of the loading-unloading curves (basically the stiffness, the inverse of the compliance) decreases (even if the crack lengths do not increase). The 1-core and 3-core

samples have higher slope decreases than the 2-core samples. This will implicate higher degree of plasticity that correlates well with their higher works of fracture. The main reason is that 1-core and 3-core samples have higher fibre volume fraction (~22 vol%) than 2-core samples (15 vol%).

5.3.9 Hardness test of the core/shell composites

Some indentation imprints of Vickers hardness test of the core/shell samples are shown in Figure 125. The Al_2O_3 part has a hardness ~1100 HV which is lower than the typical hardness (1500 HV) of a dense Al_2O_3 ceramic object (Figure 125 A). One possibility is that the stress field of the indentation extends beyond the indenter mark and therefore steel is probed as well. On the other hand, the steel part has a hardness ~300 HV which is higher than the typical hardness (200 HV) of a pure steel (Figure 125 B). A possible reason is that the steel part is smaller than the size of the indentation so the measured hardness is the hardness of a mixture of Al_2O_3 ceramic and steel fiber. The cracks coming from the tips of the diamond shaped indentation are stopped when they extend to the edge of the steel parts what qualitatively confirms the good adhesion between steel and the matrix observed during the fracture tests (Figure 125 C).

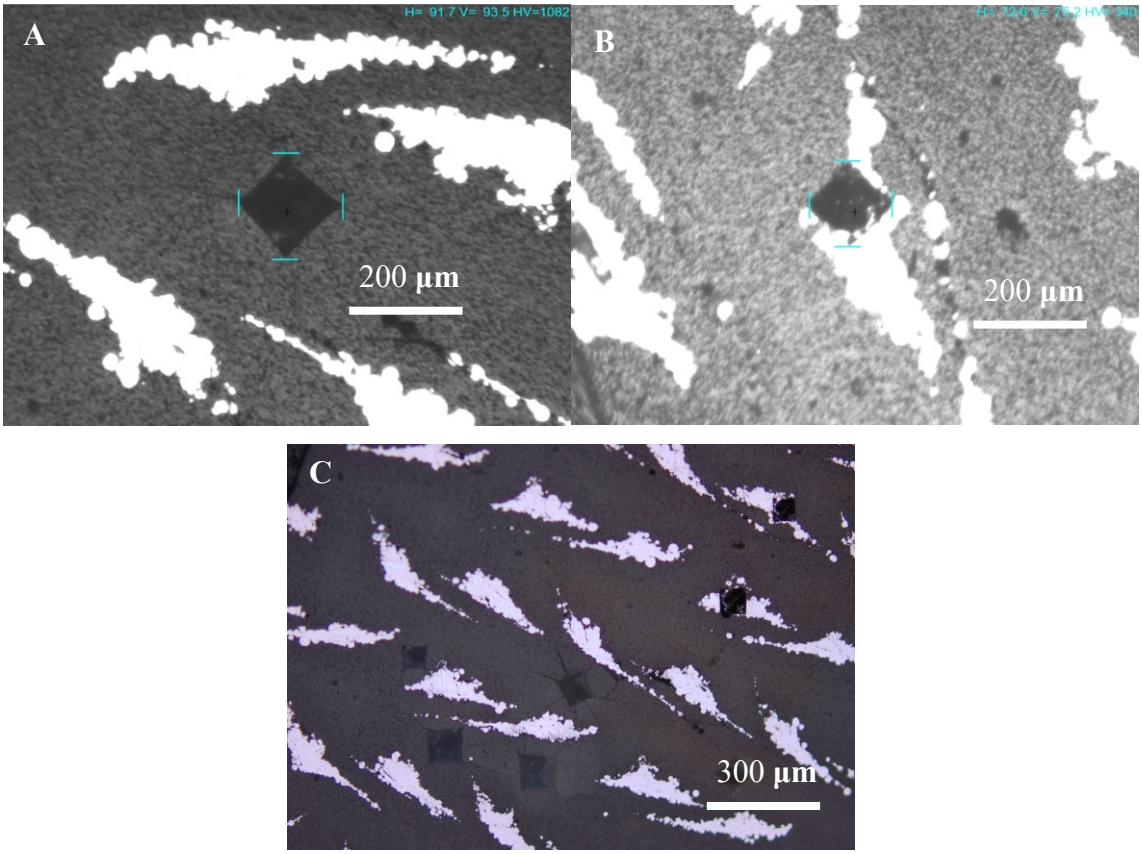


Figure 125. A) Indentation on the Al_2O_3 part; B) Indentation on the steel part; C) Indentations on the cross section.

5.3.10 The influence of the fibre shape on the mechanical properties of the products

As the steel fibres are not typically cylinder, the mechanical properties of the products may be affected by the fibre shape. Since the cores are all squeezed in the same direction, the deformation of the fibres may result in an increase in the anisotropy. This means the response after loading in the direction perpendicular to the fibres will not be exactly the same. Also, the sharp corners of the steel fibres could be the points for stress concentration that can be recognized as the defects in the structure which can have a detrimental effect on the mechanical properties. In addition, the shape will also influence the distribution of the thermal stress.

5.4 Conclusion

A model system is used to demonstrate that thermally reversible hydrogels (using Pluronic) can be used as inks to print filaments with core/shell structures containing one or multiple cores into three-dimensional composite objects. The approach also allows the addition of interlayers between the core and the shell.

The conditions for co-extrusion are demonstrated. Matching the yield stress and viscosity of the core and shell inks is required. These rheological properties are adjusted using inks based on the thermally reversible hydrogels with different solid concentrations.

The approach is demonstrated in a model system consisting of a ceramic matrix (Al_2O_3) reinforced with metallic (steel) long fibres. These composites exhibit an ideal behaviour close to what can be expected from the Aveston, Cooper and Kelly's model.[110] The mechanical properties of the composites relate to the volume fraction of steel in the system (vol% of fibres).

In this particular composite, the strength of the matrix can be retained and even improved and the work of fracture is increased by two orders of magnitude which is mainly due to the plastic deformation of the steel fibres.

The interphase between the matrix and the fibre can be manipulated using this method. However, in the Al_2O_3/Steel composite, a weak interphase does not have a significant effect on the mechanical properties. The main reason may be the low steel concentration for this type of composite (below 10 vol%) which reduces the contribution of the fibre plastic deformation.

6. Conclusion and Future work

6.1 Conclusion

Approaches are developed in this work to enable further microstructural control of porous ceramics and build complex robocasted structural ceramic composites. The approach strategy is based on inks either responsive to pH or to temperature. Two specific systems are used to demonstrate the strategy:

-The microporosity (the porosity at the 1-10 μm level) is controlled using pH responsive emulsions.

-Multimaterial ceramic matrix composites with continuous metallic fibres are fabricated using thermally reversible hydrogels to create core/shell cartridges and combining co-extrusion with co-sintering.

First, a kind of emulsion-based ink was used to produce porous ceramic with controlled pore parameters successfully by robocasting. The rheology of the ink is studied by adjusting several factors during the emulsion preparation. These factors, including the solid loading of the suspension, the volume percentage of the oil phase, the concentration of the BCS solution, the amount of GδL and the stirring speed of the emulsification, were manipulated to fabricate porous ceramics with desired microstructures.

Then, a novel structure - core/shell - was utilized in this work to produce metal/ceramic composites by robocasting. In this structure, continuous long steel fibres were used to give reinforcement to the ceramic matrix. With the aim of understanding how the steel fibres affect the mechanical properties, samples with different number of steel fibres in one filament and samples with different shapes were produced. The continuous steel fibres in the alumina matrix increase the toughness of the matrix without sacrificing the strength of the final product.

6.2 Future Work

There are three main challenges remaining for future work.

6.2.1 Light materials

As the metal/ceramic core/shell ceramic matrix composite is fabricated successfully by robocasting. The core/shell structure may also be used to produce porous/dense (or dense/porous) ceramic parts which is shown in Figure 126. The porous cores or shells could be produced using emulsion-based inks and the dense parts could be fabricated using suspension prepared with BCS (no oil added, no emulsification) or Pluronic-based inks. The rheology of these two inks should match each other in order to be able to be co-extruded. In preliminary porous/dense ceramic structures, a water droplet can flow through the porous channel gradually (Figure 127).

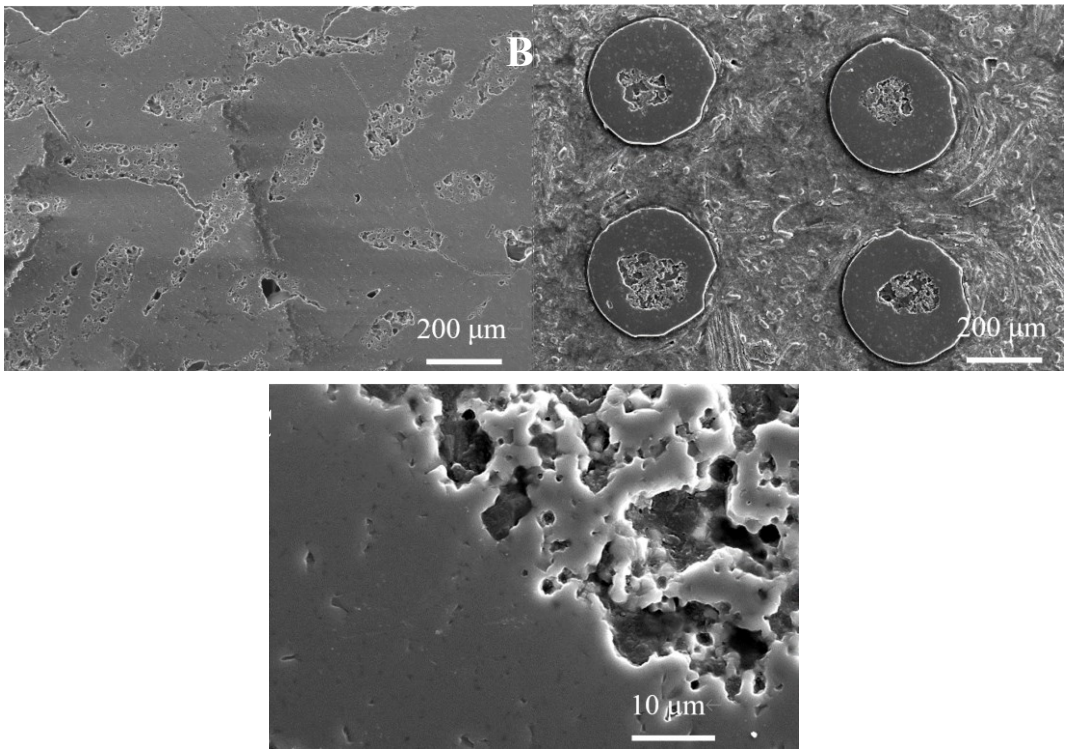


Figure 126. SEM graphs of A) polished cross section of a porous/dense core/shell bar; B) polished cross section of a porous/dense core/shell grid; C) the interface between the porous core and dense shell of a polished grid.

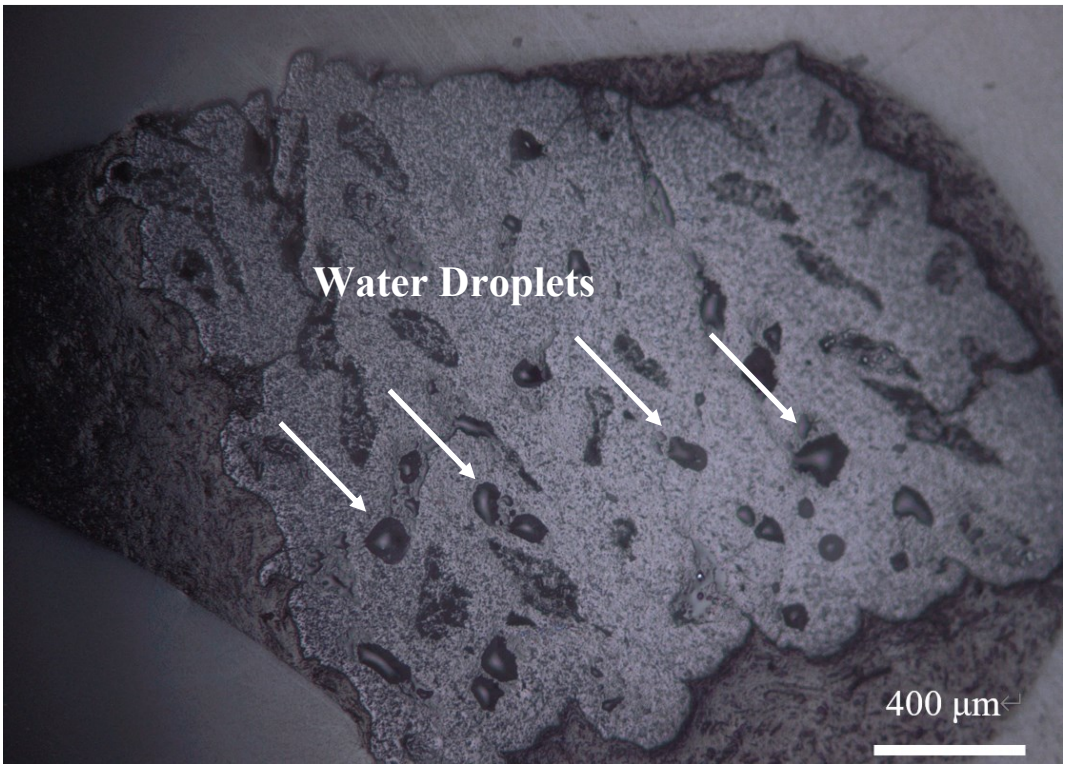


Figure 127. Optical microscopy graph of the cross section of a porous/dense core/shell bar with some water permeating through the porous channels (the arrows indicate the position of water droplets).

Further optimization can be done on the porous/dense structure to fabricate ceramic filaments or bars with better circular cores. As the pore parameters can be adjusted by using different emulsified inks, the permeability could be adjusted as well. As the ceramic parts have some porous structure, the density of the ceramic is lower than pure dense ceramic. The mechanical property of the bars and grids can be measured to see if these products still have high stiffness with lighter weights compared with dense ceramic products.

6.2.2 Core/shell ceramic/ceramic

Since the metal/ceramic system is demonstrated, the ceramic/ceramic system may also be a possibility. For example, ZrO_2 which is also a frequently used ceramic material can be used to combine with Al_2O_3 to form this system. Pluronic can be used to prepared thermally reversible hydrogels. The most important thing is that the rheology of the inks should match each other. As these two materials will undergo co-extrusion and co-sintering, the difference of thermal expansion coefficient should be taken into consideration. Also, which material should play the role as the core part should be considered.

6.2.3 Interfacial engineering

Graphene inks have been tried to function as the interfacial phase. The ink is prepared by adding Pluronic powders into graphene oxide solutions to make it thermally reversible. (20 wt% Pluronic and 17.98 mg/ml graphene oxide) However, the viscosity of this ink is relatively higher than the steel and the Al_2O_3 inks unless the graphene oxide concentration is decreased to a relatively low level. Figure 128 shows the cross section of a core/shell bar shaped sample with graphene interface. However, there are no concentric rings that can be viewed on the cross section of the graphene interface sample. This kind of ink may need more work. For example, find another solution to decrease the viscosity of the ink or try to prepare inks with lower graphene oxide concentration.

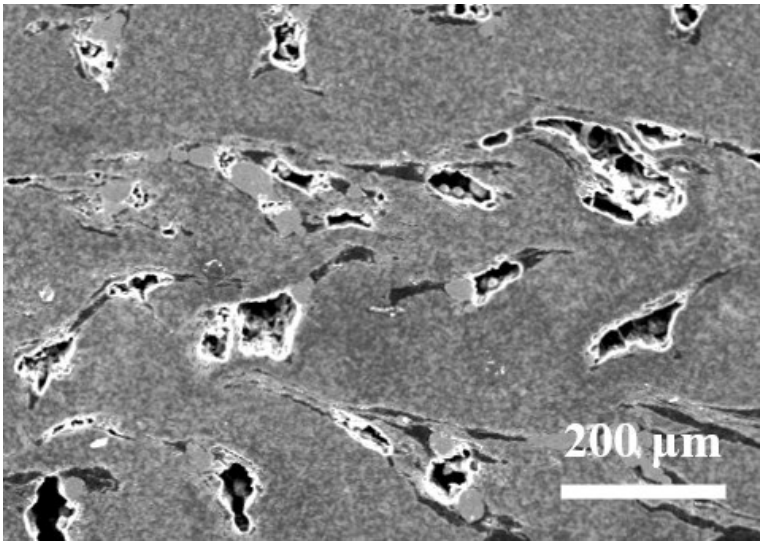


Figure 128. Cross section of a core/shell sample with graphene interface.

In addition, other approaches can be used to create weak interfaces beside carbon (e.g. monazite in oxide-oxide composites).[119]

References

1. Bird J. Exploring the 3D printing opportunity. Financial Times. 2012 8 August 2012.

2. Kodama H. *Automatic method for fabricating a three-dimensional plastic model with photo-hardening polymer*. Review of Scientific Instruments. 1981;**52**(11):p.1770-3.

3. Crump SS, inventor; Stratasys, Inc., assignee. *Apparatus and Method for Creating Three-dimensional Objects*. United States patent US005121329A. 1992.

4. Deckard C, inventor. *Method and apparatus for producing parts by selective sintering*. United States patent US4863538A. 1986.

5. Childs T, Berzins M. *Selective laser sintering of an amorphous polymer- simulations and experiments*. Proceedings of the Institution of Mechanical Engineers. 1999;**213**:p.333-49.

6. Wilkes J, Hagedorn Y-C, Meiners W, Konrad W. *Additive manufacturing of ZrO_2 Al_2O_3 ceramic components by selective laser melting*. Rapid Prototyping Journal 2013;**19**(1):p.51-7.

7. Keicher DM, Jelliosn JL, Schanwald LP, Romero JA. *Towards a Reliable Laser Spray Powder Deposition System Through Process Characterzation*. International Technical Conference of the Society for the Advancement of Material and Process Engineering Proceeding; Washington, D.C.1995.

8. Cesarano J. *A Review of Robocasting Technology*. MRS Proceedings. 1999;**542**:p.133-9.

9. Cesarano J, inventor; Sandia Corporation, assignee. *Freefroming Objects with Low-binder Slurry*. United States patent US006027326A. 2000.

10. Lewis JA, Smay JE, Stuecker J, Cesarano J. *Direct Ink Writing of Three-Dimensional Ceramic Structures*. Journal of the American Ceramic Society. 2006;**89**(12):p.3599-609.

11. Feilden E, Blanca EG-T, Giuliani F, Saiz E, Vandeperre L. *Robocasting of structural ceramic parts with hydrogel inks*. Journal of the European Ceramic Society. 2016;**36**(10):p.2525-33.

12. Schlordt T, Keppner F, Travitzky N, Greil P. *Robocasting of Alumina Lattice Truss Structures*. Journal of Ceramic Science and Technology. 2012;**3**(2):p.1-7.

13. Smay JE, Lewis JA. *Colloidal Inks for Directed Assembly of 3D periodic structures*. Langmuir : the ACS journal of surfaces and colloids. 2002;**18**(14):p.5429-37.

14. Xu M, Gratson GM, Duoss EB, Shepherd RF, Lewis JA. *Biomimetic silicification of 3D polyamine-rich scaffolds assembled by direct ink writing*. Soft matter. 2006;**2**(3):p.205.

15. Garcia-Tunon E, Barg S, Franco J, Bell R, Eslava S, D'Elia E, et al. *Printing in three dimensions with graphene (with supporting information)*. Advanced Materials. 2015;**27**(10):p.1688-93.

16. Lewis JA. *Direct Ink Writing of 3D Functional Materials*. Advanced Functional Materials. 2006;**16**(17):p.2193-204.

17. Minas C, Carnelli D, Tervoort E, Studart AR. *3D Printing of Emulsions and Foams into Hierarchical Porous Ceramics*. Advanced Materials. 2016;**28**(45):p.9993-9.

18. Costa Machado G, García-Tuñón E, Bell RV, Alini M, Saiz E, Peroglio M. *Calcium phosphate substrates with emulsion-derived roughness: Processing, characterisation and interaction with human mesenchymal stem cells*. Journal of the European Ceramic Society. 2018;**38**(3):p.949-61.

19. Muth JT, Lewis JA. *Microstructure and Elastic Properties of Colloidal Gel Foams*. Langmuir : the ACS journal of surfaces and colloids. 2017;**33**(27):p.6869-77.

20. Feilden E. Additive Manufacturing of Ceramics and Ceramic Composites via Robocasting: Imperial College London; 2017.

21. ISO/ASTM-52903-1:2020. Additive manufacturing — Material extrusion-based additive manufacturing of plastic materials. 2020.

22. Bertrand P, Bayle F, Combe C, Goeuriot P, Smurov I. *Ceramic components manufacturing by selective laser sintering*. Applied Surface Science. 2007;**254**(4):p.989-92.

23. Deckers J, Vleugels J, J.-P.Kruth. *Additive Manufacturing of Ceramics: A Review*. Journal of Ceramic Science and Technology. 2014;**05**(04):p.245-60.

24. Winslow H. Herschel RB. *Konsistenzmessungen von Gummi-Benzollosungen*. Kolloid Zeitschrift. 1926;**39**:p.291-300.

25. M'Barki A, Bocquet L, Stevenson A. *Linking Rheology and Printability for Dense and Strong Ceramics by Direct Ink Writing*. Scientific reports. 2017;**7**(1):p.6017.

26. James E. Smay JCI, Shawn Y. Lin, John N. Stuecker, Jennifer A. Lewis. *Robocasting of Photonic Band Gap Structures*. Solid Freeform Fabrication Symposium Proceeding. 2001:p.175-8.

27. Jakus AE, Taylor SL, Geisendorfer NR, Dunand DC, Shah RN. *Metallic Architectures from 3D-Printed Powder-Based Liquid Inks*. Advanced Functional Materials. 2015;**25**(45):p.6985-95.

28. Yetna N'Jock M, Camposilvan E, Gremillard L, Maire E, Fabrègue D, Chicot D, et al. *Characterization of 100Cr6 lattice structures produced by robocasting*. Materials & Design. 2017;**121**:p.345-54.

29. Paschalis Alexandridis TAH. *Poly(ethylene oxide)-poly(propylene oxide)-poly (ethylene oxide) block copolymer surfactants in aqueous solutions and at interfaces thermodynamics, structure, dynamics, and modeling*. Colloids and Surfaces A: Physicochemical and Engineering Aspect. 1995;**96**:p.1-46.

30. Lewis JA. *Colloidal Processing of Ceramics*. Journal of the American Ceramic Society. 2000;**83**(10):p.2341-59.

31. Kim F, Cote LJ, Huang J. *Graphene Oxide: Surface Activity and Two-Dimensional Assembly*. Advanced Materials. 2010;**22**(17):p.1954-8.

32. Studart AR, Gonzenbach UT, Tervoort E, Gauckler LJ. *Processing Routes to Macroporous Ceramics: A Review*. Journal of the American Ceramic Society. 2006;**89**(6):p.1771-89.

33. Bakumov V, Schwarz M, Kroke E. *Emulsion processing of polymer-derived porous Si/C/(O) ceramic bodies*. Journal of the European Ceramic Society. 2009;**29**(13):p.2857-65.

34. García-Tuñón E, Machado GC, Schneider M, Barg S, Bell RV, Saiz E. *Complex ceramic architectures by directed assembly of 'responsive' particles*. Journal of the European Ceramic Society. 2017;**37**(1):p.199-211.

35. Weaver JVM, Rannard SP, Cooper AI. *Polymer-Mediated Hierarchical and Reversible Emulsion Droplet Assembly*. Angewandte Chemie International Edition. 2009;**48**(12):p.2131-4.

36. Weaver JVM, Williams RT, Royles BJL, Findlay PH, Cooper AI, Rannard SP. *pH-Responsive branched polymer nanoparticles*. Soft matter. 2008;**4**(5):p.985.

37. Woodward RT, Hight C, Yildiz U, Schaeffer N, Valliant EM, Jones JR, et al. *Reversible aggregation of responsive polymer-stabilized colloids and the pH-dependent formation of porous scaffolds*. Soft matter. 2011;**7**(16):p.7560.

38. Sears NA, Dhavalikar PS, Cosgriff-Hernandez EM. *Emulsion Inks for 3D Printing of High Porosity Materials*. Macromolecular rapid communications. 2016;**37**(16):p.1369-74.

39. Costa Machado G. Calcium phosphate scaffolds with controlled properties for biological applications. London: Imperial College London; 2016.

40. Rocha VG, Saiz E, Tirichenko IS, García-Tuñón E. *Direct ink writing advances in multi-material structures for a sustainable future*. Journal of Materials Chemistry A. 2020;**8**(31):p.15646-57.

41. Schaller C. 4.8: Storage and Loss Modulus. Polymer Chemistry: Chemistry Libretexts; 2020.

42. Paar A. Basic of Rheology [Webpage]. 2020. Available from: https://wiki.anton-paar.com/uk-en/basics-of-rheology/#rheology-and-viscous-behavior.

43. Chan F CMF, Daniel De Kee. *Yield Stress and Small Amplitude Oscillatory Flow in Transient Networks*. Industrial & Engineering Chemistry Research. 1994;**33**:p.2374-6.

44. Glymond D, Vandeperre LJ. *Robocasting of MgO-doped alumina using alginic acid slurries*. Journal of the American Ceramic Society. 2018;**101**(8):p.3309-16.

45. Sommer MR, Alison L, Minas C, Tervoort E, Ruhs PA, Studart AR. *3D printing of concentrated emulsions into multiphase biocompatible soft materials*. Soft matter. 2017;**13**(9):p.1794-803.

46. Pilkey WD, Pilkey, D.F. . Peterson's Stress Concentration Factors. 3rd ed.1953.

47. Shimizu T, Matsuura K, Furue H, Matsuzak K. *Thermal conductivity of high porosity alumina refractory bricks made by a slurry gelation and foaming method*. Journal of the European Ceramic Society. 2013;**33**(15-16):p.3429-35.

48. Gauckler LJ, Waeber MM, Conti C, Jacob-Duliere M. *Ceramic Foam For Molten metal Filtration*. Jom. 2012;**37**(9):p.47-50.

49. Wataru Kotaui YO, Kazuhiko Kumazawa, inventor; NGK Insulators, Ltd, assignee. *Porous ceramic honeycomb filter*. United States patent US005545243A. 1996.

50. Johnson BR, Canfield NL, Tran DN, Dagle RA, Li XS, Holladay JD, et al. *Engineered SMR catalysts based on hydrothermally stable, porous, ceramic supports for microchannel reactors*. Catalysis Today. 2007;**120**(1):p.54-62.

51. Li C-J, Zou J, Huo H-B, Yao J-T, Yang G-J. *Microstructure and Properties of Porous Abradable Alumina Coatings Flame-Sprayed with Semi-molten Particles*. Journal of Thermal Spray Technology. 2015;**25**(1-2):p.264-72.

52. Jorge P. Arenas MJC. *Recent Trends in Porous Sound-Absorbing Materials*. Sound & Vibration. 2010;**44**(7):p.12-7.

53. Thorne R, Hu H, Schneider K, Bombelli P, Fisher A, Peter LM, et al. *Porous ceramic anode materials for photo-microbial fuel cells*. Journal of Materials Chemistry. 2011;**21**(44):p.18055.

54. Saiz E, Gremillard L, Menendez G, Miranda P, Gryn K, Tomsia AP. *Preparation of porous hydroxyapatite scaffolds*. Materials Science and Engineering: C. 2007;**27**(3):p.546-50.

55. Hammel EC, Ighodaro OLR, Okoli OI. *Processing and properties of advanced porous ceramics: An application based review*. Ceramics International. 2014;**40**(10):p.15351-70.

56. Mullens S. Cellular Ceramics: Structure, Manufacturing, Properties and Applications.2005.

57. Deville S, Saiz E, Tomsia AP. *Ice-templated porous alumina structures*. Acta Materialia. 2007;**55**(6):p.1965-74.

58. Deville S, Saiz E, Tomsia AP. *Freeze casting of hydroxyapatite scaffolds for bone tissue engineering*. Biomaterials. 2006;**27**(32):p.5480-9.

59. Sylvain Deville ES, Ravi K. Nalla, † Antoni P. Tomsia. *Freezing as a Path to Build Complex Composites*. Science. 2006;**311**:p.515-8.

60. Ferraro C, Garcia-Tuñon E, Rocha VG, Barg S, Fariñas MD, Alvarez-Arenas TEG, et al. *Light and Strong SiC Networks*. Advanced Functional Materials. 2016;**26**(10):p.1636-45.

61. Shan S-Y, Yang J-F, Gao J-Q, Zhang W-H, Jin Z-H, Janssen R, et al. *Porous Silicon Nitride Ceramics Prepared by Reduction-Nitridation of Silica*. Journal of the American Ceramic Society. 2005;**88**(9):p.2594-6.

62. Arita IH, Castano VM. *Synthesis and processing of hydroxyapatite ceramic tapes with controlled porosity*. Journal of Materials Science: Materials in Medicine. 1995;**6**:p.19-23.

63. Muth JT, Dixon PG, Woish L, Gibson oJ, Lewis JA. *Architected cellular ceramics with tailored stiffness via direct foam writing*. Proceedings of the National Academy of Sciences of the United States of America. 2017;**114**(8):p.1832-7.

64. Tekinalp HL, Kunc V, Velez-garcia GM, Duty CE, Love LJ, Naskar AK, et al. *Highly oriented carbon fiber–polymer composites via additive manufacturing*. Composite Science and Technology. 2014;**105**:p.144-50.

65. Hitchen SA, Ogin SL, Smith PA, Soutis C. *The effect of fibre length on fracture toughness and notched strength of short carbon fibre/epoxy composites*. Composites. 1994;**25**:p.407-13.

66. Zhang H, Zhang Z, Breidt C. *Comparison of short carbon fibre surface treatments on epoxy composites I. Enhancement of the mechanical properties*. Composite Science and Technology. 2004;**64**:p.2021–9.

67. Zhang H, Zhang Z, Friedrich K. *Effect of fiber length on the wear resistance of short carbon fiber reinforced epoxy composites*. Composite Science and Technology. 2007;**67**:p.222-30.

68. Compton BG, Lewis JA. *3D-printing of lightweight cellular composites*. Advanced Materials. 2014;**26**(34):p.5930-5.

69. Dong W, Liu HC, Park SJ, Jin FL. *Fracture toughness improvement of epoxy resins with short carbon fibers*. Journal of Industrial and Engineering Chemistry. 2014;**20**:p.1220-2.

70. Schlordt T, Schwanke S, Keppner F, Fey T, Travitzky N, Greil P. *Robocasting of alumina hollow filament lattice structures*. Journal of the European Ceramic Society. 2013;**33**(15-16):p.3243-8.

71. Luo Y, Zhai D, Huan Z, Zhu H, Xia L, Chang J, et al. *Three-Dimensional Printing of Hollow-Struts-Packed Bioceramic Scaffolds for Bone Regeneration*. ACS Appl Mater Interfaces. 2015;**7**(43):p.24377-83.

72. Moon Y-W, Choi I-J, Koh Y-H, Kim H-E. *Macroporous alumina scaffolds consisting of highly microporous hollow filaments using three-dimensional ceramic/camphene-based co-extrusion*. Journal of the European Ceramic Society. 2015;**35**(16):p.4623-7.

73. Thomas O. Powers TTH, Mary A. Peak, inventor; Geauga Company, assignee. *Rubber/Plastic Co-extrusion*. United States patent US005334458A. 1994.

74. Mueller J, Raney JR, Shea K, Lewis JA. *Architected Lattices with High Stiffness and Toughness via Multicore-Shell 3D Printing*. Adv Mater. 2018;**30**(12):p.e1705001.

75. Xia Y, Lu Z, Cao J, Miao K, Li J, Li D. *Microstructure and mechanical property of Cf/SiC core/shell composite fabricated by direct ink writing*. Scripta Materialia. 2019;**165**:p.84-8.

76. Hirschfeld DA, Stuecker, J.N., Cesarano, J., He, G.P. *Robocasting and Mechanical Testing of Aqueous Silicon Nitride Slurries*. OSTI2000. p. 1-8.

77. Therriault D, White SR, Lewis JA. *Rheological Behavior of Fugitive Organic Inks for Direct-Write Assembly*. Applied Rheology. 2007;**17**(1):p.10112-1--8.

78. García-Tuñón E, Feilden E, Zheng H, D'Elia E, Leong A, Saiz E. *Graphene Oxide: An All-in-One Processing Additive for 3D Printing*. ACS Applied Materials & Interfaces. 2017;**9**(38):p.32977-89.

79. Durig JR, Gounev TK, Guirgis GA, Zhen P,. *Infrared and Raman spectra, conformational stability, normal coordinate analysis, ab initio calculations, and vibrational assignment of 1–methylsilacyclobutane*. Journal of Molecular Structure. 2000;**500**(1):p.275-91.

80. Cullity BD, Weymouth JW. *Element of X-Ray Diffraction*. American Journal of Physics. 1957;**25**(6):p.394-5.

81. Garcia-Tunon E, Barg S, Bell R, Weaver JV, Walter C, Goyos L, et al. *Designing smart particles for the assembly of complex macroscopic structures*. Angewandte Chemie. 2013;**52**(30):p.7805-8.

82. Janna WS. Introduction to Fluid Mechanics. 6th ed.2015.

83. Duoss EB, Twardowski M, Lewis JA. *Sol-Gel Inks for Direct-Write Assembly of Functional Oxides*. Advanced Materials. 2007;**19**(21):p.3485-9.

84. Chen T. Rheological Techniques for Yield Stress Analysis: TA Instruments; [cited 2020 14/09/2020]. Available from: http://www.tainstruments.com/pdf/literature/RH025.pdf.

85. Chan SSL, Sesso ML, Franks GV. *Direct ink writing of hierarchical porous alumina-stabilized emulsions: Rheology and printability*. Journal of the American Ceramic Society. 2020;**103**(10):p.5554-66.

86. Gibson LJ. *Modelling the Mechanical Behavior of Cellular Materials*. Materials Science and Engineering: A. 1989;**110**:p.1-36.

87. Zhang X, Huo W, Liu J, Zhang Y, Zhang S, Yang J. *3D printing boehmite gel foams into lightweight porous ceramics with hierarchical pore structure*. Journal of the European Ceramic Society. 2020;**40**(3):p.930-4.

88. Thomas Ostrowski, Rodel J. *Evolution of Mechanical Properties of Porous Alumina during Free Sintering and Hot Pressing*. Journal of the American Ceramic Society. 1999;**82**(11):p.3080-6.

89. Mao X, Shimai S, Wang S. *Gelcasting of alumina foams consolidated by epoxy resin*. Journal of the European Ceramic Society. 2008;**28**(1):p.217-22.

90. Chakravarty D, Ramesh H, Rao TN. *High strength porous alumina by spark plasma sintering*. Journal of the European Ceramic Society. 2009;**29**(8):p.1361-9.

91. Ferraro C, Garcia-Tunon E, Barg S, Miranda M, Ni N, Bell R, et al. *SiC porous structures obtained with innovative shaping technologies*. Journal of the European Ceramic Society. 2018;**38**(3):p.823-35.

92. Chawla KK. Composite Materials Science and Engineering. third ed: Springer-Verlag New York.2012. 542 p.

93. ASTM-E-1820-11. Standard Test Method for Measurement of Fracture Toughness. ASTM International; 2012. p. 14.

94. Smith RL, Mecholsky JJ, Freiman SW. *Estimation of fracture energy from the work of fracture and fracture surface area: I. Stable crack growth*. International Journal of Fracture. 2009;**156**(1):p.97-102.

95. Clegg WJ, Kendall K, Alford MN, Button TW, Brichall JD. *A simple way to make tough ceramics*. Letters to Nature. 1990;**347**:p.455-7.

96. Mukai K, Zushu Li, Zeze M. *Surface Tension and Wettability of Liquid Fe–16mass%Cr–O Alloy with Alumina.pdf>*. Materials Transactions. 2002;**43**(7):p.1724-31.

97. Saiz E, Cannon RM, Tomsia AP. *High-Temperature Wetting and the Work of Adhesion in Metal/Oxide Systems*. Annual Review of Materials Research. 2008;**38**(1):p.197-226.

98. Węglewski W, Basista M, Manescu A, Chmielewski M, Pietrzak K, Schubert T. *Effect of grain size on thermal residual stresses and damage in sintered chromium–alumina composites: Measurement and modeling*. Composites Part B: Engineering. 2014;**67**:p.119-24.

99. Ellingham HJT. *Transactions and Communications*. Journal of the Society of Chemical Industry. 1994;**63**:p.125-60.

100. Powell KL, Smith PA, Yeomans JA. *Aspect of Residual Thermal Stresses in Continuous-Fibre-Reinforced Ceramic Matrix Composites*. Composite Science and Technology. 1993;**47**:p.359-67.

101. Vedula M, Pangborn RN, Queeney RA. *Fibre anisotropic thermal expansion and residual thermal stress in a graphite/aluminium composite*. Composites. 1988;**19**(1):p.55-60.

102. Ruys A. Alumina Ceramics: biomedical and Clinical Applications. Ruys A, editor: Woodhead Publishing.2019.

103. KOVACIK J. *Correlation between Young's modulus and porosity in porous materials*. Journal of Materials Science Letters 1999;**18**:p.1007-10.

104. Bertram Hopkinson, Rogers F. *The Elastic Properties of Steel at High Temperature*. Proceedings of the Royal Society of London Series A, Containing Papers of a Mathematical and Physical Character. 1905;**LXXVI**:p.419-25.

105. Latella BA, Humphries SR. *Young's modulus of a 2.25Cr–1Mo steel at elevated temperature*. Scripta Materialia. 2004;**51**(7):p.635-9.

106. COOKE GME. *An Introduction to the Mechanical Properties of Structural Steel at Elevated Tremperatures*. Fire Safety Journal. 1988;**13**:p.45-54.

107. Miranda P, Pajares A, Saiz E, Tomsia AP, Guiberteau F. *Mechanical properties of calcium phosphate scaffolds fabricated by robocasting*. Journal of biomedical materials research Part A. 2008;**85**(1):p.218-27.

108. Lidija Ćurković, Ante Bakić, Janoš Kodvanj, Haramina T. *Flexural strength of alumina ceramics: Weibull analysis*. Transcations of FEMENA. 2010:p.1-8.

109. Strobl S, Supancic P, Lube T, Danzer R. *Surface crack in tension or in bending – A reassessment of the Newman and Raju formula in respect to fracture toughness measurements in brittle materials*. Journal of the European Ceramic Society. 2012;**32**(8):p.1491-501.

110. Aveston J, Kelly A. *Theory of multiple fracture of fibrous composites*. Journal of Materials Science: Materials in Medicine. 1973;**8**:p.352-62.

111. Hoffman M, Fiedler B, Emmel T, Prielipp H, Claussen N, Dross D, et al. *Fracture Behaviour in Metal Fibre Reinforced Ceramics*. Acta Materialia. 1997;**45**(9):p.3609-23.

112. Pemberton SR, Oberg EK, Dean J, Tsarouchas D, Markaki AE, Marston L, et al. *The fracture energy of metal fibre reinforced ceramic composites (MFCs)*. Composites Science and Technology. 2011;**71**(3):p.266-75.

113. Ferraro C, Meille S, Réthoré J, Ni N, Chevalier J, Saiz E. *Strong and tough metal/ceramic micro-laminates*. Acta Materialia. 2018;**144**:p.202-15.

114. Cortie M. *Effect of Temperature on the Resistance to Tearing of Stainless-steel Sheet Type 430*. The Iron and Steel Institute of Japan International. 1994;**34**(5):p.443-50.

115. Zhao Kang, Yan Junhun, Xiulin Z. *On Notch Tensile Strength and its Probability Distribution of Thin Alumina Specimen*. Journal of the Chinese ceramic society. 1998;**26**(6):p.787-91.

116. Power N. Properties of Ferrotoc Stainless Steel- Grade 430: Nuclear Power; 2020 [cited 2020 10/09/2020]. Available from: https://www.nuclear-power.net/nuclear-engineering/metals-what-are-metals/stainless-steel/ferritic-stainless-steel/properties-of-ferritic-stainless-steel-grade-430/.

117. Materials A. Stainless Steel - Grade 430 (UNS S43000): AZO Materials; 2020 [cited 2020 10/09/2020]. Available from: https://www.azom.com/article.aspx?ArticleID=996

118. McCartnry LN. *Mechanics of matrix cracking in brittle-matrix fibre-reinforced composites*. Proceedings of the Royal Society of London Series A. 1987;**409**:p.329-50.

119. Davis JB, Marshall DB, Morgan PED. *Monazite-containing oxide/oxide composites*. Journal of the European Ceramic Society. 2000;**20**:p.583-7.